



MINISTÉRIO DA CIÊNCIA, TECNOLOGIA E INOVAÇÃO
INSTITUTO NACIONAL DE PESQUISAS ESPACIAIS

sid.inpe.br/mtc-m21b/2016/04.12.01.06-TDI

ON THE MECHANISMS THAT LEAD TO MULTIPLE GROUND CONTACTS IN LIGHTNING

Leandro Zanella de Souza Campos

Doctorate Thesis of the Graduate
Course in Space Geophysics,
guided by Drs. Osmar Pinto
Junior, and Kenneth L. Cummins,
approved in may 11, 2016.

URL of the original document:

[<http://urlib.net/8JMKD3MGP3W34P/3LG4CDL>](http://urlib.net/8JMKD3MGP3W34P/3LG4CDL)

INPE
São José dos Campos
2016

PUBLISHED BY:

Instituto Nacional de Pesquisas Espaciais - INPE

Gabinete do Diretor (GB)

Serviço de Informação e Documentação (SID)

Caixa Postal 515 - CEP 12.245-970

São José dos Campos - SP - Brasil

Tel.:(012) 3208-6923/6921

Fax: (012) 3208-6919

E-mail: pubtc@inpe.br

**COMMISSION OF BOARD OF PUBLISHING AND PRESERVATION
OF INPE INTELLECTUAL PRODUCTION (DE/DIR-544):****Chairperson:**

Maria do Carmo de Andrade Nono - Conselho de Pós-Graduação (CPG)

Members:

Dr. Plínio Carlos Alvalá - Centro de Ciência do Sistema Terrestre (CST)

Dr. André de Castro Milone - Coordenação de Ciências Espaciais e Atmosféricas (CEA)

Dra. Carina de Barros Melo - Coordenação de Laboratórios Associados (CTE)

Dr. Evandro Marconi Rocco - Coordenação de Engenharia e Tecnologia Espacial (ETE)

Dr. Hermann Johann Heinrich Kux - Coordenação de Observação da Terra (OBT)

Dr. Marley Cavalcante de Lima Moscati - Centro de Previsão de Tempo e Estudos Climáticos (CPT)

Silvia Castro Marcelino - Serviço de Informação e Documentação (SID) **DIGITAL**

LIBRARY:

Dr. Gerald Jean Francis Banon

Clayton Martins Pereira - Serviço de Informação e Documentação (SID)

DOCUMENT REVIEW:

Simone Angélica Del Ducca Barbedo - Serviço de Informação e Documentação (SID)

Yolanda Ribeiro da Silva Souza - Serviço de Informação e Documentação (SID)

ELECTRONIC EDITING:

Marcelo de Castro Pazos - Serviço de Informação e Documentação (SID)

André Luis Dias Fernandes - Serviço de Informação e Documentação (SID)



MINISTÉRIO DA CIÊNCIA, TECNOLOGIA E INOVAÇÃO
INSTITUTO NACIONAL DE PESQUISAS ESPACIAIS

sid.inpe.br/mtc-m21b/2016/04.12.01.06-TDI

ON THE MECHANISMS THAT LEAD TO MULTIPLE GROUND CONTACTS IN LIGHTNING

Leandro Zanella de Souza Campos

Doctorate Thesis of the Graduate
Course in Space Geophysics,
guided by Drs. Osmar Pinto
Junior, and Kenneth L. Cummins,
approved in may 11, 2016.

URL of the original document:

[<http://urlib.net/8JMKD3MGP3W34P/3LG4CDL>](http://urlib.net/8JMKD3MGP3W34P/3LG4CDL)

INPE
São José dos Campos
2016

Cataloging in Publication Data

Campos, Leandro Zanella de Souza.

C157m On the mechanisms that lead to multiple ground contacts in lightning / Leandro Zanella de Souza Campos. – São José dos Campos : INPE, 2016.

xxxii + 248 p. ; (sid.inpe.br/mtc-m21b/2016/04.12.01.06-TDI)

Thesis (Doctorate in Space Geophysics) – Instituto Nacional de Pesquisas Espaciais, São José dos Campos, 2016.

Guiding : Drs. Osmar Pinto Junior, and Kenneth L. Cummins.

1. Lightning. 2. Cloud-to-ground discharges. 3. Cluster analysis. 4. Ground contact points. 5. Multiple ground terminations. I.Title.

CDU 551.594.21



Esta obra foi licenciada sob uma Licença [Creative Commons Atribuição-NãoComercial 3.0 Não Adaptada](#).

This work is licensed under a [Creative Commons Attribution-NonCommercial 3.0 Unported License](#).

Aluno (a): **Leandro Zanella de Souza Campos**

Título: "ON THE MECHANISMS THAT LEAD TO MULTIPLE GROUND CONTACTS IN LIGHTNING"

Aprovado (a) pela Banca Examinadora
em cumprimento ao requisito exigido para
obtenção do Título de **Doutor(a)** em
Geofísica Espacial/Ciências Atmosféricas

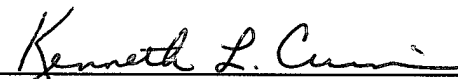
Dr. Alisson Dal Lago


Presidente / INPE / São José dos Campos - SP

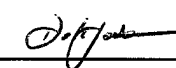
Dr. Osmar Pinto Junior


Orientador(a) / INPE / SJCampos - SP

Dr. Kenneth L. Cummins


Orientador(a) / Univ. of Arizona / Tucson - AZ

Dr. Delano Gobbi


Membro da Banca / INPE / SJCampos - SP

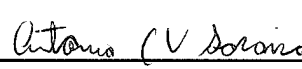
Dr. Marcelo Magalhães Fares Saba


Membro da Banca / INPE / SJCampos - SP

Dr. Vandoir Bourscheidt


Convidado(a) / UFSCAR / São Carlos - SP

Dr. Antonio Carlos Varela Saraiva


Convidado(a) / UNESP/ICT / São José dos Campos - SP

Este trabalho foi aprovado por:

() maioria simples

(x) unanimidade

São José dos Campos, 11 de maio de 2016

“Living is easy with eyes closed”

from “Strawberry Fields Forever”, by John Lennon

*À memória dos meus queridos avôs, Jairo e José, que nos deixaram enquanto eu ainda
me dedicava a este trabalho.*

ACKNOWLEDGMENTS

Este trabalho é o resultado direto do esforço, dedicação, compreensão, carinho e sacrifício de inúmeras pessoas que muitas vezes me honraram com sua presença e confiança. Agradeço a meus pais, Dimas e Sueli, e minha irmã Cristiane, pelo muitos anos de convívio diário repleto de encorajamento e incentivo irrestritos. Agradeço também a minha esposa Viviane pelo carinho, companheirismo e cumplicidade que foram sempre preciosos desde o dia em que a conheci. Sou também grato a toda a minha família, que sempre acreditou em mim e aceitou as excentricidades da vida acadêmica.

Ao Dr. Osmar Pinto Junior, por ter aceitado me orientar e ter confiado em minha capacidade e esforço para desenvolver este trabalho, dedicando muitas horas para inúmeras discussões valiosas.

Ao Dr. Kenneth Cummins, por ter me acolhido com muita dedicação durante os seis meses que passei em Tucson, compartilhando comigo um volume surpreendentemente grande de conhecimento em um período de tempo surpreendentemente curto, e pelo contínuo suporte mesmo após meu retorno. A sua esposa Suzanne, pela companhia divertida que fez com que eu me sentisse em casa em vários momentos.

(To Dr. Kenneth Cummins, for welcoming me with great care and attention during the six months I spent in Tucson, sharing with me a surprisingly large volume of knowledge in a surprisingly short amount of time, and for the continuing support even after my return. To his wife Suzanne, for the fun companionship that made me feel at home in many moments.)

Ao Dr. Phil Krider, pelo seu exemplo e sua forma gentil de contribuir, opinar e transmitir conhecimento.

(To Dr. Phil Krider, for his example and his gentle way of contributing, providing opinions and transferring knowledge.)

Ao Dr. Paul Krehbiel e ao Dr. William Rison, pelas valiosas discussões e auxílio com parte da instrumentação e dados que foram imprescindíveis para a realização desta tese.

(To Dr. Paul Krehbiel and Dr. William Rison for the valuable discussions and assistance with part of the instruments and datasets that were vital for this thesis.)

Ao Dr. Antonio Saraiva, pela colaboração e amizade, e pelos numerosos debates científicos.

Ao INPE, Instituto Nacional de Pesquisas Espaciais, e à Universidade do Arizona, por terem oferecido a infraestrutura necessária para a realização deste trabalho.

A todos os membros do ELAT, Grupo de Eletricidade Atmosférica do INPE, pelo precioso apoio técnico. Ao Dr. Marcelo Saba por ter me dado o primeiro incentivo no início da minha caminhada acadêmica. À Dra. Iara Pinto pelas disciplinas lecionadas e pelos seus preciosos conselhos.

A todos os meus amigos e colegas de todas as épocas, pelo companheirismo que sempre me impulsionou.

Aos docentes do curso de pós-graduação em Geofísica Espacial do INPE, pela sua dedicação e por todo o conhecimento transferido.

A todos os professores de todas as áreas que contribuíram com a minha caminhada, com especial reverência ao Professor Maurício Furlan.

À Vaisala, pelo apoio ao disponibilizar os dados da *U.S. National Lightning Detection Network* (NLDN). À *National Science Foundation* (projeto AGS-1205727) e o programa DARPA NIMBUS por viabilizarem a coleta de dados realizada ao longo da *Kansas Windfarm2013 Field Program* (KSWFP).

(To Vaisala, for providing me access to datasets from the U.S. National Lightning Detection Network. To the National Science Foundation, grant AGS-1205727, and the DARPA NIMBUS program for supporting the instruments and data collection during the Kansas Windfarm2013 Field Program.)

Finalmente, agradeço à CAPES, Coordenação de Aperfeiçoamento de Pessoal de Nível Superior, e à FAPESP, Fundação de Amparo à Pesquisa do Estado de São Paulo (através dos projetos 2013/18785-4 e 2014/01838-0), pelo apoio financeiro ao longo dos últimos quatro anos que tornou possível a execução desta pesquisa. Parte das análises apresentadas nesta tese também recebeu apoio dos projetos FAPESP 2008/56711-4 e 2010/01742-2.

ABSTRACT

Negative cloud-to-ground (–CG) lightning is an essentially discrete phenomenon (with multiple individual return strokes) and frequently strikes ground on more than one location. The main objective of this thesis work is to bring new light into the mechanisms through which a –CG can produce more than one ground termination and which factors modulate that characteristic. The first step towards that goal was the development of an algorithm, named *groupGCP*, that is capable of processing data provided by VLF/LF Lightning Location Systems (LLS) and deriving ground contact point (GCP) information by grouping each stroke into an optimized strike point position. This is the first method of this kind that makes full use of all error ellipse parameters provided by some of the present day sensor technologies. The second step concerns detailed individual case studies of lightning events. The first of these analyses approaches the phenomenology of forked and upward-illumination strokes. They are capable of touching ground at multiple locations within very short intervals, ranging from a few microseconds up to a few milliseconds. Some crucial differences between these two classes of events are identified and discussed in detail. Next, the more common subsequent new ground contact (NGC) stroke is analyzed from data provided by a three-dimensional VHF Lightning Mapping Array (LMA) along with auxiliary information provided by VLF/LF LLS, video and electric field records. Three very distinct mechanisms that lead to NGC subsequent strokes were identified: Type I consists of dart leaders that diverge from the path of the preceding stroke; Type II originate from in-cloud horizontally propagating channels that move away from the preceding GCP during the interstroke interval; and Type III consists of NGC subsequent strokes that originate as apparently independent stepped leader processes. The sample of events of each class suggests that Type I commonly produce ground terminations up to 1 km away from the preceding GCP, while Types II and III may lead to horizontal separations between GCPs of more than 7 km. In the third step some factors that may modulate the occurrence and characteristics of multi-grounded flashes are analyzed. Spatial distributions are compared with complex terrain features (both absolute altitude and high spatial frequency variations) for three different domains. No consistent correlation was found for all of them and, although some insights could be obtained, further investigations with additional instruments are necessary to evaluate any possible relationship. Also, diurnal climatology of the mean number of channels per flash and the separation between them were obtained. All three domains presented very similar diurnal cycles, suggesting that there may be driving factors or mechanisms that are shared among all of them. However, the possibility that the observed trends are actually caused by classification errors by the algorithm is also discussed. Finally, the thesis concludes with two examples of technological applications of the *groupGCP* algorithm: the improvement of risk assessment techniques that are suggested by international lightning protection standards, and the analysis of lightning-caused power line faults.

Keywords: Lightning. Cloud-to-ground discharges. Cluster analysis. Ground contact points. Multiple ground terminations. Lightning location systems.

SOBRE OS MECANISMOS QUE LEVAM À PRODUÇÃO DE MÚLTIPLOS PONTOS DE CONTATO EM RELÂMPAGOS

RESUMO

Relâmpagos nuvem-solo negativos são fenômenos essencialmente discretos (apresentando múltiplas descargas de retorno individuais) e frequentemente atingem o solo em mais de um local. O objetivo principal desta tese é obter novas informações acerca dos mecanismos através dos quais um relâmpago pode produzir mais de um ponto de contato. O primeiro passo nesta direção consiste no desenvolvimento de um algoritmo denominado *groupGCP*, capaz de processar dados de redes de detecção de larga escala (em VLF/LF) e obter informações de pontos de contato ao agrupar descargas de retorno individuais. Este é o primeiro método desta natureza que utiliza integralmente as informações de elipses de erro fornecidas por alguns tipos de sensores atuais. O segundo passo envolve estudos de caso detalhados de relâmpagos individuais. A primeira destas análises aborda a fenomenologia de relâmpagos bifurcados e do tipo “*upward illumination*”. Esta classe de fenômenos é capaz de tocar o solo em múltiplos locais dentro de períodos de tempo muito curtos, de alguns microssegundos até alguns milissegundos. Algumas diferenças cruciais entre os dois tipos foram identificadas e discutidas em detalhes. Em seguida, casos de formação de novos pontos de contato em descargas de retorno subsequentes são analisados através de dados de mapeamento em três dimensões fornecidos por uma rede LMA (*Lightning Mapping Array*) juntamente com dados auxiliares de redes de detecção em VLF/LF, vídeo e campo elétrico. Três mecanismos distintos de iniciação de novos pontos de contato foram identificados: Tipo I consiste em líderes contínuos que divergem do canal de uma descarga anterior; Tipo II origina-se em canais que se propagam horizontalmente no interior da nuvem de tempestade; e Tipo III consiste em descargas de retorno subsequentes que se formam em líderes escalonados independentes. A amostra de eventos de cada classe sugere que Tipo I normalmente produz pontos de contato a até 1 km do ponto anterior, enquanto Tipos II e III podem levar a separações entre contatos de até mais de 7 km. No terceiro passo alguns fatores que podem modular a ocorrência e características de relâmpagos com múltiplos pontos de contato são analisados. Distribuições espaciais foram comparadas com dados de relevo (tanto em altitude absoluta quanto em variações espaciais de alta frequência) em três domínios diferentes. Nenhuma correlação consistente entre os três domínios pôde ser encontrada, e ainda que algumas informações novas tenham sido obtidas, estudos futuros com instrumentos adicionais são necessárias. Climatologias diurnas foram geradas para o número médio de canais por raio e a separação entre eles. Os três domínios apresentaram ciclos diurnos bastante semelhantes, o que sugere que podem existir fatores ou mecanismos comuns a todos eles. Por outro lado, também se discute a possibilidade de que as tendências observadas foram na verdade causadas por erros de classificação do algoritmo. Finalmente, a tese é concluída com dois exemplos de aplicações tecnológicas envolvendo o uso do algoritmo *groupGCP*: o aprimoramento de técnicas de avaliação de risco que são sugeridas por padrões

internacionais de proteção contra descargas atmosféricas, e a análise de falhas em linhas de distribuição que são causadas por relâmpagos.

Palavras-chave: Relâmpagos. Descargas nuvem-solo. Análise de agrupamento. Pontos de contato. Múltiplas terminações no solo. Redes de detecção de relâmpagos.

LIST OF FIGURES

	<u>Page</u>
Figure 2.1 – Electric charge centers of thunderclouds.	6
Figure 2.2 – Main steps of a negative cloud-to-ground flash.	7
Figure 2.3 – Charge distributions in the classical and bidirectional leader models.	12
Figure 2.4 – Bidirectional development of (a/b) cloud-to-ground and (c/d) intracloud flashes.	13
Figure 2.5 – Bidirectional leader development in an airplane struck by lightning.	14
Figure 2.6 – Recoil leaders in the bidirectional development of a negative CG flash. ...	16
Figure 2.7 – Illustration of a “new channel flash” (NCF).	19
Figure 2.8 – Illustration of an “altered channel flash” (ACF).	19
Figure 2.9 – Space-time occurrence distribution of first subsequent strokes.	21
Figure 2.10 – Mechanism of new ground contacts suggested by Zoghzy et al. (2014).	22
Figure 2.11 – Mechanism of new ground contacts suggested by Sun et al. (2016).	23
Figure 3.1 – Picture of a slow electric field antenna and its circuitry housing.	35
Figure 3.2 – Schematic diagram of a typical slow electric field antenna.	36
Figure 3.3 – Examples of slow electric field waveforms at different distances.	38
Figure 3.4 – Lightning power spectrum and the sensor types used to detect it.	39
Figure 3.5 – The principle of the magnetic direction finding (MDF) technique.	40
Figure 3.6 – Return stroke location from two magnetic direction finders.	41
Figure 3.7 – Detection ambiguity on the baseline between magnetic direction finders.	42
Figure 3.8 – Return stroke location based on three magnetic direction finders.	43
Figure 3.9 – Return stroke location based on differences in time-of-arrival.	44
Figure 3.10 – Return stroke location ambiguity in three-sensor TOA solutions.	45
Figure 3.11 – Return stroke location through the IMPACT technology.	46
Figure 3.12 – Picture of one installed Lightning Mapping Array (LMA) station.	47
Figure 3.13 – Geometry of the TOA technique used in LMA networks.	48
Figure 3.14 – Example of a multi-grounded –CG flash mapped by an LMA network. ...	50
Figure 3.15 – Relative positions of the scientific instruments used in the KSWFP.	52

Figure 3.16 – Estimated location accuracy of the LMA used during the KSWFP.....	53
Figure 3.17 – Post-upgrade map of minimum detectable peak current for the NLDN..	55
Figure 3.18 – Location error ellipse from two-dimensional Gaussian distributions.	56
Figure 3.19 – Field of view of the standard speed fixed camera at the O&M building.	57
Figure 3.20 – Field of view of the standard speed fixed camera at the substation.....	57
Figure 3.21 – RAMMER 1 station installed at its fixed observation position.	59
Figure 3.22 – Map of the four (one mobile, three fixed) RAMMER stations that were operational during the summer 2013 campaign.	60
Figure 3.23 – Current status and future plans for the sensor deployment of BrasilDAT.	61
Figure 4.1 – Illustration of ellipse scaling.	66
Figure 4.2 – An eight-stroke CG flash being analyzed by the <i>groupGCP</i> algorithm. ...	70
Figure 4.3 – First step of “progressive k -means”: $k = 1$	71
Figure 4.4 – Second step of “progressive k -means”: $k = 2$	72
Figure 4.5 – Third step of “progressive k -means”: $k = 3$	72
Figure 4.6 – The poorly located ellipse is grouped into one existing GCP.....	73
Figure 4.7 – Example of eleven-stroke flash with a single ground contact point.	74
Figure 4.8 – Example of four-stroke flash with two ground contact points.....	74
Figure 5.1 –RAMMER sensors and the 26 MGCSs detected by BrasilDAT.....	78
Figure 5.2 – Example of a monochromatic frame displayed in false color with PyRAW.	79
Figure 5.3 – False color frames and electric field record of the forked stroke of Flash #1.	81
Figure 5.4 – False color frames and electric field record of the forked stroke of Flash #54.....	83
Figure 5.5 – False color frames and electric field record of the UI stroke of Flash #17.	85
Figure 5.6 – Evolution of UI process of Flash #17.	86
Figure 5.7 –Stepped leader evolution of the UI stroke of Flash #17.....	88
Figure 5.8 – False color frames and electric field record of the UI stroke of Flash #85.	90
Figure 5.9 – Details of the UI branch of Flash #85.	90
Figure 5.10 – Details of an attempted leader in the UI branch of Flash #85.....	92

Figure 5.11 – Stepped leader evolution of the UI stroke of Flash #85.....	93
Figure 5.12 – Example of forked stroke.....	95
Figure 5.13 – Example of upward-illumination (UI) stroke.....	96
Figure 5.14 – The most intense and the total brightened segments of a UI channel.....	98
Figure 5.15 – Example of four raw BrasilDAT electric waveforms for a forked stroke.	102
Figure 5.16 – Ratio between electric field peaks <i>versus</i> time interval between them for the ground contacts of each MGCS event.....	105
Figure 5.17 – Estimated peak current pairs <i>versus</i> time interval between them for the ground contacts of each MGCS event.....	106
Figure 6.1 – Full flash LMA plot of Case I.1.....	114
Figure 6.2 – LMA plot of the initiation of the first stroke of Case I.1.....	115
Figure 6.3 – LMA plot of the initiation of the second stroke (NGC) of Case I.1.....	116
Figure 6.4 – Slow electric field waveform of the interval between the first and second return strokes of Case I.1.....	117
Figure 6.5 – Development of Case I.1 after its second stroke.....	118
Figure 6.6 – Full flash LMA plot of Case I.2.....	119
Figure 6.7 – Selected high-speed video frames of the first two strokes of Case I.2. ...	120
Figure 6.8 – LMA plot of the initiation of the first stroke of Case I.2.....	121
Figure 6.9 – LMA plot of the initiation of the second stroke (NGC) of Case I.2.....	122
Figure 6.10 – Slow electric field waveform of the interval between the first and second return strokes of Case I.2.....	123
Figure 6.11 – Development of Case I.2 after its second stroke.....	124
Figure 6.12 – Illustration of the mechanism of a Type I new ground contact creation.....	125
Figure 6.13 – Full flash LMA plot of Case II.1.....	128
Figure 6.14 – LMA plot of the initiation of the first stroke of Case II.1.....	129
Figure 6.15 – LMA plot of the initiation of the second stroke (NGC) of Case II.1.....	130
Figure 6.16 – Waveforms of the closest three slow electric field antennas showing the first return stroke of Case II.1 and the following 50 milliseconds.....	131
Figure 6.17 – Full flash LMA plot of Case II.2.....	132
Figure 6.18 – LMA plot of the first two strokes of Case II.2.....	133

Figure 6.19 – Waveforms of the closest three slow electric field antennas showing the interval between the first and second (PEC) return strokes of Case II.2.	134
Figure 6.20 – LMA plot of the initiation of the third stroke (NGC) of Case II.2.....	135
Figure 6.21 – Waveforms of the closest three slow electric field antennas showing the interval between the second and third (NGC) return strokes of Case II.2.	136
Figure 6.22 – Development of Case II.2 after its third stroke.	137
Figure 6.23 – Illustration of the mechanism of a Type II new ground contact creation.	138
Figure 6.24 – Full flash LMA plot of Case III.1.	140
Figure 6.25 – LMA plot of the initiation of the first stroke of Case III.1.	141
Figure 6.26 – LMA plot of the initiation of the second stroke (NGC) of Case III.1....	142
Figure 6.27 – Waveforms of the closest three slow electric field antennas showing the interval between the first and second (NGC) return strokes of Case III.1.	143
Figure 6.28 – LMA plot of the initiation of the third stroke (NGC) of Case III.1.	144
Figure 6.29 – Waveforms of the closest three slow electric field antennas showing the interval between the second and third (NGC) return strokes of Case III.1.	145
Figure 6.30 – LMA plot of the initiation of the fourth stroke (NGC) of Case III.1.	146
Figure 6.31 – Waveforms of the closest three slow electric field antennas showing the interval between the third and fourth (NGC) return strokes of Case III.1.	147
Figure 6.32 – Full flash LMA plot of Case III.2.	148
Figure 6.33 – LMA plot of the initiation of the first stroke of Case III.2.	149
Figure 6.34 – LMA plot of the initiation of the second stroke (NGC) of Case III.2....	150
Figure 6.35 – Waveforms of the closest three slow electric field antennas showing the interval between the first and second (NGC) return strokes of Case III.2.	151
Figure 6.36 – Illustration of the mechanism of a Type III new ground contact creation.	152

Figure 6.37 – Selected high-speed video frames of the first stroke and subsequent attempted leader observed on May 28 th , 2013, at 00:59:01 (UT).	154
Figure 6.38 – LMA plot of the attempted leader.	155
Figure 6.39 – LMA sources height <i>versus</i> time plot compared with the electric field records of the attempted leader.	156
Figure 6.40 – High order NGC stroke, full flash LMA plot.	157
Figure 6.41 – LMA plot of the initiation of the tenth (NGC) stroke.	158
Figure 6.42 – LMA sources height <i>versus</i> time plot compared with the electric field records preceding the high order NGC stroke.	159
Figure 7.1 – Relative positions of the three domains considered in this analysis.	162
Figure 7.2 – One-dimensional illustration of the process of obtaining terrain spatial frequency.	165
Figure 7.3 – Altitude map of the Arkansas domain.	167
Figure 7.4 – Smoothed altitude map of the Arkansas domain with contour lines.	167
Figure 7.5 – Spatial frequency terrain variations of the Arkansas domain.	168
Figure 7.6 – Spatial distribution of the density of return strokes (from multi-stroke flashes only) of the Arkansas domain.	169
Figure 7.7 – Spatial distribution of the mean number of channels per flash (CPF) of the Arkansas domain.	170
Figure 7.8 – Spatial distribution of the mean separation distance between the first two ground contact points of each MGCF of the Arkansas domain.	170
Figure 7.9 – Smoothed altitude map of the mountainous region of the Arkansas domain with contour lines.	171
Figure 7.10 – Spatial frequency terrain variations of the mountainous region of the Arkansas domain.	171
Figure 7.11 – Spatial distribution of the mean separation distance between the first two ground contact points of each MGCF of the mountainous region of the Arkansas domain.	172
Figure 7.12 – Histogram of number of channels per flash for multi-stroke flashes detected in the Arkansas domain.	173

Figure 7.13 – Histogram of the separation distance between the first two ground contact points of each MGCF of the Arkansas domain.	173
Figure 7.14 – Altitude map of the Arizona domain.	175
Figure 7.15 – Smoothed altitude map of the Arizona domain with contour lines.	175
Figure 7.16 – Spatial frequency terrain variations of the Arizona domain.	176
Figure 7.17 – Spatial distribution of the density of return strokes (from multi-stroke flashes only) of the Arizona domain.	177
Figure 7.18 – Spatial distribution of the mean number of channels per flash (CPF) of the Arizona domain.	179
Figure 7.19 – Spatial distribution of the mean separation distance between the first two ground contact points of each MGCF of the Arizona domain.	179
Figure 7.20 – Histogram of number of channels per flash for multi-stroke flashes detected in the Arizona domain.	180
Figure 7.21 – Histogram of the separation distance between the first two ground contact points of each MGCF of the Arizona domain.	180
Figure 7.22 – Altitude map of the Kansas domain.	181
Figure 7.23 – Smoothed altitude map of the Kansas domain with contour lines.	182
Figure 7.24 – Spatial frequency terrain variations of the Kansas domain.	182
Figure 7.25 – Spatial distribution of the density of return strokes (from multi-stroke flashes only) of the Kansas domain.	183
Figure 7.26 – Spatial distribution of the mean number of channels per flash (CPF) of the Kansas domain.	184
Figure 7.27 – Spatial distribution of the mean separation distance between the first two ground contact points of each MGCF of the Kansas domain.	184
Figure 7.28 – Histogram of number of channels per flash for multi-stroke flashes detected in the Kansas domain.	185
Figure 7.29 – Histogram of the mean separation distance between the first two ground contact points of each MGCF of the Kansas domain.	186
Figure 8.1 – Hourly plots of the total negative CG lightning incidence and the GM of the estimated peak current of first return strokes in the Arkansas domain.	192

Figure 8.2 – Hourly plots of the total negative CG lightning incidence and the GM of the estimated peak current of first return strokes in the Arizona domain.	192
Figure 8.3 – Hourly plots of the total negative CG lightning incidence and the GM of the estimated peak current of first return strokes in the Kansas domain.	193
Figure 8.4 – Hourly plots of the AM of the number of channels per flash (CPF) and the separation distance between ground contacts in the Arkansas domain...	194
Figure 8.5 – Hourly plots of the AM of the number of channels per flash (CPF) and the separation distance between ground contacts in the Arizona domain.....	194
Figure 8.6 – Hourly plots of the AM of the number of channels per flash (CPF) and the separation distance between ground contacts in the Kansas domain.	195
Figure 8.7 – Hourly scatterplot of the mean number of channels per flash <i>versus</i> the mean separation distance between ground contacts in the Arkansas domain.....	197
Figure 8.8 – Hourly scatterplot of the mean number of channels per flash <i>versus</i> the mean separation distance between ground contacts in the Arizona domain.	197
Figure 8.7 – Hourly scatterplot of the mean number of channels per flash <i>versus</i> the mean separation distance between ground contacts in the Kansas domain.	198
Figure 9.1 – Maps of lightning flash density (N_g) and lightning strike point density (N_{sg}) for the Arkansas domain.	202
Figure 9.2 – Maps of lightning flash density (N_g) and lightning strike point density (N_{sg}) for the Arizona domain.	203
Figure 9.3 – Maps of lightning flash density (N_g) and lightning strike point density (N_{sg}) for the Kansas domain.....	204
Figure 9.4 – First example of lightning-caused power line fault.....	206
Figure 9.5 – Second example of lightning-caused power line fault.	207
Figure 9.6 – Second example of lightning-caused power line fault, zoomed into the three strokes that hit the power line (first, second and fourth strokes). ..	208

Figure B.1 – Spatial distribution of the mean error ellipse semi-major axis (SMA) in kilometers of the Arkansas domain.	237
Figure B.2 – Spatial distribution of the mean chi-squared value of the Arkansas domain.	238
Figure B.3 – Spatial distribution of the mean number of sensors reporting (NSR) of the Arkansas domain.	238
Figure B.4 – Spatial distribution of the mean estimated peak current (I_p) in kiloamperes of the Arkansas domain (negative return strokes only).	239
Figure B.5 – Spatial distribution of the mean error ellipse semi-major axis (SMA) in kilometers of the Arizona domain.	239
Figure B.6 – Spatial distribution of the mean chi-squared value of the Arizona domain.	240
Figure B.7 – Spatial distribution of the mean number of sensors reporting (NSR) of the Arizona domain.	240
Figure B.8 – Spatial distribution of the mean estimated peak current (I_p) in kiloamperes of the Arizona domain (negative return strokes only).	241
Figure B.9 – Spatial distribution of the mean error ellipse semi-major axis (SMA) in kilometers of the Kansas domain.	241
Figure B.10 – Spatial distribution of the mean chi-squared value of the Kansas domain.	242
Figure B.11 – Spatial distribution of the mean number of sensors reporting (NSR) of the Kansas domain.	242
Figure B.12 – Spatial distribution of the mean estimated peak current (I_p) in kiloamperes of the Kansas domain (negative return strokes only).	243
Figure C.1 – Hourly plots of the AM of the number of sensors reporting (NSR) and the chi-squared value of all return stroke solutions in the Arkansas domain.	245
Figure C.2 – Hourly plots of the AM of the number of sensors reporting (NSR) and the chi-squared value of all return stroke solutions in the Arizona domain.	246
Figure C.3 – Hourly plots of the AM of the number of sensors reporting (NSR) and the chi-squared value of all return stroke solutions in the Kansas domain.	246

Figure C.4 – Hourly plots of the AM of the number of sensors reporting (NSR) and the GM of the estimated peak current of all return stroke solutions in the Arkansas domain.	247
Figure C.5 – Hourly plots of the AM of the number of sensors reporting (NSR) and the GM of the estimated peak current of all return stroke solutions in the Arizona domain.	247
Figure C.6 – Hourly plots of the AM of the number of sensors reporting (NSR) and the GM of the estimated peak current of all return stroke solutions in the Kansas domain.	248

LIST OF TABLES

	<u>Page</u>
Table 2.1 – Summary of previous studies on the occurrence of multiple ground contact flashes.....	25
Table 5.1 – Daily number of flashes and MGCSs recorded by each RAMMER station.	77
Table 5.2 – Statistics of 2-D leader speeds preceding UI strokes.	97
Table 5.3 – Statistics of the most intense and total brightened segments of UI channels.	99
Table 5.4 – Proportion of forked and UI strokes over the total daily number of MGCSs.	99
Table 5.5 –Statistics of the estimated separation between ground contacts of MGCSs.	100
Table 5.6 – Statistics on the time interval between contacts in forked and UI strokes.	103
Table 5.7 – Summary of previous studies on forked and upward illumination strokes.	108
Table A.1 – Performance efficiency for different combinations of input parameters of the <i>groupGCP</i> algorithm.	233

LIST OF ACRONYMS AND ABBREVIATIONS

ACF	Altered Channel Flash
AM	Arithmetic Mean
BrasilDAT	Brazilian Total Lightning Network
CBH	Cloud Base Height
CG	Cloud-to-Ground
CPF	Channels Per Flash
DE	Detection Efficiency
DTOA	Difference in the Time-Of-Arrival
ENTLS	EarthNetworks Total Lightning System
EUCLID	EUropean Cooperation for LIghtning Detection
FOV	Field Of View
fps	Frames per second
GCP	Ground Contact Point
GM	Geometric Mean
IC	Intracloud
IMPACT	IMProved Accuracy through Combined Technology
I_p	Estimated peak current
KSWFP	Kansas Windfarm2013 Field Program
LA	Location Accuracy
MDF	Magnetic Direction Finder
MGCF	Multiple Ground Contact Flash
MGCS	Multiple Ground Contact Stroke (divided into forked and upward illumination strokes)
NCF	New Channel Flash
NLDN	(also U.S. NLDN) United States National Lightning Detection Network
PEC	Pre-Existing Channel
RAMMER	Portuguese acronym “Rede Automatizada Multi-câmeras para o Monitoramento e Estudo de Raios” (Automatized multicamera network to observe and study lightning)
RL	Recoil Leader
SD	Standard Deviation

SE	Standard Error
SGCF	Single Ground Contact Flash
SMA	Semi-Major Axis
SmA	Semi-minor Axis
SRT	Shuttle Radar Topography Mission
TOA	Time-Of-arrival
UI	Upward Illumination
VHF	Very High Frequency (30 MHz to 300 MHz)

TABLE OF CONTENTS

	<u>Page</u>
1 INTRODUCTION	1
2 LITERATURE REVIEW	5
2.1. Fundamental background and definitions	5
2.2. Negative cloud-to-ground lightning, step-by-step	7
2.3. Differences between positive and negative cloud-to-ground lightning	10
2.4. The bidirectional leader model.....	11
2.4.1. Overview	11
2.4.2. The role of K processes (or recoil leaders)	15
2.5. Previous studies on the occurrence and characteristics of lightning with multiple ground terminations.....	16
2.5.1. Influence of the preceding interstroke and no-current intervals	17
2.5.2. Scenarios and mechanisms.....	18
2.5.3. Relationship with return stroke electric field peak values	23
2.5.4. Statistical incidence.....	24
2.5.5. Stroke order and channel conditioning	27
2.5.6. Identification and detection of flashes with multiple ground contacts by large scale Lightning Location Systems (LLS).....	28
2.5.7. Forked and upward illumination strokes.....	30
3 INSTRUMENTS, CAMPAIGNS AND DATASETS.....	35
3.1. Instruments.....	35
3.1.1. Slow electric field antennas	35
3.1.2. Lightning Location Systems (LLS).....	38
3.1.2.1. VLF/LF wide-area Lightning Location Systems (LLS).....	39
3.1.2.2. Three-dimensional Lightning Mapping Array (LMA).....	46
3.1.3. Video cameras.....	50
3.2. Observational campaigns	51
3.2.1. Kansas Windfarm2013 Field Program (KSWFP).....	51
3.2.1.1. Slow electric field and LMA network.....	52

3.2.1.2.	U.S. National Lightning Detection Network (NLDN)	54
3.2.1.3.	Video cameras	57
3.2.2.	Summer 2013 RAMMER campaign.....	58
3.2.2.1.	Automatized Multi-camera Network to Observe and Study Lightning (RAMMER)	58
3.2.2.2.	BrasilDAT Total Lightning Network	61
3.3.	Shuttle Radar Topography Mission (SRTM) dataset.....	62
4	ALGORITHM FOR IDENTIFYING GROUND CONTACT POINTS FROM DATA PROVIDED BY LIGHTNING LOCATION SYSTEMS.....	63
4.1.	Description of the <i>groupGCP</i> algorithm.....	63
4.1.1.	“Innermost layer”: augmented <i>k</i> -means clustering method	64
4.1.2.	“Mid-layer”: the “progressive <i>k</i> -means” algorithm	67
4.1.3.	“Outermost layer”: the <i>groupGCP</i> algorithm	68
4.2.	Algorithm validation	75
5	MULTIPLE GROUND CONTACT STROKES: FORKED AND UPWARD- ILLUMINATION.....	77
5.1.	Overview of the dataset.....	77
5.2.	PyRAW	78
5.3.	Case studies	79
5.3.1.	Forked strokes	80
5.3.1.1.	Flash #1, February 18 th , 2013	80
5.3.1.2.	Flash #54, February 19 th , 2013	82
5.3.2.	Upward illumination (UI) strokes	83
5.3.2.1.	Flash #17, February 19 th , 2013	84
5.3.2.2.	Flash #85, March 6 th , 2013	89
5.4.	Visual differentiation between forked and UI strokes	94
5.5.	Statistical analysis	97
5.5.1.	Photogrammetric parameters of UI strokes.....	97
5.5.1.1.	Stepped leader speeds.....	97
5.5.1.2.	UI channel total brightening length.....	98

5.5.2. Relative occurrence of Multiple Ground Contact Strokes (MGCS) by thunderstorm day	99
5.5.3. One-dimensional distance between ground contact points	100
5.5.4. Time interval between contacts.....	101
5.5.5. Peak current estimates.....	103
5.6. Relative incidence of flashes with MGCS	107
5.7. Concluding remarks	108
6 FORMATION MECHANISMS OF NEW CONTACT POINTS IN SUBSEQUENT STROKES: CASE STUDIES AND INTERPRETATION.....	111
6.1. Methodology	111
6.2. Case studies and their interpretation	113
6.2.1. Type I: Altered channel.....	113
6.2.1.1. Case I.1: May 28 th , 2013, 01:08:26 (UT).....	113
6.2.1.2. Case I.2: May 28 th , 2013, 01:20:37 (UT)	118
6.2.1.3. Type I conceptual scenario and mechanism.....	124
6.2.2. Type II: New channel with common branches	127
6.2.2.1. Case II.1: May 28 th , 2013, 01:16:55 (UT).....	127
6.2.2.2. Case II.2: July 14 th , 2013, 09:35:15 (UT)	132
6.2.2.3. Type II conceptual scenario and mechanism	137
6.2.3. Type III: New channel with common origin.....	139
6.2.3.1. Case III.1: May 29 th , 2013, 16:08:43 (UT)	139
6.2.3.2. Case III.2: July 14 th , 2013, 09:55:52 (UT).....	147
6.2.3.3. Type III conceptual scenario and mechanism	151
6.3. Unique events.....	153
6.3.1. Attempted leader: May 28 th , 2013, 00:59:01 (UT)	153
6.3.2. New ground contact of high stroke order: May 29 th , 2013, 16:11:47 (UT).....	156
6.4. Concluding remarks	160
7 REGIONAL DISTRIBUTION OF MULTIPLE GROUND CONTACT FLASHES AND THEIR CHARACTERISTICS	161
7.1. Domains, datasets and computational process	161
7.2. Previous works and hypothesis outline	163

7.3. Obtaining spatial frequency terrain variations	164
7.4. Results and discussions	166
7.4.1. Arkansas	166
7.4.2. Arizona	174
7.4.3. Kansas	181
7.5. Concluding remarks	186
8 DIURNAL CLIMATOLOGY OF MULTIPLE GROUND CONTACT FLASHES	189
8.1. Computational method	189
8.2. Results	191
8.3. Concluding remarks	198
9 TECHNOLOGICAL AND ENGINEERING APPLICATIONS OF THE GROUND CONTACT POINT IDENTIFICATION ALGORITHM	201
9.1. Evaluating the lightning strike point density (N_{sg})	201
9.2. Analysis of lightning-caused power line faults	205
10 CONCLUSIONS	209
REFERENCES	215
APPENDIX A – SUMMARY OF THE PERFORMANCE EVALUATION OF THE CONTACT POINT IDENTIFICATION ALGORITHM	233
APPENDIX B – MAPS OF LIGHTNING LOCATION SYSTEM DATA QUALITY PARAMETERS OF THE THREE ANALYZED DOMAINS	237
APPENDIX C – DIURNAL VARIATIONS OF LIGHTNING LOCATION SYSTEM DATA QUALITY PARAMETERS OF THE THREE ANALYZED DOMAINS	245

1 INTRODUCTION

The near-ground component of negative cloud-to-ground lightning is an essentially discrete phenomenon, normally composed of multiple individual discharges typically separated by tens of milliseconds that cause the “flickering” effect when they are observed through the naked eye. Each of these individual discharges is called “return strokes”, and they are collectively grouped into a “flash”. The return strokes are terminated after a process called “channel current cutoff”, and after every return stroke that goes through cutoff there is a possibility of a new ground termination being formed for the following stroke typically tens of milliseconds later. Other documented ways through which multiple ground terminations can be produced are related to more than one leader branch completing their downward development almost simultaneously (with temporal separations ranging from a microseconds up to a few milliseconds).

There have been a number of scientific studies on the incidence and characteristics of multiple ground contact flashes with the help of various instruments, but there is still no widely accepted description of the processes responsible for the formation of a new ground contact point. Up to this moment, only two mechanisms have been proposed.

From multiple station electric field observations of the processes following some return strokes, Krehbiel (1981) obtained evidences that, after current cutoff has taken place, negative electric charges continue to move into the upper parts of the lightning channel without reaching ground. According to him, the presence of such charges may reduce the potential difference in that direction for the next downward moving leader, effectively deviating it from the original channel and leading to the creation of a new ground termination.

More recently, Zoghzy et al. (2014) conducted a statistical study on the spatial and temporal distributions of return strokes, comparing those that shared the same ground strike point of the first stroke of the flash with those that created a new channel (up to seven kilometers away from the first stroke). For the latter, it was found that their peak occurrence in a space-time histogram is constantly moving away from the first stroke at a speed of approximately 230 km s^{-1} . In order to

explain this result, they proposed that in-cloud leaders are formed from the initial vertical lightning channel, propagating away from it horizontally inside the cloud. Eventually this in-cloud leader would be converted into a downward stepped leader, creating a new ground termination up to several kilometers away from the original one.

In addition to the scientific relevance of understanding the phenomenology and physics of how multiple ground flashes occur, from the technological and engineering standpoint, a better characterization of this phenomenon will be useful for the design of systems aimed at lightning protection, detection and location. Factors such as large electric charge transfers (caused by long continuing currents) and numerous large current surges (a consequence of subsequent strokes) have their impact amplified by the fact that a single cloud-to-ground flash may strike multiple locations (given the formation new ground contacts) over a wide range of distances. Human safety is another aspect that must be considered: knowing how far a subsequent stroke can be from its predecessors might be useful when establishing practical rules for individuals to decide when they should seek shelter after hearing thunder.

The goals that encompass all analyses of this thesis are to improve our understanding on how multiple ground terminations may be formed in lightning, to isolate the main factors that influence their occurrence and characteristics, and to provide a reliable tool for the identification of this type of event by improving the amount of information provided by Lightning Location Systems. With those objectives in mind, the present thesis is organized in the following way: Chapter 2 provides a review of the literature available on different aspects related to multi-grounded lightning. In Chapter 3 all instruments, observational campaigns and datasets that were used in the analyses are introduced in an attempt to facilitate the understanding of their characteristics, scope and limitations. Next, Chapter 4 presents a detailed description of the *groupGCP* algorithm, developed with the aim of deriving information on lightning ground contact points (GCP) from individual return stroke data provided by large-scale Lightning Location Systems (LLS). Chapter 5 is dedicated to a brief study on two phenomena that lead to multiple ground terminations within a relatively small timescale (from tens of microseconds up to a few milliseconds), known as forked and upward-

illumination strokes, with special attention given to their relative occurrence and differences. A number of detailed case studies of multiple ground contact flashes are described in Chapter 6, from which three different mechanisms/scenarios that lead to new ground terminations were identified and characterized. Chapters 7 and 8 address scientific applications of the *groupGCP* algorithm: the former presents an analysis of the regional distribution of multi-grounded flashes (and their characteristics), comparing them with terrain characteristics and variations for three different domains; and the latter describes a diurnal climatology for those events, detected over the same three domains. A brief discussion on possible engineering and technology applications of the *groupGCP* algorithm is presented in Chapter 9, with particular interest on lightning protection of grounded structures. Finally, Chapter 10 summarizes the main conclusions of all the analyses and new questions that remain unanswered, providing a few suggestions on future works.

2 LITERATURE REVIEW

This chapter presents a brief review of the literature on lightning physics, describing the main known steps of lightning formation and the bidirectional leader model in a didactic approach. It is then followed by a more detailed review of previous studies on multiple ground contact flashes (MGCFs).

2.1. Fundamental background and definitions

A lightning flash is a short-duration (usually shorter than one second), high peak intensity (ranging from tens to more than one hundred kiloamperes) and large extension (up to tens of kilometers long) electric discharge that occurs in the lower atmosphere. It is commonly associated with thunderclouds, particularly (but not exclusively) the cumulonimbus (or Cb, for short). A number of observational studies conducted throughout the 20th century led to the conclusion in the 1980s that thunderclouds generally have a tripolar electrical structure (e.g., WILLIAMS, 1989).

According to the literature summary and review by Williams (1989), in general terms, the tripole structure of a Cb consists of a positive charge region close to its top, a negative charge region below it (at a range of temperatures between -10°C and -15°C), and a second, smaller positive charge region close to the 0°C level. Figure 2.1 illustrates the position of each charge region in thunderclouds from very distinct climatological and geographical locations: convective summer season storms in humid (Florida, USA) and in desert (New Mexico, USA) regions, and winter storms in Japan. As commented by Krehbiel (1986), even with the contrast between the storms observed in Florida (whose cloud bases are located at altitudes with temperatures above freezing level due to its high humidity) and in New Mexico (whose cloud bases are right below freezing level due to its low humidity), the charge regions that compose the aforementioned tripole are still located at heights with very similar temperature ranges. This fact suggests that the microphysical mechanisms responsible for the electrification of thunderstorms are the same for both locations, acting at temperatures right below 0°C . Detailed descriptions of these mechanisms and evidences of the existence of

more complex electrical structures (e.g., STOLZENBURG et al., 1998) are beyond the scope of the present work and will not be discussed.

Figure 2.1 – Electric charge centers of thunderclouds.

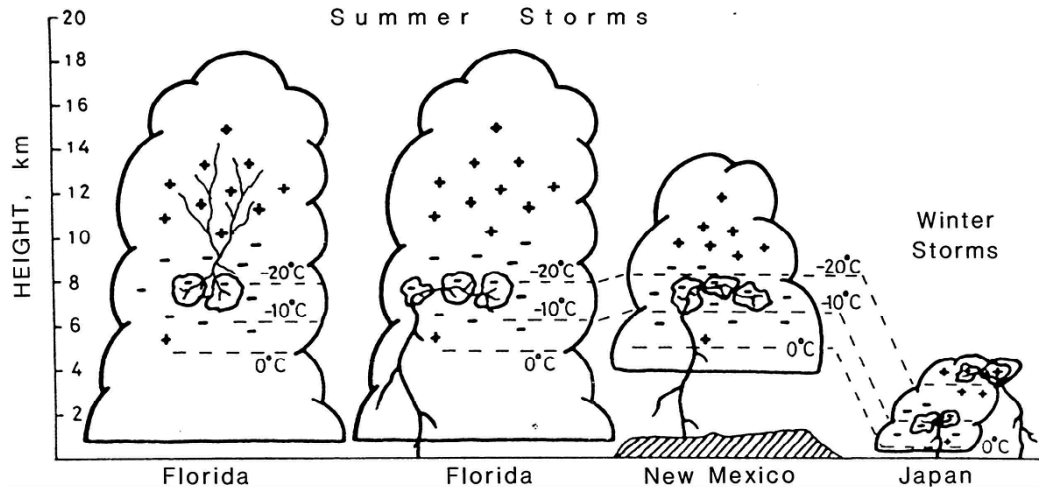


Diagram illustrating how electric charge centers of thunderclouds from different locations are situated at the same temperature levels. The exact heights will depend on the temperature profile of the considered region

Source: Krehbiel (1986).

Lightning flashes are usually named after their origin and termination points. The main classifications are intracloud (IC), cloud-to-ground (CG) and upward flashes. IC flashes are those whose occurrence does not involve the ground, and this classification usually embraces cases whose channel development do not leave the thundercloud as well as those that present some branches becoming visible outside the cloud opaque region. Flashes that transfer charge to the ground also carry the polarity of the charge transferred into the terminology. This is the case of CG flashes, initiated in the thundercloud and that make contact with ground. They can be positive cloud-to-ground (+CG) flashes when the net electric charge transferred to ground is positive (i.e., negative charges are removed), and negative cloud-to-ground (–CG) if it transfers charges of negative sign to ground.

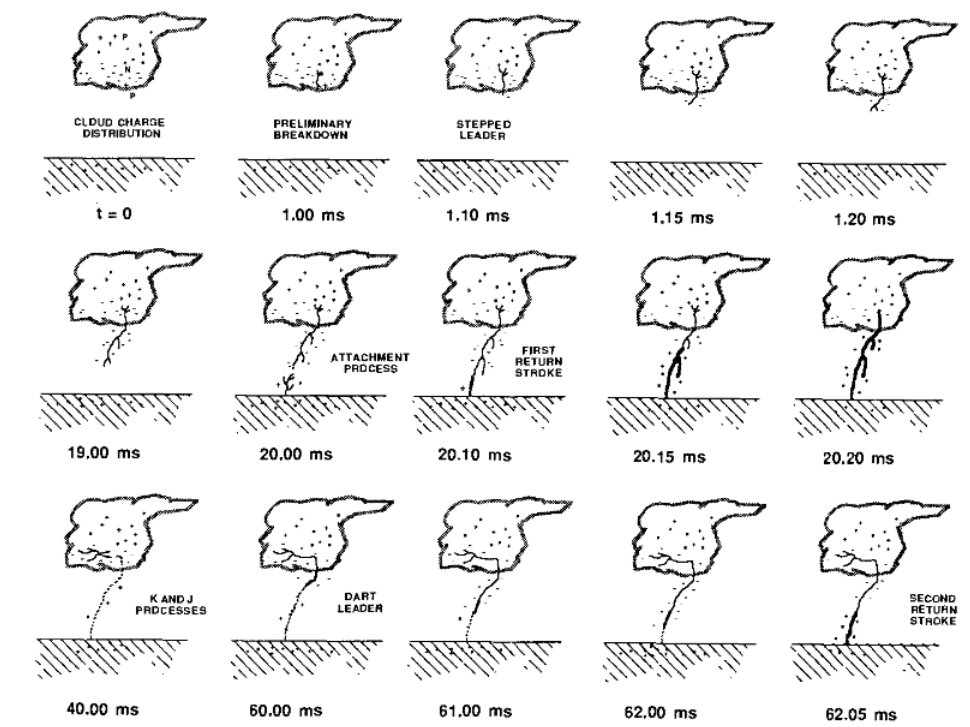
IC flashes are the most frequent, usually accounting for approximately 75% of the total lightning activity (as suggested in the extensive literature review by Rakov and Uman, 2003, p.44). The remaining ~25% of the atmospheric discharges correspond to both CG and upward flashes, with the latter being much rarer (as

they are usually related to the presence of a tall grounded object). Early studies suggested that the exact IC/CG ratio depend mainly on the latitude (e.g., PRENTICE; MACKERRAS, 1977) and storm type and phase (e.g., LIVINGSTON; KRIDER, 1978). However, Boccippio et al. (2001) found no evidences that the latitudinal modulation exists from combined satellite- and surface-based data; instead, their conclusions endorsed the result that storm type and morphology may be the dominant factors.

2.2. Negative cloud-to-ground lightning, step-by-step

Observational studies of –CG flashes have showed that they follow eight basic steps, among which some can be either repeated (once or multiple times) or not occur at all: (i) initial or preliminary breakdown; (ii) propagation of a stepped leader; (iii) initiation of an upward connecting leader and the attachment process; (iv) first return stroke; (v) current cutoff; (vi) K and J processes; (vii) development of a dart leader; and (viii) subsequent return stroke. They are illustrated in Figure 2.2 and described in detail in the next paragraph.

Figure 2.2 – Main steps of a negative cloud-to-ground flash.



Summary of the temporal sequence of the main steps of a negative cloud-to-ground flash.

Source: Uman (1987).

Following the description presented in the books by Uman (1987) and Rakov and Uman (2003), illustrated in Figure 2.2, the electrical structure of the thundercloud creates the conditions necessary for the **initial (or preliminary) breakdown** (shown at $t = 1.0$ ms in Figure 2.2). They are associated with the creation of electrically conductive conditions for the stepped leader to initiate its propagation. Even though the essential physics of the breakdown process are not entirely known, they can be observed with the help of electric field sensors as a characteristic and easily identifiable waveform (e.g., BEASLEY et al., 1982, 1983). Very recent works (STOLZENBURG et al., 2013; CAMPOS; SABA, 2013) presented optical evidences that there is a fast (10^6 m s⁻¹) channel development simultaneously with the production of the characteristic initial breakdown electric field pulses. Other works suggest that the breakdown is actually caused by runaway electron avalanches induced by cosmic rays (e.g., GUREVICH; KARASHTIN, 2013).

Following the initial breakdown activity, the **stepped leader** (depicted in Figure 2.2 between times $t = 1.10$ ms and $t = 20.0$ ms) begins its propagation towards ground, creating a plasma channel. Its development occurs through steps whose length ranges from 3 to 200 m (with a typical value around 50 m) and that are separated by intervals ranging from 5 to 100 μ s, which results in average propagation speeds typically of the order of 10^5 m s⁻¹ (e.g., SCHONLAND, 1938; ORVILLE; IDONE, 1982; CAMPOS et al., 2014a).

Once the stepped leader tip is sufficiently close to ground, the intensified low-level electric field induces the initiation of one or more **upward leaders**, which are responsible for the **attachment process** (between times $t = 20.00$ ms and $t = 20.10$ ms). Their inception preferentially occurs at pointed objects and structures, where the electric field is enhanced and charges induced by the leader tip proximity have a tendency to be accumulated.

When one of the upward leaders connects to one of the branches of the stepped leader, the gap between cloud and ground is bridged and the **return stroke** process occurs (between times $t = 20.10$ ms and $t = 20.20$ ms). Intense light is emitted, associated with a peak current typically of the order of several kiloamperes that lasts a few tens of microseconds (RAKOV; UMAN, 2013,

p.146). In the case of –CG, electrons are transferred to ground, which can be depicted as an ascending current wave. The return stroke itself is regarded as the wavefront that travels at one-third of the speed of light (JORDAN et al., 1997) from the ground towards the cloud, carrying the information that electrical contact has been made. On average, –CGs produce about four return strokes per flash (e.g., SABA et al., 2006a; SARAIVA et al., 2010), but high-speed video records have confirmed flashes with up to twenty strokes (ANTUNES et al., 2015, Figure 4 and section 3.1). Antunes et al. (2015) have also observed that the average multiplicity (number of return strokes per flash) may vary for different thunderstorm days (ranging from 2.6 to 5.0).

Some time after the return stroke, **current cutoff** takes place (at some instant between times $t = 20.20$ ms and $t = 40.00$ ms), interrupting charge transfer to ground. If the flash is finished at this point, it is called a single stroke flash, which corresponds to about one fifth of the cases (SABA et al., 2006a; SARAIVA et al., 2010; ANTUNES et al. 2015). However, in the majority of the cases, **J and K processes** (detectable with the help of electric field sensors, such as those used by Rakov et al., 1992) take place inside the cloud (and are depicted at time $t = 40.00$ ms in Figure 2.2). They are related to the initiation of a **dart leader** (time $t = 60.00$ ms) that begins its descent typically from a few to tens of milliseconds after the K process takes place. Normally, the dart leader propagates continuously (not in a stepped fashion) through the region of reminiscent increased conductivity created earlier by the stepped leader, moving faster than the latter by two orders of magnitude (typically 10^7 m s⁻¹, as estimated by Schonland et al., 1935; Orville and Idone, 1982; Jordan et al., 1997; and Campos et al., 2014a). When the dart leaders reaches ground, completely re-ionizing the remaining channel, a **subsequent return stroke** occurs.

One important process observed in cloud-to-ground lightning that is not depicted in Figure 2.2 is the continuing current (CC), which is defined by Rakov and Uman (2013, p.173) as “the relatively low-level current of typically tens to hundreds of amperes that immediately follows a return stroke, in the same channel to ground, and typically lasts for tens to hundreds of milliseconds”. According to Medeiros (2011), approximately 55% of all negative return strokes are followed by a continuing current of some sort, but in only 7% of the –CGs they last longer than

40 milliseconds (typically categorized as being “long”, following the definition by Kitagawa et al., 1962).

Previous estimates show that between 17% (KRIDER, 1966) and 51% (SABA et al., 2006a) of the –CG flashes include return strokes that do not follow a single path to ground, with an average number of contacts per flash that ranges from 1.45 (VALINE; KRIDER, 2002) to 1.70 (SABA et al., 2006a). These events are the main topic of the present thesis and the previous relevant studies on this topic are reviewed in greater detail in Section 2.5.

2.3. Differences between positive and negative cloud-to-ground lightning

Given the fact that the scope of this thesis is limited to multi-grounded –CGs, positive lightning will not be detailed in this literature review. For the sake of completeness, though, their main features and differences from their negative counterpart are listed:

- a) +CGs are the dominant type of cloud-to-ground flashes in certain meteorological conditions, particularly cold season thunderstorms, dissipating stage of Mesoscale Convective Systems (MCSs) and Cbs, and specific regions such as the U.S. Central Great Plains (CAREY; BUFFALO, 2007; FLEENOR et al., 2009);
- b) positive flashes are frequently preceded by IC activity, which frequently lasts longer than 100 ms (RUST et al., 1981; FUQUAY, 1982), while other observations have shown that they may be initiated branching from horizontal IC channels propagating outside the thundercloud opaque region (SABA et al., 2009);
- c) while +CGs present initial breakdown pulses during its earliest phases, there are two remarkable differences: about 90-100% of the cases are preceded by a single pulse instead of a pulse train (e.g., GOMES; COORAY, 2004; SCHUMANN et al., 2013), and the breakdown waveform polarity is reversed when compared to –CGs (see Figure 3 of Campos and Saba, 2013, and Figure 7a of Schumann et al., 2013);

- d) after the initial breakdown, the channel of a positive flash is formed by a downward propagating positive leader whose luminosity is normally less intense when compared to stepped leaders (in –CGs) and, although they initially tend to be slower (10^4 m s^{-1}), in the final stages of their development their speeds become comparable to those observed in stepped leaders (10^5 m s^{-1} , as reported by Saba et al., 2008, and Campos et al., 2014a);
- e) in positive return strokes, electrons are removed from ground (i.e., transferring a net positive charge to ground) and almost 70% of them are followed by CCs whose duration are longer than 40 milliseconds (SABA et al., 2010), an incidence almost ten times larger than in –CGs (MEDEIROS, 2011). Additionally, while the dataset of Saba et al. (2006b, 2010) suggests that negative strokes that are followed by long CCs (longer than 40 ms) have an upper peak current limit of 20 kA (estimated from LLS data), positive strokes did not hold on to this limit, as their largest reported estimated peak current (142 kA) was followed by the longest observed CC in their 2010 paper (approximately 800 ms);
- f) 80-96% of all +CGs are single stroke flashes (FLEENOR et al., 2009; SABA et al., 2010) and in the rare occasions in which more than one stroke occurs, video studies show that they almost always create a new ground contact separated by distances that range from 2 to 53 km, with about 70% of the cases with separation distances greater than 10 km (SABA et al., 2010).

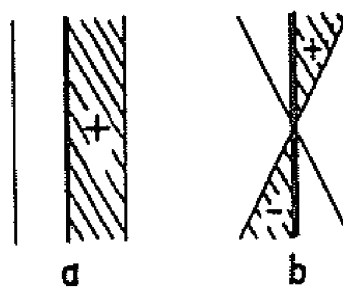
2.4. The bidirectional leader model

2.4.1. Overview

The idea that lightning develops as a unidirectional, unipolar (with a non-zero electric charge) leader may be implied from Figure 2.2 and the early optical studies in the 1920s and 1930s (e.g., Schonland, 1938). However, in two papers originally published in 1950 and 1960 that were recently compiled by V. Mazur and L. H. Ruhnke into a book, Kasemir (2012a,b) presented an alternative view

that not only is more physically sound but also better reflects many of the more recent observations. He proposed that CG flashes are formed bidirectionally, simultaneously downwards (in its lower region) and in-cloud (in its upper region). In the original publications a qualitative model is introduced in which the developing lightning channel is described as a conductive spheroid under the influence of a constant electric field, presenting charge density that is zero in its mid-point (from which it originates) and increases linearly towards the spheroid extremities. Macroscopically the channel is electrically neutral with the charge distribution shown in Figure 2.3b (which is compared to the “classical” unipolar, non-zero net charge distribution of Figure 2.3a).

Figure 2.3 – Charge distributions in the classical and bidirectional leader models.



Comparison between the charge distributions that are assumed in the (a) classical (unidirectional, unipolar, non-zero net charge) and (b) bidirectional (bipolar, zero net charge) leader models of lightning formation.

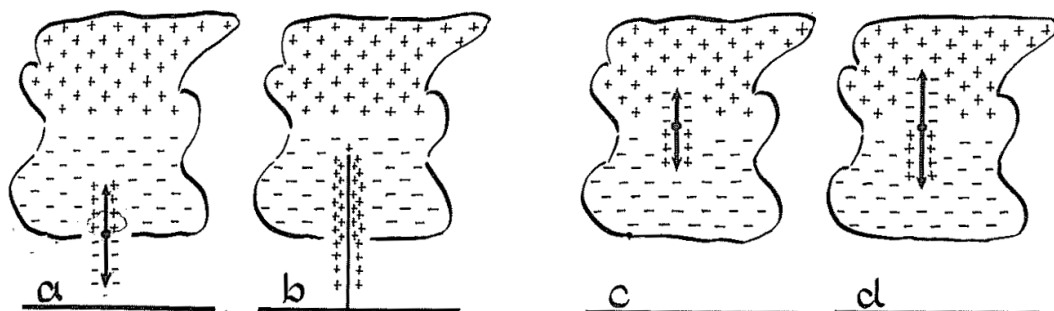
Source: adapted from Kasemir (2012b).

Later on, in a conference paper originally published in 1983, Kasemir (2012c) further advanced the bidirectional leader model (that he named “uncharged leader”) by calculating the necessary energy for its development and compared it to the same estimate regarding the classical model (that he called “charged leader”) introduced by Schonland (1938). For the classical/charged leader he showed that it would discharge the cloud during its downward development, collecting and concentrating same-sign electrical charges along its channel. He argued that such process would require an amount of energy that is not possible to obtain from a thundercloud, as the flux of electrical charges would not follow the electric field lines produced by the known cloud charge distribution. Kasemir (2012c, p.426) also states that “there is an energy deficit in the charged leader

model”, adding that “the introduction of the cloud charge collecting mechanism has never been explained or justified” (by previous authors). The conclusion is that “the charged leader is not a workable physical concept”.

After the theoretical development corresponding to the bidirectional/uncharged leader model, Kasemir (2012c, p.425) states that it does not collect charges from the cloud; instead it “produces positive (positive ions) and negative (electrons) charges inside its channel by ionization”. This charge separation would be caused by the electric field external to the leader channel, produced by the cloud charge distribution. He concludes by justifying the term “uncharged leader” due to the fact that “one half of the channel carries positive and the other half negative induced charges”, leading to a zero net charge. A graphical representation of the conditions assumed in the demonstrations by Kasemir (2012c) is shown in Figure 2.4. Parts *a* and *b* correspond to a negative CG flash while parts *c* and *d* correspond to an IC flash, which follows the same principle previously described.

Figure 2.4 – Bidirectional development of (a/b) cloud-to-ground and (c/d) intracloud flashes.



Charge distribution in a negative cloud-to-ground flash (a) during the bidirectional leader development and (b) right after the return stroke. An intracloud discharge is also shown (c) during its early development and (d) at the end of its propagation.

Source: Kasemir (2012c).

Observational support to the model introduced and further developed by Kasemir (2012a,b,c) was first given by Mazur (1989), who studied lightning strikes to two aircrafts (NASA F-106B and FAA CV-580) instrumented with electric field sensors, electric field mills, resistive current shunts, photodiodes and video cameras. In the experiment the pilot would penetrate the thunderstorm, eventually initiating a lightning flash whose processes could be recorded by the instruments

on board. The data collected supported the idea that a negative corona discharge is formed on the plane nose, causing electric charge separation over its conductive fuselage, which leads to the intensification of the electric field on its tail to the point at which a positive leader is initiated from there. As the positive leader develops there is an intensification of the corona at the nose that eventually gives rise to a stepped leader. The lightning flash initiated at the plane develops bidirectionally, resembling the regular IC discharge described in the double-ended tree concept by Kasemir (2012a,b,c). Figure 2.5 shows a photograph by Z. Kawasaki that has been reproduced in many other papers (e.g., WILLIAMS, 2006) in which lightning initiation occurred below cloud base, with the airplane as its starting point. The orientation of the branching (both above and below the plane) strongly suggests that the leader development was indeed bidirectional (in agreement with the data interpretation by Mazur, 1989).

Figure 2.5 – Bidirectional leader development in an airplane struck by lightning.



Photograph of a bidirectional leader development from an airplane, visible below cloud base. The orientation of the branching in both directions strongly suggests that the plane is the origin of the double-ended lightning tree.

Source: Williams (2006), from a photograph provided by Z. Kawasaki.

The bidirectional leader model became particularly relevant with the use of VHF radiation interferometry (SHAO et al., 1995) and difference in time-of-arrival (RISON et al., 1999) for lightning mapping. These techniques are able to detect and locate processes associated with the development of negative leaders, providing important insights on the development of lightning channels inside the thundercloud. Particularly the Lightning Mapping Array (LMA), based on the

time-of-arrival (TOA) technique as described by Rison et al. (1999), is one of the main instruments used in the analyses of this thesis work. Its main features and characteristics are discussed in section 3.1.2.2.

2.4.2. The role of K processes (or recoil leaders)

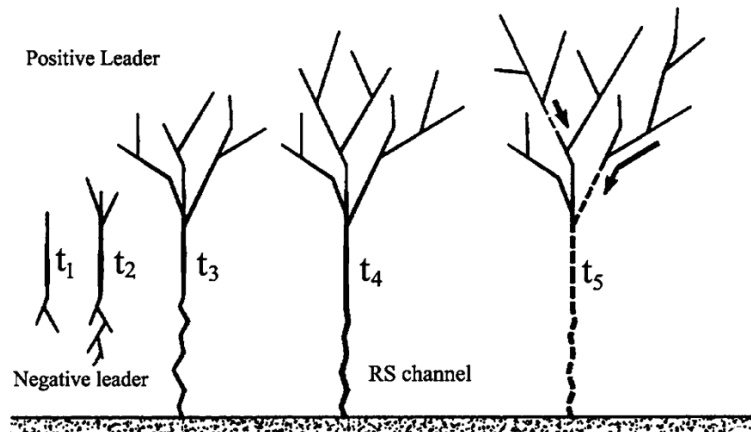
In the context of the bidirectional leader model, K processes play an important role. As mentioned in Section 2.2, they are usually observed during the time interval between return strokes in –CG flashes. This type of discharge was originally observed by Kitagawa and Kobayashi (1959) through electric field changes (usually termed “K changes”) with durations of the order of one millisecond or shorter and frequently accompanied by pulses of even shorter duration (THOTTAPPILLIL et al., 1990; RAKOV et al., 1992).

Mazur et al. (1995) observed and mapped K processes with VHF interferometry and they noted that they are very similar to dart leaders and M components (a channel current intensification that may occur during the continuing current period). With time, K changes were also termed “recoil streamers” and then “recoil leaders” by Mazur (2002, p.1394), who argued that “they are negative leaders, i.e., self-propagating discharges, moving along previously developed trails of the positively charged parts of bi-directional and zero-net charge leaders”. Later, Saba et al. (2008) presented optical confirmation of the behavior described by Mazur (2002) while studying downward positive leaders with the help of digital high-speed cameras. Time integration of the imagery obtained by Saba et al. (2008) revealed profuse branching of the positive leader (which had not been reported up to that time), and their careful analysis suggested that their speeds ranged from 10^6 to 10^7 m s⁻¹ in a retrograde fashion (i.e., towards the origin point of the positive leader).

When one adds the presence of recoil leaders to the bidirectional leader model it is possible to describe the in-cloud structure of the dart leader-subsequent return stroke cycle in –CG flashes. From the interpretation of LMA data, Mazur (2002) describes the scenario illustrated in Figure 2.6. At instant t_1 the bidirectional leader starts to propagate (positive leader into the cloud and the negative, stepped leader moving towards ground), with both ends developing through t_2 and t_3 ,

when it makes ground contact. The complete return stroke channel is shown at t_4 , and some time later (t_5) current cutoff takes place (represented by the segmented lines). According to Mazur and Ruhnke (1993), those are the right channel conditions for the initiation of recoil leaders, shown as black arrows in Figure 2.6 (at t_5). Eventually, recoil leader activity initiated in the upper, in-cloud portion of the bidirectional leader may move all the way to the ground, manifesting itself as a dart leader and giving rise to a subsequent return stroke. Similar processes may occur during the continuing current (MAZUR; RUHNKE, 2011) or during the stepped leader development (CAMPOS et al., 2014b), leading to the occurrence of M components and β_2 leaders, respectively. Mazur (2002) describes additional detailed scenarios for IC and +CG flashes, but they are not reproduced here because they are not critical for this work.

Figure 2.6 – Recoil leaders in the bidirectional development of a negative CG flash.



Schematic representation of a negative cloud-to-ground flash including the occurrence of recoil leaders in the upper, in-cloud positive portion of the bidirectional leader.

Source: Mazur (2002).

2.5. Previous studies on the occurrence and characteristics of lightning with multiple ground terminations

The occurrence and characteristics of negative flashes that present multiple ground contacts were studied by a large number of researchers using different techniques and approaches. These works are reviewed and summarized in this section, which was divided into subsections according to different scopes and aspects of the results. Some studies are mentioned in more than one subsection as

they presented results that were relevant in more than one context. An attempt was made towards obtaining a comprehensive list and summary of all previous contributions on this topic, including results that were reported only in dissertations or conference papers.

2.5.1. Influence of the preceding interstroke and no-current intervals

Considering that the ionization created by a lightning return stroke tends to decrease after current cutoff as time advances due to channel cooling (UMAN; VOSHALL, 1968), it is intuitive to expect that the preceding interstroke and no-current intervals might influence the chances of formation of new ground terminations within a flash. However, as research on this aspect evolved, data suggested that other factors are more important.

Kitagawa et al. (1962) studied photographic records from a rotating-film camera and electric field changes of about 193 CG flashes. They concluded that subsequent strokes that occur after no-current periods (i.e., after both return stroke and continuing current were interrupted) longer than 100 milliseconds form a new path to ground.

Later, Winn et al. (1973) conducted a similar analysis of a somewhat larger dataset using a standalone camera with a temporal resolution of 60 frames per second (fps). Contrary to what was reported by Kitagawa et al. (1962), Winn et al. (1973) observed the formation of new ground contacts (NGCs) after periods shorter than 100 milliseconds.

From the analysis of simultaneous TV and electric field records of 76 –CG flashes, Rakov et al. (1994) concluded that the geometric mean (GM) of the interstroke intervals that preceded NGC strokes were about 60% longer than those preceded by strokes that followed a pre-existing channel (PEC).

Saba et al. (2006a) analyzed digital high-speed video records (1000 fps) of 233 negative CG flashes (253 intervals preceding PECs and 101 preceding NGCs). Although pre-NGC interstroke intervals tended to be slightly longer (their GMs were 60 ms for PECs and 68 ms for NGCs), they did not show any statistically significant difference at the 5% confidence level for the Student's *t*-test.

More recently, Ferro et al. (2012) revisited this subject after adding a large amount of new cases to the dataset of Saba et al. (2006a), including events from both southeastern Brazil and southern Arizona, USA (SARAIWA et al., 2010). The analysis of 736 interstroke intervals (445 preceding PECs and 291 preceding NGCs) resulted in the corroboration of the Saba et al. (2006a) results: GM of 62 and 66 milliseconds for interstroke intervals preceding PECs and NGCs, respectively. Ferro et al. (2012, p.132) also state that “although time interval may play a role in the creation of a new channel, it is probably not the predominant factor”.

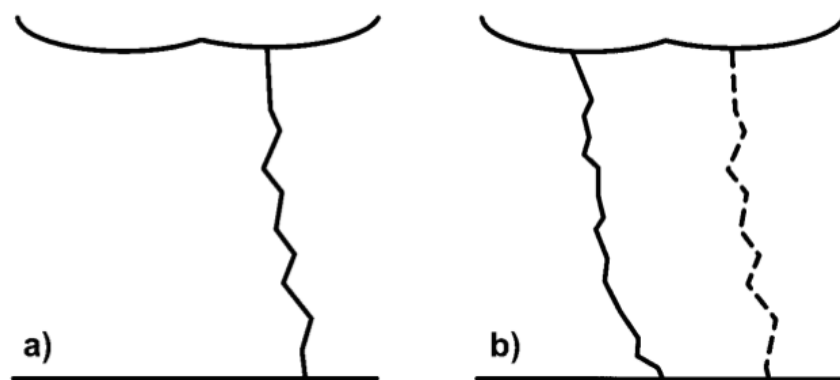
2.5.2.Scenarios and mechanisms

In his doctoral thesis work, Krehbiel (1981) analyzed multiple-station electric field records of CG flashes. Among numerous other results, he had noticed a field “overshoot”, followed by a polarity reversal leading to a lower stable value in the electric field, seen more clearly in close lightning when compared to more distant observations. This behavior was particularly pronounced after first strokes and was interpreted as the deposit of one coulomb (or more) of negative residual charge in the bottom 1-2 kilometers from ground. Krehbiel (1981) speculated that these residual charges would be responsible for deviating the subsequent dart leaders from the original channel. Later VHF interferometry observations of dart-stepped and attempted leaders, conducted by Shao et al. (1995) and Mazur et al. (1995), seemed to agree with the conclusions of Krehbiel (1981). However, no further studies on this charge deposit and its relationship with not only the creation of NGCs but also current cutoff have been conducted.

Rakov et al. (1994, p.10746), in a compilation of results from preceding works based on multiple-station TV observations (including Thottappillil et al., 1990, 1992, Rakov and Uman, 1990a,b, 1992, among others), stated that, most commonly, “multiple ground terminations within a given flash are associated not with an individual multigrounded leader but rather with the deflection of a subsequent leader from the previously formed channel”. Although no inferences were made on distributions or displacements of electric charges, their data supported the idea of Krehbiel (1981).

Valine and Krider (2002) studied 386 videotape (33 ms temporal resolution) CG flashes in near Tucson, Arizona, with an emphasis on 35% (136) of the events that presented multiple ground locations. These could be either a “new channel flash” (NCF), in which the NGC subsequent stroke followed a completely new path between cloud base and ground (illustrated in Figure 2.7), or an “altered channel flash” (ACF), consisting of events that share a common upper portion with a bifurcation point that is visible below cloud base in time-integrated images (illustrated in Figure 2.8).

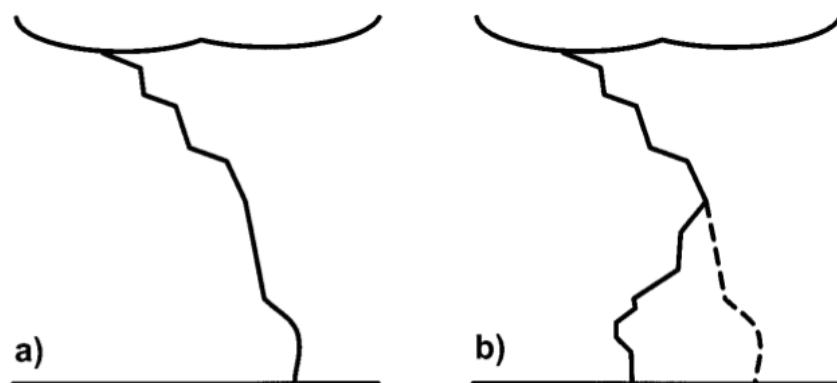
Figure 2.7 – Illustration of a “new channel flash” (NCF).



Schematic representation of a negative CG NCF: (a) channel of the first stroke; and (b) a subsequent stroke that follows a completely new channel below cloud base.

Source: Valine and Krider (2002).

Figure 2.8 – Illustration of an “altered channel flash” (ACF).



Schematic representation of a negative CG ACF: (a) channel of the first stroke; and (b) a subsequent stroke that deviates from the first channel at a point visible below cloud base.

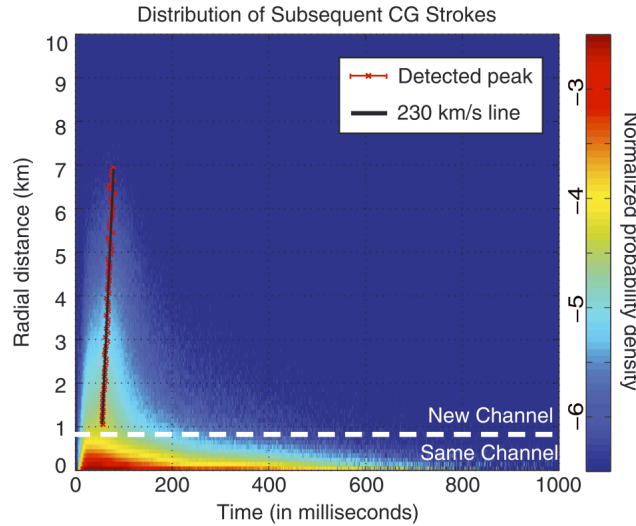
Source: Valine and Krider (2002).

As acknowledged by Valine and Krider (2002), though, an ACF whose branching point from the first stroke channel is located above cloud base will appear an NCF to an optical instrument such as a camera. The NCF to ACF ratio they found for Arizona is 2.1, significantly lower than what was found for Florida (3.1) by Rakov and Uman (1990a). This is expected due to the notable differences in the cloud base height (CBH) between these two locations (see, for instance, Figure 2.1, considering that the humidity conditions in Arizona are closer to New Mexico). In order to account for that, Valine and Krider (2002) reanalyzed their data as if the CBH of Arizona (~ 3 km) was similar to Florida (~ 1 km), obtaining a ratio of 3.2, much closer to the 3.1 obtained by Rakov and Uman (1990a).

Zoghzoghy et al. (2014) adopted a different approach in the analysis of MGCFs by applying a statistical method to obtain spatial and temporal distributions of subsequent strokes detected by the United States National Lightning Detection Network (U.S. NLDN). One of their key results is shown in Figure 2.9, in which the vertical axis corresponds to the radial distance from the initial stroke to its first subsequent stroke (given by the relative position provided by their U.S. NLDN solutions), and the horizontal axis shows the interstroke interval between them (also obtained from the solution time of the U.S. NLDN data). They assumed that all subsequent strokes that were over 750 m away from the initial stroke were NGCs (based on the results by Stall et al., 2009), as indicated by the horizontal dashed line in Figure 2.9. As commented by Zoghzoghy et al. (2014), there is a horizontal feature (below the white dashed line) that extends in time up to 800 milliseconds and a vertical (but tilted) feature that extends from 1 to 7 kilometers (shown by the solid black line). The horizontal feature is believed to correspond to the occurrence of PEC subsequent strokes and its width may be related to the NLDN geolocation errors. It is the vertical feature, however, that is of interest to the present work. Zoghzoghy et al. (2014) argue that it corresponds to NGC subsequent strokes whose contact points are 1 to 7 km away from their initial strokes, with their peak occurrence moving away from the initial strike point at a speed of approximately 230 km s^{-1} , as calculated from the slope of the linear fit of the peak occurrence points in Figure 2.9. When different months were analyzed separately (August 2010, July 2011 and August 2011), they found that this slope

could vary from 200 to 280 km s⁻¹, an indication that storm type and season may modulate the resulting distribution of NGCs around their initial return strokes.

Figure 2.9 – Space-time occurrence distribution of first subsequent strokes.



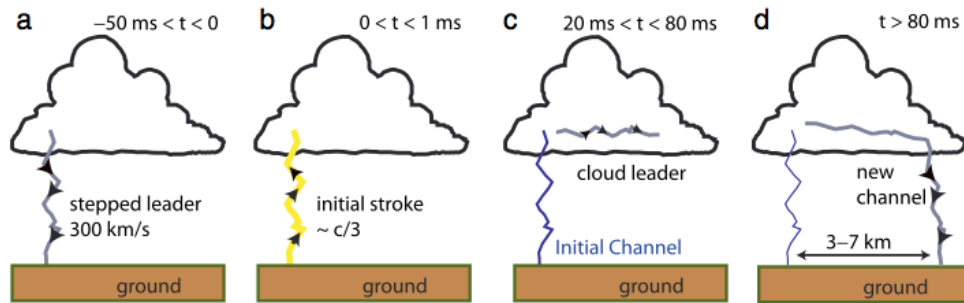
Spatial and temporal histogram of first subsequent strokes with respect to their initial strokes accumulated over more than two million –CG flashes. The total probability of the histogram is normalized to unity and color coded to a logarithm scale (shown to the right). A given subsequent stroke is considered to produce an NGC when its separation distance from the initial stroke greater than 750 meters, as visually represented by the horizontal dashed white line. The solid black line corresponds to the linear fit of the peaks of occurrence (indicated by the small red bars) and its slope is equivalent to a propagation speed of 230 km s⁻¹.

Source: Zoghzoghy et al. (2014).

The interpretation by Zoghzoghy et al. (2014) of their statistical results reported is presented in Figure 2.10. Given the fact that the slope of the linear fit of the peak occurrence of NGC strokes in the histogram that resulted from their analysis (Figure 2.9) is compatible with typical stepped leader speeds (e.g., SCHONLAND, 1938; ORVILLE; IDONE, 1982; CAMPOS et al., 2014a), the horizontal development of in-cloud leaders during the interstroke interval preceding an NGC stroke could possibly explain the observed distribution. This in-cloud leader may eventually become downward propagating, leading to a new ground termination that is statistically more distant from the initial stroke if preceded by longer interstroke intervals. Although this scenario is not specifically incompatible with the presence of a residual charge proposed by Krehbiel (1981),

it is significantly different from the sequence of events observed in ACFs, shown in Figure 2.8 (RAKOV; UMAN, 1990a; VALINE; KRIDER, 2002). It may, however, explain part of the incidence of NCFs (Figure 2.7) whose separation distances are too large to be related to the deviation from the initial stroke channel.

Figure 2.10 – Mechanism of new ground contacts suggested by Zoghzy et al. (2014).



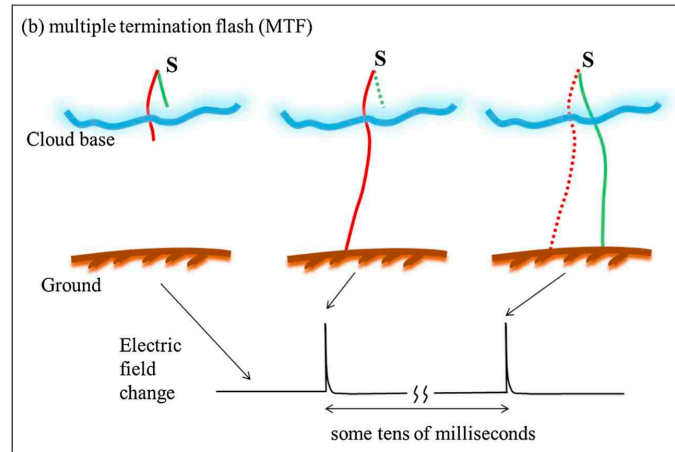
Schematic representation of the formation of a distant NGC in a -CG flash as suggested by their statistical distribution: (a) the channel of the initial stroke is created by a downward stepped leader developing at a speed within the $100\text{-}300 \text{ km s}^{-1}$ range; (b) the return stroke occurs after contact with ground is made; (c) an in-cloud leader branch propagates away from the initial stroke contact point during the interstroke interval (also at a speed within the $100\text{-}300 \text{ km s}^{-1}$ range); (d) the horizontal, in-cloud leader eventually moves downwards, touching ground at a point $3\text{-}7 \text{ km}$ away from the initial stroke location.

Source: Zoghzy et al. (2014).

At the time of the elaboration of the present work, Sun et al. (2016) have published a detailed discussion of a -CG flash with multiple ground terminations that was observed by a two-dimensional (elevation and azimuth) short-baseline (eight meters) DTOA VHF mapping system that functions much like an interferometer. In addition to the presence of two upward illumination strokes in that flash (to be discussed in subsection 2.5.7), Sun et al. (2016) analyzed the formation of a NGC subsequent stroke. As illustrated in Figure 2.11, they observed that the second leader-return stroke sequence initiated in the same region of the preliminary breakdown that started the flash (indicated by the S in the figure), 82.9 milliseconds after the first stroke. This new leader propagated partly through a previously developed channel segment, indicated in Figure 2.11 by the green channel, before splitting into three branches that moved downward. Sun et

al. (2016) also stressed the fact that optical and electric field observations are incapable of providing enough information for a precise and detailed description of how a multi-grounded flash is formed, arguing that VHF mapping is vital for the study of this kind of phenomenon.

Figure 2.11 – Mechanism of new ground contacts suggested by Sun et al. (2016).



The downward stepped leader forms two channel branches in the cloud (red and green, to the left of the figure). Only one makes contact (red channel, center of the figure) at first, with the secondary (green) branch going through current cutoff. Eventually, after current in the initial channel is interrupted (dashed red channel to the right of the figure), a new leader-return stroke sequence is initiated at the same origin point (indicated by the S) the secondary (green) branch

Source: adapted from Sun et al. (2016).

2.5.3. Relationship with return stroke electric field peak values

Rakov and Uman (1990a), based on the same dataset of 76 electric field and TV records of –CGs in Florida, USA, that was mentioned in the previous subsection, presented a statistical analysis suggesting that NGC return strokes tend to present a larger normalized electric field peak value when compared to PEC strokes (their GM is about 30% larger and their statistical distribution is skewed towards more intense values).

Thottappillil et al. (1992) studied the same dataset of Rakov and Uman (1990a) with an emphasis on flashes in which the subsequent stroke presented a field peak greater than its first stroke. When the ratio between normalized electric field peaks of subsequent strokes over their first stroke peaks were analyzed, NGC

strokes still were more intense: the GM of their ratios were approximately 40% greater than what was observed for PEC strokes. Both studies were later reviewed and summarized by Rakov et al. (1994).

Ferro (2008) and Ferro et al. (2009) analyzed the peak current estimated by wide-area Lightning Location Systems (which, in turn, are based on magnetic and/or electric field measurements, as discussed extensively by Cummins and Murphy, 2009) for first, subsequent NGC and subsequent PEC strokes that were followed by continuing currents with different ranges of durations. Data from São Paulo, southeastern Brazil, and southern Arizona, USA, were combined in that analysis. When comparing the GM of estimated peak currents that are followed by either no continuing current or by short (i.e., shorter than 40 ms) continuing currents, it was found that first strokes are more intense than NGC subsequent strokes and these, in turn, are more intense than PEC subsequent strokes (and that relation is statistically significant). For strokes followed by long continuing currents (i.e., longer than 40 ms), however, even though the GMs of the estimated peak currents follow the same relationship, their differences were not statistically significant.

These results are corroborated by the findings of Stall et al. (2009). They also argue that the estimated peak current values “clearly contain valuable information about whether a given stroke has produced an NGC” (STALL et al., 2009, p.2398). That work is discussed in greater detail in subsection 2.5.6, which is focused on the use of LLS data to identify MGCFs.

2.5.4. Statistical incidence

The frequency of occurrence of MGCFs is probably the most exhaustively studied aspect of this category of CG lightning. So far, sixteen journal and conference papers have explored this topic based on different instruments and methodologies. Table 2.1 summarizes their results and, when enough information was available, the relative occurrence of MGCFs is presented not only with respect to multiple-stroke flashes but also for their entire datasets (i.e., including all single- and multiple-stroke flashes). These works do not address forked or upward illumination (UI) strokes, two types of phenomena that are discussed in subsection 2.5.7.

Table 2.1 – Summary of previous studies on the occurrence of multiple ground contact flashes.

Study	Instrument	Location	Occurrence over all dataset	Occurrence over multi-stroke flashes
Kitagawa et al. (1962)	Rotating-film camera and electric field	Socorro, NM, USA	42.2% (35/83)	48.61% (35/72)
Krider (1966)	Photodiode and still photographs	Tucson, AZ, USA	17%	-
Barasch (1970)	Spectral intensities from narrow band radiometers	Los Alamos, NM, USA	18%	-
Winn et al. (1973)	Standard video	Langmuir Lab, NM, USA	31.8% (35/110)	-
Brantley et al. (1975)	Standard video	Ocala and Kennedy Space Center, FL, USA	21.5% (44/205)	-
Thomson et al. (1984)	Standard video and electric field	Tampa, FL, USA	-	43.6% (44/78)
Rakov and Uman (1990a)	Standard video and electric field	Tampa, FL, USA	50.0% (38/76)	60.3% (38/63)
Nagai et al. (1994)	Standard video	Tochigi, Japan	30.3%	-
Berger et al. (1996)	Standard video	Central France	34.1% (1020/2995)	-
Ishii et al. (1998)	Network of fast electric field antennas	Fukui area, Japan	-	81.8% (9/11)
Valine and Krider (2002)	Standard video	Tucson, AZ, USA	35.2% (136/386)	53.1% (136/256)
Parker and Krider (2003)	Standard video, photodiode and electric field	Tucson, AZ, USA	31.7% (79/249)	-
Saba et al. (2006a)	High-speed video	São José dos Campos, SP, Brazil	50.7% (70/138)	67.3% (70/104)
Fleenor et al. (2009)	Standard video and electric field	Central Great Plains, USA	33.0% (34/103)	54.8% (34/62)
Saraiva et al. (2010)	High-speed video	Tucson, AZ, USA	48.1% (99/206)	58.6% (99/169)
Antunes et al. (2015)	High-speed video	São José dos Campos, SP, Brazil	46.5% (168/361)	58.7% (168/286)

Source: Produced by the author after information gathered through literature review.

A brief analysis of Table 2.1 shows that there is considerable variation in the results obtained for the proportion of MGCFs over both multi-stroke only flashes and their entire datasets (including single-stroke flashes as well). If one takes a single instrument type, such as standard video cameras, it may give similar results for different locations: from 30% to 35% (MGCFs over the full dataset) in New Mexico, USA (WINN et al., 1975), Tochigi, Japan (NAGAI et al., 1994), Central France (BERGER et al., 1996), Arizona, USA (VALINE; KRIDER, 2002; PARKER; KRIDER, 2003) and the Central Great Plains, USA (FLEENOR et al., 2009). However, for the same location, when standard video cameras are compared to digital high-speed cameras, results can diverge greatly: 32-35% (VALINE; KRIDER, 2003; PARKER; KRIDER, 2003) versus 48% (SARAIVA et al., 2010) for Tucson, Arizona, USA.

Antunes et al. (2015) have documented a similar range of variability for a single location (São José dos Campos, São Paulo, Brazil) over five different thunderstorm days in late February and early March, 2013. The percentage of MGCFs over their total dataset ranged from 38% (March 8th) to 54% (February 18th), with an overall percentage (accumulating all five days) of 47%. This result is in agreement with Saba et al. (2006a), who analyzed the same region using an older high-speed camera and obtained 51%. Finally, it is worth noting that very similar results are obtained even at different locations for datasets accumulated over many storms if only high-speed camera studies are considered (and assuming that their temporal resolution, generally of one millisecond or less, is sufficiently high for accurate-stroke-count analyses): 48% for Tucson, Arizona, USA (SARAIVA et al., 2010) and 47-51% for São José dos Campos, São Paulo, Brazil (SABA et al., 2006a; ANTUNES et al., 2015).

Another related parameter that is not provided in all studies is the average number of strike points per flash. Valine and Krider (2002) obtained 1.45 for their dataset, smaller than what has been reported by Rakov et al. (1994) and Saba et al. (2006a), which were very similar: 1.67 and 1.70, respectively. Antunes et al. (2015) obtained consistent values for five thunderstorm days, although higher than the aforementioned studies: 1.9 (March 6th) to 2.1 (February 19th), with an overall mean (considering all days accumulated) of 2.0 contact points per flash. Some authors (e.g., BOUQUEGNEAU, 2014; VISACRO, 2015) argue that the

knowledge of this parameter is very relevant for the design of lightning protection systems and for more efficient standards. This topic (along with a few practical applications of some results of the present thesis) is further explored in Chapter 9.

2.5.5. Stroke order and channel conditioning

Intuitively, one might expect that the effect of consecutive return strokes occurring in the same channel could accumulate its reminiscent ionization during the interstroke interval (after current cutoff has taken place). Despite their short durations, the plasma heating caused by the return stroke high peak currents might delay the cooling normally associated with plasma ion recombination.

Rakov and Uman (1990a) and Rakov et al. (1994) analyzed this effect in Florida, USA, by evaluating the probability of creation of an NGC with the stroke order. They noted that about 37% of the second strokes did not follow the first stroke channel to ground. This proportion, however, drops significantly as the stroke order grows: 27% for third strokes and only 2% for fourth strokes. They did not observe any flash with an NGC created at a stroke order greater than four, although their dataset was small.

Saba et al. (2006a), in São Paulo, Brazil, obtained a similar distribution from high-speed video data: 41% for second strokes and 27% for third strokes, however, the incidence of NGCs in strokes or order four was considerably higher: 12%. They also reported 5% of NGCs being formed in the fifth stroke, contrarily to the results of the previous two works, but every single stroke with order six or greater were PECs.

Stall et al. (2009), in Arizona, USA, reported an even larger proportion of NGCs in second strokes: 59%, from standard video records. The same overall behavior was observed: 27% in order three, 7% in order four, 5% in order five, no NGCs in order six and 2% in order seven.

Finally, Ferro et al. (2012), combining digital high-speed video data recorded in São Paulo, Brazil, and Arizona, USA, reported the percentage of their total NGC subsequent strokes that occurred for each stroke order, although the proportion of NGCs among all strokes of a given order were not provided. They did not discuss

any possible regional differences in that analysis. It is worth noting, however, that Ferro et al. (2012, Section 3.2 and Figure 1) have observed two cases of NGCs being formed in stroke order nine, probably the first cases of this kind to be reported in literature.

2.5.6. Identification and detection of flashes with multiple ground contacts by large scale Lightning Location Systems (LLS)

The identification of MGCFs is not only of scientific interest but also has relevant applications. As further discussed in Chapter 9, they present additional risks of more than one structure (or individuals) being struck by a single lightning flash, a reason why some researchers have tried to obtain patterns that would allow the efficient identification of this type of event.

Willett et al. (1995) analyzed video and wideband electric field records of 32 CG flashes. Through careful comparison between both instruments, they concluded that standalone electric field data is enough to separate strokes that follow PECs and those that create NGCs. It was found that initial stroke and NGC waveforms had jagged return stroke electric field (E) peaks, with a relatively noisy time derivative (dE/dt), while PECs had smoother waveforms with “quiet” time derivatives.

On a more practical approach, Stall et al. (2009) compared video records with data provided by the U.S. NLDN in an attempt to determine if the latter is capable of differentiating NGCs and PECs. They concluded that the NLDN can frequently identify whether or not a stroke created a new ground termination based solely on its location solutions, but suggested that additional parameters (return stroke order, rise time and estimated peak current) could be used to improve the methodology for events with small separation distances between strike points.

Building on the conclusions presented by Stall et al. (2009), Cummins (2012) used the NLDN parameters of the events of the same dataset (separated between 59 PEC and 60 NGC subsequent strokes) to conduct a Linear Discriminant Analysis (LDA). He has trained a discriminant function that could differentiate NLDN solutions of PEC and NGC strokes with a correctness of approximately 87%. This result is currently being used in an ongoing effort (CUMMINS, 2014)

to analyze the impact of complex terrain features in the number of ground contacts and motivated some of the analyses of the present thesis.

Pédeboy (2012) adopted a distinct approach, trying to identify MGCFs with LLS by using a data clustering method based on the k -means algorithm. After using a regular space-time flash-grouping algorithm to group individual return strokes of a given dataset into flashes, the k -means iterates over every individual flash included in that set. It is assumed that the first stroke location corresponds to the first ground contact point (GCP) then each subsequent stroke is analyzed sequentially. If the distance between each new stroke and all previously determined GCPs is below a maximum distance (defined according to the location accuracy of the network), that stroke is grouped into the closest GCP (and the GCP position is recalculated accordingly); if not, a new GCP is added to the list (located at the stroke currently being analyzed) and then it iterates over the next subsequent stroke. After each stroke is processed by the algorithm, the positions of all GCPs are recalculated as typically done in normal implementations of the k -means algorithm, i.e., as the mean centroid of the solution positions of all strokes grouped to each GCP. There is one important difference, though, as in the algorithm by Pédeboy (2012) the mean centroid is weighed by the inverse of the error ellipse semi-major axis (SMA) of each stroke associated with that GCP. More recently, Pédeboy and Schulz (2014) have evaluated the identification efficiency of the algorithm over a dataset of 227 –CG flashes recorded with digital high-speed cameras in Austria and France in 2012 and 2013, respectively. Both countries are well covered by the EUCLID (EUropean Cooperation for LIghtning Detection). They have obtained a stroke classification effectiveness of 83%, corresponding to 636 return strokes that were not only correctly classified as NGC or PEC but also assigned to their corresponding GCP. When undetected strokes are removed (i.e., return strokes that were recorded on camera but were not detected by the LLS), the efficiency goes up to 92%. Further, 56% (126 out of the 227) of their analyzed flashes were perfectly classified by the algorithm, i.e., all their return strokes were correctly labeled as either PEC or NGC and grouped into the correct GCP when compared to the video data. That percentage goes up to 57% when strokes undetected by EUCLID are removed.

For the statistical analysis conducted by Zoghzoghy et al. (2014), described in greater detail in subsection 2.5.2, a much simpler criterion was used to determine whether a subsequent stroke was a NGC or PEC. As shown by the dashed white line of Figure 2.9, first subsequent strokes whose solution location was more than 750 meters away from their initial strokes were considered to be NGCs. That threshold was chosen in an attempt to identify NGC strokes that were 1 to 7 km away from the first GCP of their flashes, based on the results previously presented by Stall et al. (2009). Despite the simplicity of this classification criterion, Zoghzoghy et al. (2014) were able to provide valuable insights in the topic of multi-grounded lightning flashes, as previously discussed in this literature review.

2.5.7. Forked and upward illumination strokes

During the development of a stepped leader to ground, several branches are usually formed and, in some events, they reach ground virtually at the same time. Those events have received different names in literature, such as twin strokes (SCHONLAND et al., 1935), double-ground strokes (RAKOV; UMAN, 1994), two-channel strokes (WANG et al., 2000), forked strokes (BALLAROTTI et al., 2005), multiple ground contact strokes (GUO; KRIDER, 1982), multiple-ground terminations strokes (KONG et al., 2009) and the somewhat different upward illumination (STOLZENBURG et al., 2012, 2013b). Even though they comprise a different class of events if compared to the typical, “sequential” MGCFs, multiple ground contact strokes are also analyzed in this thesis as their final results are similar: producing more than one ground termination within a single lightning flash. Also, even though the terminology used by different authors was kept in the present subsection when each work is discussed, the term “multiple ground contact stroke” (MGCS) will be used when referring to them collectively. The specific terminology and differentiation between each “subclass” of phenomenon, along with the importance of the time interval between ground contacts, will be explored in Chapter 5 of this thesis work as part of its results.

Schonland et al. (1935) presented the first reports of these events through streak-camera records that showed two ground attachments within a time interval of only 73 microseconds. They pointed out that these branches probably shared one

common trunk higher up in the thundercloud, arguing that they were probably two strokes and not different flashes.

Later, Guo and Krider (1982) obtained evidences of double-grounded strokes from different branches of the same downward leader when analyzing optical and electric field sensors. The data collected at the time indicated that those strokes were separated by intervals of the order of tens of microseconds.

Rakov and Uman (1994), in the same work described in previous subsections, studied 13 double-ground strokes registered in standard video records (among which 9 also had simultaneous electric field measurements). Generally, these double-grounded strokes occurred in the initial stroke of a flash, but second and third strokes were also reported to present that behavior. The temporal separation intervals they reported ranged from 15 microseconds to 3.3 milliseconds (RAKOV; UMAN, 1994, Table 1).

Willett et al. (1995), in the aforementioned work (see subsection 2.5.6), have also observed three double-ground events (two with good quality video records and one with poor imagery). These cases had temporal separations between ground contacts of 6.7, 8.4 and 9.9 microseconds. Also, they have shown that both terminations in double grounded events radiated as initial/NGC strokes (e.g., WILLET et al., 1995, Figure 3).

Wang et al. (2000) analyzed two cases of “branched-strokes” recorded by a photodiode array system called ALPS (Automatic Lightning Progressing Feature Observation System) whose version operated at the time is described by Wang et al. (1999). One of them, identified as a “two-channel” stroke, was similar to those studied by Guo and Krider (1982) and Rakov and Uman (1994) and touched ground at two different locations almost simultaneously. Through the analysis of the light waveforms as a function of time for both branches, Wang et al. (2000, Figure 5) concluded that the left channel touched ground only 200 nanoseconds prior to the right channel. They argue that such a small temporal separation would not have been detected in electric field records, and also that this event exhibited the shortest interval ever documented to occur between return stroke waves propagating in two channels.

Qie et al. (2005) presented evidences from digital high-speed video and electric field measurements of the occurrence of a single stroke –CG flash that touched ground in four points almost simultaneously. The observations were made in the Qinghai–Tibetan Plateau in China and they reported temporal differences between each successive contact of 4, 9 and 10 microseconds. Further details on that event were later presented by Qie and Kong (2007).

More recently, Ballarotti et al. (2005) analyzed MGCSs with digital high-speed cameras. Forked strokes were observed in six flashes recorded in São José dos Campos, São Paulo, Brazil, in the summer seasons between 2003 and 2005 (including data from 40 different thunderstorms). In four of these events the temporal separation between contacts were less than 1-2 milliseconds long (limited by the temporal resolution of the camera, operating at 1000 fps), and in the two events for which electric field records were available, the temporal separation could be determined as being 31 and 253 microseconds. Ballarotti et al. (2005) reported these events in strokes of order 1, 2 and 4. Also, in three events, one of the ground terminations lasted longer (suggesting that it was the one that touched ground first), while for those in which both branches persisted simultaneously their duration could be as long as 5 milliseconds (BALLAROTTI et al., 2005, Figure 1 and paragraphs 16-17).

Kong et al. (2009) analyzed 59 –CG flashes among which nine (15% of the total sample) were initiated by a multiple-ground-termination stroke. The observations were conducted in 2002, 2006 and 2007 in three different regions in China. High-speed video (1000 fps) records were obtained along with fast and slow electric field measurements. When each different region is considered, the percentage of occurrence of MGCSs ranged from 11% to 20%. Separation distances between ground strike points ranged from 0.2 to 1.9 km, and the time intervals between them ranged from 4 to 486 microseconds. Kong et al. (2009) also argue that the proportion of multi-grounded strokes found by them (15.3%) suggests that it is a significantly more common phenomenon than previous studies indicated, stressing the fact that Ballarotti et al. (2005) and Valine and Krider (2002) observed this type of event in only 1.3% and 3.8% of their datasets, respectively. It is worth noting, however, that of the 15 (out of 386) apparently simultaneous multiple strike points described by Valine and Krider (2002, p.8-6), they

acknowledge that “with a time resolution of 33 ms, it was not possible to determine if these forks were truly simultaneous”.

More recently, Stolzenburg et al. (2012) introduced what seems to be an entirely new class of MGCS they termed “upward illuminations” (UIs). From their high-speed video data (operating at 54,000 fps with 18.1 microseconds of exposure time), an UI is described as having these four defining characteristics:

(a) a new ground connection, within 2 ms of a normal RS, that follows a different channel to ground from any prior strokes in the flash; (b) no apparent visible connection to the preceding or concurrent RS (*return stroke*) channel; (c) only the lowest channel portion, 1-3 km above ground, illuminates, and the luminosity moves upward, as with a return stroke but without visible channel at higher altitudes; (d) the main part of the UI’s upward path follows a stepped leader or branch that was moving toward the ground simultaneously with the successful leader (i.e., the one that results in the return stroke) (STOLZENBURG et al., 2012, p.2).

Four –CG flashes presented UIs and were described in detail by Stolzenburg et al. (2012). The separation distances between the ground contact of UIs and their “parent” return strokes were estimated to range from 0.7 to 2.5 km, and their luminosity propagated more slowly than the associated return strokes. After detailed case studies, Stolzenburg et al. (2012) hypothesize that UIs are initiated by stepped leader branches that become effectively cut off from the “main trunk” of the leader, continuing its development until it reaches ground shortly (less than 2 milliseconds) after the regular return stroke occurred.

Additional twenty cases of UIs (from eighteen flashes) were later observed and analyzed in detail by Stolzenburg et al. (2013b). One very interesting feature that was observed in part of their new dataset is the presence of stepping in the development of the UI downward leader after the main return stroke has occurred. Stolzenburg et al. (2013b, Section 3.3.4 and Figure 9) argues that this feature strongly suggests that the UI channel is disconnected from the main trunk as, otherwise, it would be neutralized (and illuminated) by the return stroke as commonly observed in “regular” stepped leader branches. Also, by combining the information provided by the numerous events they analyzed, they have identified and described seven fundamental luminosity stages of a UI-type stroke. These stages will be discussed in detail in Chapter 5, which is dedicated to both known categories of MGCS, forked and UI-type strokes.

Finally, a very recent paper by Sun et al. (2016) presented two-dimensional (elevation and azimuth) VHF and electric field observations of a four-stroke flash in which the first two leader-return stroke sequences produced UI-type strokes. The UI channels in both of them produced considerably smaller electric field peaks when compared to their main return strokes (by factors of 2.9 and 4.4). The temporal separations between the contacts were 1.5 and 2.7 milliseconds. Sun et al. (2016) also argue that these separations are further evidence that the UI channel is cut off from the main trunk of the flash, considering the distance that would be traveled by a typical return stroke wave (propagating at 10^8 m s^{-1}) during the observed time interval.

3 INSTRUMENTS, CAMPAIGNS AND DATASETS

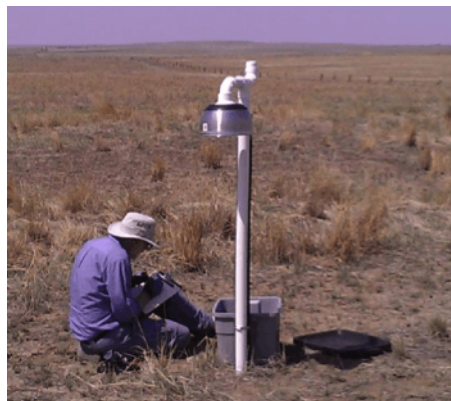
The present chapter consists of an overview of the scientific instruments, data collection campaigns and dataset sources that have been used for the development of this thesis work. Whenever it was possible, the basic principles of the instruments are described, listing the main references related to their development and use.

3.1. Instruments

3.1.1. Slow electric field antennas

In order to measure the variations of the electrostatic field produced by lightning flashes, a network of slow antennas were used. They are named “slow” because their relaxation time constant (typically of a few seconds) is relatively long in comparison to the electric field changes produced by lightning processes. The field changes were sensed through the charges induced on a flat, circular plate antenna, such as the one shown in Figure 3.1. The plate itself is protected by the conductive upside-down bowl that surrounds it in an attempt to minimize the impact of rain and external boundary variations. The battery and supplementary electronic circuitry is housed inside the box that lies near the station.

Figure 3.1 – Picture of a slow electric field antenna and its circuitry housing.

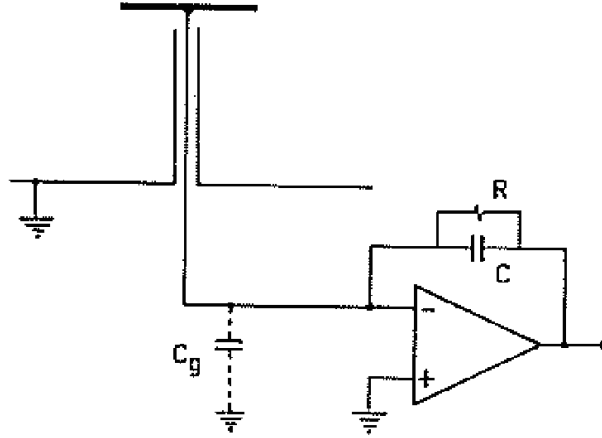


Picture showing a field installation of one of the slow electric field antennas used in the present work. The circular plate is not shown due to the conductive bowl used to protect its measurements from external boundary conditions.

Source: provided by K. Cummins (2013, unpublished).

The basic schematics of the analog sensing circuit of the slow electric field sensor are essentially equal to the one presented in Figure 3.2. The plate antenna is connected to the inverting input of an operational amplifier set to operate as an integrator (as established by the feedback capacitor C) with a decay time constant set by the product RC .

Figure 3.2 – Schematic diagram of a typical slow electric field antenna.



Schematic diagram of a slow electric field antenna and its associated electronic circuitry. The operational amplifier is set to operate as an integrator of the signal generated by the flat plate antenna.

Source: adapted from Krehbiel et al. (1979).

The output signal of the antenna is integrated over time by the operational amplifier, which makes it possible to estimate the electric field change. By modeling the plate antenna as a parallel-plate capacitor (with the ground surface as the “second plate”), it can be shown that the electrical charge Q on a disc of area A induced by an electric field of magnitude E is given by:

$$Q = \varepsilon_0 A E \quad (3.1)$$

The output current of the antenna can be obtained by deriving (3.1) with respect to time:

$$i = \frac{dQ}{dt} = \varepsilon_0 A \frac{dE}{dt} \quad (3.2)$$

By using the expression that relates the input and output voltages of an integrator circuit, the capacitance of the feedback capacitor (C) and (3.2), one can obtain the output voltage change (ΔV) of the circuit in terms of the temporal variation of the electric field that causes it:

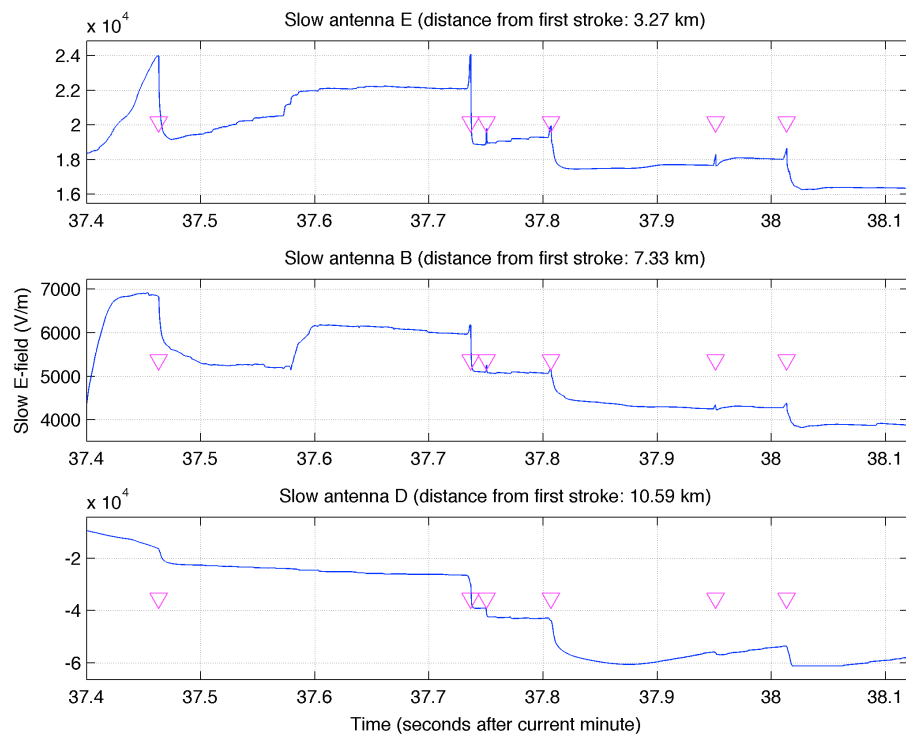
$$\Delta V = -\frac{1}{C} \int i dt = -\frac{1}{C} \int \left(\epsilon_0 A \frac{dE}{dt} \right) dt \quad (3.3)$$

By integrating the right-hand side of (3.3) it is possible to obtain the expression that relates the electric field changes (ΔE) that are short in comparison to the characteristic time constant of the circuit:

$$\Delta V = -\frac{1}{C} \epsilon_0 A \Delta E \quad (3.4)$$

The relatively long decay time of the system makes the slow antenna particularly useful to analyze long lasting variations, such as those associated with continuing currents and quasi-static charge geometry within a cloud. Figure 3.3 presents three waveforms obtained from different stations for the same three-stroke negative CG flash. The removal of negative charges aloft the antenna is associated with a downward deflection in the waveform plots. Each return stroke is indicated by a magenta triangle (whose time of occurrence was given by its U.S. National Lightning Detection Network solution) and is associated with a relatively small and rapid downward deflection in the waveform plots. The first and fourth strokes are followed by long continuing currents, which can be identified by the continued downward deflection following both of them in the most distant waveform (slow antenna D, 10.6 km from the first stroke). It is important to stress that the aspect and polarity of the leader-return stroke waveform sequences are highly dependent on the distance between strike point and antenna: in the records from antennas E and B the field deflects upward as the leader approaches ground, before the downward deflection of the stroke itself; however, in antenna D only the stroke downward deflection was detected. Networks of these sensors can be used to study the nature and movement of charge during lightning flashes (e.g., KREHBIEL et al., 1979; KREHBIEL, 1981).

Figure 3.3 – Examples of slow electric field waveforms at different distances.



Slow electric field waveforms of a six-stroke –CG flash observed from three different stations (located at 3.3, 7.3 and 10.6 km away from the location of the first stroke). Each magenta triangle represents the instant a stroke happens (as provided by U.S. NLDN solutions). The removal of negative charges aloft causes a downward deflection in the recorded waveform.

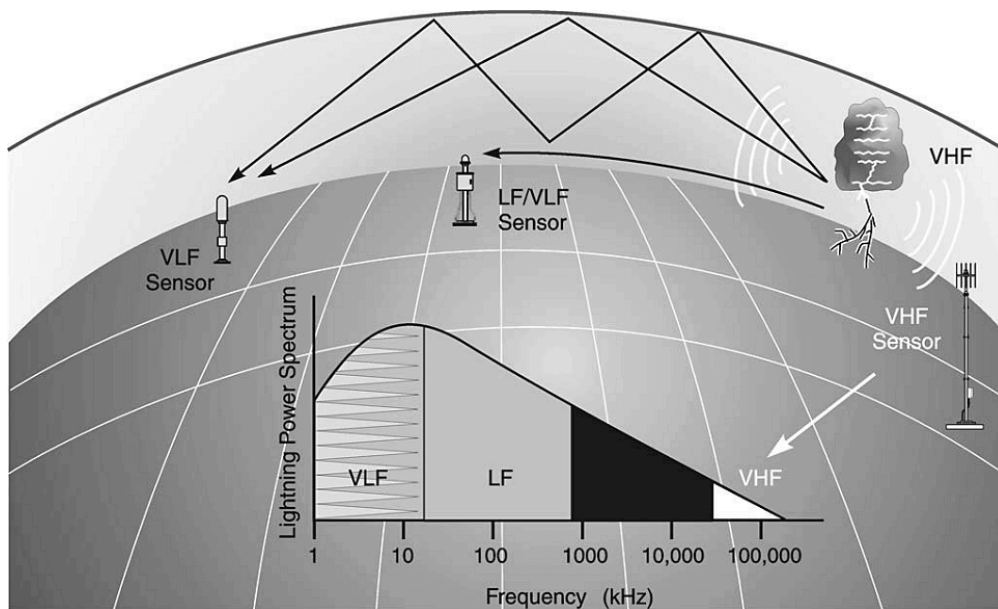
Source: produced by the author.

3.1.2. Lightning Location Systems (LLS)

Lightning emits electromagnetic radiation over a wide spectrum of frequencies. Its different processes and characteristics can be detected and located if the instruments are designed to measure the appropriate frequencies. That is usually done with the help of a Lightning Location System (LLS), which is made up of multiple electromagnetic sensors, their communication systems and a central processing unit responsible for geolocation and analysis of lightning flashes based on the data sent by each sensor. Figure 3.4 summarizes the lightning power spectrum at different frequency ranges, from VLF (very low frequency) to VHF (very high frequency), and shows the different classes of sensors used to detect radiation at each range. VLF sensors are commonly used to detect very distant

(thousands of kilometers) flashes from waves reflected between the ground and the ionosphere. On the opposite side of the spectrum, VHF sensors are only capable of detecting close lightning, from which they have a line-of-sight. Their advantage, however, is the fact that they can be used to detect and locate in three dimensions the radiation emissions associated with breakdown processes and leader propagation, making them extremely useful for mapping channels inside the thundercloud. Finally, in between the VLF and VHF sensors, the VLF/LF networks can locate transient pulses that propagate along the surface of the Earth, making them a class of “middle-ranged” sensors when compared to the other two types shown in Figure 3.4.

Figure 3.4 – Lightning power spectrum and the sensor types used to detect it.



Source: Cummins and Murphy (2009).

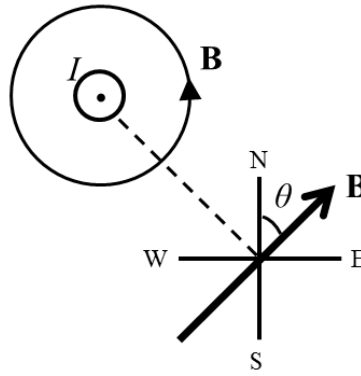
In the present work only data provided by VLF/LF and VHF networks are used, and a brief overview of each class is provided. Later, in the description of each of the data collection campaigns, details on specific networks are also given.

3.1.2.1. VLF/LF wide-area Lightning Location Systems (LLS)

The VLF/LF networks that are used in this work employ three basic location techniques: magnetic direction finding (MDF), time-of-arrival (TOA) and their combination, called IMPACT (IMProved Accuracy through Combined Technology).

The MDF element of the sensors consists of two vertical and orthogonal loops with planes oriented in the north-south and east-west directions, illustrated in Figure 3.5. As a consequence of Faraday's Law, the output signal voltage of each loop is directly proportional to the cosine of the angle between the detected magnetic field vector \mathbf{B} and the normal vector of the loop plane. Assuming that the channel of a lightning flash is perfectly vertical, the magnetic field lines produced by its current are concentric horizontal circles, coaxial with the channel (shown in Figure 3.5 for a current I that comes out of the page).

Figure 3.5 – The principle of the magnetic direction finding (MDF) technique.



Source: produced by the author.

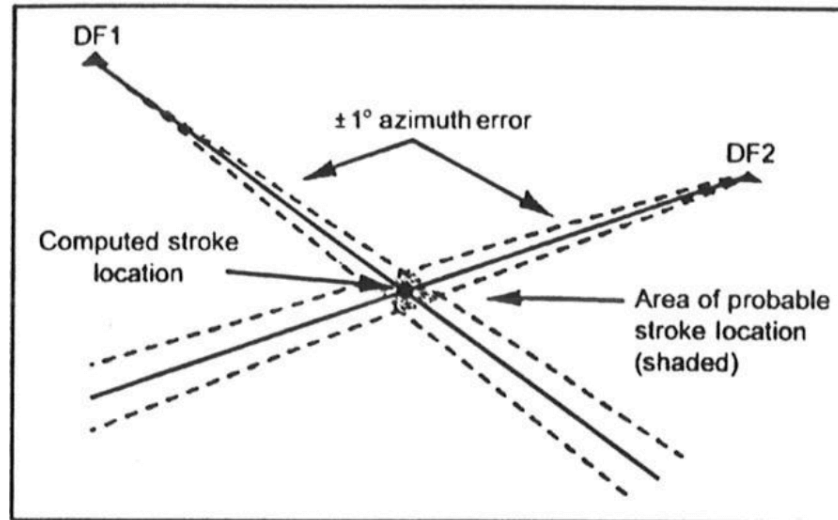
The output voltage of the east-west (V_{EW}) loop will be proportional to the cosine of the angle θ (complementary of the azimuth of the lightning source with respect to the sensor), and the output voltage of the north-south (V_{NS}) loop will be proportional to the cosine of the complementary angle of θ (i.e., the azimuth itself). As the sine of an angle is equal to the cosine of its complementary angle, the ratio between V_{NS} and V_{EW} will be proportional to the tangent of θ :

$$\frac{V_{NS}}{V_{EW}} \propto \tan \theta \quad (3.5)$$

Once the angle θ is determined, the azimuth of the detected stroke will simply be its complementary angle. In the next step to locate the stroke, it is necessary to obtain its azimuth with respect to at least two different MDF sensors (named DF1 and DF2 in Figure 3.6). However, data provided by standalone magnetic loops are ambiguous due to the fact that two different solutions are possible depending on

whether the detected stroke was positive or negative. This ambiguity can be solved by including one electric field antenna to detect its polarity (e.g., KRIDER et al., 1976).

Figure 3.6 – Return stroke location from two magnetic direction finders.

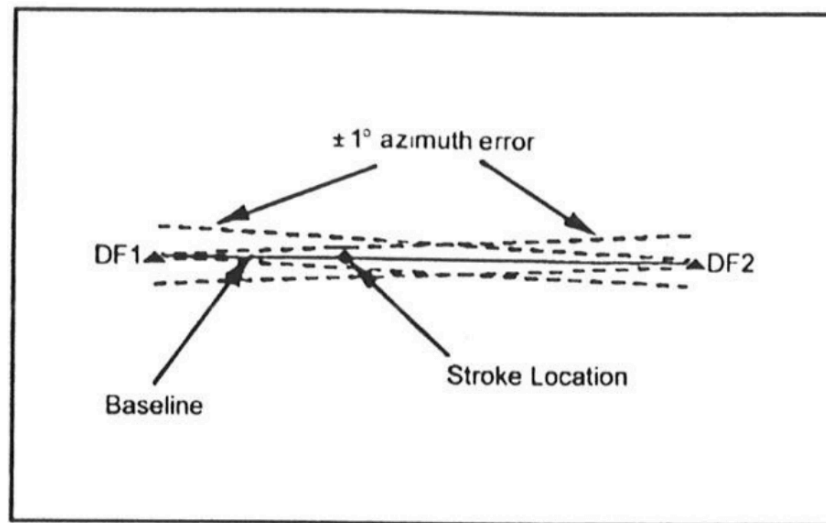


Example of stroke location based on two magnetic direction finders (DF1 and DF2). The solid lines represent the measured azimuths, providing the computed stroke location. The dashed line represents 1° uncertainties on each azimuth estimate, leading to an area of probable stroke location (shaded in the figure).

Source: Rakov and Uman (2003), adapted from Holle and Lopez (1993).

In addition to the stroke polarity ambiguity, with only two sensors there may also be problems for flashes whose strike points lie on the baseline between the sensors, as in the example of Figure 3.7. In this case even a small azimuth error can lead to large resulting errors in the final stroke location, as shown by the large area enclosed by the dashed lines. For this type of event it is assumed that the strike point lies on the baseline and the location is estimated based on the ratio of the signal amplitudes detected by each sensor.

Figure 3.7 – Detection ambiguity on the baseline between magnetic direction finders.

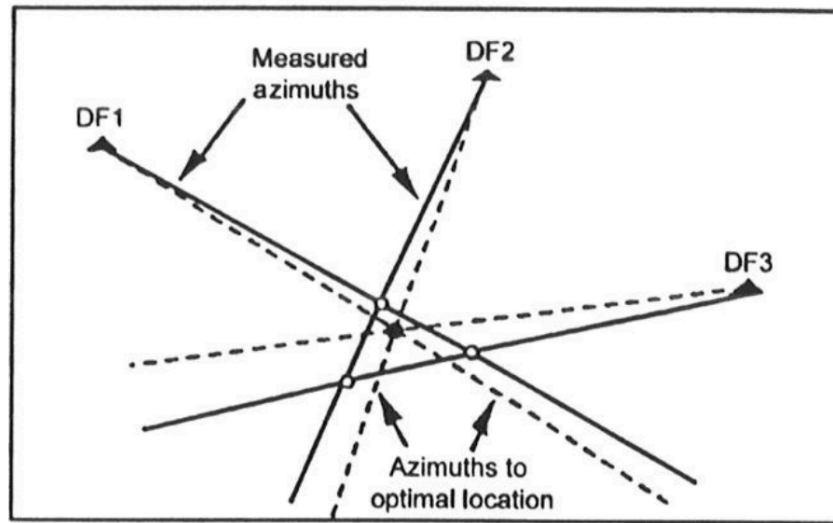


Example of return stroke detection ambiguity due to the proximity of the actual location to the baseline between the two MDF sensors (DF1 and DF2). In cases like this, even relatively small uncertainties (such as 1°) can lead to very large errors.

Source: Rakov and Uman (2003), adapted from Holle and Lopez (1993).

There is a significant improvement in the location solutions if at least three MDF sensors are used, as in the case shown in Figure 3.8. Now there are three possible locations, as defined by each pair of sensors. The optimal return stroke location, which lies in the intersection between the three dashed lines, is defined by applying the minimum χ^2 estimation (minimizing the sum-of-squares of all the angle deviations).

Figure 3.8 – Return stroke location based on three magnetic direction finders.



Example of return stroke location based on three MDF sensors (DF1, DF2 and DF3). Each sensor pair provides a possible location (open circles) over which the minimum χ^2 estimation can be applied in order to obtain an optimal solution (closed circle).

Source: Rakov and Uman (2003), adapted from Holle and Lopez (1993).

The time-of-arrival (TOA) technique to locate lightning is currently used in both VLF/LF and VHF networks (the latter will be discussed in the next subsection). For this method the differences of the time-of-arrival of the lightning electromagnetic signal to each sensor of the network are computed. In the case of VLF/LF networks, from which lightning strokes are located over the surface of Earth, for each pair of sensors the difference between the signal arrival times define a hyperbola, such as those illustrated in Figure 3.9. Sources located on any point of this hyperbola would lead to the difference calculated for that pair, so data from at least one additional sensor is required to solve the ambiguity. Now the intersection between the two calculated hyperbolas define the estimated stroke location (shown as the open circle of Figure 3.9).

Figure 3.9 – Return stroke location based on differences in time-of-arrival.

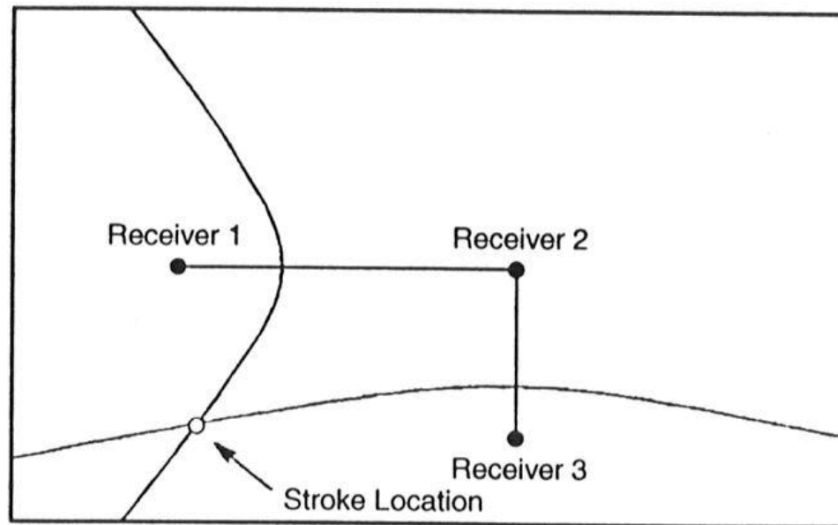
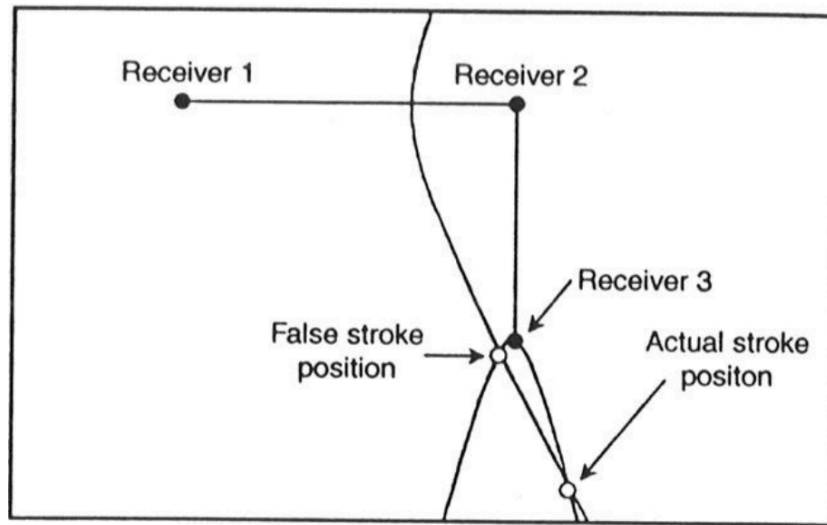


Illustration of the time-of-arrival (TOA) technique used in a VLF/LF lightning locating system. For each pair of sensors one hyperbola can be calculated over which an electromagnetic source may be located. The intersection between the two hyperbolas provides the stroke location.

Source: Rakov and Uman (2003), adapted from Holle and Lopez (1993).

When only three sensors are used in the TOA technique, there is a possibility that the position of the return stroke to be located relative to the network geometry might lead to a detection ambiguity, such as the case illustrated in Figure 3.10. In the example the hyperbolas intersect in two different locations and with only three sensors it is impossible to determine which solution corresponds to the actual location. This ambiguity can be solved if data from at least four sensors are available.

Figure 3.10 – Return stroke location ambiguity in three-sensor TOA solutions.



One case of TOA detection in which the calculated hyperbolas have two intersections, leading to an ambiguity. Data from at least four sensors are needed to obtain a unique solution for this type of geometry.

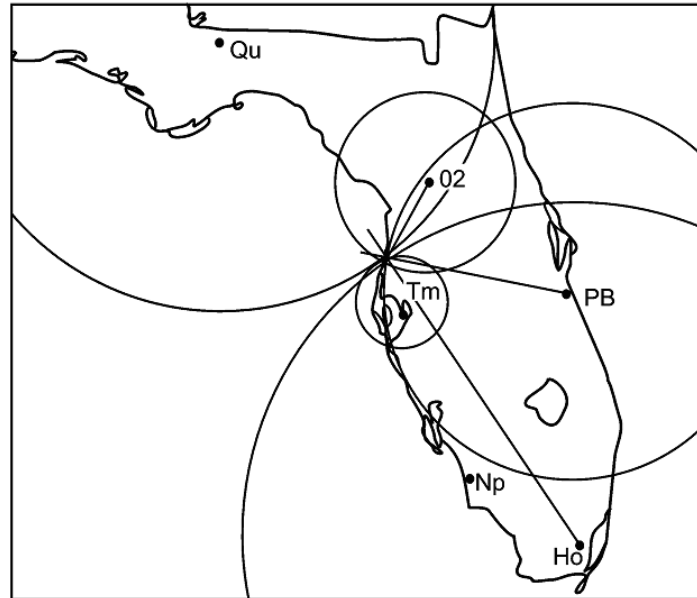
Source: Rakov and Uman (2003), adapted from Holle and Lopez (1993).

Many modern lightning locating systems (LLS) combine both MDF and TOA techniques into the “IMProved Accuracy through Combined Technology” (IMPACT). This combined method consists of an algorithm that uses both azimuth information from MDFs and timing data from sensors that are based on TOA (such as the LPATS, Lightning Position and Tracking System) in addition to a new class of IMPACT sensors that combined both technologies. The additional information allows this technique to provide latitude, longitude and time of occurrence for the detected strokes. Also, if the magnetic loops of the MDFs and IMPACTs are calibrated, it is even possible to obtain return stroke peak current estimates.

The IMPACT sensors are designed in such a way that information from only two of them is enough to provide a solution, given the redundant information provided by the combination of the TOA and MDF techniques (CUMMINS; MURPHY, 2009). One example of stroke detected by the IMPACT technique is shown in Figure 3.11, where three IMPACT and two LPATS (TOA) sensors participate in the solution of a flash that was detected in Florida, USA. The straight lines correspond to the MDF azimuth data obtained by each IMPACT sensor (PB, Ho

and 02) and each circle corresponds to the TOA estimates of the time taken for the electromagnetic signal to propagate from the ground strike point to each one of the five participating sensors (i.e., Qu and Tm provide only TOA information and Np does not contribute).

Figure 3.11 – Return stroke location through the IMPACT technology.



Example of return stroke location through the IMPACT technique. The LPATS sensors (which work based solely on TOA) are Qu and Tm, while the IMPACT sensors are PB, Ho and 02. Sensor Np does not participate in this solution.

Source: Cummins and Murphy (2009).

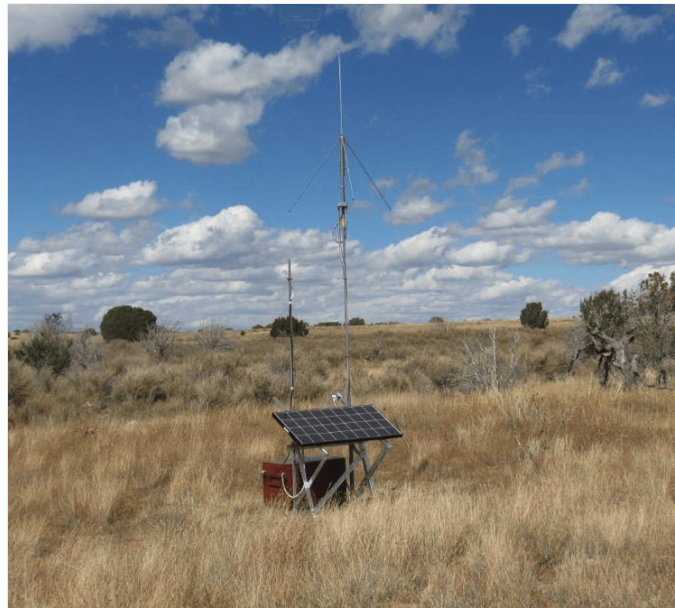
3.1.2.2. Three-dimensional Lightning Mapping Array (LMA)

Oetzel and Pierce (1969) proposed the use of VHF sensors to locate lightning, outlining the basic concepts of such a technique. They suggested that it would be possible to use time-of-arrival (TOA) information obtained by closely spaced antennas (separated by up to a few meters) to estimate the angle of arrival of the radiation emitted by distant lightning flashes (located at tens to hundreds of kilometers from the sensor). More recently, Rhodes et al. (1994) and Shao et al. (1995) were able to apply this concept in single-station interferometry systems capable of projecting lightning trajectories and channels onto a plane, allowing them to map both IC and CG flashes.

Proctor (1971) followed a different path from the one proposed by Oetzel and Pierce (1969) by creating a lightning mapping system that used five widely spaced (of the order of tens of kilometers) time-synchronized (to 100 nanoseconds accuracy) VHF sensors. He was able to map radiation sources during the early subsequent strokes and interstroke intervals of CG flashes with errors of less than 200 meters (PROCTOR, 1971, Figure 5). Instead of using interferometry, Proctor (1971) used a three-dimensional extension of the (two-dimensional) TOA hyperbolic method described in the previous section for VLF/LF wide-area networks.

Further advances based on the early work of Proctor (1971) were seen in the real-time Lightning Detection and Ranging (LDAR) developed by NASA to monitor the incidence of lightning over the Kennedy Space Center (MAIER et al., 1995). Rison et al. (1999) applied the same 3-D TOA technique to develop a GPS-based portable Lightning Mapping Array (LMA), the type of VHF sensor that was used in the present thesis work. Figure 3.12 shows a picture of one installed LMA station, where it is possible to see the sensor itself (the taller antenna), the solar panel responsible for providing power to the instrument and the housing for its electronic systems.

Figure 3.12 – Picture of one installed Lightning Mapping Array (LMA) station.



Source: provided by K. Cummins (2013, unpublished).

The basic geometry considered in the TOA technique used in LMA networks is illustrated in Figure 3.13. A radiation pulse emitted at time t from the position (x,y,z) will be detected by a sensor located at (x_i,y_i,z_i) at the arrival time t_i according to:

$$c^2(t - t_i)^2 = (x - x_i)^2 + (y - y_i)^2 + (z - z_i)^2 \quad (3.1)$$

Where c is the speed of light. The four unknowns (x,y,z,t) can be determined uniquely if at least four sensors provide measurements of their corresponding times-of-arrival t_i . Information from each sensor are transmitted to a central processing unit that applies algorithms to obtain solutions for as many individual radiation sources as possible. Thomas et al. (2004) estimated that sources that emit from positions over the network could be located with uncertainties of 6 to 12 meters (rms) in the horizontal and 20 to 30 meters (rms) in the vertical dimensions. The instant at which each source was emitted can be estimated with a 40 to 50 nanoseconds (rms) uncertainty, making the LMA a very reliable tool for mapping lightning channels that occur near or above their network area.

Figure 3.13 – Geometry of the TOA technique used in LMA networks.

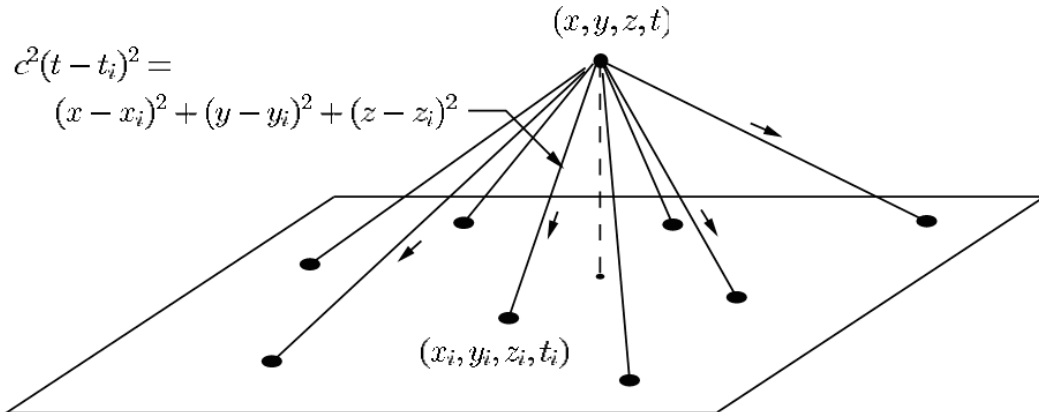
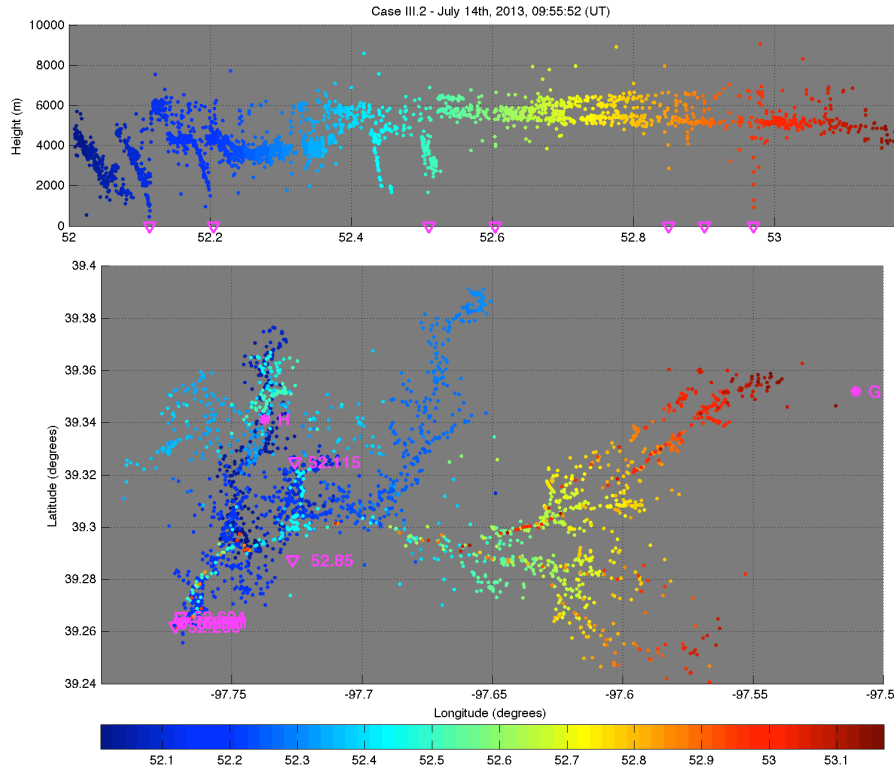


Illustration of the three-dimensional time-of-arrival technique used by the Lightning Mapping Array (LMA) to locate VHF radiation sources emitted by lightning breakdown. Each black dot over the plane represents i -th LMA sensor located at (x_i,y_i,z_i) .

Source: Thomas et al. (2004).

An example of MGCF observed by an LMA network in the state of Kansas, USA, and that was analyzed for the present thesis is shown in Figure 3.14. The flash occurred at 09:55:52 (UT) on July 14th, 2013, lasted about 1.2 seconds and produced 3401 individual VHF sources that were detected and included in the plot. The occurrence time of each source is color-coded according to the colorbar shown in the bottom of the plot (earlier and later sources are shown as shades of blue and red, respectively), which is defined in terms of seconds after the current minute. The upper plot shows the height of the radiation sources *versus* time, allowing the visualization of the vertical development of the flash at different instants. The lower plot is a top-view representation of the horizontal development of the flash, shown in terms of latitude *versus* longitude and following the color-coding of the colorbar. The six return strokes that composed the flash were detected by the NLDN and are shown as magenta triangles in both plots (in the lower plot they are labeled according to their time of occurrence, but it is difficult to see due to the large number of close VHF sources). Slow electric field antennas are shown as magenta asterisks and are labeled G and H (information on this specific network is given in subsection 3.2.1.1). Particularly for the present work, a MATLAB program was written to animate the LMA plots progressively, making it easier to visualize the channel development as time advances and leading to a more complete interpretation of the data.

Figure 3.14 – Example of a multi-grounded –CG flash mapped by an LMA network.



LMA plot example of one MGCF that occurred on July 14th, 2013, in Kansas, USA, and was analyzed in the present work.

Source: produced by the author.

LMA networks have been used for a wide range of scientific and practical applications. They can be used not only to study the development features of individual lightning flashes (as is the case of the present work) but also to provide estimates of the electrical charge structure of a thunderstorm. This use is illustrated in the works by Rust and MacGorman (2002) and Rust et al. (2005), who used LMA data in addition to balloon-borne electric field measurements to obtain evidences of the existence of inverted-polarity electrical structures in thunderstorms, i.e., their data indicated the presence of positive and negative charges in regions that would be normally occupied by negative and positive charges in “normal polarity” storms, respectively.

3.1.3. Video cameras

Data from different video cameras, standard and high-speed, were also used for different objectives and analyses of the present thesis work. GPS-time synchronization allows the temporal correlation between the imagery provided by each camera and the data provided by the other instruments. Specific information about the cameras that were used on each campaign is provided in their respective subsections (3.2.1.3 and 3.2.2.1).

3.2. Observational campaigns

Data from two campaigns were used in the present work, each one aiming to fulfill different objectives. The Kansas Windfarm2013 Field Program (KSWFP) provided slow electric field, LMA, video and LLS data for the understanding of the mechanisms involved in the production of new ground contacts by subsequent strokes. The data obtained during the Summer 2013 RAMMER campaign, on the other hand, was used in the analysis of forked and UI strokes. Details are given on each campaign in their respective subsections.

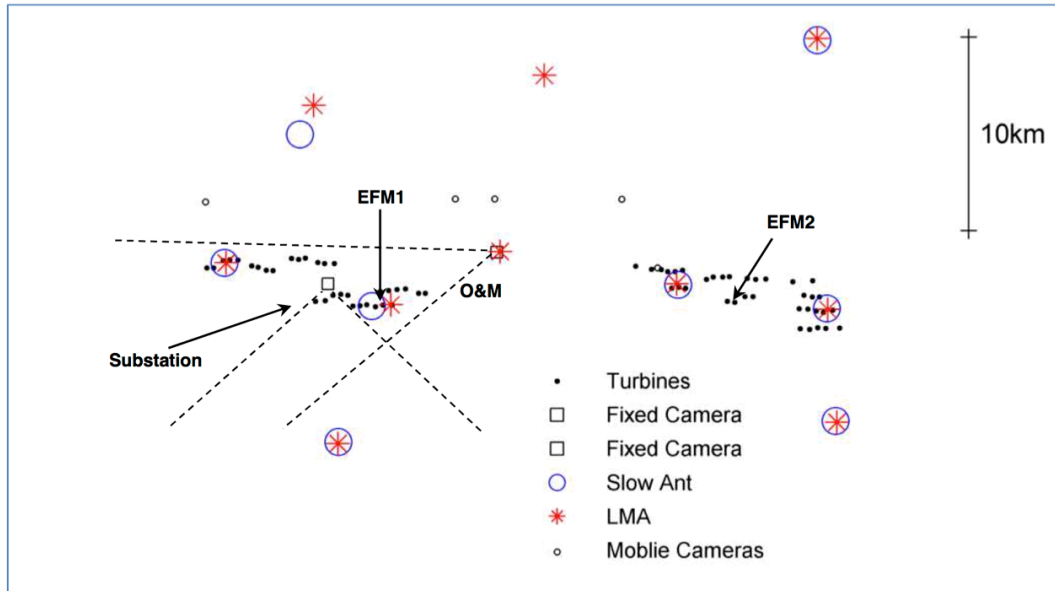
3.2.1. Kansas Windfarm2013 Field Program (KSWFP)

Between May 21st and September 3rd, 2013, a joint project called Kansas Windfarm2013 Field Program (KSWFP) that involved ten research groups was conducted to analyze lightning strikes to wind turbines operating in north-central Kansas, USA, within Cloud County. As described by Cummins et al. (2014), the wind farm is located in a region with small rolling hills and is composed of more than 60 turbines, which are divided into east and west groups. Although the main objectives of the KSWFP were aimed towards protection technology for turbines (e.g., RISON et al., 2014), the collected data are also being used for additional scientific studies, such as this thesis.

The relative positions of the observational instrumentation used in the KSWFP are shown in Figure 3.15. Cummins et al. (2014) provides a complete list of the instruments that were operating during the campaign period, but for this work only the following instruments were used: 10-station LMA; 8-station slow electric field antenna network; two fixed standard speed video cameras (continuously recording); three mobile high-speed digital cameras; data from the U.S. NLDN.

Each of these instruments and their respective datasets are described in the following subsections.

Figure 3.15 – Relative positions of the scientific instruments used in the KSWFP.



The two fixed, standard speed cameras (black squares) were installed at the substation and operations and Maintenance (O&M) buildings, as indicated. The areas defined by the dashed lines coming out of the squares represent the approximate field of view (FOV) of the cameras. EFM1 and EFM2 correspond to the two electric field mills that were installed during the campaign (not used in this work).

Source: adapted from Cummins et al. (2014).

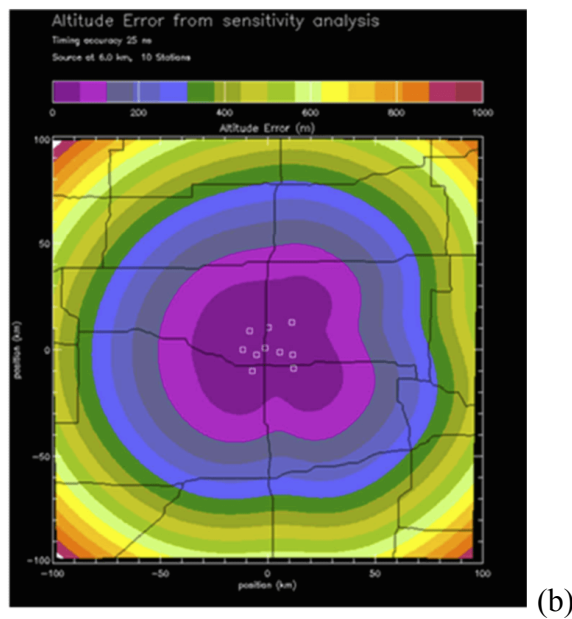
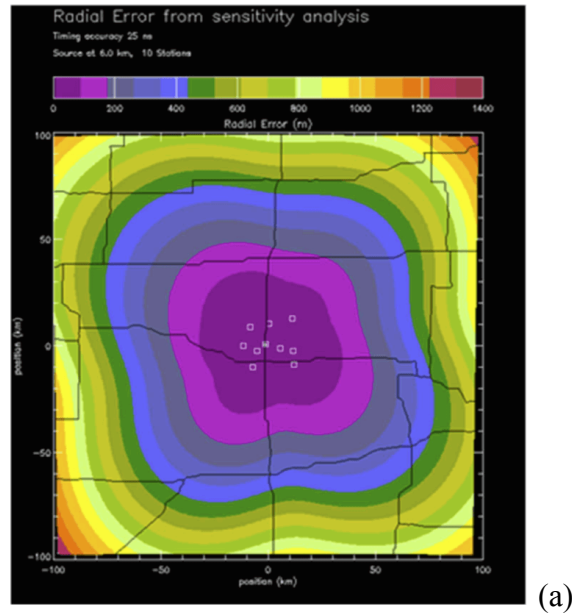
3.2.1.1. Slow electric field and LMA network

A network of ten LMA sensors and eight slow electric field antennas were operated during the KSWFP. As shown in Figure 3.15, six of the slow antennas were installed at the same sites of some of the LMA sensors.

The baseline between each LMA sensor ranged from 7 to 10 km, which leads to a expected flash detection efficiency close to 100% within 150 km from the center of the network, even though the number of VHF sources located per flash that occur outside the sensors perimeter will fall uniformly with increasing distance (CUMMINS et al., 2014). Figure 3.16 shows the estimated radial and altitude location accuracy of the KSWFP LMA for a radiation source located at six kilometers above ground with 25 nanoseconds RMS timing error. Radial errors

remain below 100 meters up to approximately 25 kilometers away from the center of the network (Figure 3.16a), and altitude errors are expected to be less than 100 meters up to 50 kilometers from the network center (Figure 3.16b).

Figure 3.16 – Estimated location accuracy of the LMA used during the KSWFP.



Expected (a) radial and (b) altitude errors for the KSWFP LMA based on numerical calculations for a VHF radiation source located at 6 km above ground. The model assumed a RMS timing error of 25 nanoseconds based on the used sensor baseline.

Source: adapted from Cummins et al. (2014).

Each of the slow antennas had a time constant of 10 seconds with an upper frequency response of 25 kHz and a sampling rate of 50 thousand samples per second. Based on their nominal sensitivity, it is assumed that each station could measure electric fields ranging from 10 mV m^{-1} to 10 kV m^{-1} (CUMMINS et al., 2014, p. 4).

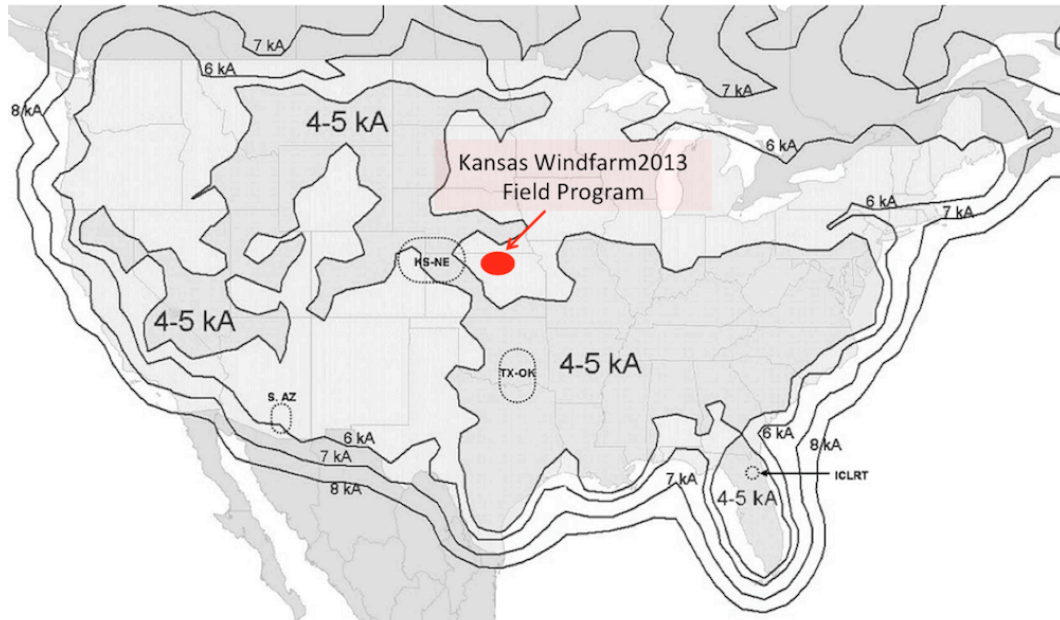
3.2.1.2. U.S. National Lightning Detection Network (NLDN)

For the analysis of flashes observed during the KSWFP, access was granted to datasets from the U.S. National Lightning Detection Network (NLDN), a VLF/LF lightning locating system that covers the continental USA. It has been operating entirely based on the IMPACT technology since a major upgrade made in 2002-2003 (CUMMINS; MURPHY, 2009). In 2003-2004, validation campaigns were conducted for natural lightning in Arizona, Texas and Oklahoma (BIAGI et al., 2007) and for rocket-triggered lightning in Florida (JERAULD et al., 2005). At the time, median location accuracy (LA) was 450 meters for triggered lightning and ranged from 280 to 420 meters for natural lightning. The detection efficiency (DE) for return strokes was 63% for triggered and ranged from 76% to 85% for natural lightning. The DE for CG flashes was 95% for rocket-triggered lightning and 92-93% for natural lightning.

Cramer and Cummins (2014) and Mallick et al. (2014) have documented more recent improvements to the LA of the NLDN based on tall tower strikes and triggered lightning, respectively. Through the analysis of 22 tall radio towers located in different states of the USA, Cramer and Cummins (2014, Table I) have shown that the median location error was continuously reduced from 226 meters in 2010 to 83 meters in 2013. The percentage of events whose error ranged from 500 meters to one kilometer dropped from 7.4% (in 2010) to 1.1% in 2013, along with the percentage of strokes with error greater than one kilometer: 0.5% in 2010 to 0.05% in 2013. Based on a dataset of 388 return strokes from 90 rocket-triggered flashes at Camp Blanding, Florida, Mallick et al. (2014, Table IV) reported that the median location error have been constantly decreasing after 2011, resulting in 173 m in 2013 with an overall median (for the full 2004-2013 period) of 309 meters.

Particularly for the region where the KSWFP was conducted, the minimum detectable return stroke current is estimated to be 6 kiloamperes, as shown in Figure 3.17.

Figure 3.17 – Post-upgrade map of minimum detectable peak current for the NLDN.



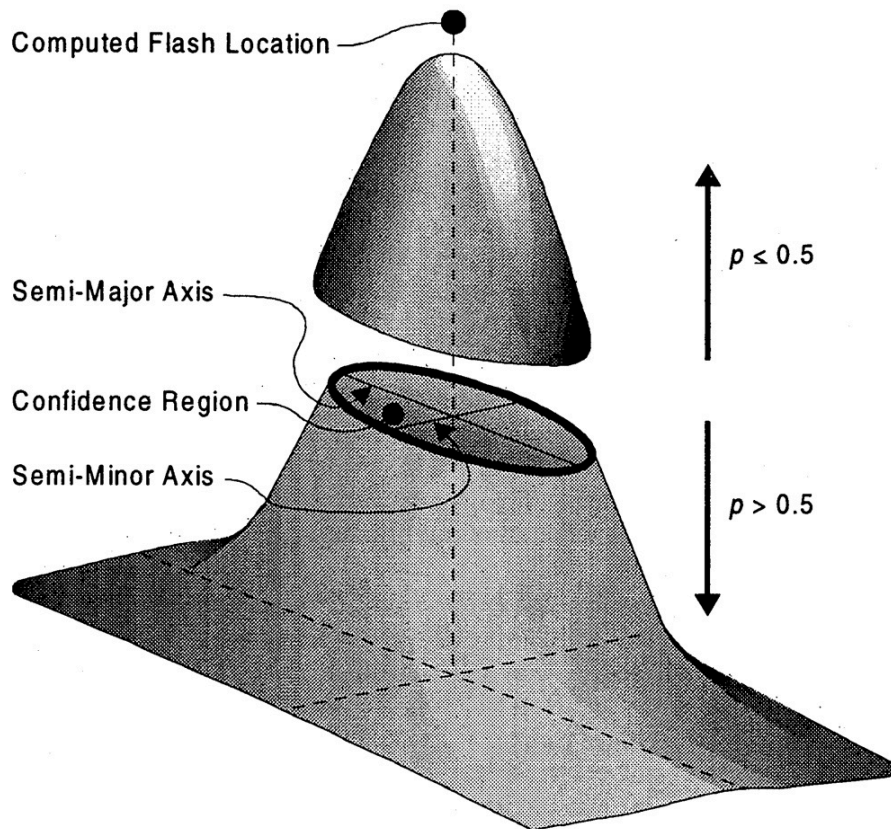
Map of the estimated minimum detectable estimated peak current (50% probability) for the NLDN after the 2002-2003 upgrade. The approximate region where the KSWFP campaign occurred is indicated in red and lies in a region of minimum detectable current of 6 kA. The other four regions (surrounded by dotted circles) were evaluated in the post-upgrade validations studies (JERAULD et al., 2005; BIAGI et al., 2007).

Source: adapted from Cummins and Murphy (2009).

The NLDN and other LLS networks composed of sensors produced by Vaisala (and formerly by Global Atmospheric Inc.) use a location accuracy model from which it is possible to obtain an estimate of the error associated with individual return stroke solutions. It is assumed that the random errors in timing and angle measurements of the sensors are uncorrelated and Gaussian, which leads to a two-dimensional Gaussian distribution for each return stroke location estimated by the LLS (CUMMINS et al., 1998, Appendix). As illustrated in Figure 3.18, it is possible to derive an error ellipse from that distribution by taking a cross-section at a given probability level p . There is, then, a probability p that the actual return stroke location is contained within the area enclosed by the error ellipse. In the

case of the NLDN, $p = 0.5$, i.e., there is a 50% chance that the stroke occurred within the error ellipse (and it describes the median location accuracy). The return stroke position that is reported by the LLS corresponds to the peak of the probability distribution (indicated by “Computed Flash Location” on Figure 3.18), and the shape and size of its error ellipse will depend on the relative position of the stroke with respect to the geometry of the sensors (CUMMINS et al., 1998, p.9043). In practical terms, the NLDN data output used in this thesis work provides the latitude and longitude of the peak of the distribution, along with the length of the semi-major axis (SMA) and the semi-minor axis (SmA) in kilometers, and the azimuth (angle between the north direction and the semi-major axis) in degrees of the error ellipse. These three parameters fully describe the error ellipse probability distribution, assuming that it is Gaussian.

Figure 3.18 – Location error ellipse from two-dimensional Gaussian distributions.



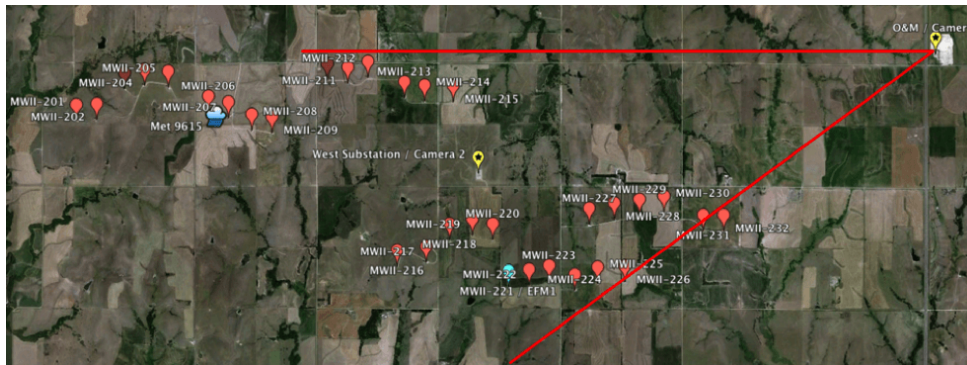
The solution location is on the peak of the distribution (“Computed Flash Location”) and the surrounding error ellipse comes from a cross section at the desired probability level p (which is 0.5 in the case of the NLDN).

Source: Cummins et al. (1998).

3.2.1.3. Video cameras

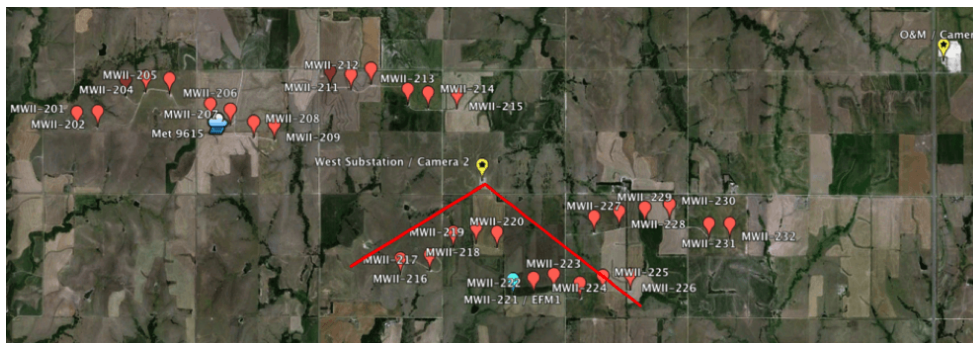
A total of four video cameras, operated during the KSWFP period, were used in the present thesis work in order to identify GCPs as unambiguously as possible. Two of them were fixed, standard speed cameras set to record continuously. One was installed at the Operations and Maintenance (O&M) building and the other was fixed at the west substation (their relative positions and approximate fields of view are shown in Figure 3.15 and in greater detail in Figures 3.19 and 3.20). Additional imagery was provided by two mobile digital high-speed video cameras, models Phantom v310 (operating at either 11,000 or 35,000 fps) and Miro 4 (operating at 1000 fps), which alternated their recording positions among the four options indicated by the small black circles in Figure 3.15. It is important to note, however, that only the fixed, standard speed cameras were operational during the entire KSWFP period. The high-speed cameras were available for lightning observations only from May 21st to June 8th, 2013,

Figure 3.19 – Field of view of the standard speed fixed camera at the O&M building.



Source: provided by K. Cummins (2013, unpublished).

Figure 3.20 – Field of view of the standard speed fixed camera at the substation.



Source: provided by K. Cummins (2013, unpublished).

3.2.2. Summer 2013 RAMMER campaign

Some of the analyses of the present thesis work are based on lightning observations conducted during February and March 2013 in the region of São José dos Campos, São Paulo, Brazil. That campaign was part of the RAMMER project (Portuguese acronym for “Automatized Multi-Camera Network to Observe and Study Lightning”), whose resulting dataset have already been used for studies on the formation mechanisms of bipolar CG lightning (SARAIVA et al., 2014a) and day-to-day differences in the characteristics, incidence and parameters of –CG flashes (ANTUNES et al., 2015).

3.2.2.1. Automatized Multi-camera Network to Observe and Study Lightning (RAMMER)

The RAMMER network, first described by Saraiva et al. (2012), is composed of one mobile and three fixed stations. Each fixed station (RAMMER 1 to 3) contains one monochromatic Phantom v9.1 high-speed digital camera (set to operate at 2500 fps with a spatial resolution of 1200 x 500 pixels) along with a GPS antenna (for temporal synchronization), a photodiode (for autonomous operation) and a modified desktop personal computer (for control, data collection and storage). The housing of each station has been designed to be weatherproof, allowing outdoor operation (RAMMER 1 is shown in Figure 3.21 as a reference). Figure 3.22 shows the relative locations of the three fixed RAMMER stations, which were strategically positioned and aimed in order to maximize the number of flashes recorded for the same thunderstorm. The mobile station (also shown in Figure 3.22) was installed in a car and consisted of a full-color Phantom v9.1 set to operate with the same temporal and spatial resolutions used in the monochromatic, fixed stations, also with a GPS antenna but with a laptop personal computer (instead of a desktop) for control, data collection and storage.

Figure 3.21 – RAMMER 1 station installed at its fixed observation position.



Source: adapted from Saraiva et al. (2012).

Figure 3.22 – Map of the four (one mobile, three fixed) RAMMER stations that were operational during the summer 2013 campaign.

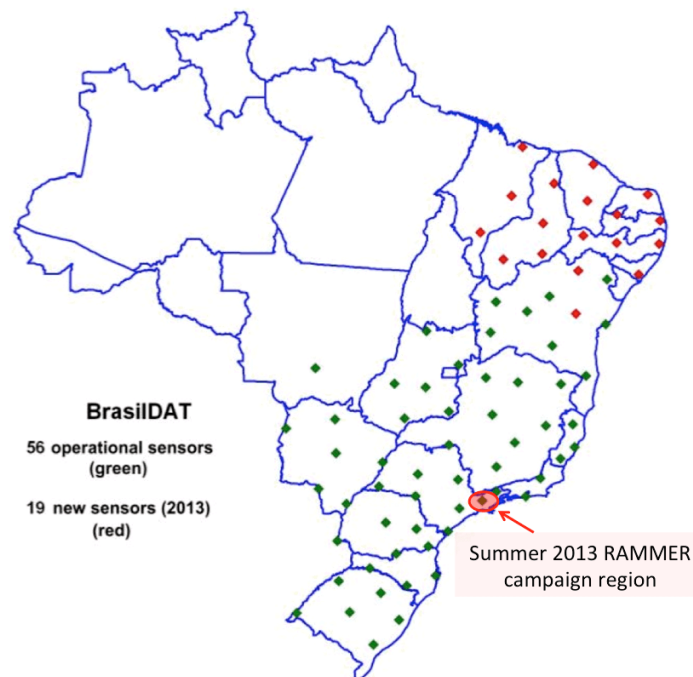


Source: Antunes et al. (2015).

3.2.2.2. BrasilDAT Total Lightning Network

For the RAMMER observational campaign, the Brazilian Total Lightning Network (BrasilDAT) provided additional VLF/LF LLS data. As described by Naccarato et al. (2012), BrasilDAT is based on the EarthNetworks Total Lightning System (ENTLS), which uses a relatively dense network of TOA sensors (operating at VLF/LF) aimed at detecting both CG and IC discharges. Figure 3.23 shows the current status of the BrasilDAT (56 sensors that already are operational are shown as green diamonds) along with the plan for its future expansion (additional 19 sensors that were originally planned to be installed by 2013 but are still on hold). The red oval area shows the approximate region where the RAMMER observations occurred, showing that it is well covered by the network (despite technically being on its edge, due to the proximity to the coast of São Paulo state).

Figure 3.23 – Current status and future plans for the sensor deployment of BrasilDAT.



Map of BrasilDAT showing the 56 ENTLS sensors currently operational (green diamonds). The red diamonds indicate the planned locations of the 19 additional sensors to be installed in the future. The red oval shows the approximate region where the summer 2013 RAMMER observations occurred.

Source: adapted from Naccarato et al. (2012).

Between November 2011 and March 2012, RAMMER operated in its first data collection campaign also in São José dos Campos. Naccarato et al. (2012) used the resulting dataset to evaluate the DE of BrasilDAT and concluded that it was able to detect 88% of CG flashes and 54% of individual return strokes when compared to the high-speed video records, with the DE steadily increasing for strokes of higher order. Additionally, data from sixteen tower-initiated upward flashes that started from one of the two towers located on the Jaraguá Peak, in the city of São Paulo, were used to evaluate the LA of the network. Fourteen out of the sixteen upward flashes observed were reported by the BrasilDAT, and by comparing the location of the tower that was struck and the solution provided by the LLS, Naccarato et al. (2012, Figure 8) found that the mean location error was 362 meters (with 70% of the sample with errors smaller than 400 meters).

3.3. Shuttle Radar Topography Mission (SRTM) dataset

For the analysis of the influence of complex terrain features on the incidence and characteristics of MGCFs carried out in this research, it was necessary to use terrain elevation data obtained by the Shuttle Radar Topography Mission (SRTM), described in detail by Farr et al. (2007). The SRTM was conducted from aboard the space shuttle *Endeavour* between February 11th and 22nd, 2000, and during that period radar data of over 80% of the land surface of the Earth was collected. The resulting data were processed from raw radar signals with a 1-arc-second resolution (approximately 30 meters). Initially only 3-arc-second data was made publicly available for regions outside the USA, but the United States Geological Survey has been progressively including the full resolution datasets for the rest of the world. Specific details on how the SRTM data were processed and analyzed for the present work are given in Chapter 7.

4 ALGORITHM FOR IDENTIFYING GROUND CONTACT POINTS FROM DATA PROVIDED BY LIGHTNING LOCATION SYSTEMS

In order to derive ground strike point (GSP) information from return stroke data provided by Lightning Location Systems (LLS), the *groupGCP* algorithm was developed. This chapter presents a detailed description on the structure of the algorithm along with some validation based on standard and high-speed video data. The criteria for grouping decision and determination of centroid (in this case, GSP) positions are based on the k -means clustering method. The algorithm was created in such a way that it is capable of determining the optimal number of strike points (the k value) numerically based on the location accuracy (LA) for each individual discharge, embodied in the error ellipse information discussed in Chapter 3.

Campos et al. (2015) have already presented a conference paper with the description of this algorithm, for which the author received the “Best Young Scientist Award” at the 2015 Asia-Pacific International Conference on Lightning in Nagoya, Japan.

4.1. Description of the *groupGCP* algorithm

There are three main “layers” that compose the *groupGCP* algorithm. The main, “outermost layer” is responsible for organizing and sorting the return stroke solution ellipses into those that have either low or high semi-major axis (SMA) values, allowing different grouping criteria according to the location error associated with each solution. It first groups the most accurately located events (i.e., with low SMA values) among themselves, creating a first set of GCPs. It then tries to group the less accurately located strokes into these GCPs. And finally, it creates new GCPs for those strokes that could not be grouped into this first, accurately located set. There is a user-defined input parameter called *maxSMA_grouping* that is responsible for initial partitioning of the strokes; those stroke solutions whose SMA values are less than or equal to *maxSMA_grouping* are considered when the first set of GCPs is calculated. Those whose SMA values are above that parameter are left for the “low accuracy” grouping process.

The “mid-layer” of the algorithm is called “progressive k -means”, which is called by the “outer layer” whenever it tries to group a set of return stroke solutions. As the standard implementations of the k -means method typically found in literature requires the user (or caller) to choose a value of k (i.e., the algorithm needs to be told how many centroids are to be assumed in the dataset being analyzed), a set of conditions were created in order to obtain an optimized k value. This is relevant because finding out the number of GSPs for a given CG flash is an essential part of the problem that the *groupGCP* algorithm tries to solve, so there is no safe *a priori* assumption that can be made. In its current implementation, the algorithm chooses the minimum number of GCPs (i.e., the value of k) for which the greatest distance (not necessarily Euclidean, as described in the next paragraph) between a GCP (centroid) and all its associated strokes (data points) is smaller than a user-defined tolerance value (which should be defined according to the worst-case LA of the LLS whose data are being analyzed).

Finally, the “innermost” and most basic layer of the algorithm is an augmented implementation of the standard k -means clustering method. It is called by the “progressive k -means” each time it attempts to group the return strokes into a certain number of GCPs. There are no significant changes between this k -means implementation and those usually found in literature (i.e., Lloyd, 1982). We have, however, included mechanisms that allow the algorithm to use a different distance metric, whenever necessary (and determined by the user). In addition to the common Euclidean distance as grouping criteria, in the case of lightning research based on LLS data it was relevant to add the option of using a probability value (embodied in an error ellipse scaling factor) as the determining parameter.

In the following three subsections each layer of the algorithm is described in detail, step by step. For the sake of clarity, however, they are presented from the “innermost” (most basic) to the “outermost” (most general) layer, as the latter uses the other two layers as a pre-existing toolset of functions.

4.1.1. “Innermost layer”: augmented k -means clustering method

Our implementation of the basic k -means method (Algorithm 1) takes a group of n points as an input, along with the number k of unique centroids that they must be grouped into. The algorithm can be outlined in four general steps:

Algorithm 1:

1. obtain random initial positions of the k centroids;
2. assign each point to its “nearest” (using the selected distance metric) centroid;
3. recalculate each centroid position as the average of the coordinates of the points associated with it;
4. repeat steps 2 and 3 until the recalculated centroid positions stop changing between iterations.

In our implementation it is possible to specify the distance metric to be used for centroid grouping. If chosen as “Euclidean”, the absolute distance between the latitude and longitude of each return stroke solution and each calculated centroid is used. Alternatively, when applied to LLS datasets that provide error ellipse information, the algorithm can be set to use the scaling factor as the decisive metric (“Elliptical”). The calculation of the scale factor can be derived from the equations of Cramer and Cummins (2014, Appendix I). Let φ be the azimuth between the return stroke solution and the centroid (taken clockwise from the North), r the Euclidean distance between them, and A and B the semi-major (SMA) and semi-minor (SmA) axes of the error ellipse of the stroke, respectively. Taking x and y as the horizontal (longitude direction) and vertical (latitude direction) distances between the stroke solution and the centroid, respectively, they can be calculated as:

$$x = r \sin \varphi \quad (4.1)$$

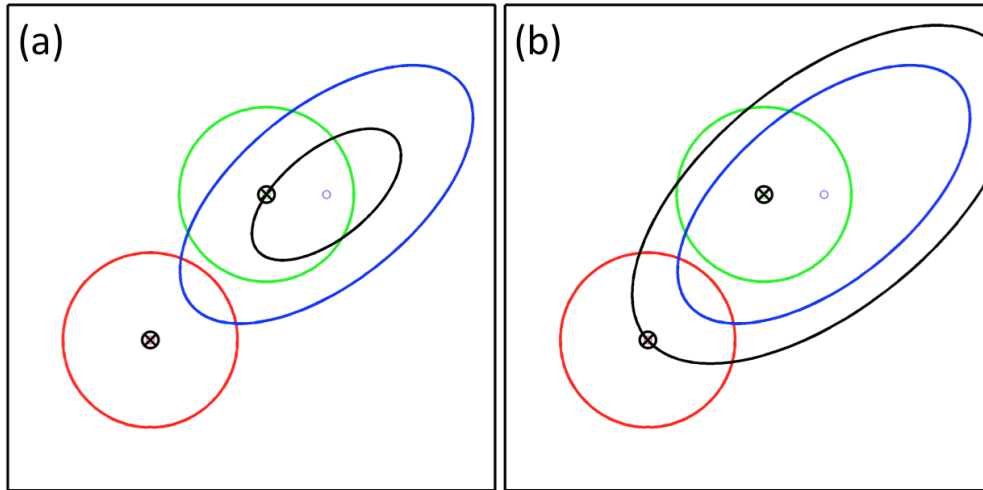
$$y = r \cos \varphi \quad (4.2)$$

The ellipse scaling factor f is then given by:

$$f = \frac{\sqrt{\left(\frac{A}{B}\right)^2 x^2 + y^2}}{A} \quad (4.3)$$

The value of f indicates the factor by which the scale ellipse is larger (or smaller) than the original ellipse. It is also directly proportional to the total probability enclosed by the scaled ellipse. The geometrical meaning of the value of f is illustrated in Figure 4.1, where the blue ellipse is the one being scaled and the black ellipse corresponds to its scaled version. In Figure 4.1a, the blue ellipse is scaled in order to intersect the center of the green ellipse, and in this case f is 0.51 (i.e., it is smaller than the original ellipse from which it is derived). On the other hand, if the blue ellipse is scaled to intersect the center of the red one (Figure 4.1b), f will be 1.3. In the case of the implementation of the k -means algorithm used in the present work, when the chosen metric is elliptical, the algorithm will group a given stroke solution with the centroid whose position yields the smallest value of f among all centroids. This grouping can be very different than the Euclidean grouping when the error ellipses are not circular.

Figure 4.1 – Illustration of ellipse scaling.



Visual representation of the process of ellipse scaling, in which the blue ellipse (a) is being scaled to the center of the green one, yielding $f = 0.51$; and (b) it is then scaled to the center of the red ellipse, then yielding $f = 1.3$. Note that the scale factor f adopts values greater than unity when the ellipse is scaled beyond its original dimensions, while it then becomes less than one if the scaling causes the ellipse to become smaller.

Source: produced by the author, previously presented by Campos et al. (2015).

4.1.2. “Mid-layer”: the “progressive k -means” algorithm

As the number of GCPs of a given flash is not known *a priori*, the basic k -means method by itself is of little use when grouping return stroke solutions into GCPs. For this reason, another algorithm called “progressive k -means” was developed aiming at finding the smallest k (number of GCPs) for which the maximum distance between each return stroke and its associated GCP is below a maximum value (defined by the user according to the LA of the LLS being analyzed). The input data must consist of strokes that have already been grouped into flashes by an adequate flash-grouping algorithm (e.g., the location-based illustrated by Cummins et al., 1998, Figure 6). Additionally, the user (or function caller) must specify the metric to be used (Euclidean or elliptical) and the adequate maximum distance for each centroid-point (i.e., GCP-stroke) pair. This maximum distance must be given either as linear distance in kilometers (Euclidean metric) or maximum ellipse scale factor (elliptical metric). The “progressive k -means” algorithm can be outlined in five basic steps (among which, steps 3 through 5 are nested in a while-loop):

Algorithm 2:

1. determine tolerance (which can be either the maximum Euclidean distance or the maximum ellipse scale factor f , depending on the need) and define k to be initially zero;
2. repeat steps 3 through 5 while k is smaller than or equal to the number n of strokes that compose the flash being analyzed and the maximum distance between each centroid (GCP) and all its associated strokes is greater than the tolerance defined in step 1. If either condition (or both) stops being true (i.e., if either k becomes equal to n or the maximum distance between each GCP-stroke pair becomes smaller than the tolerance), terminate the loop;
3. increment the value of k (i.e., $k = 1$ in the first iteration);
4. apply the augmented k -means method (Algorithm 1) to all strokes using the current value of k ;

5. calculate the distances between each centroid-point pair (i.e., each GCP-stroke pair) according to the chosen metric. Go to step 2.

If the obtained GCPs are always farther away from the associated strokes than the maximum distance allowed, the number of GCPs will eventually be equal to the flash multiplicity (i.e., number of strokes n) and the algorithm will terminate when the while-loop is checked in step 2. In these particular cases, each subsequent return stroke is identified as a new ground termination.

In the implementation of “progressive k -means” used in this thesis work the maximum distance between each GCP-stroke pair is defined by an input parameter called *pScale*. It will act differently according to the chosen metric: for Euclidean, the maximum distance will be the product between *pScale* and the largest SMA among the ellipses being analyzed (this is the case when the method iterates over the well located strokes, i.e., those with small SMA values). On the other hand, for the elliptical metric, the maximum distance (i.e., scale factor f) will be simply equal to *pScale* due to the normalized nature of this distance metric.

4.1.3. “Outermost layer”: the *groupGCP* algorithm

Finally, the *groupGCP* algorithm uses both Algorithms 1 and 2 (basic and “progressive” k -means) in order to group return stroke LLS solutions into different GCPs. The way it processes strokes and flashes can be adapted by the user (or function caller) according to the quality of the data of the LLS being used. To that end, the main input parameter is called *maxSMA_grouping* and defines the maximum SMA value of any given return stroke solution that should be considered in the first grouping process. That is, the algorithm initially places the “low-SMA strokes” (i.e., those with relatively small location error) into a single group. In the current implementation of the algorithm, this initial grouping is conducted with the Euclidean metric (as these ellipses commonly have equal values of SMA and SmA). After that, the algorithm tries to group the remaining strokes (i.e., those with an SMA value greater than *maxSMA_grouping*) with the existing GCPs (obtained from the low-SMA strokes). This second grouping process is conducted using the elliptical metric, with each high-SMA stroke ellipse being scaled to all previously obtained GCPs. The resulting scale factors

are then compared to another input value, *maxScaleFactor*; the ellipses with f values that are less than that parameter are then grouped to the corresponding GCP. Finally, the remaining ellipses (that could not be grouped into previously obtained GCPs) are grouped among themselves through one final execution of “progressive k -means” using the elliptical metric. It is helpful to outline the complete *groupGCP* algorithm into seven basic steps:

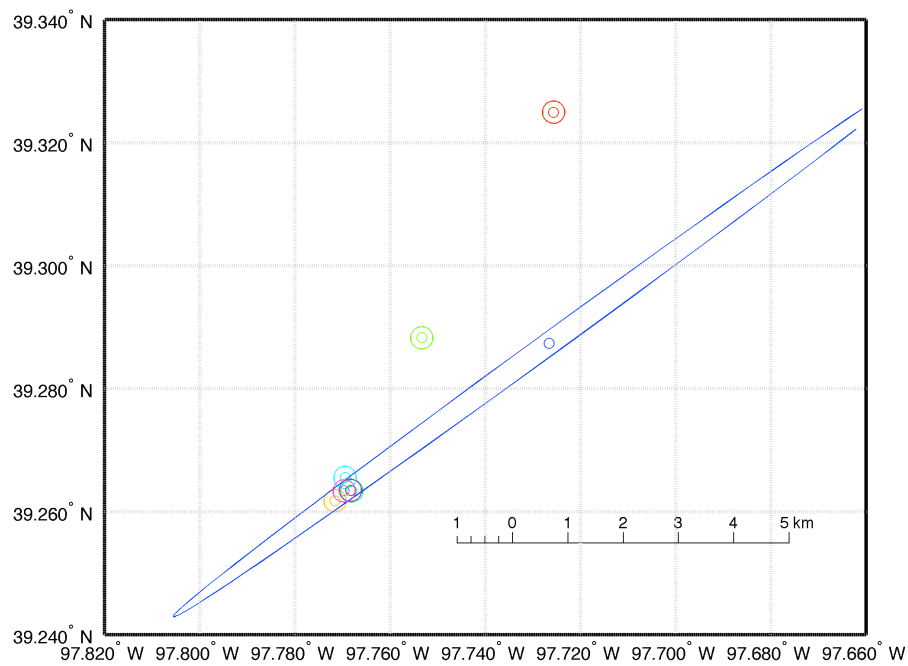
Algorithm 3:

1. sort return stroke error ellipses according to their SMA and the maximum value defined by the user (*maxSMA_grouping*);
2. apply “progressive k -means” (Algorithm 2) to the return strokes whose SMA values are lower than *maxSMA_grouping*, generating a first set of centroids (GCPs);
3. check if there is at least one return stroke with an SMA greater than *maxSMA_grouping*. If not, skip to step 7;
4. calculate the error ellipse scale factor of each high-SMA stroke (i.e., those with SMA values greater than *maxSMA_grouping*) with respect to each existing GCP (obtained in step 2 from low-SMA strokes);
5. check if each high-SMA return stroke can be grouped into any of the existing GCPs, i.e., if the scale factor f for each GCP-stroke pair is less than *maxScaleFactor*. If all of them could be grouped this way, skip to step 7;
6. apply “progressive k -means” (Algorithm 2) to all high-SMA strokes that were not grouped into existing GCPs in step 5;
7. organize and sort all GCPs that were obtained for both groups of return strokes (low- and high-SMA, in steps 2 and 6) according to their stroke order, exporting that data into an output text file.

All the steps of the *groupGCP* algorithm can be more easily understood by using a visual example of a real cloud-to-ground flash. Figure 4.2 shows the

geographical distribution of the error ellipses of all eight strokes of a negative cloud-to-ground flash observed in July 14th, 2013, in Kansas, USA, by the NLDN. Seven strokes were accurately located, with SMA values of 0.2 km (the minimum value reported by the NLDN since 2011), but one of them (blue ellipse) was poorly located, with an SMA of 8.4 km. In this particular example, the input parameters of the algorithm were: *maxSMA_grouping* = 0.2 (in kilometers), *maxScaleFactor* = 1.5 and *pScale* = 1.8.

Figure 4.2 – An eight-stroke CG flash being analyzed by the *groupGCP* algorithm.



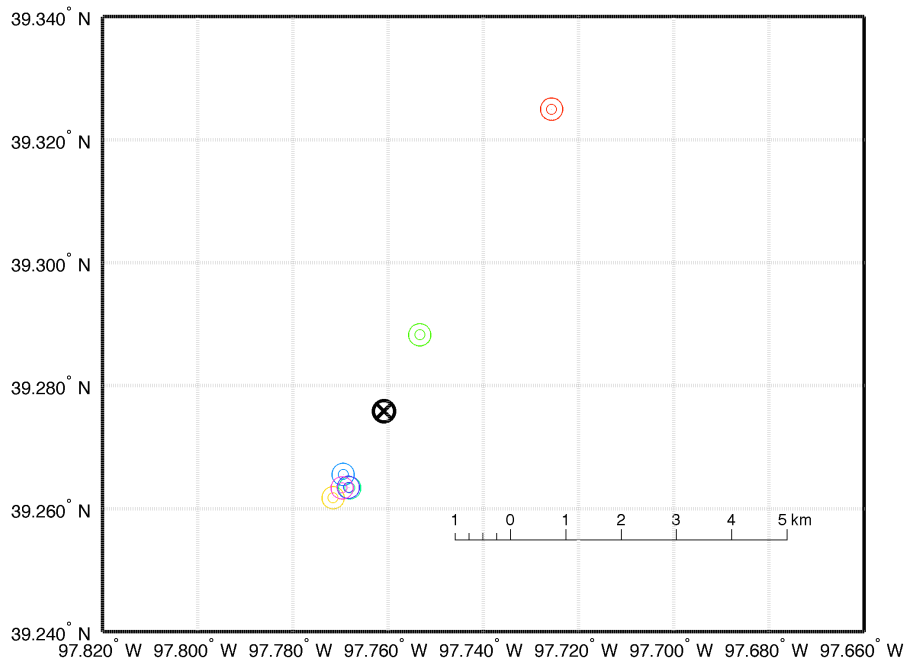
One case of eight-stroke –CG flash that occurred in Kansas, USA, and was detected by the NLDN. It was processed step-by-step by the *groupGCP* algorithm to illustrate how it works. With the exception of the blue ellipse (with an SMA of 8.4 km), all the other ones had SMA values of 0.2 km.

Source: produced by the author.

Given the chosen value for *maxSMA_grouping* (0.2 km), the large blue ellipse is removed from the first use of the “progressive *k*-means” algorithm. The initial iteration then assigns *k* = 1, i.e., assuming that the flash had only one GCP. The algorithm then applies the augmented *k*-means clustering method, obtaining the optimal position of the single GCP as shown by the black symbol in Figure 4.3.

However, the product between the chosen $pScale$ (1.8) and the maximum SMA value among the low-SMA ellipses (0.2 km) is only 360 meters, so the distances between all GCP-stroke pairs are much larger than the tolerance (check the distance scale ruler in Figure 4.3 for comparison). The “progressive k -means” algorithm then increments k , calling the basic k -means method with $k = 2$.

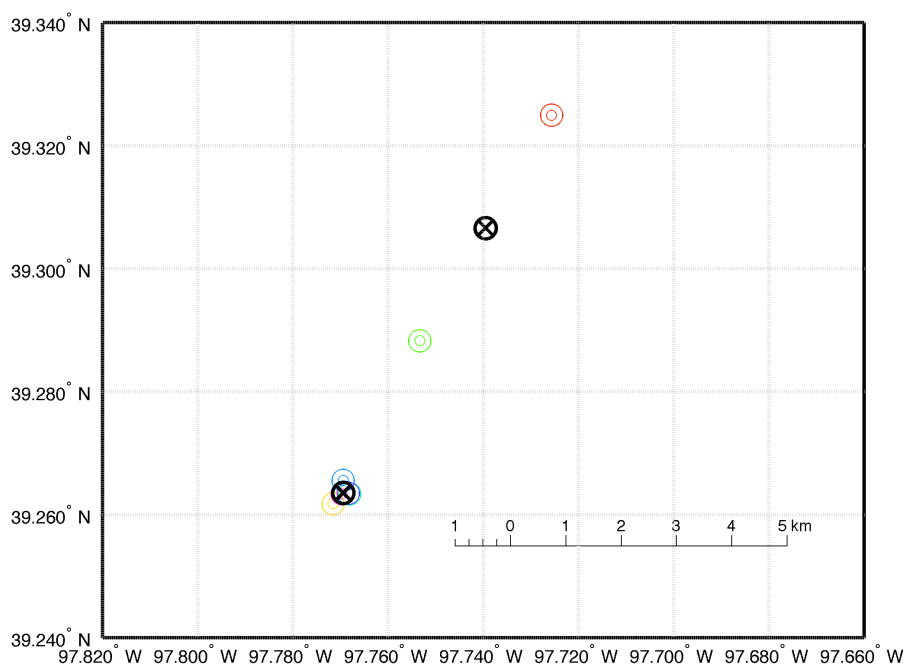
Figure 4.3 – First step of “progressive k -means”: $k = 1$.



Source: produced by the author.

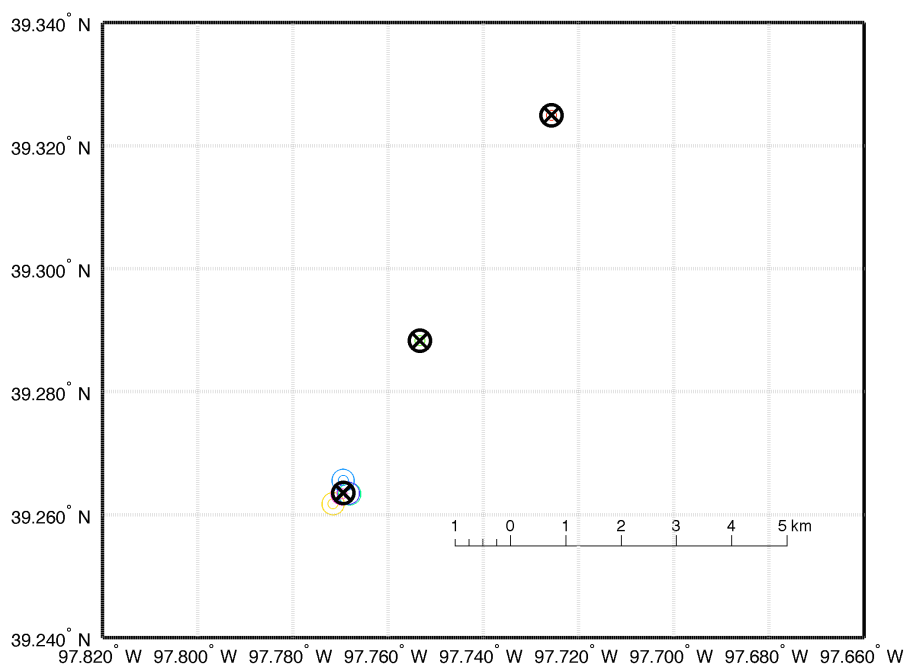
When the augmented k -means algorithm is applied for $k = 2$, it is possible to see that the cluster of strokes in the southwest corner of Figure 4.4 is properly grouped (i.e., the maximum distance for all GCP-stroke pairs were not greater than 360 meters, as dictated by $pScale$ and their maximum SMA value). However, the other centroid/GCP, to which the red and green ellipses were grouped, is too distant from its corresponding return strokes. The “progressive k -means” algorithm then decides to increment k again, now iterating over the ellipses under the assumption that there are three centroids. When that is done, the algorithm concludes that both the red and green strokes produced their own ground strike points, so the low-SMA strokes of this flash touched ground on three different locations, as shown in Figure 4.5.

Figure 4.4 – Second step of “progressive k -means”: $k = 2$.



Source: produced by the author.

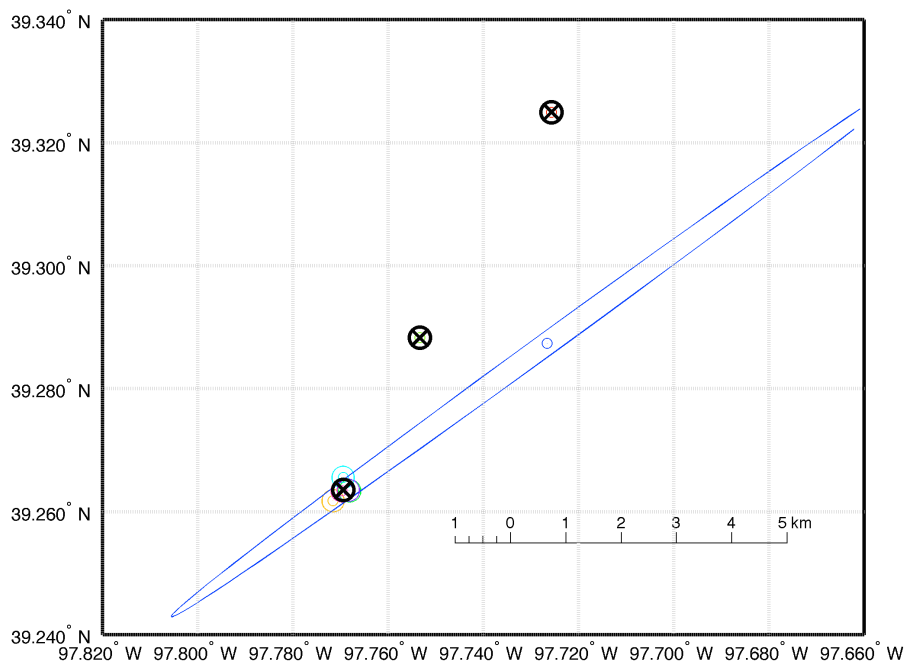
Figure 4.5 – Third step of “progressive k -means”: $k = 3$.



Source: produced by the author.

Finally, steps 3-5 of Algorithm 3 are executed as shown in Figure 4.6. When the blue ellipse is scaled to each of the three existing GCPs, the algorithm finds that the resulting scale factor f is less than one for the southeastern GCP, fulfilling the requirements set by the input parameters (i.e., f in this case is less than $maxScaleFactor$, set to be 1.5). The blue ellipse is then grouped into that GCP. Please note that, if the Euclidean metric were used, the blue ellipse would have been grouped into the GCP of the green stroke, considering that the blue ellipse center (i.e., its peak probability position) were closer to that GCP. However, visual inspection makes it clear that the southeastern GCP were much more probable to be its correct strike location given the ellipse size and orientation (azimuth). It is also worth noting that if that final condition were not fulfilled (i.e., f being less than $maxScaleFactor$), the algorithm would then apply “progressive k -means” to the blue ellipse alone, concluding that it would have its own separate, fourth GCP.

Figure 4.6 – The poorly located ellipse is grouped into one existing GCP.

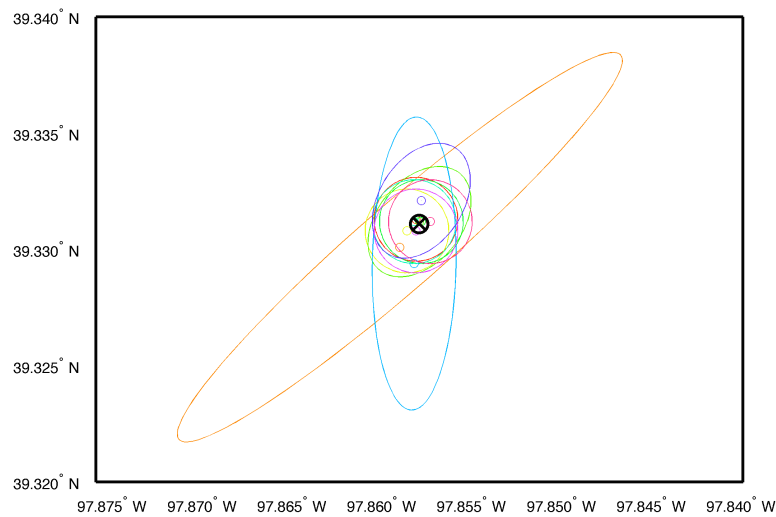


Source: produced by the author.

Figures 4.7 and 4.8 show two additional examples of flashes whose return strokes were grouped with the help of the *groupGCP* algorithm. One presented a single

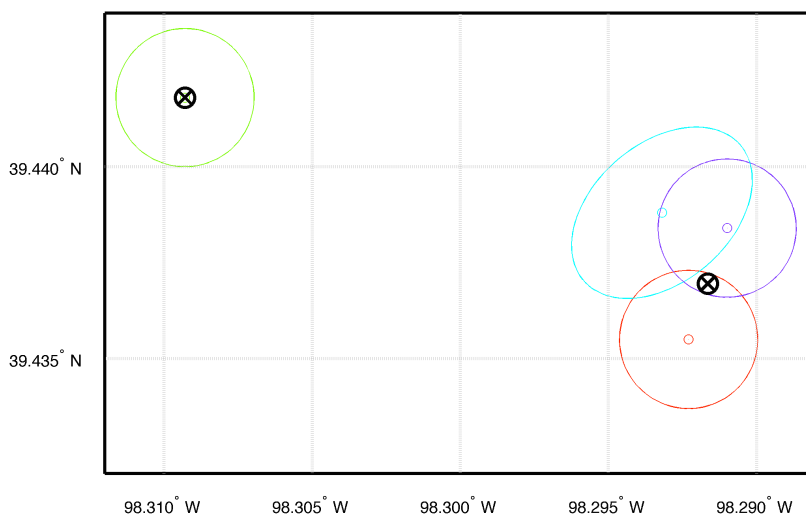
GCP (Figure 4.7) that was used by eleven return strokes (whose error ellipse SMAs ranged from 0.2 to 1.4 km). The other example (Figure 4.8) had four return strokes with two strike points. The first stroke (red ellipse) created the first GCP, but the second (green ellipse) created a new ground termination. The third (cyan) and fourth (purple), though, returned to the GCP of the first stroke, as shown by the black symbols. Three of the four strokes had very small ellipses, with SMA and SmA equal 0.2 km, and the third (cyan ellipse) stroke had an SMA of 0.3 km and an SmA of 0.2 km. Both flashes occurred on July 2013 in Kansas and were reported by the NLDN.

Figure 4.7 – Example of eleven-stroke flash with a single ground contact point.



Source: produced by the author.

Figure 4.8 – Example of four-stroke flash with two ground contact points.



Source: produced by the author.

4.2. Algorithm validation

In order to evaluate the performance of the *groupGCP* algorithm in correctly identifying ground contact points, a sample of video records was selected from the KSWFP datasets. For an analysis of this nature, it was necessary to restrict it to video records in which all channels to ground could be unambiguously identified. That has limited the sample to 25 –CG flashes, which produced 114 return strokes. Among them, 16 were single ground contact flashes (SGCFs) with a total of 80 strokes, and 9 were multiple ground contact flashes (MGCFs) with 34 strokes.

The algorithm processed U.S. NLDN data for those events with 36 different combinations of input parameters: *maxSMA_grouping* (in kilometers) was set to 0.1, 0.2, 0.3 and 0.5; *maxScaleFactor* to 1.5, 1.8 and 2.0; and *pScale* to 1.0, 1.5 and 2.0. It is worth noting that in the combinations with *maxSMA_grouping* = 0.1 kilometers the algorithm considered that all strokes had “high-SMA” ellipses, i.e., they were all processed with the elliptical metric as if they were all poorly located. Two “performance efficiency” (PE) evaluations were then made for all combinations: one for individual strokes, in which it was analyzed whether the algorithm correctly grouped each stroke to its GCP; and one for flashes, in which the number of flashes in which all its strokes were correctly grouped into their GCPs (i.e., a given flash was considered to be incorrectly classified if as little as one of its strokes were grouped to the wrong GCP).

The PE for individual strokes ranged from 96.5% to 98.2%, and for flashes it ranged from 88% to 92%. The small variability on both PEs was due to the limited number of flashes that could be used in this analysis. All combinations that involved *maxSMA_grouping* presented the maximum performance on both DE evaluations, suggesting that the use of elliptical metric for all strokes is a robust way to process the data. A summary of the PE evaluation of the algorithm is presented in Appendix A.

In a future work we plan to apply *groupGCP* to the dataset used by Pédeboy and Schulz (2014) to evaluate the algorithm presented by Pédeboy (2012). The sample of 227 –CG flashes (with 767 individual strokes) used in that analysis will provide

a deeper insight on the performance of the algorithm. Additionally, it would be a chance to apply the algorithm to data from a different LLS, as Pédeboy and Schulz (2014) conducted that analysis on data provided by EUCLID. Even though it is based on the same technology used in the NLDN, differences in their sensor deployment and positions may affect the optimal input parameters for data processing. Additional evaluation on the coastal edge of the NLDN is planned with the upcoming availability of a large dataset (over 300 return strokes) of high-speed video records of –CG flashes recorded at the NASA Kennedy Space Center in Florida, USA (J. Hill, personal communication, 2016).

5 MULTIPLE GROUND CONTACT STROKES: FORKED AND UPWARD-ILLUMINATION

In this chapter the phenomenology and characteristics of 35 forked and upward-illumination (UI) strokes, collectively referred to in this work as multiple ground contact strokes (MGCSs), is described. Selected case studies are presented in order to give an overview on the phenomenology of and the differences between these two classes of phenomenon, followed by a brief statistical analysis and a summary of the contributions of this work.

5.1. Overview of the dataset

The analysis on MGCSs is based on a dataset of –CG flashes collected by the RAMMER network during the 2012/2013 summer season. Five thunderstorm days were particularly prolific, presenting a significant amount of lightning being recorded that totaled 361 individual –CG flashes. Antunes et al. (2015) presented a detailed statistical study on many parameters of these flashes (e.g., multiplicity, duration, continuing currents) and how they changed from day to day. Among these data it was possible to identify the 35 flashes with MGCSs (as shown in Table 5.1) that are analyzed in this chapter.

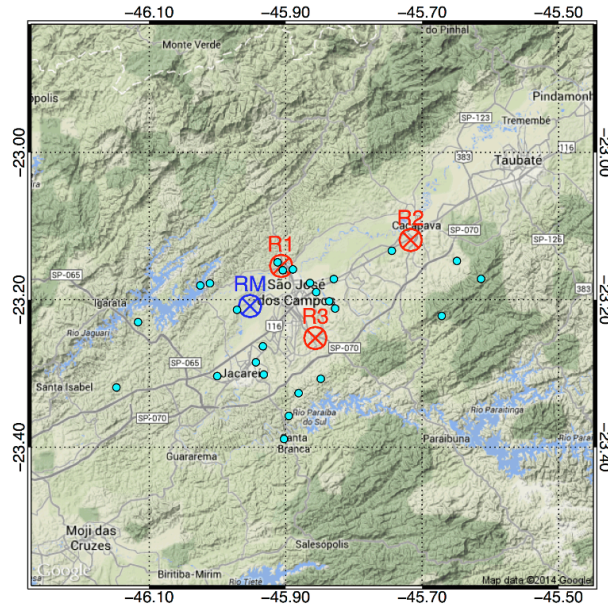
Table 5.1 – Daily number of flashes and MGCSs recorded by each RAMMER station.

Day	R1	R2	R3	RM	Subtotal	# of MGCS	% of MGCS
02/18	0	25	24	19	68	5	7.4%
02/19	11	17	19	27	74	11	14.9%
02/22	6	14	13	22	55	4	7.3%
03/06	14	31	34	38	117	11	9.4%
03/08	18	8	1	20	47	4	8.5%
Total	49	95	91	126	361	35	9.7%

Source: produced by the author and coworkers, partially presented by Campos et al. (2014c), Saraiva et al. (2014b) and Antunes et al. (2015).

Figure 5.1 shows the positions of the RAMMER stations (R1, R2, R3 and RM) with respect to the MGCSs that were not only observed by at least one of the cameras but also located by BrasilDAT (shown as green circles, totaling 26 cases).

Figure 5.1 –RAMMER sensors and the 26 MGCSs detected by BrasilDAT.



Map of the positions of the RAMMER (R1, R2, R3 and RM) stations with respect to the 26 MGCSs (cyan circles) analyzed in this study that were detected and located by BrasilDAT.

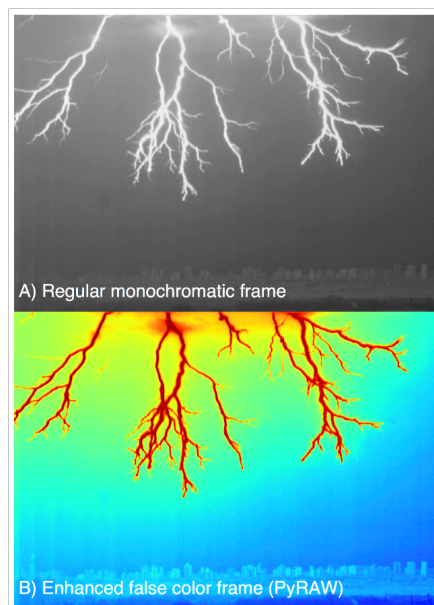
Source: produced by the author and coworkers, previously presented by Campos et al. (2014c) and Saraiva et al. (2014b).

5.2. PyRAW

The visual inspection of the high-speed video records of the MGCSs was facilitated through the use of PyRAW, a multi-purpose Python library developed by the author and coworkers (previously used by Campos et al., 2013, and Saraiva et al., 2014a). It allows the manipulation and enhanced visualization of RAW image files, which, in turn, can be obtained from high-speed camera records whose manufacturer software allows the user to convert individual frames into RAW files (either ASCII or binary). Some of its functionalities include image background removal, the creation of luminosity *versus* time graphs, and time integrations over multiple frames. For the present work, however, it was used only to create false color versions of frames of interest from the MGCS records. Figure 5.2 shows an example of a downward leader very close to the R1 station camera. Figure 5.2A is the original, monochromatic (grayscale) frame and 5.2B is a false color version of the same frame. Note that the channel details become clearer, making it easier to visually study the relative intensity of different channel

segments. For monochromatic cameras this function allows the visualization of the grayscale as a colored palette, with the blue pixels representing lower values (closer to zero) while the red pixels indicate those that are closer to saturation (very bright). For colored cameras (which is the case of the one used in the mobile RAMMER station), the user is allowed to choose which color channel (red, green or blue) or combination of channels (e.g., the sum of two of the channels) should be considered in the creation of the false color visualization. Full documentation of the PyRAW library and all its functionalities will be presented in a future work.

Figure 5.2 – Example of a monochromatic frame displayed in false color with PyRAW.



(A) One selected frame from the high-speed video of a downward negative leader recorded by a monochromatic Phantom v9.1 camera; (B) the same frame now enhanced with the help of the PyRAW library functionalities using a rainbow color palette.

Source: produced by the author and coworkers, previously presented by Campos et al. (2014c) and Saraiva et al. (2014b).

5.3. Case studies

Among the 361 –CG flashes recorded by the RAMMER stations in February and March 2013, a total of 35 events presented strokes with more than one ground termination within a very short period (up to a few milliseconds). This section presents a few selected MGCS from that dataset to be discussed in greater detail. This is intended not only to discuss some of their peculiarities but also to serve as

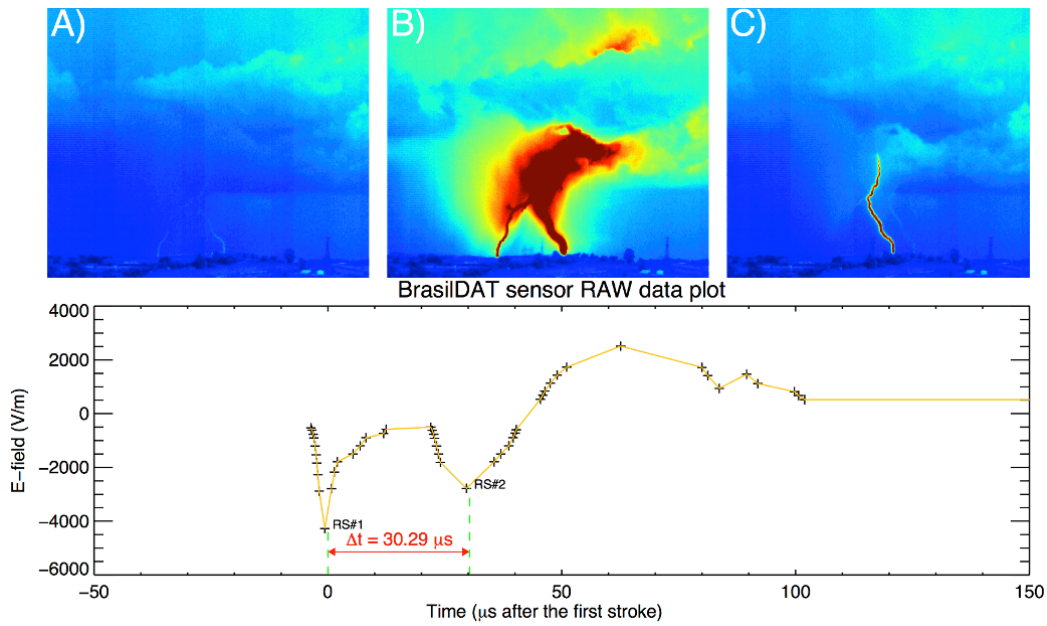
a reference for how the parameters and characteristics discussed in later sections were determined. Two “classical” forked stroke events are described in the first subsection, each one representing an extreme of the spectrum of interstroke intervals (one had them separated by about 30 microseconds while the other had a delay of more than 200 microseconds before the second ground contact was established). UI strokes are the subject of the second part, where two cases that had about 2 and 1 milliseconds between ground contacts, respectively, are discussed. Finally, the differing characteristics that allow the separation between types (forked and UI strokes) are discussed in section 5.4. This separation was done *a posteriori*, i.e., after the case studies were conducted and it was possible to determine that there were two distinct classes of phenomena.

5.3.1. Forked strokes

5.3.1.1. Flash #1, February 18th, 2013

The first selected forked stroke was Flash #1, observed at 20:16:39 (UT) on February 18th, 2013. The very first stroke of this flash was forked, producing two ground terminations that could be observed in the same video frame. The left-hand termination becomes inactive in the following frame while the luminosity of the right-hand termination lasted for about 12.6 milliseconds. Both are shown in Figure 5.3A,B,C. The time interval between these ground contacts was determined to be 30.9 microseconds from the analysis of the electric field waveforms retrieved from six different BrasilDAT sensors (one of which is presented on the lower part of Figure 5.3). About 88 ms after the first (forked) stroke of Flash #1 another return stroke occurred, following the path to ground that was formed by the right-hand branch. It must be noted, however, that about half of the left-hand branch was re-illuminated by the dart leader preceding the second stroke (not shown in the frames included in the figure). A fourth return stroke followed the third after 36 milliseconds, but this time its dart leader did not penetrate the channel of the left-hand termination.

Figure 5.3 – False color frames and electric field record of the forked stroke of Flash #1.



Above: (A), (B) and (C), selected video frames displayed with false color from the monochromatic camera. Below: BrasilDAT waveform of the forked stroke of Flash #1.

Source: produced by the author and coworkers, previously presented by Campos et al. (2014c) and Saraiva et al. (2014b).

Although visually the brightness of the left-hand channel of the forked stroke is considerably less intense than the right-hand channel (as suggested by the apparent saturation on the latter, see Figure 5.3B), the analysis of multiple electric field waveforms provided by BrasilDAT has shown that their peak values were very similar, with a first-to-second peak ratio of 0.9. BrasilDAT reported the earlier (right-hand) stroke with an estimated peak current of -7 kA, so from the ratio between their peaks it is reasonable to assume that the second, left-hand termination had a peak of approximately -6 kA. This apparent inconsistency may be due to the continuing current that lasted 12.6 ms in the right-hand channel. The LLS solution also allowed the estimation of the distance from the camera, calculated to be approximately 29 km, allowing the photogrammetric analysis of the video frames. It was possible to estimate the two-dimensional distance between each ground termination and the forking point, visible below cloud base. The distances were: 1320 m for the right-hand channel and 1530 m for the left-hand channel, with the forking point estimated to be about 1280 m above ground.

Their horizontal separation in the plane parallel to the camera image plane is about 1420 meters, but this should be taken as a lower bound estimate.

Considering the photogrammetric results for this event, it is possible to estimate the upper bound value for the return stroke speed (of the first, right-hand contact) if one assumes that its wave did not reach the extremity of the left-hand channel before it made ground contact (leading to the successful double ground termination). The return stroke wave would need to travel about 2850 meters (the sum of the lengths of both branches up to the forking point) in no more than 30.9 microseconds (their temporal separation estimated through the electric field waveform inspection). This leads to a return stroke speed of $9.22 \times 10^7 \text{ m s}^{-1}$, which is close to the range of maximum values ($1.2\text{-}2.8 \times 10^8 \text{ m s}^{-1}$) usually found in literature for natural lightning (see, for a summary, Table 4.5 of Rakov and Uman, 2003). Note, however, that this estimate is influenced by the uncertainties involved in the determination of the temporal separation, which will vary depending on which phase of the peaks are considered.

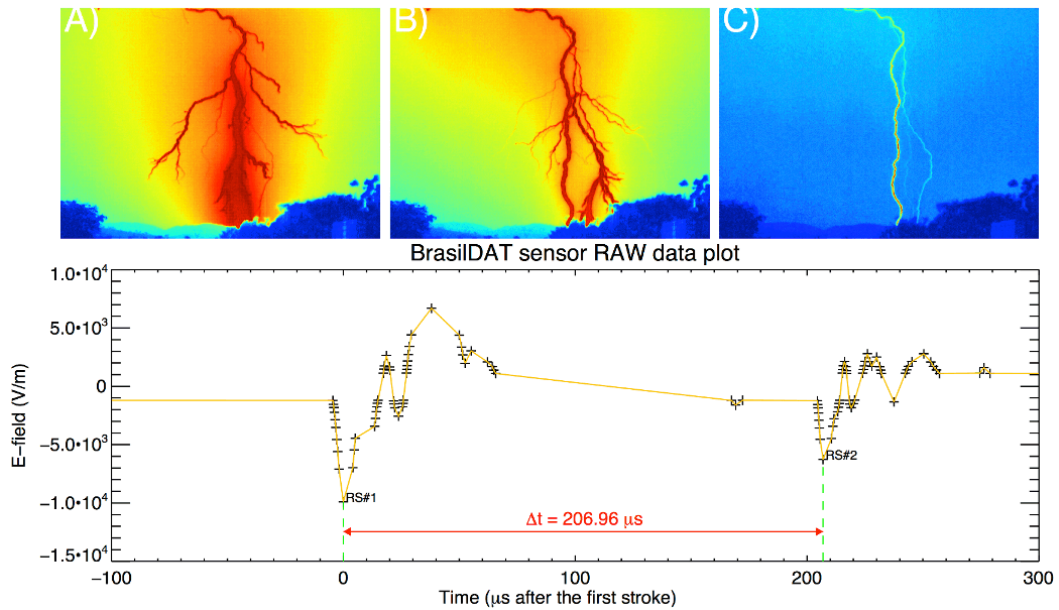
5.3.1.2. Flash #54, February 19th, 2013

The second forked stroke event is Flash #54, observed at 19:10:13 (UT) on February 19th, 2013. Two return strokes preceded the MGCS, following two different paths to ground and with no apparent (i.e., visible below cloud base) channel segments shared with the forked stroke of interest (which was observed 52 milliseconds after the second stroke). Two other strokes were recorded after the MGCS (after 56 and 166 ms later) sharing a single new channel to ground (i.e., that was different from those of all preceding strokes).

In this MGCS event the ground contacts were observed in two consecutive video frames, as shown in Figure 5.4A,B. Through the analysis of electric field waveforms provided by BrasilDAT sensors (one of them is shown in the bottom of Figure 5.4) it was found that the temporal separation from the left-hand (first) channel to the right-hand (second) channel was about 205 microseconds and the ratio between the first and second peaks was found to be 0.6. As the solution provided for the first contact had a peak current estimate of -39 kA , it is reasonable to assume that the second ground termination had a peak of -23 kA .

BrasilDAT data also allowed the calculation of the distance from the camera to the flash strike points, found to be 18.4 km. From this information it was possible to estimate the two-dimensional length between each ground contact point and the forking point, which is more visible in Figure 5.4C (upper, central region of the frame). The left-hand and right-hand channels had their distances estimated 5060 and 5100 meters, respectively (it is worth mentioning that they left the cloud opaque region above cloud base). As done for the previous analyzed event, if one considers the time between each ground contact (205 μs) and the total distance between the ground contact points (totaling about 10160 m) it is possible to estimate the upper bound for the return stroke traveling wave, assuming that it needs to travel the full measured distance in order to prevent the right-hand channel from reaching ground. The value found is $5.0 \times 10^7 \text{ m s}^{-1}$, also in good agreement with the speeds commonly found in literature (see previous case study).

Figure 5.4 – False color frames and electric field record of the forked stroke of Flash #54.



Above: (A), (B) and (C), selected video frames displayed with false color from the monochromatic camera. Below: BrasilDAT waveform of the forked stroke of Flash #54.

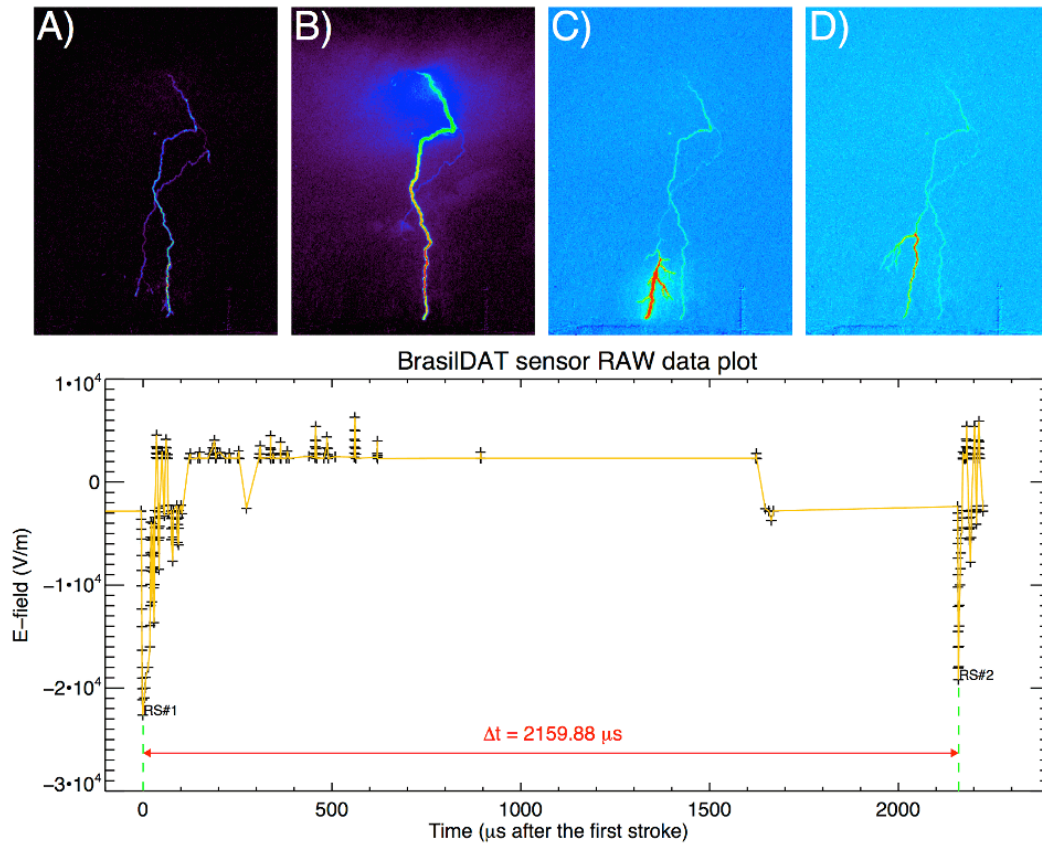
Source: produced by the author and coworkers, previously presented by Campos et al. (2014c) and Saraiva et al. (2014b).

5.3.2. Upward illumination (UI) strokes

5.3.2.1. Flash #17, February 19th, 2013

The first selected UI event was Flash #17, observed at 18:19:34 (UT) on February 19th, 2013, about 40 minutes before the occurrence of Flash #54 (discussed in the previous section). This flash produced one return stroke and, 70 milliseconds later, a second return stroke that was an UI stroke. There are no visible common branches between them, although they leave the opaque region of the thundercloud in the same approximate region shown in the high-speed video frames. About 35 milliseconds prior to the occurrence of the main return stroke of the UI event its stepped leader became visible below cloud base. As shown in the selected frames of Figure 5.5A and 5.5B, there are two main leader branches, but the right-hand one touched ground first, producing the main return stroke. However, five frames after the stroke (approximately 2 ms later), the left-hand branch made ground contact, producing an upward illumination that can be seen in the two consecutive frames of Figure 5C,D. From the analysis of the electric field waveforms recorded by five BrasilDAT sensors (one of them shown in the bottom of Figure 5.5), a more precise interval between the ground contacts was determined to be 2170 microseconds. The ratio between the electric field peaks was 0.3, so as the main stroke had its estimated peak current to be -15 kA, it is reasonable to assume that the UI had a peak current of approximately -5 kA. It is important to notice that the false color enhancing technique used in the first half of the sequence of images (Figure 5.5A and B) is different from all other examples in this work, in an attempt to show the weak luminous connection between the UI and the main branch.

Figure 5.5 – False color frames and electric field record of the UI stroke of Flash #17.



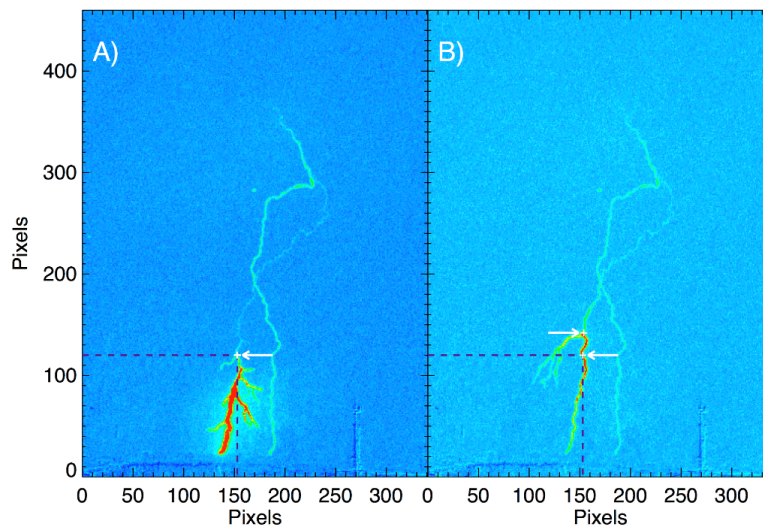
Above: (A), (B) and (C), selected video frames displayed with false color from the monochromatic camera. Below: BrasilDAT waveform of the UI stroke of Flash #17.

Source: produced by the author and coworkers, previously presented by Campos et al. (2014c) and Saraiva et al. (2014b).

The analysis of the false color visualization of the video frames clearly show that the UI channel remains luminous even after the main return stroke occurred, suggesting that although there may be effective current cutoff between them (as argued by Stolzenburg et al., 2012, 2013b) the intervening channel segment is not completely extinguished. This characteristic can be seen in greater detail in Figure 5.6, which shows the evolution of the UI process in two consecutive frames. It is possible to see that many secondary branches are illuminated as the UI process advances. In the second frame (Figure 5.6B) one can see that these branches continue to have their luminosity intensified as the UI return stroke moves further up, so that the upper branches are brightened as well. The arrows allow a comparison of the advancement between the two frames and show how in Figure 5.6B no branching below the lower arrow is visible. Also, it is noticeable that

portions of the UI channel located even further up are also intensified, although no other secondary branches are re-illuminated. Through a photogrammetric analysis it was possible to calculate that each pixel is equivalent to about 20 meters, so the total length of the intensified channel up to the lower arrow was estimated to be about 2000 m, and the segment between the two arrows is about 500 m long. The two-dimensional distances between each ground contact and their forking point that lead to each one of the two main branches could also be estimated: 5600 m for the left-hand (UI) channel and 5900 m for the right-hand (main stroke) channel. This adds to a total distance of approximately 11500 meters, so, considering the time interval between contacts (2170 microseconds), if the branches were still electrically connected (as in a forked stroke), the return stroke propagation speed could not be greater than $5.3 \times 10^6 \text{ m s}^{-1}$ to allow the UI to reach ground. This value is considerably lower than what is usually found in literature, so this result supports the idea that the main and UI branches are effectively cut off from each other (or else there is some other physical mechanism that restricts the penetration of the return stroke wave into its lower part, possibly reducing its propagation speed, but no currently known process could cause that).

Figure 5.6 – Evolution of UI process of Flash #17.

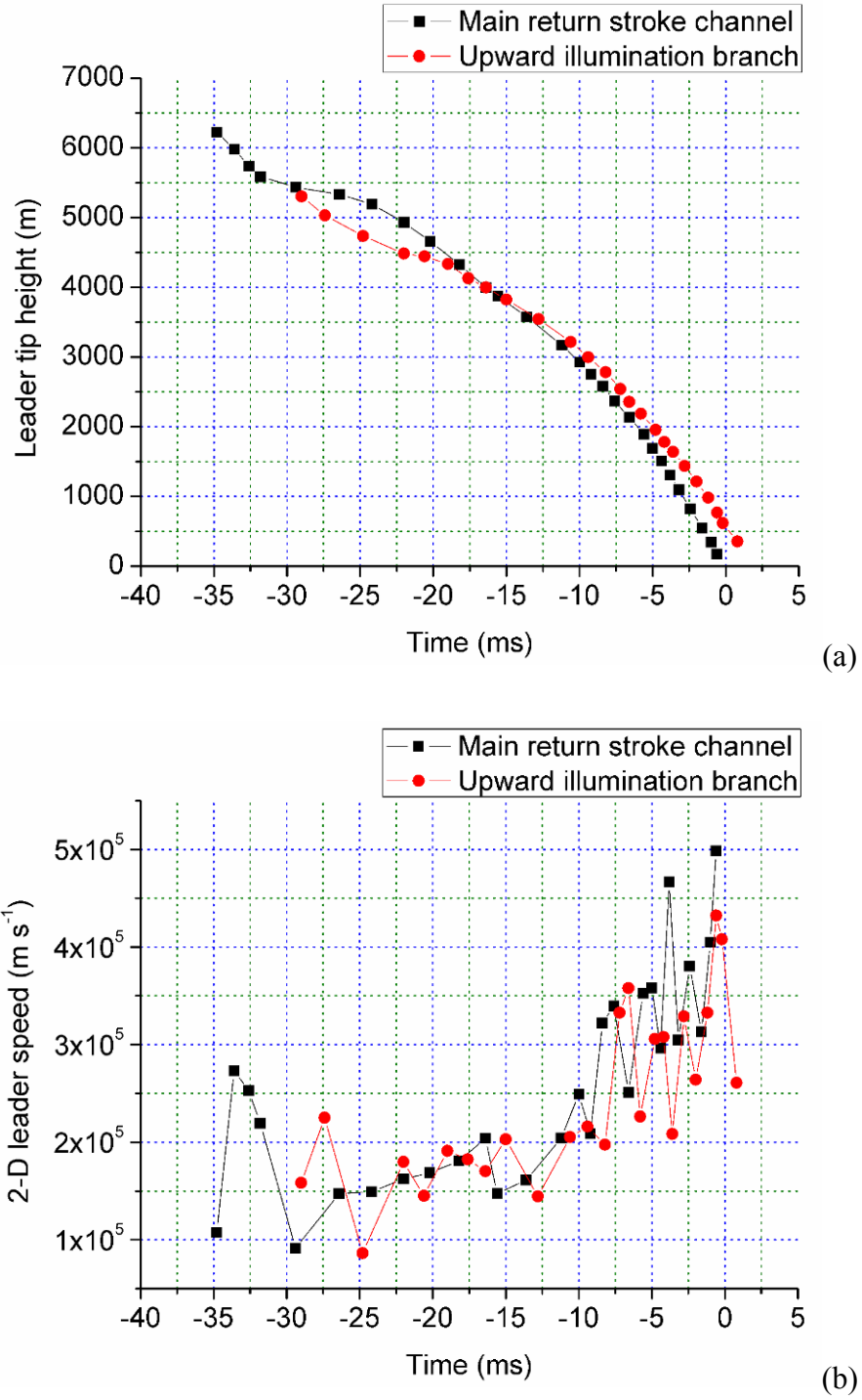


Two consecutive frames of the UI process observed in Flash #17. Each pixel corresponds to approximately 20 meters.

Source: produced by the author and coworkers, previously presented by Campos et al. (2014c) and Saraiva et al. (2014b).

The photogrammetric analysis of Flash #17 also allowed the tracking of downward stepped leaders. Plots of leader tip height and leader two-dimensional speed *versus* time are presented in Figure 5.7, in which time $t = 0$ corresponds to the time of occurrence of the main (right-hand) return stroke. Due to the fact that the leader exited the cloud opaque region above its cloud base (as in Flash #54), a considerably long portion of its channel was visible (about 6000 meters). The UI branch was formed around 5500 m above ground (30 ms prior to the main return stroke) and presented a two-dimensional (2-D) speed that was initially higher than the one calculated for the main stroke branch (i.e., that produced the right-hand channel). Both leader branches developed almost synchronously up to the final 2000 meters (5 milliseconds) before ground contact is made. After this time, the leader tip *versus* time plot (Figure 5.7a) shows that the UI branch is progressively left behind, presenting lower speeds when compared to the main return stroke branch (as shown by the 2-D speed *versus* time graph as well, Figure 5.7b), there is acceleration in the final part of the development of both leader branches. The UI branch becomes less bright after the stroke, reaching ground about 2.2 ms later. As its final development is not visible to the camera, its last speed measurement ($2.6 \times 10^5 \text{ m s}^{-1}$) is a lower bound estimate.

Figure 5.7 –Stepped leader evolution of the UI stroke of Flash #17.



Temporal evolution of (a) stepped leader tip height and (b) 2-D leader speed of the UI stroke of Flash #17.

Source: produced by the author and coworkers, previously presented by Campos et al. (2014c) and Saraiva et al. (2014b).

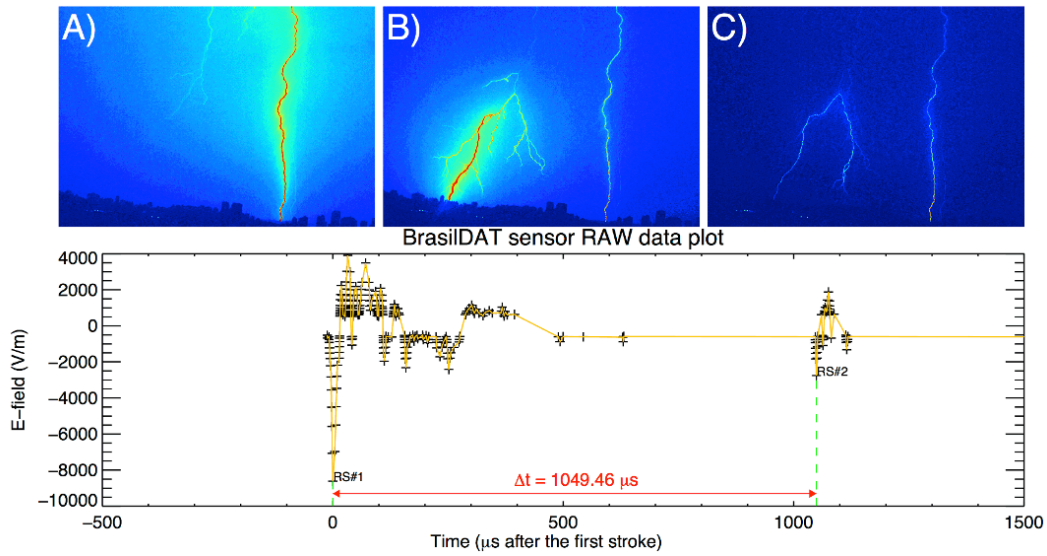
5.3.2.2. Flash #85, March 6th, 2013

The second selected UI event was Flash #85, observed at 22:41:01 (UT), March 6th, 2013. Unlike Flash #17, presented in the previous subsection, the very first return stroke of Flash #85 produced a UI stroke. A subsequent stroke occurred 171 milliseconds after the UI and followed its path to ground. During this interstroke interval, however, an attempted leader occurred in the UI branch, and will be discussed later in this subsection.

The forking point of this UI event was located outside the camera FOV, but the discontinuity of the brightness of the UI branch was clear enough to allow its identification as such. Figure 5.8A shows the channel of the main (right-hand) stroke, two frames (800 microseconds) after contact with ground was made. On the next frame (i.e., three frames after the first stroke) the UI occurred, as shown in Figure 5.8B. Electric field waveforms from five BrasilDAT sensors provided an estimate of the time interval between their ground connections, resulting in 1040 microseconds. In the analyzed waveforms the ratio between their peaks was 0.3 (similar to Flash #17). As the main stroke had an estimated peak current of -20 kA in the reported solution, we assume that the UI had a peak of about -6 kA.

Careful inspection of the UI frames, shown in greater detail in Figure 5.9 (generated from the data provided by the blue channel of the colored camera of the RAMMER mobile station), indicates a relationship between the branches illuminated by the return stroke and those illuminated by the UI development. Each pixel is equivalent to approximately 9.3 meters at the estimated distance from the camera to the ground strike point (given by the BrasilDAT solution). Figure 5.9A shows one of the branches that were illuminated by the return stroke. By comparing the positions of the mid and upper arrows of Figures 5.9A and 5.9B it is clear that the UI did not travel into the segments illuminated by the return stroke, even though it is not possible to conclusively confirm that with the available imagery. This indicates that there is effective current cutoff between the main stroke channel and the UI branch, even though the video data shows that the upper region of the UI channel remains luminous (possibly going up to the forking point of this flash, similar to what was observed for Flash #17 in the previous subsection).

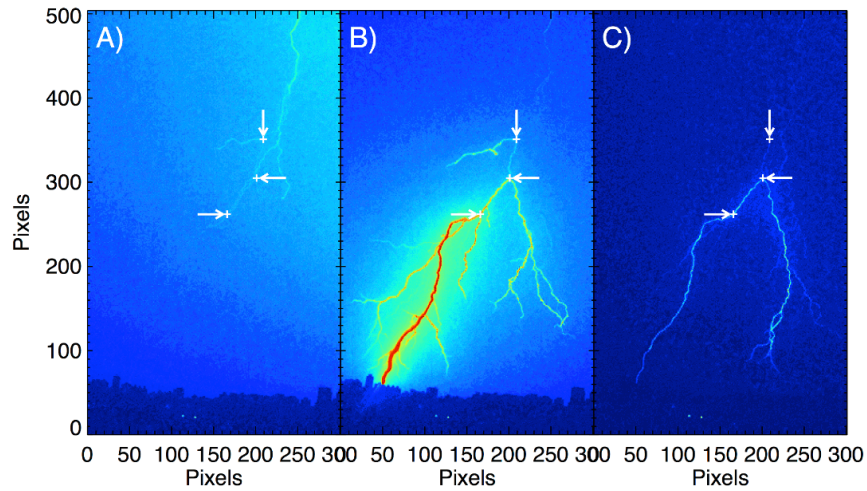
Figure 5.8 – False color frames and electric field record of the UI stroke of Flash #85.



Above: (A), (B) and (C), selected video frames displayed with false color (blue channel of the colored camera). Below: BrasilDAT waveform of the UI stroke of Flash #85.

Source: produced by the author and coworkers, previously presented by Campos et al. (2014c) and Saraiva et al. (2014b).

Figure 5.9 – Details of the UI branch of Flash #85.



UI branch of Flash #85 shown in greater detail (false color from the blue channel data of RAMMER mobile station). (A) was cut from the main stroke frame, while (B) and (C) were cut from the first and second frames of the UI process (three and four frames after the main stroke), respectively. Each pixel is equivalent to approximately 9.3 meters.

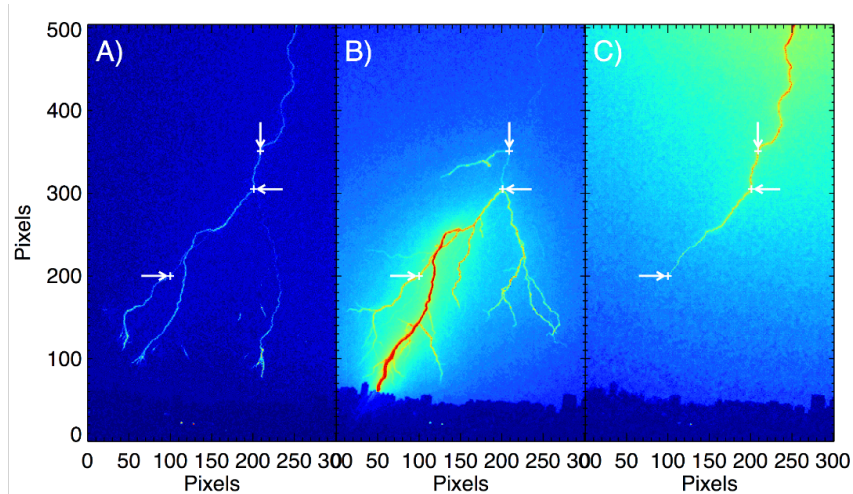
Source: produced by the author and coworkers, previously presented by Campos et al. (2014c) and Saraiva et al. (2014b).

It is also possible to note three distinct levels of intensity in the UI development. The bottom arrow shows where the most intense pixels (i.e., red) ended in the upward propagation of the UI (Figure 5.9B). Photogrammetric analysis indicates that this segment is about 2200 meters long. The middle arrow shows the second level of intensity, where the green/yellow pixels are located. This point is about 2700 meters from the UI strike point and it is possible to see that the illuminated right-hand branch presented similar intensity values, which persisted and moved farther down that branch in the consecutive frame (Figure 5.9C). Finally, the top arrow shows the upper level of illumination, mostly made of light blue pixels up to 3100 meters from the strike point (and was not illuminated in the following frame). This false color imagery suggests that the UI attenuates as it moves towards the forking point, and that the illumination of its branches may continue if conditions allow (as Figure 5.9B indicates). It is possible that this non-uniformity could be caused either by the timing of the frames exposure or by the fact that the three-dimensional channel morphology is being investigated through two-dimensional data. However, earlier frames (associated with the development of the stepped leader) do not support the idea of geometry being responsible for this effect. If that attenuation is real, it may support the idea that the discontinuity in channel conductivity is progressive as one goes nearer the forking point, moving into less and less conductive regions instead of going into a suddenly cutoff channel segment.

About 125 milliseconds after the main stroke occurred, an attempted leader was observed in the UI branch. As shown in Figure 5.10C, it retraced the UI branch while propagating towards ground, but its development was interrupted at about 1600 meters above ground. The comparison of the selected frames, however, shows that the attempted leader followed the leftmost branch of the UI channel and would not have reached the same ground strike point if it had persisted in its development. It is also worth noting that the attempted leader moves beyond the point where the UI interrupted its development (Figure 5.10B), favoring the idea that there was no complete cutoff throughout that branch (i.e., a progressive reduction in channel conductivity seems more likely). This observation, added to the fact that the upper region of the UI branch remains luminous, suggests that there is a transition in the channel conductivity régime between the UI-intensified

branches and those that were illuminated by the return stroke (Figure 5.9A). Further support to this idea is given by Flash #115, which occurred in the same day as Flash #85 but is not presented in detail in this work, which had three subsequent strokes following the same channel to ground as the UI.

Figure 5.10 – Details of an attempted leader in the UI branch of Flash #85.



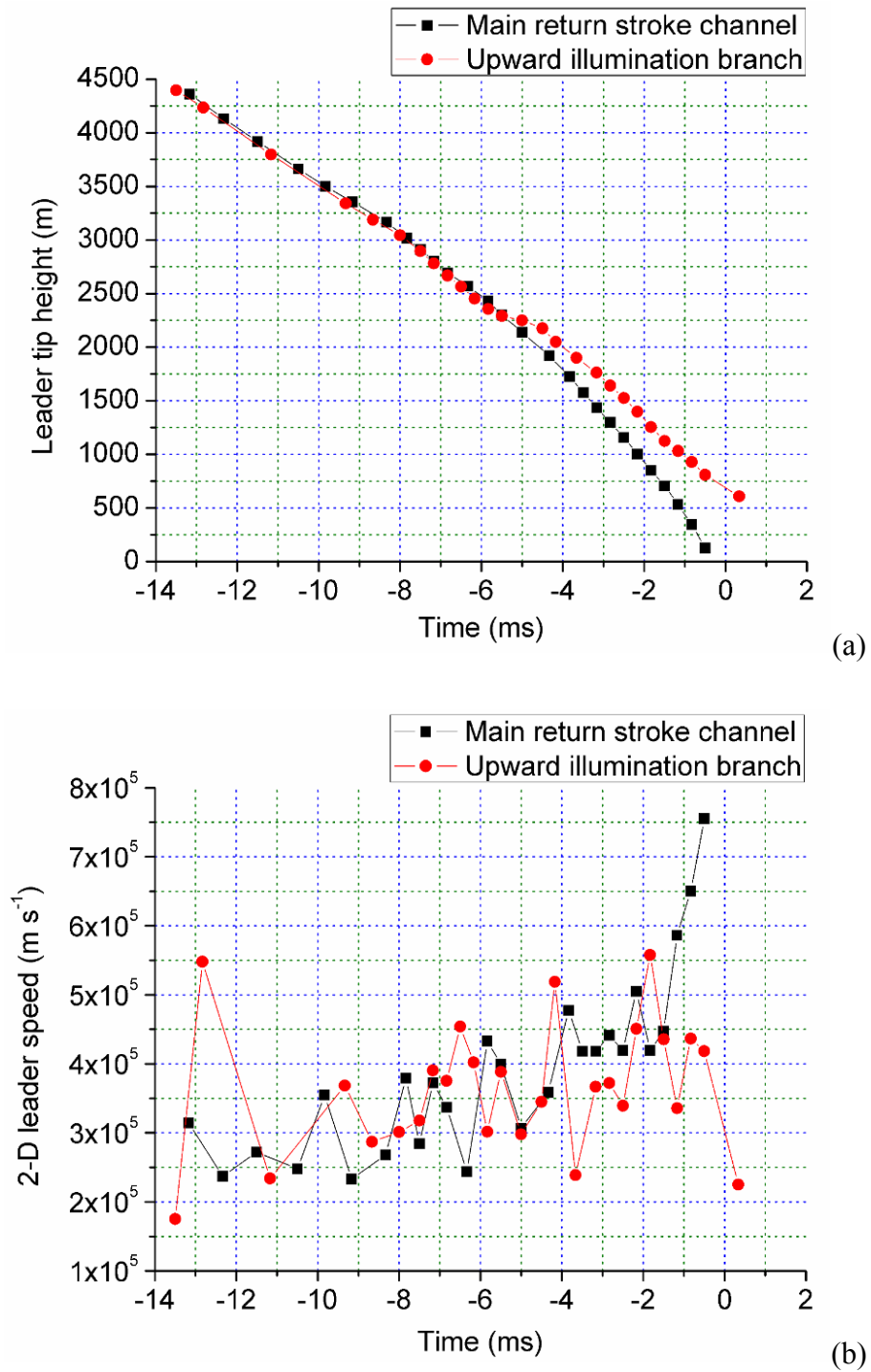
Detailed comparison of (A) stepped leader, (B) UI process and (C) subsequent attempted leader that occurs after the UI stroke of Flash #85. All frames are false color from the blue channel data of the colored camera (RAMMER mobile station). Each pixel is equivalent to approximately 9.3 meters.

Source: produced by the author and coworkers, previously presented by Campos et al. (2014c) and Saraiva et al. (2014b).

The photogrammetric technique also allowed a detailed analysis of the stepped leader development in the bottom 4500 meters of the UI and main stroke channels. Figures 5.11a and 5.11b show the leader tip height and 2-D speeds *versus* time plots. It seems that the leader speeds oscillate up to the final 2 ms (1000-1250 m) prior to the main stroke, although it is worth noting that this variation may be due measurement uncertainties. Both branches propagated almost synchronously up to the final 5 ms (2000-2250 m), but after that moment the UI branch became slower and did not present the final acceleration of the main stroke channel (Figure 5.11b). Figure 5.11c shows the instant the UI branch starts to be left behind in greater detail. In this event the slower development of the UI branch at later times seems more prominent than what was observed for Flash #17 (Figure 5.7). It is important to note, however, that this reduction does not coincide

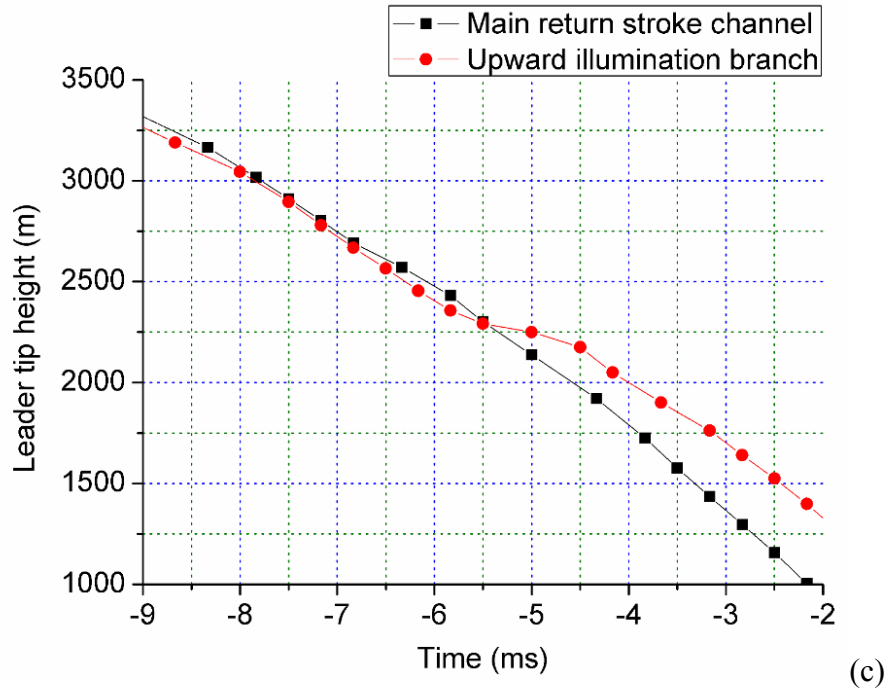
with the upper region of UI development: the speed reduction took place in the 2000-2250 m range of heights, while the UI propagated almost up to 3000 m above ground.

Figure 5.11 – Stepped leader evolution of the UI stroke of Flash #85.



(Continues)

Figure 5.11 – Continued.



Temporal evolution of (a) stepped leader tip height and (b) 2-D leader speed of the UI stroke of Flash #85. Panel (c) is equivalent to (a) but zoomed into the instant the leader tips (main and UI) stopped being mostly synchronous.

Source: produced by the author and coworkers, previously presented by Campos et al. (2014c) and Saraiva et al. (2014b).

5.4. Visual differentiation between forked and UI strokes

The full dataset of 35 MGCSs was sorted between forked and UI strokes through careful visual inspection of the high-speed vide records after specific visual patterns were identified. An event was considered to be a *forked stroke* when it fulfilled three main conditions: (i) presented two or more ground terminations that occurred temporally close in the high-speed video record (either in the same frame or separated by no more than two frames); (ii) both ground terminations appeared actively luminous at the same time on at least one video frame; and (iii) all the grounded branches were fully and mostly uniformly illuminated after ground contact has been made. Conditions (ii) and (iii) are assumed to indicate that both terminations were responsible for injecting electrical currents into the same

channel trunk, shared by both branches at their forking point. One example of a high-speed video frame of a forked event is shown on Figure 5.12.

Figure 5.12 – Example of forked stroke.



Cropped high-speed video frame of a MGCS event classified as a forked stroke. It was provided by the colored camera that operated at the RAMMER mobile station. The forking point is visible below cloud base and both grounded branches are uniformly illuminated.

Source: produced by the author and coworkers, previously presented by Campos et al. (2014c) and Saraiva et al. (2014b).

UI strokes were identified following the visual similarities compared to the events previously studied by Stolzenburg et al. (2012, 2013b) and the digital imagery presented and discussed in their works. For these processes condition (i) of the forked strokes also needed to be met (the second will frequently not be valid for sufficiently high camera frame rates), with a relevant difference in its third defining characteristic: (iii) the upward-propagating luminosity enhancement in one of the branching channels needs to be non-uniform, i.e., it should not illuminate the entire channel branch where it occurred (and never reach its forking

point, for those events in which it was distinguishable and visible below cloud base). An example of this class of event is shown in Figure 5.13. It is important to note that for the statistical analysis of section 5.5 only these visual criteria were applied when sorting out the dataset of MGCS events into forked and UI strokes. This is very relevant for some of the analyses that will be presented on that section.

Figure 5.13 – Example of upward-illumination (UI) stroke.



Cropped high-speed video frame of a MGCS event classified as an UI stroke. As in Figure 5.12, it was provided by the colored camera that operated at the RAMMER mobile station. The left-hand side branch corresponds to the UI process, as the non-uniform brightening suggests. Even though there is still visible (although dim) luminosity in the upper part of the UI channel, its lower region is considerably brighter.

Source: produced by the author and coworkers, previously presented by Campos et al. (2014c) and Saraiva et al. (2014b).

5.5. Statistical analysis

5.5.1. Photogrammetric parameters of UI strokes

5.5.1.1. Stepped leader speeds

Five UI strokes had their downward stepped leader speeds calculated for both the main channel, which produced the initial return stroke, and the channel that lead to the UI. As discussed in the case studies of section 5.3, it was shown that the UI branch develops most of its extension with speeds comparable to that of the main stroke channel, usually diverging from it in the latest moment of its development. Additionally, if one takes all the speed measurements obtained for all analyzed UI events, it can be shown that they are statistically very similar. The five different UI strokes allowed 114 and 87 individual measurements of downward stepped leader speeds for the main and UI branches, respectively. The statistical summary of these measurements is presented in Table 5.2.

Table 5.2 – Statistics of 2-D leader speeds preceding UI strokes.

	Main branch	UI branch
Number of observations	114	87
Arithmetic Mean ($\times 10^5 \text{ m s}^{-1}$)	3.1	3.1
Minimum ($\times 10^5 \text{ m s}^{-1}$)	0.91	0.87
Maximum ($\times 10^5 \text{ m s}^{-1}$)	6.5	5.6
Geometric Mean ($\times 10^5 \text{ m s}^{-1}$)	3.0	2.9

Statistical parameters of the two-dimensional leader speeds estimated for the main and upward-illumination branches for the analyzed UI events.

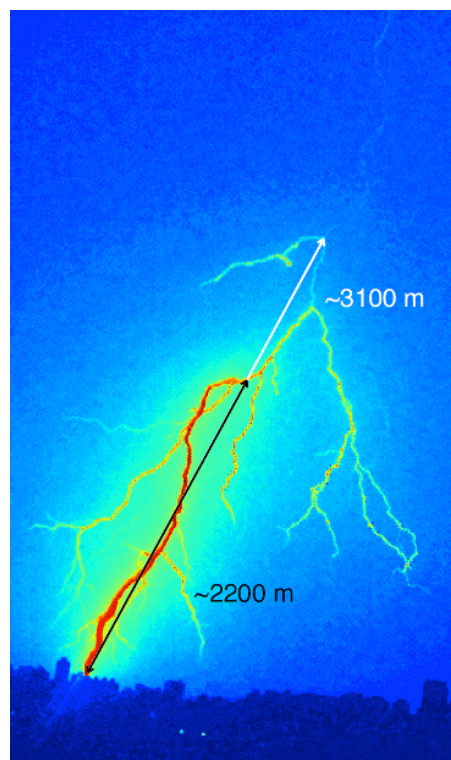
Source: produced by the author and coworkers, previously presented by Campos et al. (2014c) and Saraiva et al. (2014b).

Simple comparison of each parameter strongly suggests that both branches propagate with the same range (and typical values) of two-dimensional speeds. The higher maximum found for the main branches is probably related to the final acceleration of the leader that was not as pronounced on the UI branches (see Figures 5.7 and 5.11). Additionally, although not shown in the present work, histograms of speeds for both branches are also very similar, endorsing the idea that there is no statistically significant difference between them (except, of course, for their final stages of development).

5.5.1.2. UI channel total brightening length

As discussed in the case studies of section 5.3.2, the UI processes usually do not illuminate its branch uniformly over the whole length. It was also found that the lower part is usually brighter than the upper region of the UI channel (which connects to the main stroke branch), as shown in Figure 5.14. The length of both the complete brightened channels and the section that were most intensely illuminated are analyzed for six events (the same five that had their leader speeds estimated in the previous subsection along with a sixth event whose leader development could not be tracked) and the results are presents in Table 5.3. On average, the brightest segment corresponded to about 70% of the total length illuminated by the complete UI process.

Figure 5.14 – The most intense and the total brightened segments of a UI channel.



Examples of the most intense (black double-ended arrow) and the total brightened (black double-ended plus white arrows) segments of the UI channels of one event. The false color version of the frames makes it considerably easier to identify the boundaries for each region.

Source: produced by the author and coworkers, previously presented by Campos et al. (2014c) and Saraiva et al. (2014b).

Table 5.3 – Statistics of the most intense and total brightened segments of UI channels.

	Total brightened channel length	Length of the brightest channel segment
Number of observations	6	5*
Arithmetic Mean (m)	2300	1600
Minimum (m)	1400	1100
Maximum (m)	3100	2200
Geometric Mean (m)	2200	1500

*For one of the analyzed events there was no distinguishable brightest segment

Statistical parameters of the length of the total and brightest channel segments illuminated by each UI stroke.

Source: produced by the author and coworkers, previously presented by Campos et al. (2014c) and Saraiva et al. (2014b).

5.5.2. Relative occurrence of Multiple Ground Contact Strokes (MGCS) by thunderstorm day

The number of –CG flashes recorded during the five days of RAMMER observations was sufficiently large to allow the analysis of day-to-day variations of the relative occurrence of MGCSs. While Table 5.1 shows the daily variation of the percentage of flashes with MGCSs over the total amount of –CGs observed, Table 5.4 summarizes the daily percentages of forked and UI strokes (separately) over the total number of MGCSs. There is a large variability in the daily relative incidence of each class of event, indicating that there is no clear most common proportion. In one of the five days (February 22nd) no cases of UI strokes were reported, and only on March 6th the incidence of UI strokes was greater than the proportion of forked strokes.

Table 5.4 – Proportion of forked and UI strokes over the total daily number of MGCSs.

Day	% of forked strokes	% of UI strokes
02/18	80.0%	20.0%
02/19	63.6%	36.4%
02/22	100%	0%
03/06	45.4%	54.6%
03/08	50.0%	50.0%

Source: produced by the author and coworkers, previously presented by Campos et al. (2014c) and Saraiva et al. (2014b).

5.5.3. One-dimensional distance between ground contact points

For 25 of the 35 MCGSs analyzed it was possible to estimate the horizontal separation between their ground strike points through photogrammetric analysis of the high-speed video records. A limitation of the estimate obtained through this technique, however, is the fact that only the component that is parallel to the camera sensor can be taken into account.

Table 5.5 provides a statistical summary of the values that were obtained from the camera records. Forked strokes (16 events) and UI (9 events) were considered separately (one column for each) and then grouped into a single sample (on the right-hand column). A simple comparison of each group of data suggests that they do not present statistically significant differences. The average separations for both types of phenomenon were close to 1200 meters, with very similar maximum values as well (3350 to 3800 meters for UI and forked, respectively). Although the relative difference between their minimum values is large (120 to 280 meters), this value should be considered with caution due to the underestimation that is inherent to this one-dimensional technique applied to estimate a two-dimensional parameter. Overall, these results suggest that forked strokes and UI events are produced by leader branches that do not have any significant differences between them in terms of separation, i.e., neither type of MGCS events are associated with branches that are exceptionally distant from the main channel of the return stroke.

Table 5.5 –Statistics of the estimated separation between ground contacts of MGCSs.

	Forked strokes	UI strokes	Overall
Number of observations	16	9	25
Arithmetic Mean (m)	1200	1250	1220
Minimum (m)	280	120	120
Maximum (m)	3800	3350	3800
Geometric Mean (m)	920	910	920

Statistical parameters of the horizontal distance estimates between ground contacts of each analyzed MGCS event for which there was an available LLS solution. These values must be seen as lower bound estimates for this parameter due to the fact that it was measured on the plane parallel to the camera sensor.

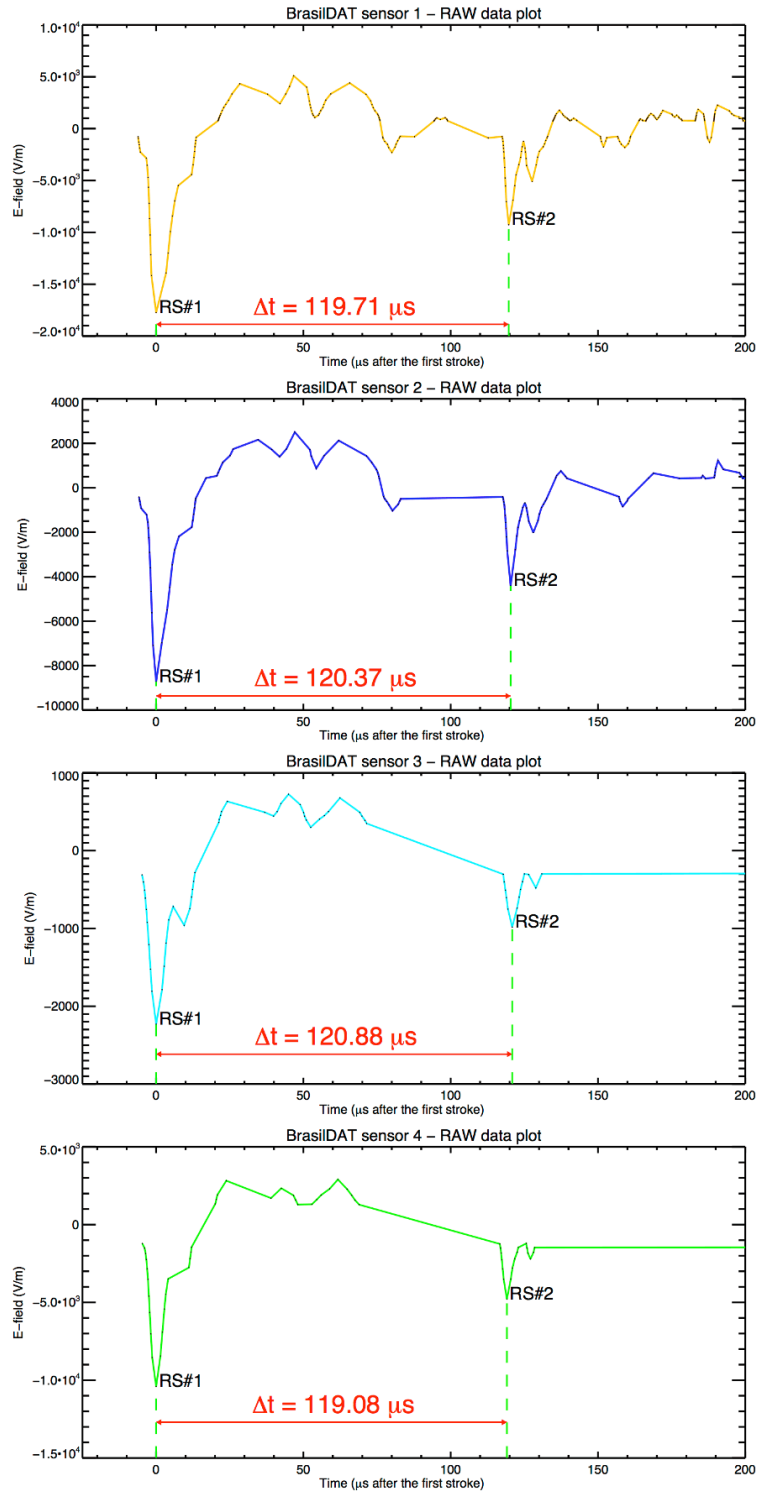
Source: produced by the author and coworkers, previously presented by Campos et al. (2014c) and Saraiva et al. (2014b).

5.5.4. Time interval between contacts

The high-speed cameras that compose the RAMMER network had frame rates of 2500 fps (with exposure times ranging from 330 to 390 microseconds), which means that any intervals between strokes within this time range would be impossible to estimate without the assistance of BrasilDAT sensor waveforms. The very short time interval makes it very difficult for a LLS to properly obtain solutions for both strokes of a MGCS. In this database only one UI stroke had both of its strokes (main and UI) detected by BrasilDAT, and probably not coincidentally these detections correspond to the UI event with the longest observed time interval in our sample (2.65 milliseconds).

As discussed in the case studies of section 5.3, raw electric field data obtained by BrasilDAT sensors were used in the evaluation of the time interval between contacts with a resolution of tens of nanoseconds. Each ENTLS sensor that composes BrasilDAT (NACCARATO et al., 2012) records the electric field waveforms for each stroke, all noise is eliminated and the remaining data is sent to the data processing central. Even though the network is unable to geolocate both pulses in most events, the raw electric field data includes the second peak of each MGCS, thus allowing the estimation of the interval between contacts. Information from several sensors has been used, with the amplitudes normalized by the peak field of the first stroke on the closest sensor to the location of the stroke solution. After normalization, data from all sensors were put side by side and the peaks that were present in all waveforms were chosen. The calculated time differences between those peaks were assumed to correspond to the individual contacts made by each MGCS. An example illustrating this analysis is presented in Figure 5.15 for a forked stroke with its waveforms stacked vertically. Table 5.6 presents the statistical summary of the intervals obtained for both classes of events. A very clear distinction can be seen between forked and UI strokes, with the UI presenting considerably larger temporal separations (with an average value more than ten times longer than what was observed for forked strokes). These differences and the corresponding distributions are further explored in the next subsection (5.5.5), along with another differentiating factor between each type of MGCS.

Figure 5.15 – Example of four raw BrasilDAT electric waveforms for a forked stroke.



Raw electric field waveform data provided by four different BrasilDAT sensors for a forked stroke event. The temporal separation between contacts is taken as their mean.

Source: produced by the author and coworkers, previously presented by Campos et al. (2014c) and Saraiva et al. (2014b).

Table 5.6 – Statistics on the time interval between contacts in forked and UI strokes.

	Forked strokes	UI strokes
Number of observations	16	12
Arithmetic Mean (μ s)	118.7	1392
Minimum (μ s)	5.31	254.1
Maximum (μ s)	554.3	2648
Geometric Mean (μ s)	44.4	1125

Statistical parameters of the temporal separation between contacts in both forked and UI events. The estimates were obtained from the combined analysis of the electric field waveforms of all BrasilDAT sensors that participated in the solution of the first (main) stroke of each event.

Source: produced by the author and coworkers, previously presented by Campos et al. (2014c) and Saraiva et al. (2014b).

5.5.5. Peak current estimates

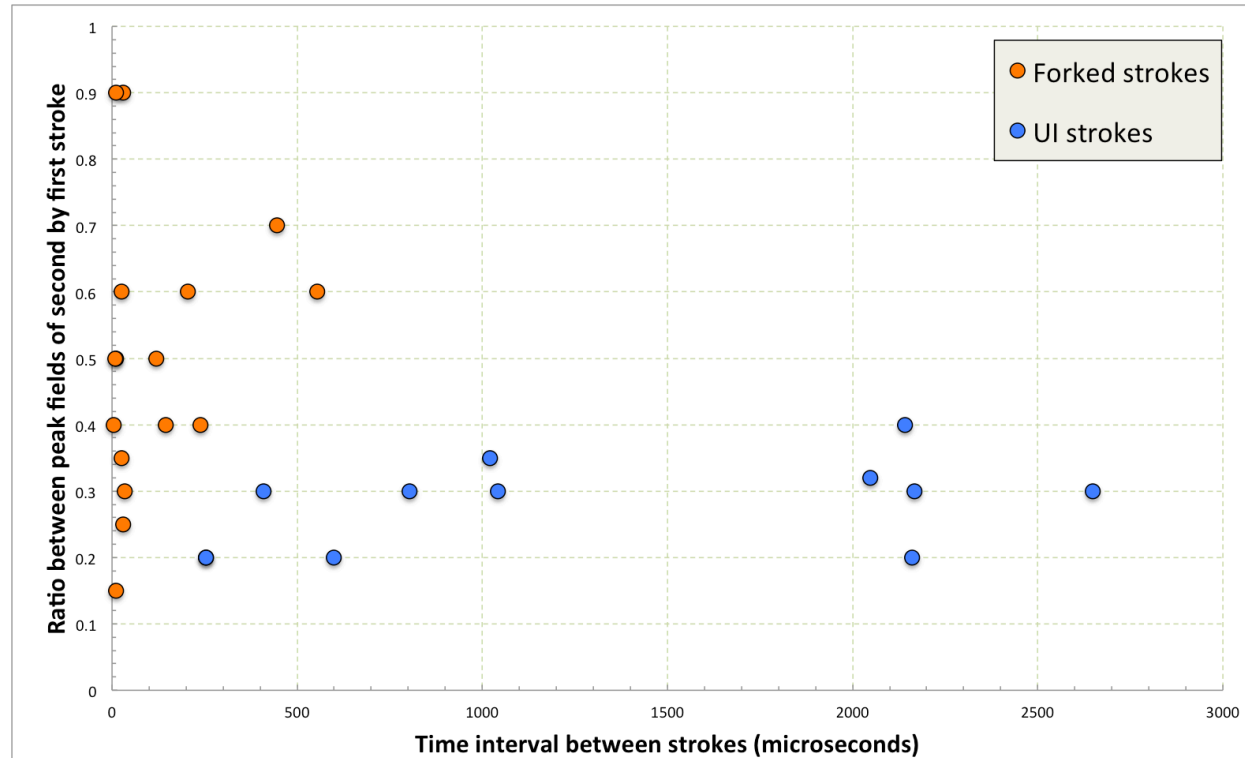
The short intervals between ground contacts in MGCSs makes it very difficult for LLS to locate them and, consequently, provide peak current estimates for both contacts. As commented in the previous subsection, Flash #65 observed on February 19th, 2013, was the only exception and had both its ground contacts reported by BrasilDAT. The interval between them was 2.65 ms, the longest of the dataset (considering both forked and UI strokes). As expected, the estimated peak current of the UI was lower than that of the main discharge by a factor of four (–33 kA for the first contact and –8 kA for the second, UI contact). For the other MGCSs, their estimated peak current values of their second ground contacts were estimated from the raw waveform data retrieved from BrasilDAT sensors. Initially, for each forked and UI stroke the ratio between the peak electric fields of the second over the first contact was calculated. Then, considering that the distance between them is small when compared to their distance to any of the BrasilDAT sensors, it is assumed that the second peak current can be obtained by multiplying the ratio of each MGCS by the peak current estimate of its first (detected) contact. This assumption was tested for Flash #65: the ratio between the electric field peaks was 0.3, and multiplying this by the first stroke peak current estimate (–33 kA) yields a peak of –10 kA for the second (UI) contact. This estimate is 2 kA (25%) greater than what was reported, so these estimates must be viewed with some caution.

Figure 5.16 shows a plot of the calculated ratios *versus* the time interval between the contacts of each MGCS. Blue circles correspond to the UI strokes and orange circles represent the forked strokes, as identified solely by the video records (following the characteristics outlined in section 5.4). There is a clear separation between the two types of MGCS: UI strokes tended to have larger intervals compared to forked strokes (as discussed in the previous subsection) and, generally, peak fields lower than 40% of the peak values of their corresponding main strokes. On the other hand, forked strokes barely crossed the barrier of 400 microseconds of interval between contacts and the peak electric fields of their second contacts can be as high as about 90% of the peak values of their first contacts. It is also worth noting that forked strokes with small ratios (below 0.4) also presented very short interval between contacts. It is possible that these are related to measurement errors, as the visual identification of both peaks may be difficult when they are very close.

Figure 5.17 presents the same data points but with respect to the calculated peak currents for the first and second contacts (estimated from their ratios). All peak currents are in absolute values, but all MGCS are of negative polarity. The vertical bars represent each MGCS, their upper limit corresponding to the main stroke and the lower to the second contact. One important feature is the fact that the second peaks of all UI strokes were lower than 10 kA, independently of the value of their main stroke.

Stolzenburg et al. (2013b, Table 1) presented mean values of the time intervals (1.5 milliseconds for 20 events) and current peaks (−14.5 kA for 16 main strokes and −5.0 kA for 14 UIs, yielding a ratio of 0.34) that are in agreement with what is shown in Figure 5.16. Also, the two UI events observed by Sun et al. (2016, Table 1) are in agreement with the results of the present work: ratios of 0.23 and 0.35 associated with intervals of 1.5 and 2.7 milliseconds, respectively.

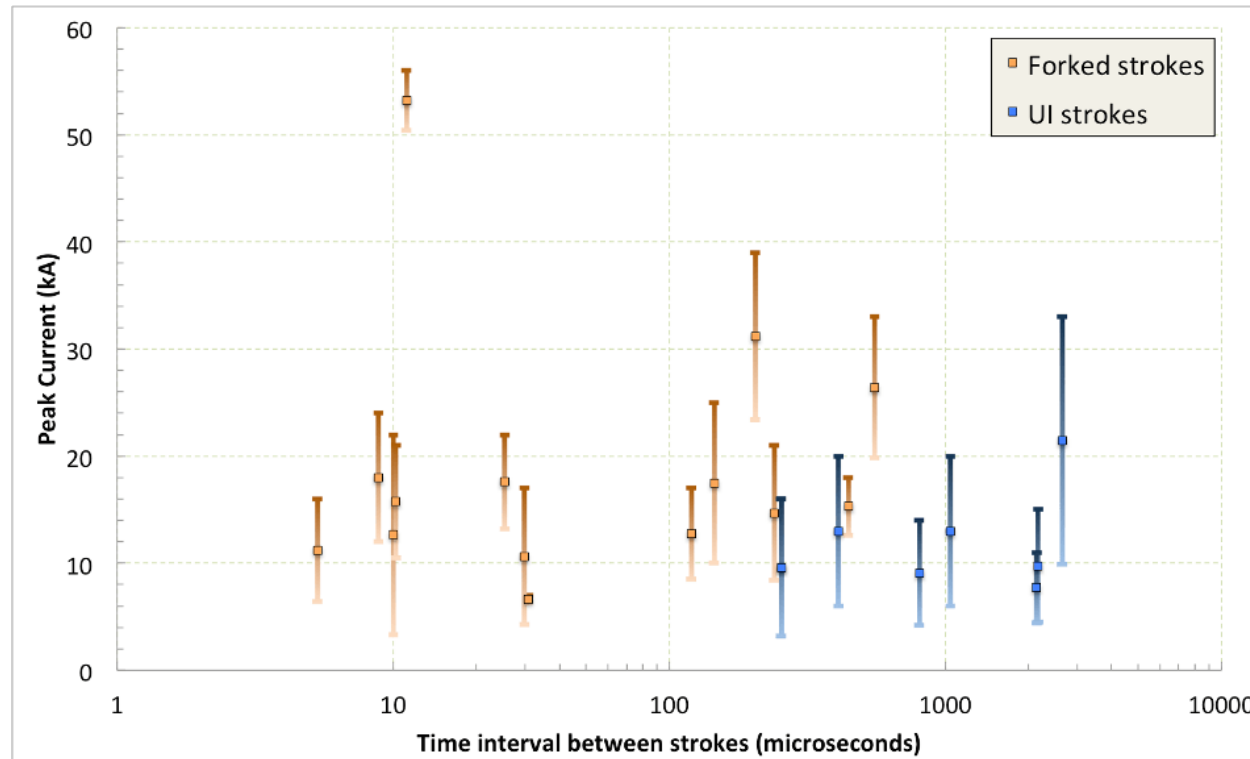
Figure 5.16 – Ratio between electric field peaks *versus* time interval between them for the ground contacts of each MGCS event.



The ratios correspond to the peak of the first (main) stroke over the second contact and the intervals correspond to the period between them. Orange circles correspond to forked strokes and the blue circles to UI events (as classified by visual inspection).

Source: produced by the author and coworkers, previously presented by Campos et al. (2014c) and Saraiva et al. (2014b).

Figure 5.17 – Estimated peak current pairs *versus* time interval between them for the ground contacts of each MGCS event.



The upper and lower values of the vertical bars correspond to the main (first) and second ground contacts on each MGCS and the time intervals correspond to the periods between them. Orange bars correspond to forked strokes and blue bars to UI events (as classified by visual inspection).

Source: produced by the author and coworkers, previously presented by Campos et al. (2014c) and Saraiva et al. (2014b).

5.6. Relative incidence of flashes with MGCS

Table 5.7 presents a summary of two parameters analyzed in the present work (percentage of MGCS over all flashes and time interval between contacts) in perspective with what has been previously reported in other studies. Part of the variability between studies (particularly Rakov and Uman, 1994, and Kong et al., 2009, with incidences above 15%) is in agreement with our day-to-day results (which ranged from 7.3% to 14.9%, as shown in Table 5.1). The percentage that was found when all five days are combined (9.7%) is very similar to not only the percentage reported by Willet et al. (1995), 9.4%, but also with what was reported by Stolzenburg et al. (2013b), who had only considered flashes with UI stroke. It is important to note that none of the individual days of the present work had percentages as low as those reported by Schonland et al. (1935), Guo and Krider (1982) and Ballarotti et al. (2005). Considering that the latter is based on observations conducted in the same region of our analysis, however, it is possible that this discrepancy is due to limitations in the instruments available at the time. Particularly the high-speed camera that was operated then, with a frame rate of 1000 fps, was frequently saturated at the return stroke frame, probably rendering a significant part of the forked strokes undetectable. Additionally, electric field records were available only for a limited number of events from their dataset, limiting the identification of multiple terminations in those saturated return strokes.

Another relevant result not only of the present work but all other preceding studies is the very short interval between ground contacts in MGCS and the inability of VLF/LF LLS to locate all of them. One may argue that nearly 10% of all –CG flashes have one or more GCPs that are like “ghosts” to LLS. In the database of the present work, the 35 analyzed flashes with MGCS (both forked and UI) developed a total of 109 different GCPs among all their strokes, with 40 of them produced by MGCSs (corresponding to about 37% of all GCPs of those 35 flashes). Considering the complete RAMMER summer 2013 database, a total of 647 ground strike points were observed (75 single-stroke flashes plus 286 multi-stroke flashes with a mean number of GCPs of 2.0, as reported by Antunes et al., 2015), this means that about 6.2% of all observed GCPs were produced by MGCS. Some may argue that such a percentage is high enough to be

taken into account in the design of future lightning location and protection techniques and devices.

Table 5.7 – Summary of previous studies on forked and upward illumination strokes.

Study	Location	Sample size (flashes)	% of MGCS flashes	Time between contacts (ms)
Schonland et al. (1935)	South Africa	1/95	1.1%	0.073
Guo and Krider (1982)	NASA Kennedy Space Center, FL, USA	5/246	2.0%	0.046-0.110
Rakov and Uman (1994)	Tampa, FL, USA	15/79*	19.0%	0.015-3.335
Willett et al. (1995)	NASA Kennedy Space Center, FL, USA	3/32	9.4%	0.007-0.010
Wang et al. (2000)	Camp Blanding, FL, USA	1	-	0.0002
Qie et al. (2005)	Qinghai-Tibetan Plateau, China	1 [‡]	-	0.004-0.010
Ballarotti et al. (2005)	São José dos Campos, SP, Brazil	6/455	1.3%	0.031-< 2
Kong et al. (2009)	Four cities in China	9/59	15.3%	0.004-0.486
Stolzenburg et al. (2012)	NASA Kennedy Space Center, FL, USA	4 [§]	-	0.519-1.858 (UI only)
Stolzenburg et al. (2013b)	NASA Kennedy Space Center, FL, USA	18/170	10.6%	1.25 (UI only)
Sun et al. (2016)	Binzhou, Shandong, China	1 [†]	-	1.5-2.7 (UI only)
Present work	São José dos Campos, SP, Brazil	35/361	9.7%	0.126 (forked) 1.39 (UI)

* two of the fifteen events did not have electric field records, and only nine (out of the remaining thirteen) presented two return stroke field waveforms.

[‡]a single MGCS with four ground terminations, the range of interstroke intervals corresponds to the three pairs of successive contacts.

[§]there is no information on the proportion of flashes with UI-strokes over the entire recorded dataset.

[†]a single flash presented two UI-strokes.

The sample size is presented in terms of number of flashes with MGCSs/total number of flashes (when available). Information on interstroke intervals consists of either the mean (if only one number is given) or range of values.

Source: produced by the author and coworkers based on a literature review, partially presented by Campos et al. (2014c) and Saraiva et al. (2014b).

5.7. Concluding remarks

In February and March 2013, the RAMMER network registered five days of thunderstorm activity with sufficient data to allow the study of each day individually. A significant number of the observed flashes presented multiple ground contact strokes (MGCS), with a daily incidence that ranged from 7.3% to 14.9% (Table 5.1). Based on previous results in literature and the clear differences in their video records (section

5.4), the MGCSs were divided into two classes: forked and UI (upward-illumination) strokes. Several analyzes were performed, allowing the basic characterization of the phenomenology of each class of event and their differing features.

The time intervals of forked strokes ranged from 5 to 554 microseconds, in agreement with those found in literature (Table 5.17). However, Figure 5.17 shows that only two events had intervals greater than 300 microseconds. In datasets with no discrimination between forked and UI it is, therefore, likely that larger intervals were actually associated with UI strokes (e.g., Rakov and Uman, 1994, whose range extended above 3 ms, as shown in Table 5.17).

Horizontal separations between contacts that were estimated from the video frames (with means around 1200 meters) were considerably small, even with errors associated with perspective (as only the distance parallel to the camera sensors could be considered). None of these events presented one-dimensional separations greater than 4 km (Table 5.5). These distances are particularly low when compared to the results that are presented later in the thesis (Chapters 6 through 8) for regular subsequent stroke NGCs. This is probably related to lower altitude forking points in MGCS when compared to the various mechanisms observed in regular multi-grounded flashes, as discussed particularly on Chapter 6.

The non-uniform luminosity observed in UI channels may be related to a discontinuity in conductivity régimes. The analysis of the temporal evolution of leader speed analysis show that the UI branch slows down (compared to the main stroke branch) near ground until contact is made (Figures 5.7 and 5.11). This behavior may be caused by a progressive reduction of the charge density in the UI channel as it continues to extend towards ground without additional charges being provided by the main stroke channel (due to the aforementioned discontinuity). Also, in Flash #85 (subsection 5.3.2.2) it is shown that a later downward moving attempted leader develops into its UI branch, interrupting its propagation below the highest point reached by the UI process (see Figures 5.9 and 5.10). These characteristics, combined with the fact that false color imagery show that there is a faintly luminous channel between the UI branch and the

forking point of all analyzed events, suggest that there is not always complete cutoff from the main trunk of the flash and the UI branch. This does not contradict the idea presented by Stolzenburg et al. (2012, 2013b) that the UI channel is “effectively cutoff” from the main trunk. Actually, the false color imagery shown earlier in the present chapter corroborates what is stated in their more recent work, that “with appropriate optical data, an effectively cutoff gap along a leader could take the form of very dim or no observable luminosity over some portion of the UI leader length” (STOLZENBURG et al., 2013b, p.7185).

6 FORMATION MECHANISMS OF NEW CONTACT POINTS IN SUBSEQUENT STROKES: CASE STUDIES AND INTERPRETATION

This chapter summarizes a few selected case studies that were conducted on multiple ground contact flashes observed during the KSWFP in 2013. Some common patterns among groups of those events lead to the introduction of three possible classes of scenarios/mechanisms through which a subsequent stroke can create a new ground termination. Two examples of each class are discussed (each one with distinguishing characteristics) before a general description is provided. At the end, two unique events are also briefly presented.

6.1. Methodology

This work consisted of two main phases of event selection for the case studies. In the first phase only events with video data (either standard or high speed) were considered, choosing those for which the creation of new ground contact strokes (NGCs) was unambiguously identified. After the initial video analysis, data from the Lightning Mapping Array (LMA), the electric field antennas and the U. S. National Lightning Detection Network (NLDN) were organized and compared in time, matching the occurrence of each return stroke. The author developed dedicated software (written in MATLAB) that provided an animated visualization of the LMA data, facilitating the identification of the development of lightning channels between return strokes. In this first phase, only six multiple ground contact flashes (MGCFs) were selected, two observed by high-speed cameras only, three by standard speed cameras only and one observed by both standard and high speed.

Given this very limited sample, a computational search of the NLDN dataset was conducted in order to increase the number of analyzed MGCFs. Experience gained from the cases with video data provided the necessary background to evaluate these new cases. The first step was processing NLDN data for the entire period of the KSWFP with the *groupGCP* algorithm, then filtering them using two criteria: (i) flashes that had at least two GCPs identified; and (ii) flashes whose first stroke occurred no more than 2.5 kilometers from at least one of the LMA and electric field sensors of the KSWFP

network. Over 60 flashes were found at this point, and then a more strict selection was conducted by seeing if the number of VHF sources detected by the LMA were sufficiently large to allow not only the clear tracking of in-cloud development of the flashes but also to confirm the *groupGCP* output data. This step needed to be very strict due to the lack of video data to back the GCP information derived from the NLDN dataset, and only 17 additional flashes were selected in this second phase.

All case studies followed the same four basic steps when the LMA data was analyzed: (i) grouping each return stroke to its respective GCP (based on either video or NLDN data only); (ii) producing LMA animations for the full flash, identifying its overall in-cloud development; (iii) “slicing” that animation into shorter ones, comprised of the initiation of the first stroke and then for each one of its interstroke intervals; (iv) identifying the inception point of each leader-return stroke process and seeing not only how they change between each subsequent return stroke but also how the in-cloud branches evolved during the interstroke intervals. Once this was concluded, the electric field records were analyzed for the period preceding the creation of a new ground termination, with particular interest in searching for the field changes described by Krehbiel (1981) and mentioned in subsection 2.5.2 of the literature review.

From the sample of 23 MGCFs (six from the first phase and seventeen from the second), a total of 33 processes of NGC creation were analyzed and some common patterns were observed, leading to the description of three basic scenarios/mechanisms. Each type of scenario is illustrated by two case studies briefly presented in the next subsection, followed by a description of our interpretation of the LMA data and a summary of the main common characteristics observed among all events that were classified into each type.

6.2. Case studies and their interpretation

6.2.1. Type I: Altered channel

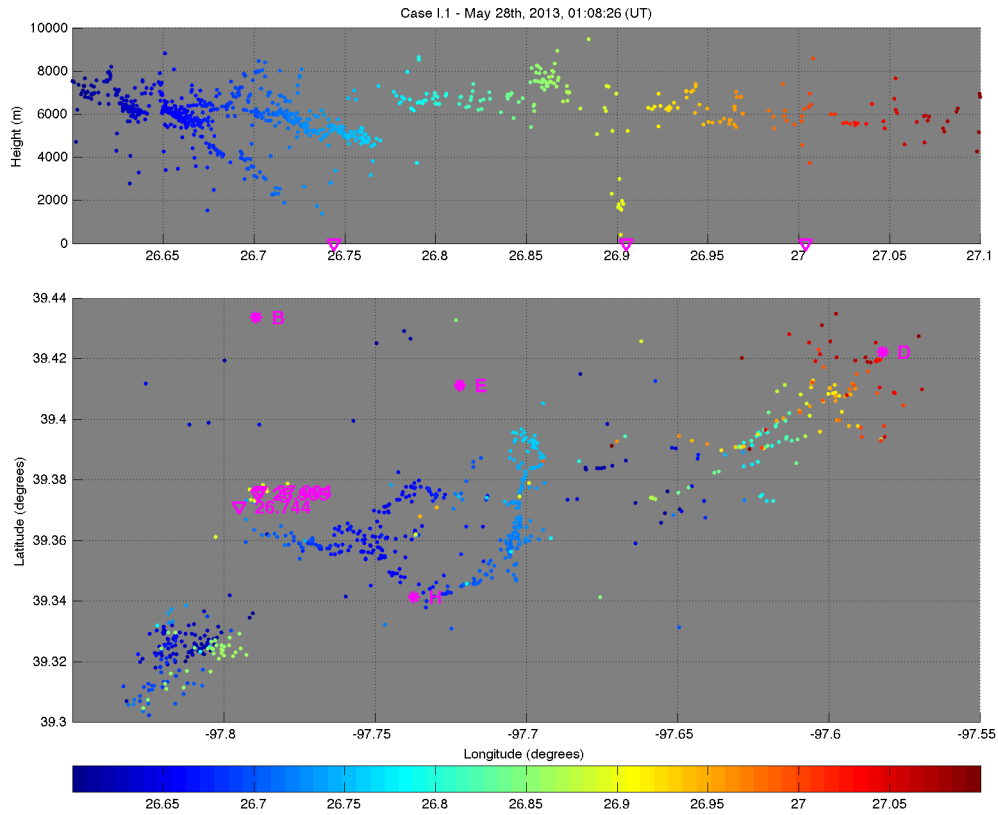
Type I was observed in six of the 33 NGC initiations that were analyzed. Despite being the least common type among all three, it was the first to be identified, as the LMA records were the simplest to interpret with no *a priori* assumptions.

6.2.1.1. Case I.1: May 28th, 2013, 01:08:26 (UT)

The first example of NGC creation of Type I was observed in May 28th, 2013 at 01:08:26 (UT) and was recorded by a high-speed camera at 1000 fps. It produced three return strokes, with the second one creating a NGC that was then followed by the third stroke as well and was located about 750 meters away from the first stroke GCP. Figure 6.1 presents an LMA plot of the VHF sources that composed the entire flash.

Figure 6.2 shows the initiation of the first stroke of Case I.1. It was preceded by some VHF sources located at the southwest corner of the bottom panel, but its leader development came later (around time 26.65 s), moving bidirectionally (one branch moving west and towards ground and two branches moving horizontally towards east). Ground contact was made at 26.744 seconds (shown by the magenta triangle on the bottom view). The first stroke was followed by a short continuing current (about 11 ms long) and had an estimated peak current of -14.2 kA.

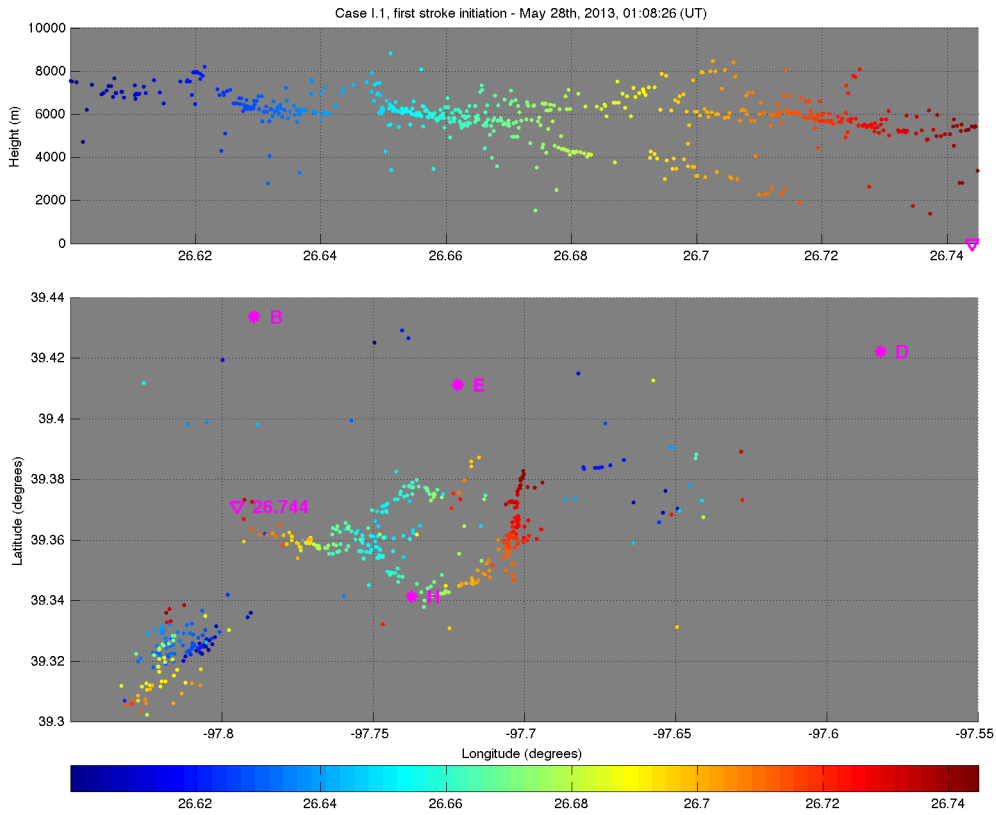
Figure 6.1 – Full flash LMA plot of Case I.1.



VHF source height *versus* time (top panel) and top-view latitude *versus* longitude (bottom panel) of the LMA data of Case I.1. Each source is color-coded according to its time of occurrence (dark blue for the earliest and dark red for the latest sources). Time and location of the strokes detected by the NLDN are shown as down-pointing magenta triangles and the magenta asterisks show the relative location of the VHF and electric field sensors.

Source: produced by the author.

Figure 6.2 – LMA plot of the initiation of the first stroke of Case I.1.



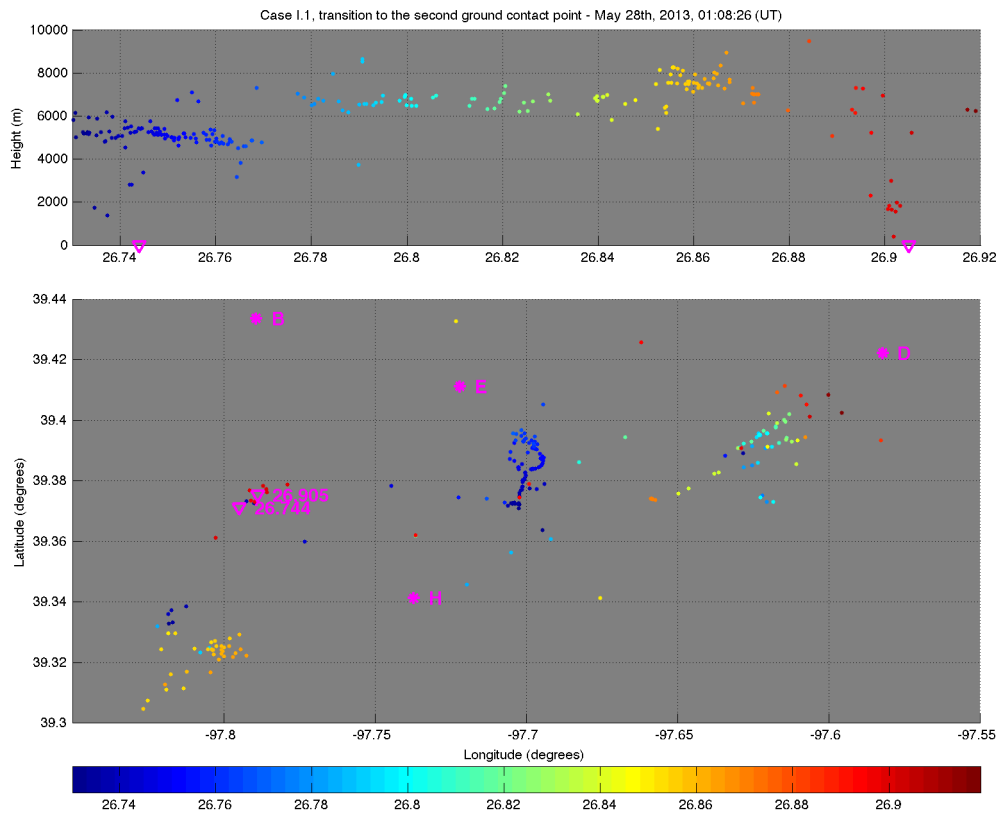
See description of Figure 6.1.

Source: produced by the author.

The development between the first and second strokes of Case I.1 is shown in Figure 6.3. A branch that was moving north (shown in dark blue) had its development interrupted, but other branches continued to move east. The visible “gap” of VHF sources seen in the bottom panel is probably related to the fact that it is a positive leader, so the main source of radiation detectable by the LMA is related to the occurrence of recoil leaders (RLs). One of these RLs give rise to a downward moving dart leader around 26.89 s (red sources), which is also mostly VHF-silent until it leaves the original channel to ground (created by the initial leader of the first stroke), producing the red VHF sources seen below 3000 m at the top panel. If one compares their colors with the sources that are close to the magenta triangles of the bottom panel, it is possible to relate them to the transition between dart and stepped leader, which

emits more VHF radiation and can ionize new lightning channels to ground. The second stroke is then initiated at 26.905 s, with an estimated peak current of -32.8 kA, over two times more intense than its preceding return stroke.

Figure 6.3 – LMA plot of the initiation of the second stroke (NGC) of Case I.1.



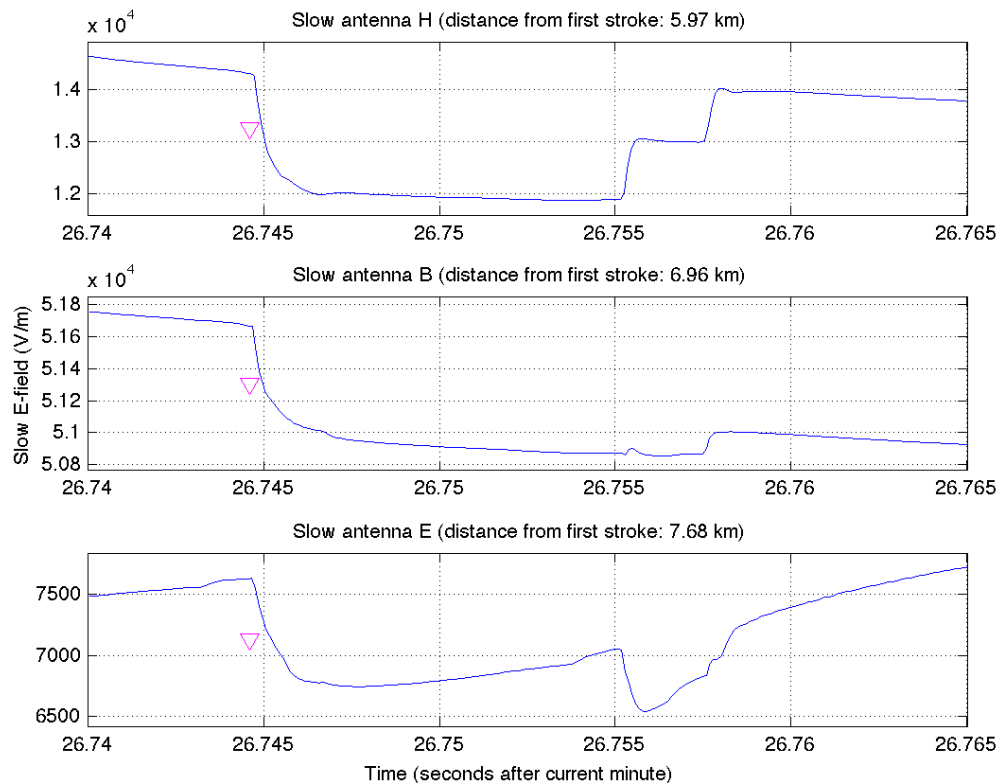
See description of Figure 6.1.

Source: produced by the author.

The slow electric field waveforms corresponding to the interstroke interval between the first and second strokes were analyzed and presented in Figure 6.4 (for the three closest sensors). A noticeable field change is observed after 26.755 s in all three sensors, coinciding with the end of the continuing current observed from the high-speed video data. From the record of the closest antenna (H, 5.97 km from the first stroke GCP), it is identified as two short duration steps occurring over a period of 3 milliseconds, the first lasting 500 microseconds and the second 600 microseconds. The ratios of their

amplitudes over the amplitude of the first stroke were 0.50 (for the first step) and 0.43 (for the second), causing the field level to become very close to what it was prior to the stroke.

Figure 6.4 – Slow electric field waveform of the interval between the first and second return strokes of Case I.1.



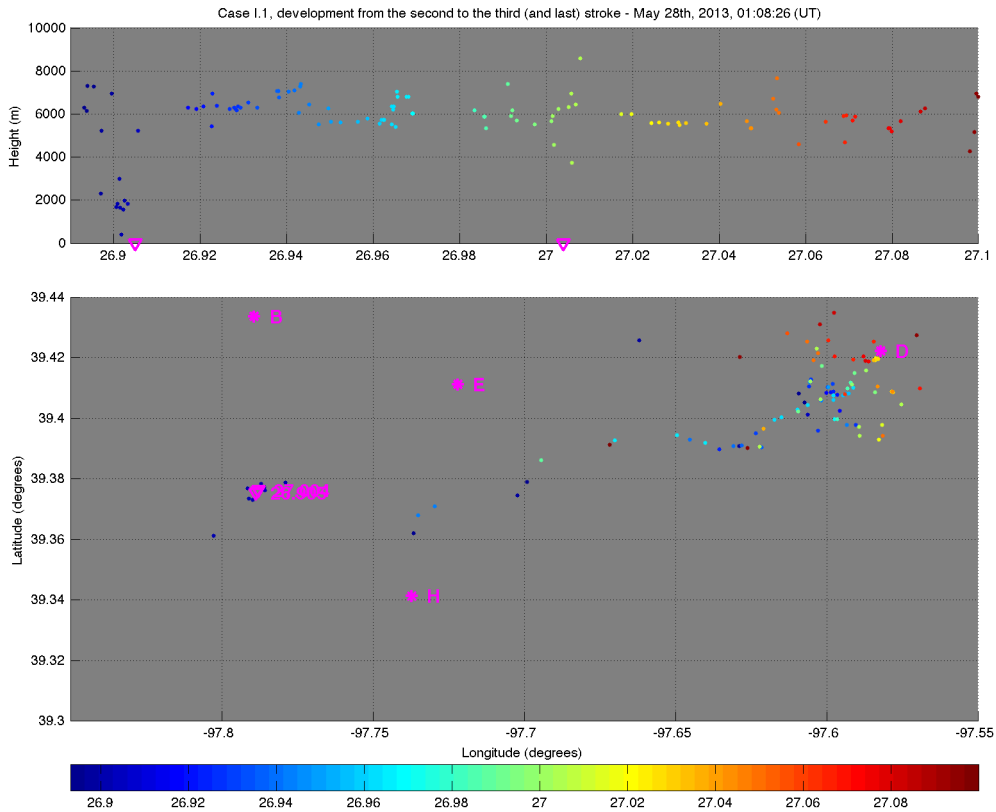
Down-pointing magenta triangles indicate the time of occurrence of the first stroke of Case I.1.

Source: produced by the author.

The remainder of the flash development is shown in Figure 6.5, following the interval between the second and third strokes and then its end. After the second stroke the in-cloud branches continued to develop towards east. Video record indicates that they had continuing currents that lasted 27 ms (second stroke) and 106 ms (third), with the latter being associated with the very late channel development (yellow, orange and red sources of Figure 6.5). The third stroke had an estimated peak current of -11.6 kA. Note

the large horizontal extension between the strike points and the eastern extreme of the in-cloud channels, which are associated with the continuous development of a positive leader, visible to the LMA only through the RLs that occur in its branches.

Figure 6.5 – Development of Case I.1 after its second stroke.



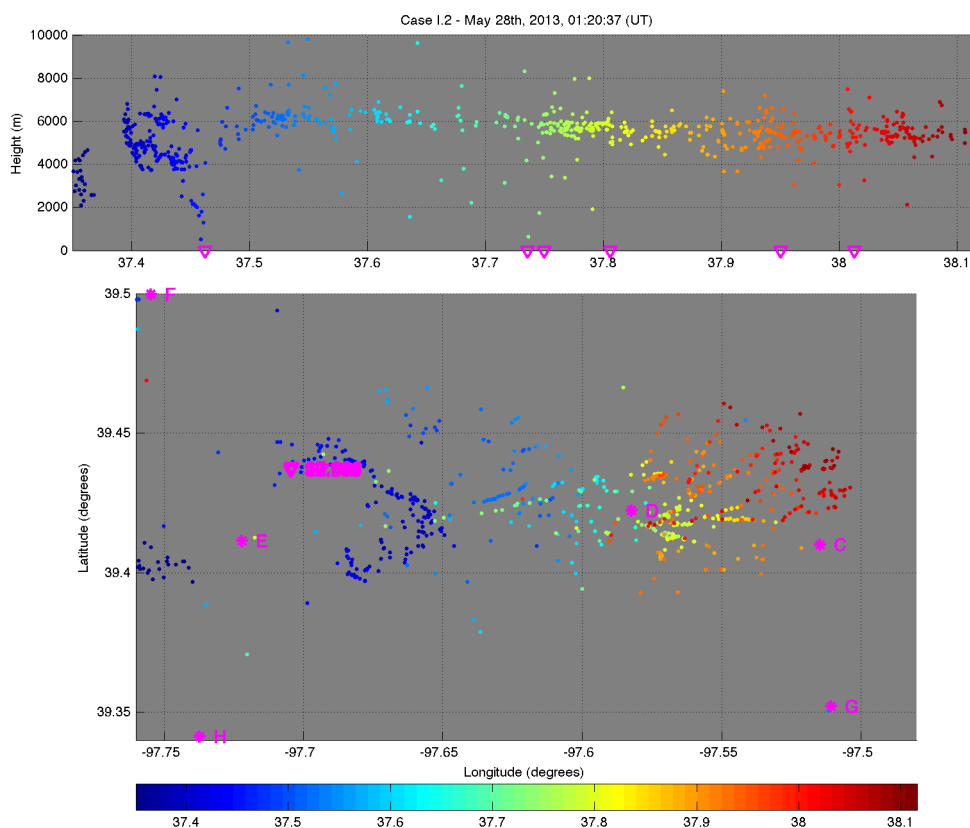
See description of Figure 6.1.

Source: produced by the author.

6.2.1.2. Case I.2: May 28th, 2013, 01:20:37 (UT)

The second example of Type I NGC creation occurred on the same day, May 28th, 2013, only a twelve minutes later at 01:20:37 (UT). Case I.2 produced a total of six return strokes, all of them recorded by one standard speed camera and one high-speed camera (at 35,000 fps). Its full flash development observed by the LMA is shown in Figure 6.6.

Figure 6.6 – Full flash LMA plot of Case I.2.



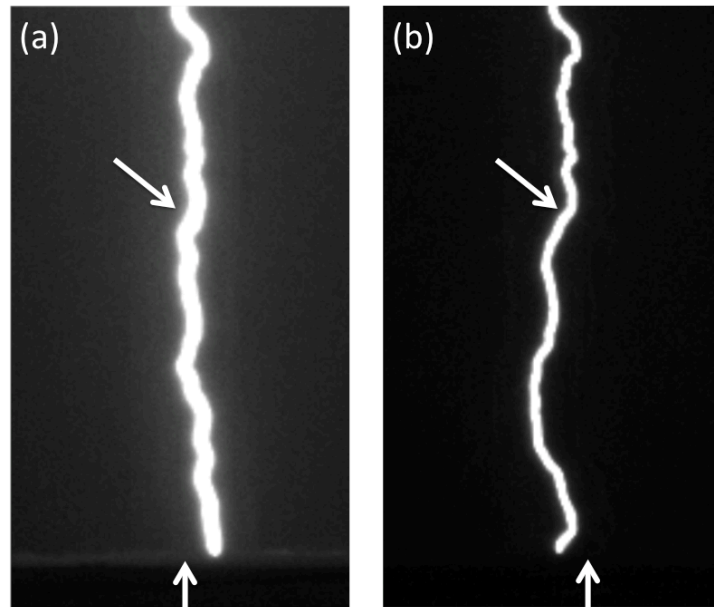
See description of Figure 6.1.

Source: produced by the author.

Analysis of the high-speed video data for Case I.2 conclusively showed that the second stroke produced an NGC that was followed by all other subsequent strokes, even though their strike points were very close in the video (shown in Figure 6.7). The NLDN solution error ellipses of all strokes were overlapping, and the *groupGCP* algorithm was incapable of differentiating them (note that all magenta triangles seem to overlap almost perfectly on the bottom plot of Figure 6.6). Considering that all error ellipses had semi-major axis (SMA) values of 0.2 km (the minimum value provided by NLDN) and were all within 73 meters of the arithmetic mean of their positions, it is reasonable to assume that the separation distance between the two GCPs was less than 200 meters (possibly less than 100 meters, but it was not possible to obtain a better estimate with the available data). The two frames of Figure 6.7 shows not only the point at which the

channel of the second stroke diverged from the first (upper white arrows) but also the relative position of the other strike point (lower white arrows).

Figure 6.7 – Selected high-speed video frames of the first two strokes of Case I.2.

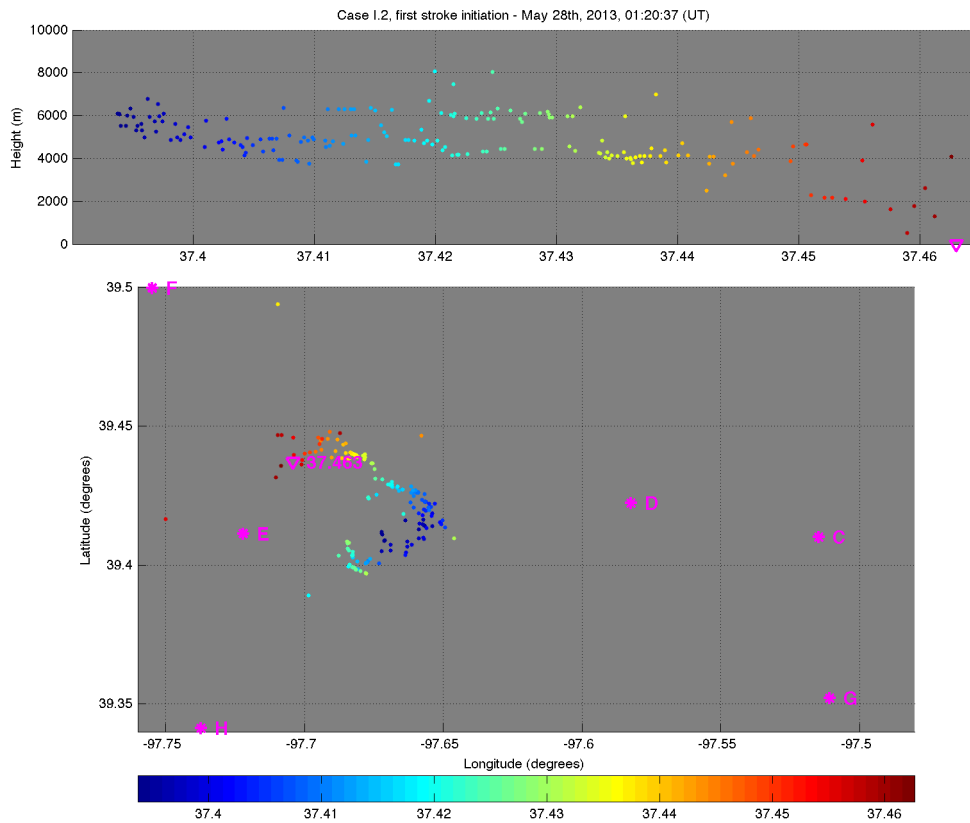


The selected high-speed video frames show the channel morphology of the (a) first and (b) second strokes of Case I.2. The upper white arrows on both frames show the approximate point from which the channel of the second stroke branched from the first. The lower arrows show the location of the strike point of the other stroke, i.e., the arrow on (a) corresponds to the strike point of the second stroke and the arrow on (b) to the first.

Source: produced by the author.

The first stroke occurred at 01:20:37.463 with an NLDN-reported estimated peak current of -14.0 kA. The VHF sources emitted during its initiation are shown in Figure 6.8. Note that channel development started at the dark blue sources in a bidirectional fashion, with upper, in-cloud sources emitted towards southwest simultaneously with the downward-propagating leader (towards northwest) that touched ground at the magenta triangle that indicates the first stroke occurrence.

Figure 6.8 – LMA plot of the initiation of the first stroke of Case I.2.



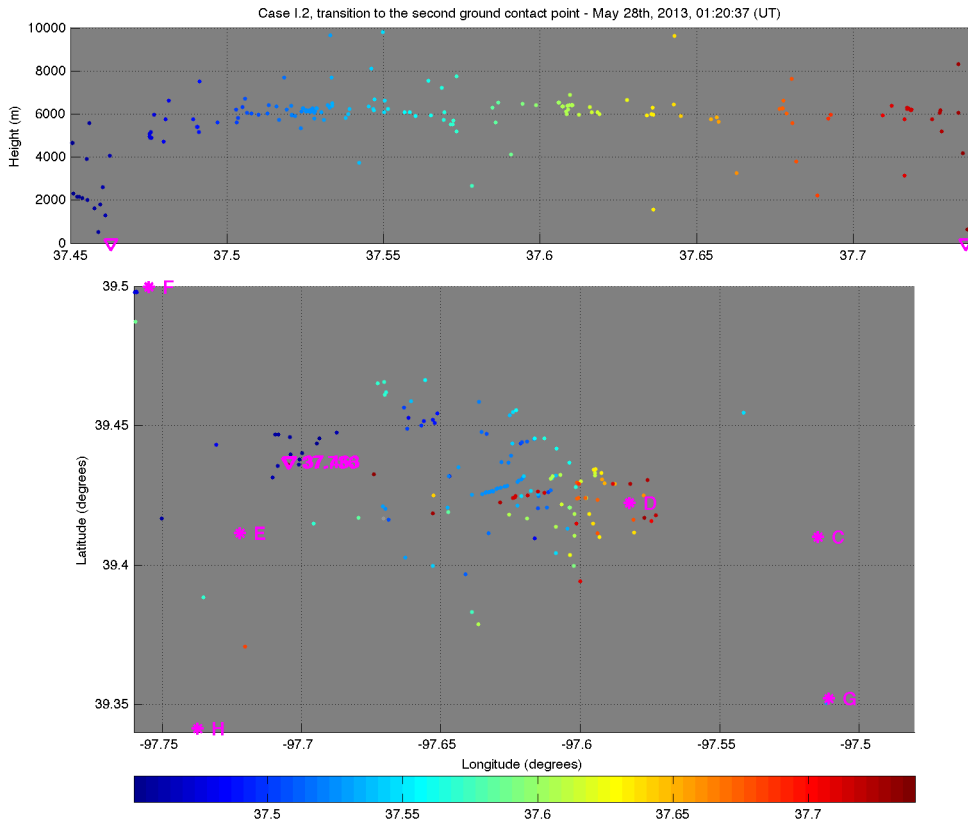
See description of Figure 6.1.

Source: produced by the author.

Video records indicate that the first stroke was followed by a long continuing current that lasted about 110 milliseconds. Then, at 37.736 s the second stroke occurred at a very close location, with its initiation shown at Figure 6.9 from the LMA data. As in Case I.1, the in-cloud development during the interstroke interval produced temporally sparse VHF sources. The sources show that the upper, positive portion of the leader channel kept propagating eastward from the inception region of the first stroke. The recoil-dart leader sequence that gave rise to the second stroke initiated at the eastern extreme of the channel, indicated by the red sources near sensor station D (magenta asterisk). The downward development remains VHF silent during most of its duration, until a single source was located about 600 meters above ground (possibly related to the divergence point shown in Figure 6.7). The second stroke was more intense than the

first by a factor of three, being reported by the NLDN with an estimated peak current of -42.1 kA, and video data suggest that it was followed by a short continuing current (14 ms long).

Figure 6.9 – LMA plot of the initiation of the second stroke (NGC) of Case I.2.



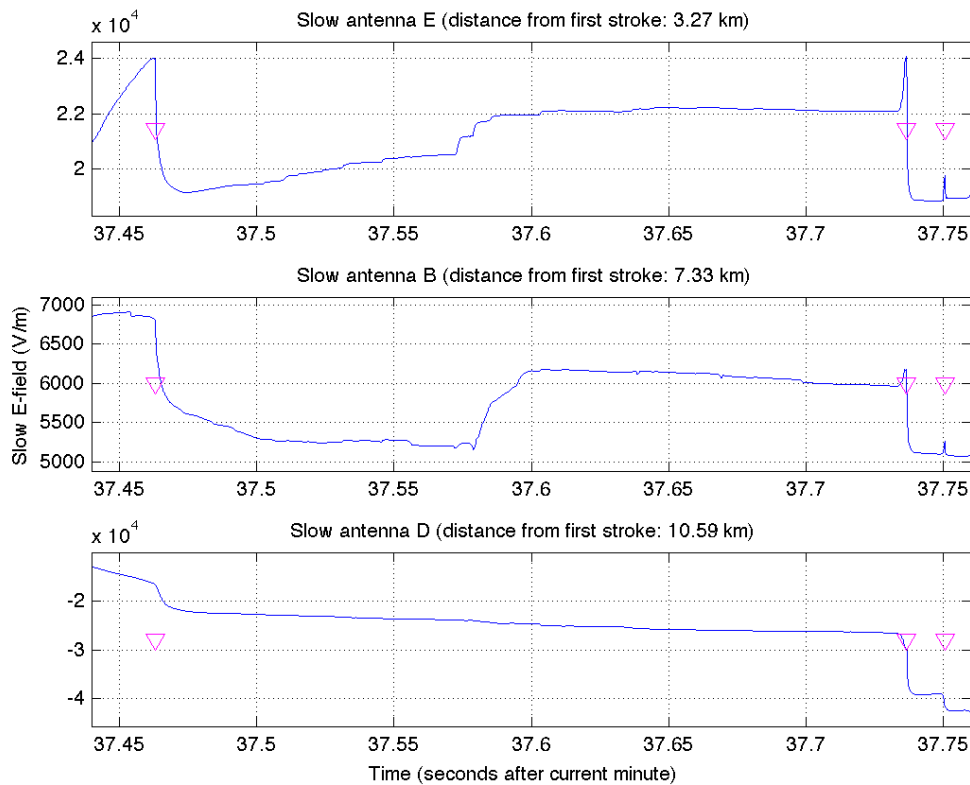
See description of Figure 6.1.

Source: produced by the author.

Figure 6.10 shows the electric field waveforms measured at the three sensors closest to the first stroke GCP (stations B, D and E) during the interval between leading to the second stroke. Similar to Case I.1 (Figure 6.4), at 37.5728 s two step-like field changes are clearly observed at station E (3.27 km away), coinciding with the end of the continuing current estimated from the high-speed video records. The steps presented durations of 1.2 ms and 0.8 ms and occurred over a period of 6 ms, but they were not as intense as the steps observed in Case I.1 when compared to their preceding return stroke

(presenting normalized amplitudes of 0.12 and 0.8). However, the corresponding field changes measured at station B were more intense, with a total normalized amplitude of 0.83, suggesting that there is a distance dependence in the waveforms. It is worth noting, however, that the exact timing and steepness of the two steps are not perfectly matched when data from both sensors are compared.

Figure 6.10 – Slow electric field waveform of the interval between the first and second return strokes of Case I.2.



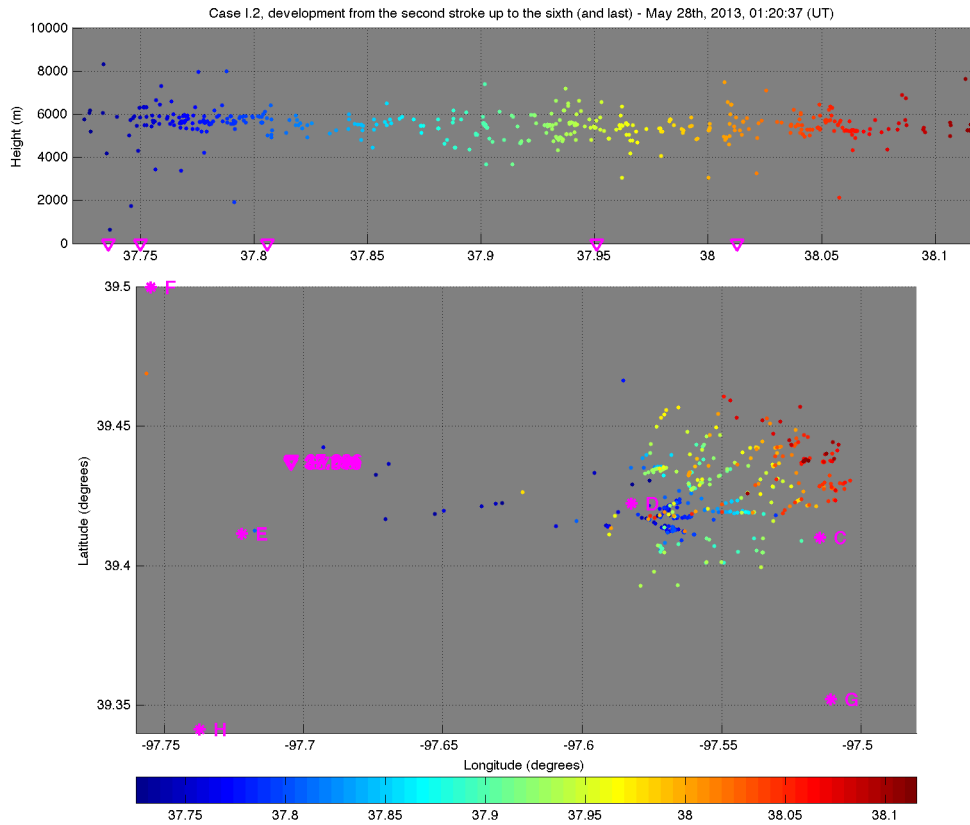
The down-pointing magenta triangles indicate the return strokes reported by the NLDN. From left to right, each triangle corresponds to the first, second and third strokes of Case I.2.

Source: produced by the author.

After the occurrence of the second stroke, the in-cloud channels continue to develop and branch eastward, as shown in the LMA plot of Figure 6.11. Each later subsequent stroke (up to the sixth and final stroke) is initiated by a recoil/dart leader sequence whose

inception point is at the farthest ends of the positive leader branches that move mostly horizontally at a 6 km height level.

Figure 6.11 – Development of Case I.2 after its second stroke.



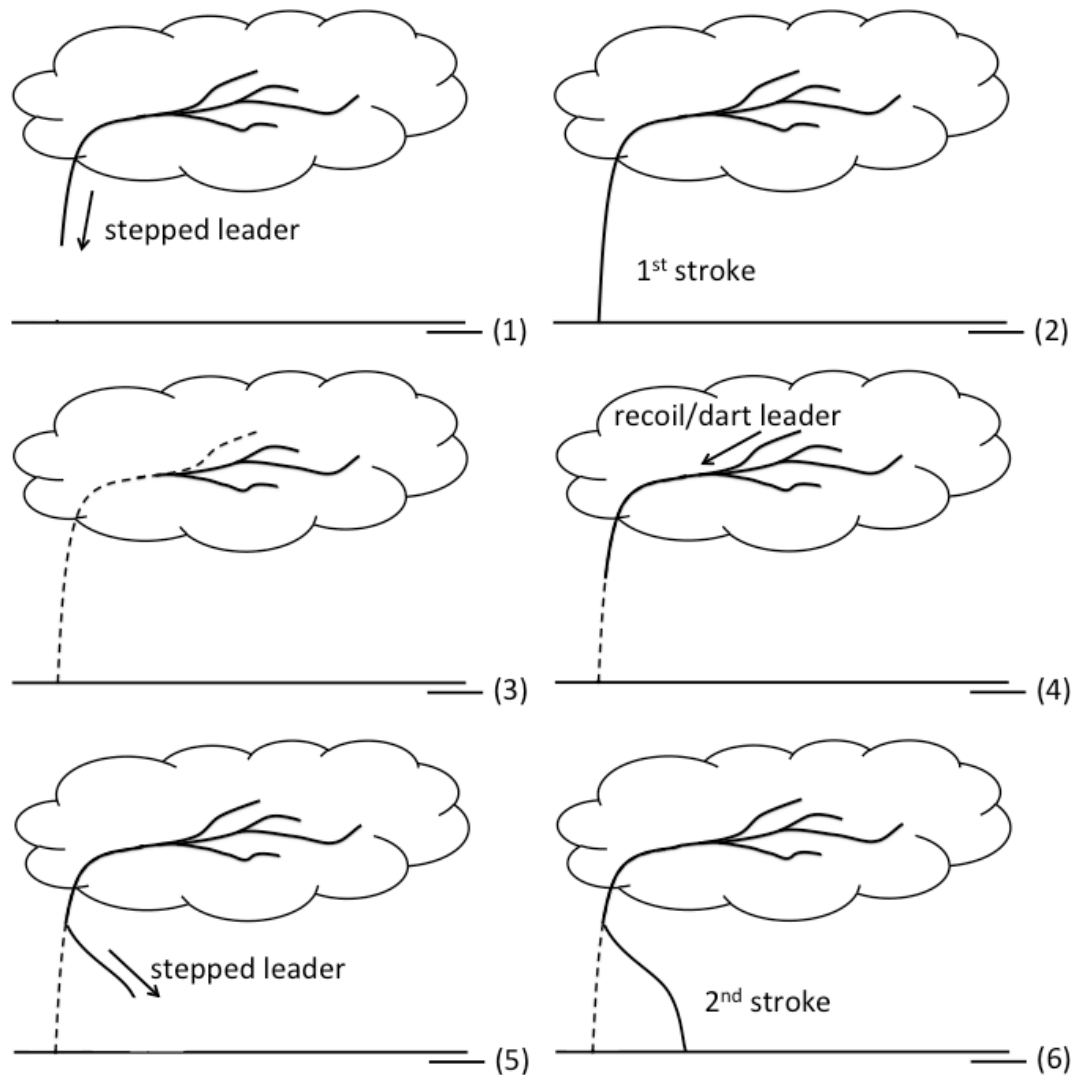
See description of Figure 6.1.

Source: produced by the author.

6.2.1.3. Type I conceptual scenario and mechanism

The interpretation of the common characteristics observed in six out of the 33 processes of creation of new ground contact strokes is illustrated in Figure 6.12. These are the six main steps identified in all the Type I events analyzed in this study.

Figure 6.12 – Illustration of the mechanism of a Type I new ground contact creation.



Source: produced by the author.

Following each element of Figure 6.12, Type I NGC events occur in –CG flashes that start with (1) a downward-moving stepped leader that initiates a plasma channel that lead to (2) the first return stroke. Later, (3) eventually channel current cutoff occurs in that channel (indicated by the dashed lines) as the in-cloud, positive end of the bidirectional leader process continues to develop mostly horizontally. After some time, (4) a recoil/dart leader sequence is initiated in one of the positive branches, retracing it and moving towards ground through the reminiscent conductive channels created by the initial leader. However, (5) at some point during the dart leader development, the leader

diverges from the channel of the first stroke and starts to propagate as a stepped leader, either ionizing a new plasma channel to ground or moving into an earlier branch that did not complete its development. Finally, (6) the second stroke occurs in the newly created channel, touching ground at a different location.

The very limited sample of Type I events makes it unclear whether or not there is a direct relationship between step-like changes observed at the end of the continuing current of the earlier stroke in the two case studies and this processes of NGC creation. Cases I.1 and I.2 are the only ones (among the six) for which high-speed video data were available, so it is unclear whether the other first strokes that preceded a Type I NGC were also followed by continuing currents (in case these are somewhat related to the changes), which may be ambiguous to identify and quantify in some slow electric field antenna records. Arguably, those two events support the idea by Krehbiel (1981) that there is the deposition of negative charges into the upper regions of the lightning channel, or, alternatively, stranded charges below the branching point where the NGC stroke diverged from the original channel. In either of these two scenarios, those charges would be responsible for reducing the potential difference that would drive the propagation of the dart leader of a subsequent stroke to retrace that original channel. However, only one other Type I event (that occurred in May 29th, 2013, at 16:13:48 UT) presented clear field changes preceding the NGC stroke, suggesting that this may not be a necessary condition for this type of strike point transition process to occur. Future studies, with a broader sample, may address this issue, gathering enough waveforms to allow detailed modeling of the charge deposition proposed by Krehbiel (1981).

Another common characteristic shared by Type I events is the relatively small distance between their ground contact points. Four out of the six events had separation distances that ranged from less than 200 meters (Case I.2) to 750 meters (Case I.1), with a mean value of 530 m (calculated by assuming that Case I.2 had exactly 200 meters between contact points). The other two events, however, had larger separations (estimated to be about 830 and 1134 meters) that may be related to higher divergence points. Their LMA records indicate that they diverged from the previous channel at 3 and 5 km above ground, even though their initiation is also associated with recoil leaders moving

towards the previously ionized channel (as seen in the other four events). In both cases there was some horizontal development of the stepped leader before its propagation turned towards ground, suggesting that the height at which the leader leaves the previously created path is highly influential on the separation distance from its strike point to the preceding one. This possible correlation should also be addressed in a future study with a larger sample of Type I NGC initiations.

6.2.2. Type II: New channel with common branches

Type II NGC creation process was observed in twelve of the 33 that were analyzed in the present study. It was found to be associated with the largest horizontal separations between ground contacts, given the nature of its in-cloud development. Two very distinct examples are discussed in this subsection.

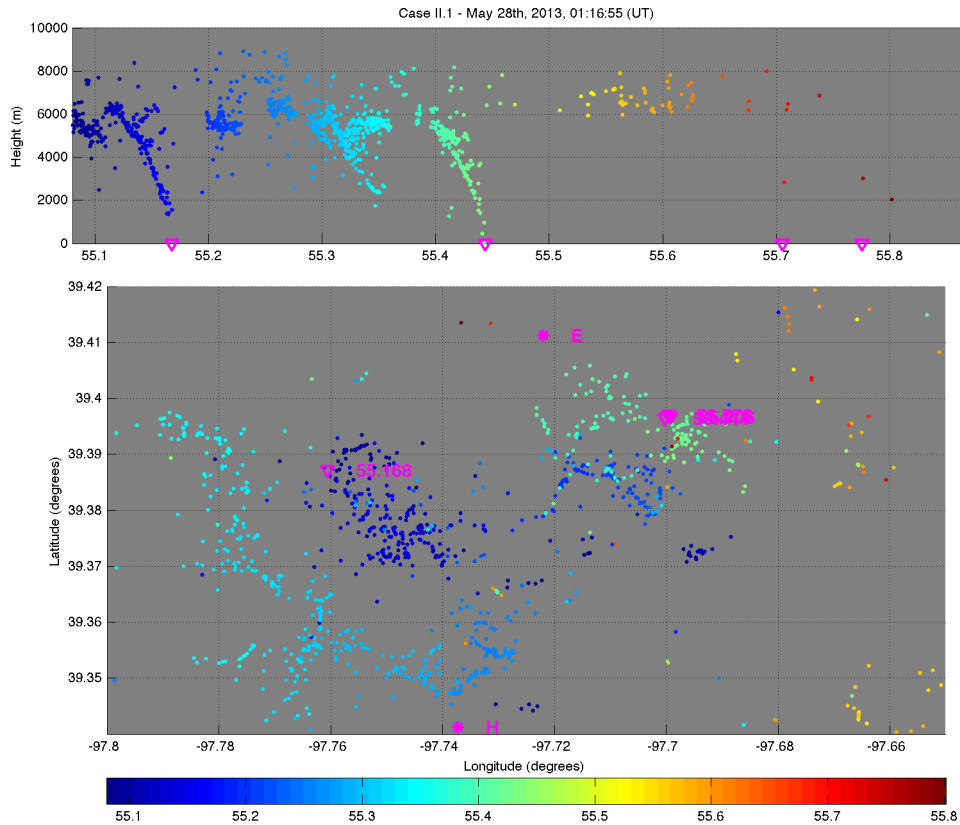
6.2.2.1. Case II.1: May 28th, 2013, 01:16:55 (UT)

The first example of Type II NGC initiation, Case II.1, was observed on May 28th, 2013, at 01:16:55 (UT) and produced a total of four return strokes. Only standard speed video, recorded at the substation (see Figure 3.20), was available and the first stroke GCP was the only one that could be unambiguously identified. However, even though excessive pixel saturation was present at the frames corresponding to the subsequent strokes, by contrast manipulation it was possible to conclude that none of them followed the path of the first stroke to ground. In this case, as the video data shows that the NGC is apparently a completely new and separate channel to ground, it would have been classified by Valine and Krider (2002) as a “new channel flash” (NCF, see Figure 2.8). All four return strokes were clearly identified in the NLDN, electric field and LMA data, allowing the confirmation that the second stroke was a NGC and that its path to ground was later retraced by the third and fourth strokes.

The full flash development observed by the LMA network is shown in Figure 6.13, giving an overview of the flash extent and in-cloud development. The horizontal separation between the two GCPs is 5.3 km, as estimated from the NLDN location

solutions. It is worth noting that this distance is much larger than the distances observed in all Type I events analyzed in the present study.

Figure 6.13 – Full flash LMA plot of Case II.1.



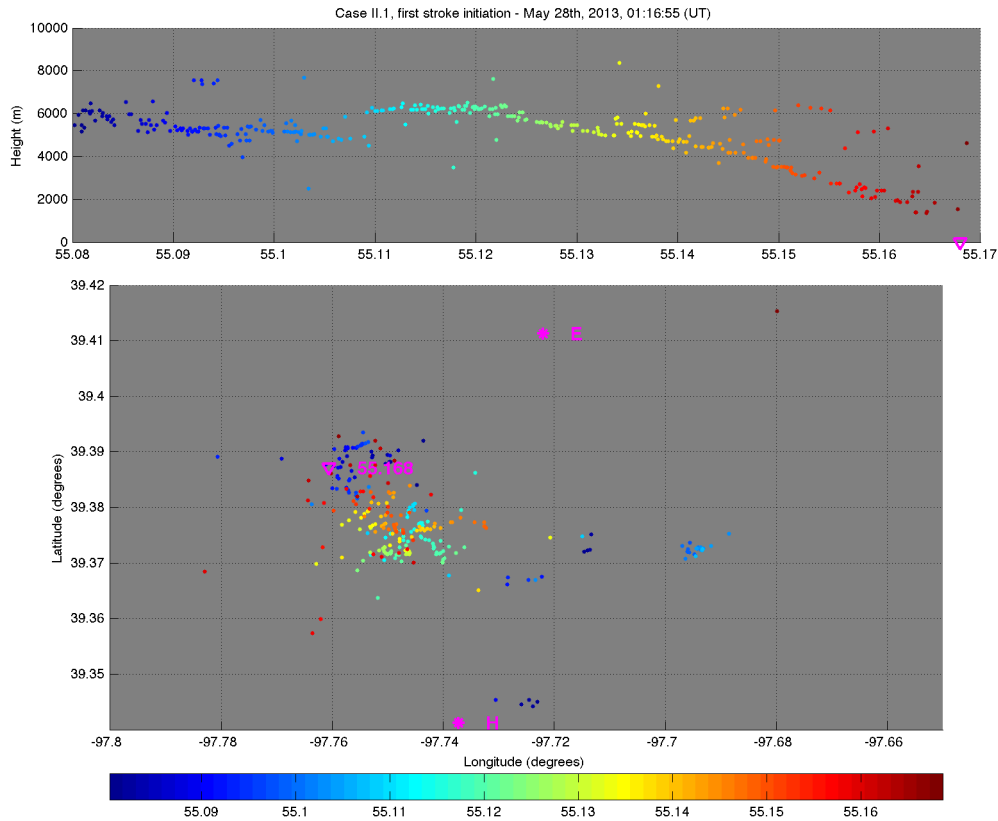
See description of Figure 6.1.

Source: produced by the author.

The first stroke occurred at 01:16:55.168 (UT) with an estimated peak current of -14.7 kA. Details on the initiation of the first stroke are given in Figure 6.14. An isolated, somewhat downward horizontal channel (dark blue sources) is observed before the actual downward stepped leader initiates its descent (light blue sources to the southeast of the return stroke GCP). The leader initially develops towards south before branching profusely towards northwest and eventually reaching ground. Video data did not have enough temporal resolution to provide accurate information on persistent luminosity

associated with continuing current, but it suggests that the channel persisted for over one frame (whose exposure time is 16.7 milliseconds long).

Figure 6.14 – LMA plot of the initiation of the first stroke of Case II.1.



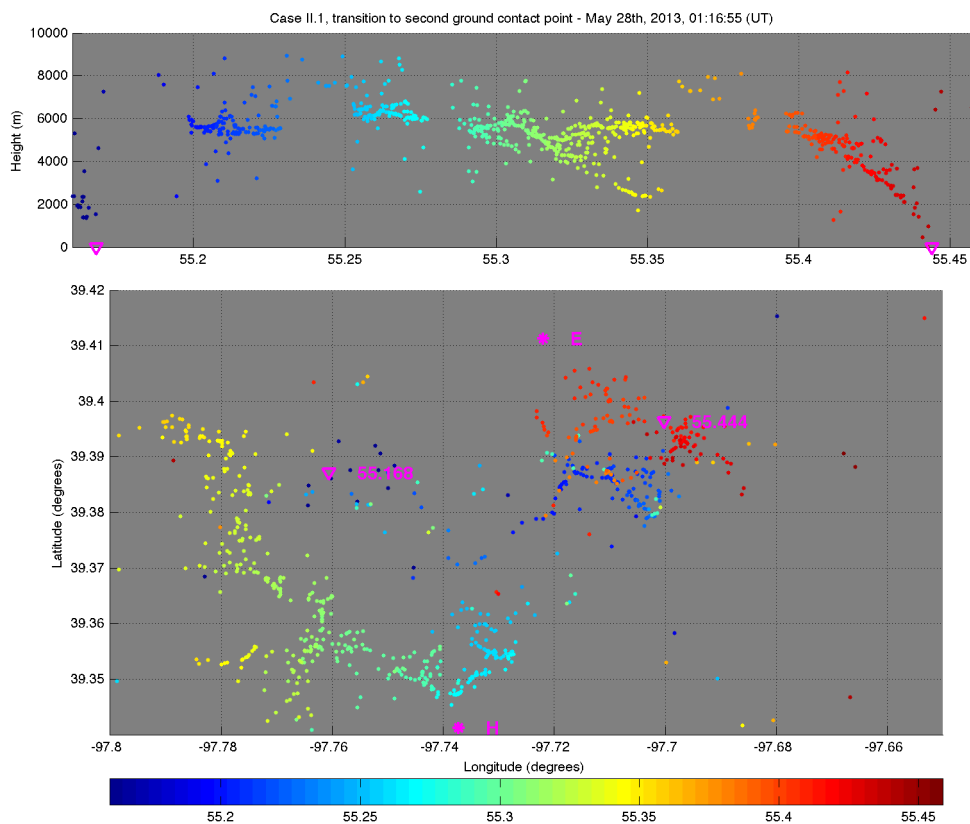
See description of Figure 6.1.

Source: produced by the author.

VHF sources mapped by the LMA during the interstroke interval between the first and second (NGC) stroke are shown in Figure 6.15. There was a “lull” period that lasted about 30 milliseconds in which almost no VHF sources were detected. Around 55.2 seconds there is a number of blue sources being detected towards the east, probably related to recoil leaders retracing branches of the in-cloud positive leaders moving that way, until that development is interrupted. Some branches (light blue, green and yellow sources) slowly move towards south, then west and northwest and are also interrupted. Finally, the eastern branches (initially mapped by the blue sources) start to be retraced

around 55.4 seconds, probably by recoil leaders propagating towards east. The dark orange and red sources show that, after being initiated at the previously ionized horizontal channels, that leader process starts to create new channels towards ground, branching in two directions during its descent. Finally, its development is concluded at 01:16:55.444 (UT) when the second, NGC return stroke is produced, with an estimated peak current of -12.2 kA, 276 milliseconds after the first stroke and at a location about 5.3 km away from it.

Figure 6.15 – LMA plot of the initiation of the second stroke (NGC) of Case II.1.



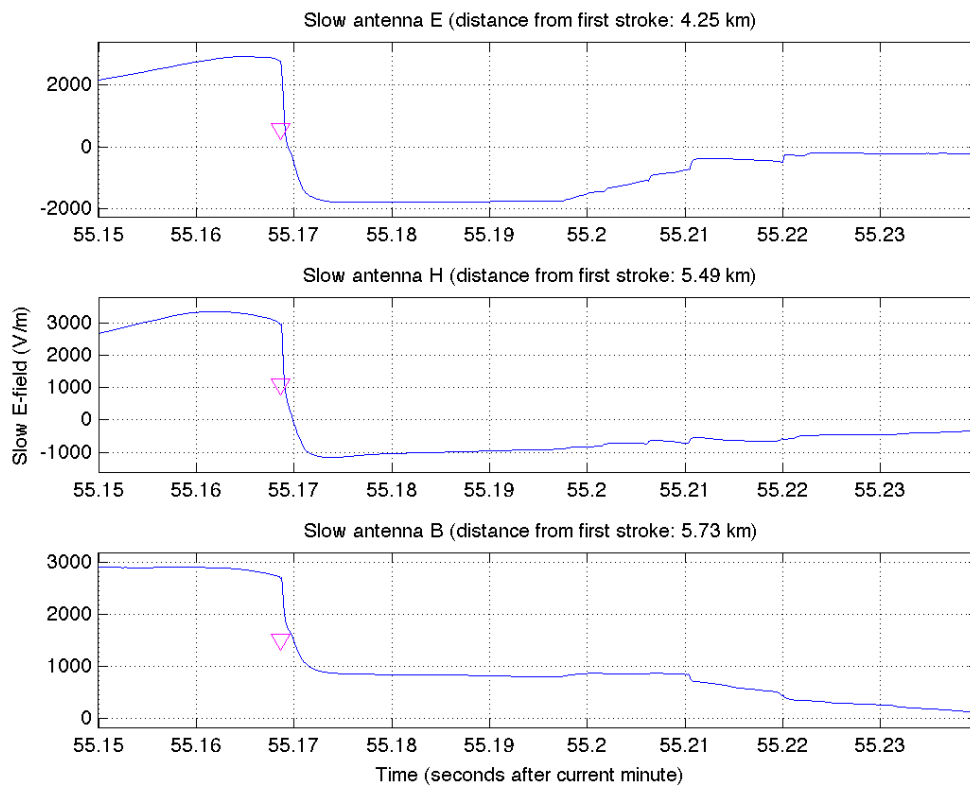
See description of Figure 6.1.

Source: produced by the author.

Figure 6.16 shows the electric field waveforms following the first stroke of Case II.1. The field at the closest sensor (station E) remains mostly flat for about 24 milliseconds, probably due to a continuing current (as suggested by the aforementioned luminosity

persistence in the video record). Following that period there is no clear short duration, large amplitude field reversal as observed in Cases I.1 (Figure 6.4) and I.2 (Figure 6.10), only a steady and long (about 14 ms long) ramp. There are, however, a few small amplitude isolated steps that are probably related to K changes.

Figure 6.16 – Waveforms of the closest three slow electric field antennas showing the first return stroke of Case II.1 and the following 50 milliseconds.



The down-pointing magenta triangles indicate the first return stroke instant as reported by the NLDN.

Source: produced by the author.

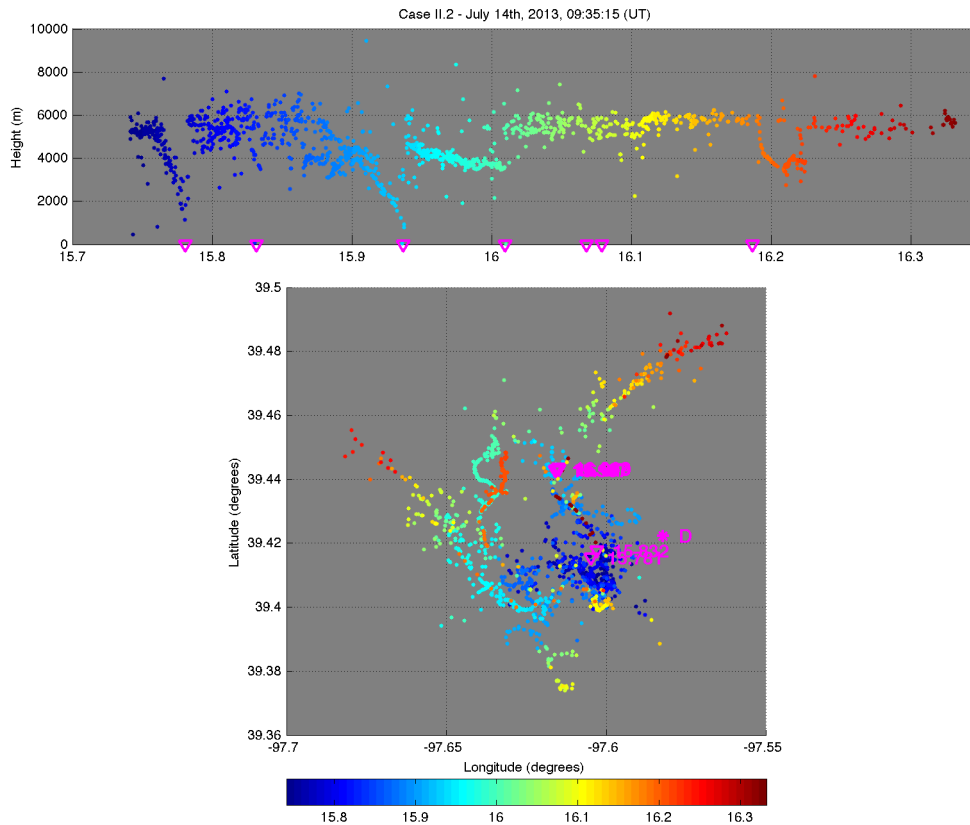
There is almost no detectable in-cloud activity following the second stroke, with the third and forth probably being initiated by recoil leaders in some branches of a positive leader propagating northeast (orange and red sources in Figure 6.13). Interestingly, these final strokes were the most intense of the flash and occurred at 01:16:55.706 (UT)

and 01:16:55.776 (UT) with estimated peak currents of -31.3 kA and -17.7 kA, respectively.

6.2.2.2. Case II.2: July 14th, 2013, 09:35:15 (UT)

The second example of Type II NGC creation occurred on July 14th, 2013, at 09:35:15 (UT) and was a seven-stroke flash. LMA and NLDN data combined strongly suggests that the first two strokes occurred in the same channel at 09:35:15.781 (UT) and 09:35:15.832 (UT) with estimated peak currents of -48.3 kA and -38.8 kA, respectively, and a separation distance between their return stroke solutions of about 300 meters. The full flash development of this case, as mapped by the LMA network, is shown in Figure 6.17.

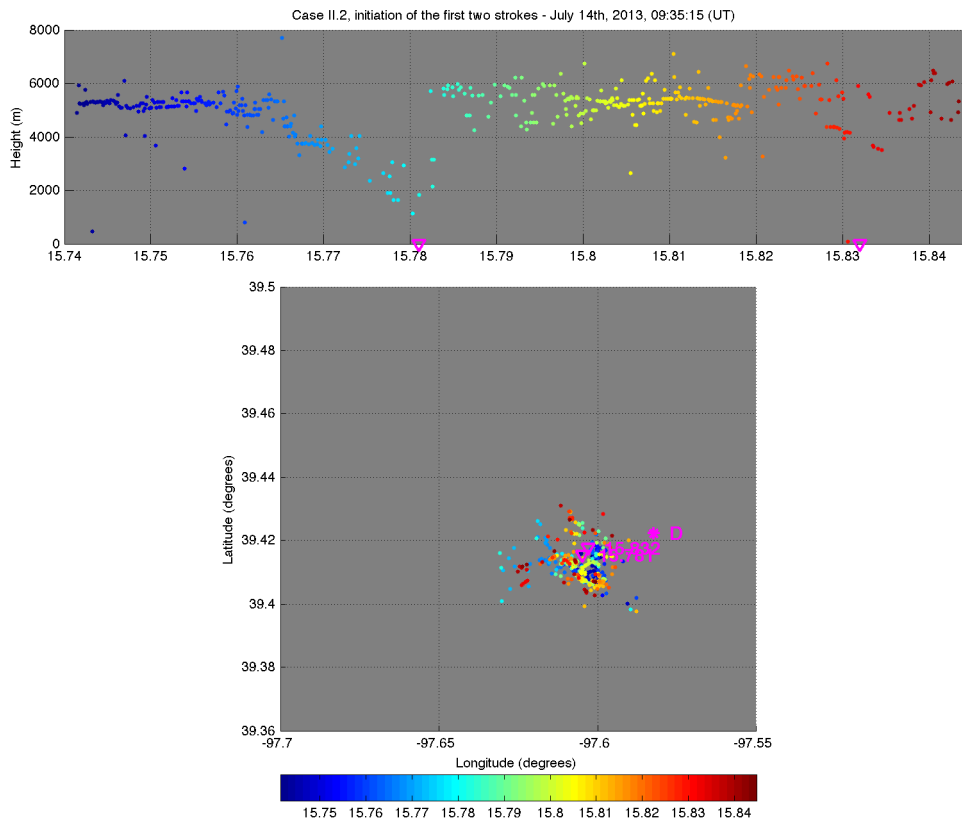
Figure 6.17 – Full flash LMA plot of Case II.2.



Source: produced by the author.

The initiation and development of the first two strokes are shown in greater detail in Figure 6.18. Note that there is little horizontal channel development, but some branches move north of their GCP.

Figure 6.18 – LMA plot of the first two strokes of Case II.2.

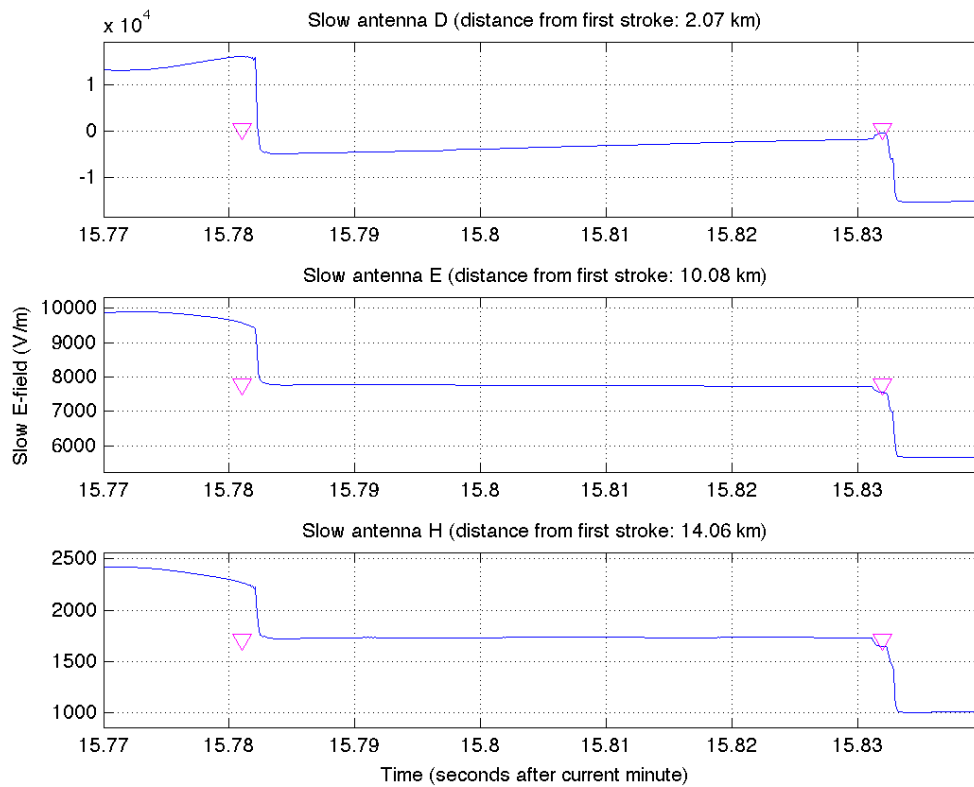


See description of Figure 6.1.

Source: produced by the author.

The LMA reported no clear descending leader during the few milliseconds prior to the second stroke, supporting the assertion that the first two strokes shared a common channel. Electric field waveforms of that period were examined and shown in Figure 6.19. The field following the first stroke remained essentially flat as measured in the three closest stations.

Figure 6.19 – Waveforms of the closest three slow electric field antennas showing the interval between the first and second (PEC) return strokes of Case II.2.

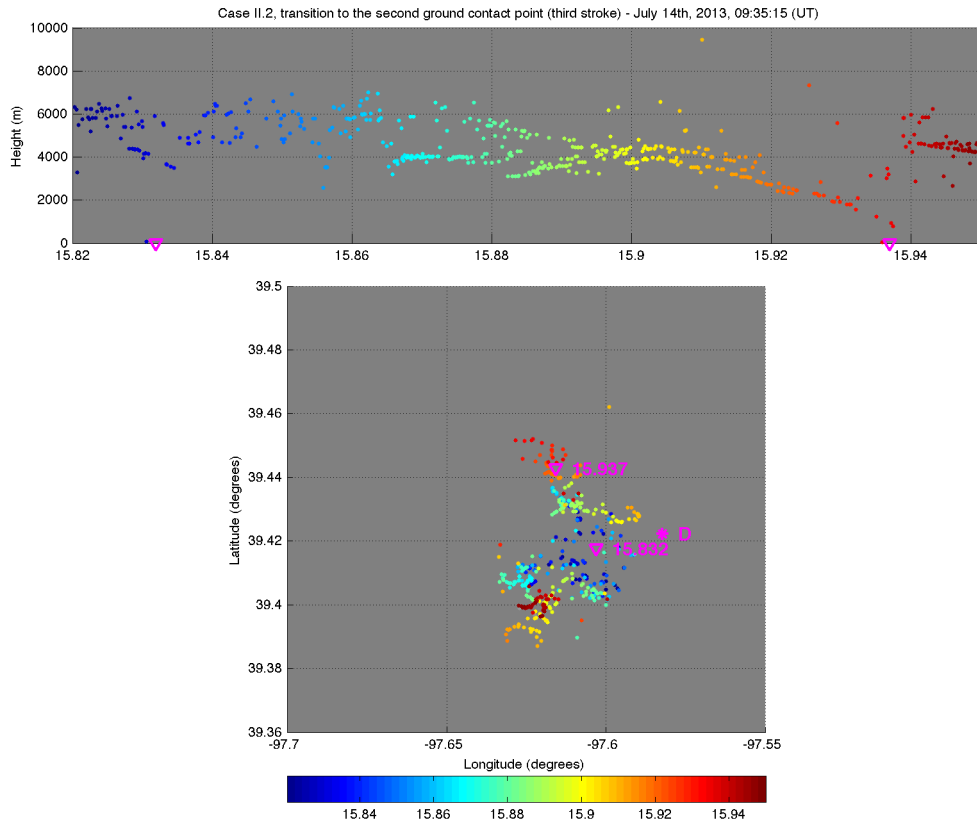


The down-pointing magenta triangles indicate the instant of occurrence of the first and second return strokes as reported by the NLDN.

Source: produced by the author.

Figure 6.20 shows the VHF sources produced in the transition from the second stroke to the third, which produced an NGC. Note that there is some horizontal channel development to the north of the strike point of the first two strokes. The large number of VHF sources that were mapped suggests that such development is related to negative leaders. Eventually one of the branches starts to propagate towards ground from those horizontal channels, leading to the third (NGC) stroke at 09:35:15.937 (UT), with an estimated peak current of -16.2 kA and a GCP about 3.1 km away from where the first stroke occurred.

Figure 6.20 – LMA plot of the initiation of the third stroke (NGC) of Case II.2.

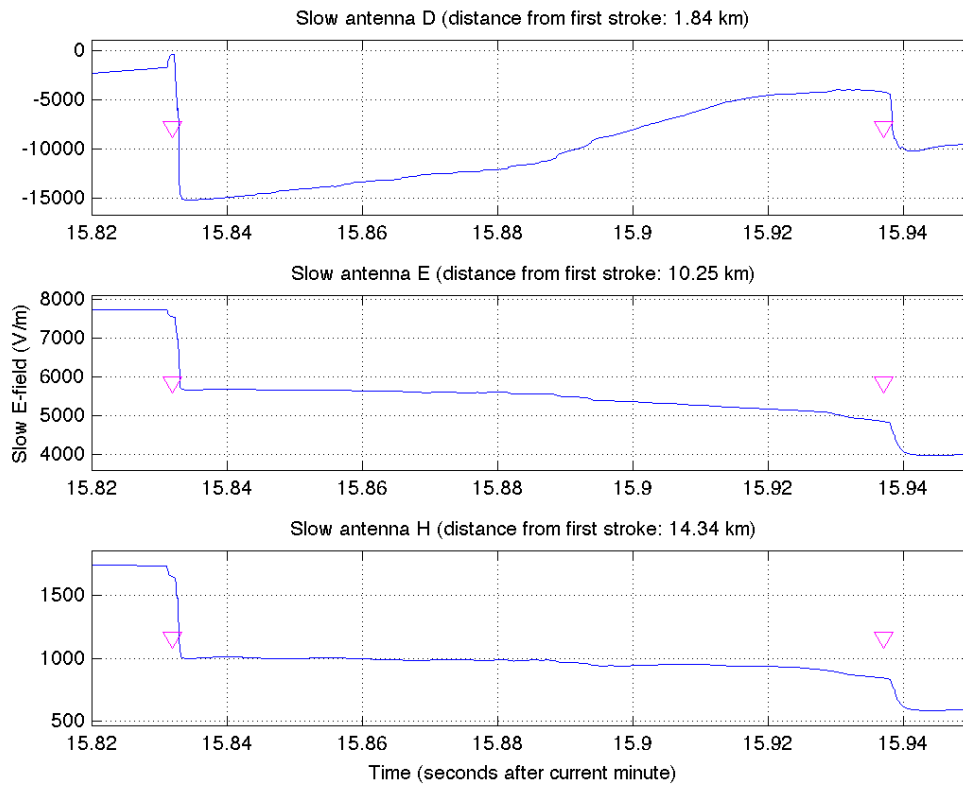


See description of Figure 6.1.

Source: produced by the author.

Electric field records of the interval preceding the third stroke are shown in Figure 6.21. No pronounced field changes are found in the closest record (at station D, 1.84 km from the second stroke NLDN solution), although there is a steady increase in negative charge above this sensor during the 6 milliseconds prior to the NGC stroke, concurrent with the descending leader development.

Figure 6.21 – Waveforms of the closest three slow electric field antennas showing the interval between the second and third (NGC) return strokes of Case II.2.

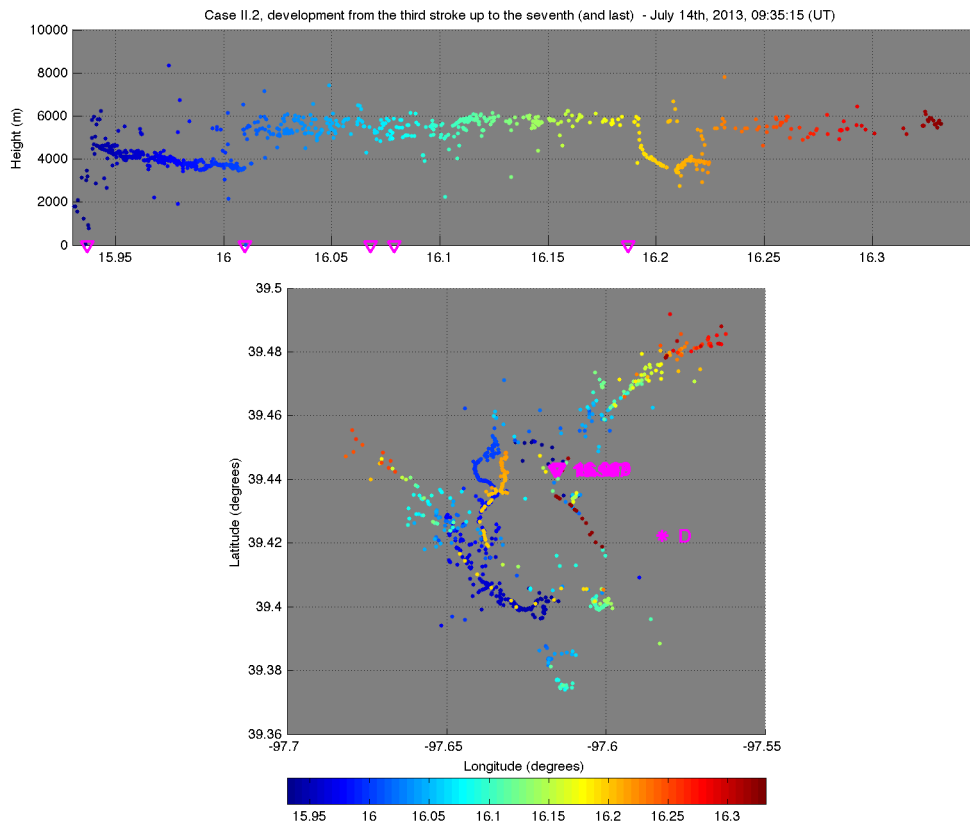


The down-pointing magenta triangles indicate the instant of occurrence of the second and third return strokes as reported by the NLDN.

Source: produced by the author.

All strokes from the fourth to the seventh (and final) followed the same path to ground, retracing the channel created by the third stroke. Channel development for that entire period is shown in Figure 6.22. Apparently those subsequent strokes were fed by two fronts of in-cloud leader development, one to the northeast of the GCP of the third stroke and another moving from the south of the GCP of the first two strokes. It is worth noting that, despite having no new VHF sources being emitted in the channel that connects both fronts (whose development can be seen in Figure 6.17), they seem to remain connected as the flash continues to expand its horizontal extension in the thundercloud.

Figure 6.22 – Development of Case II.2 after its third stroke.



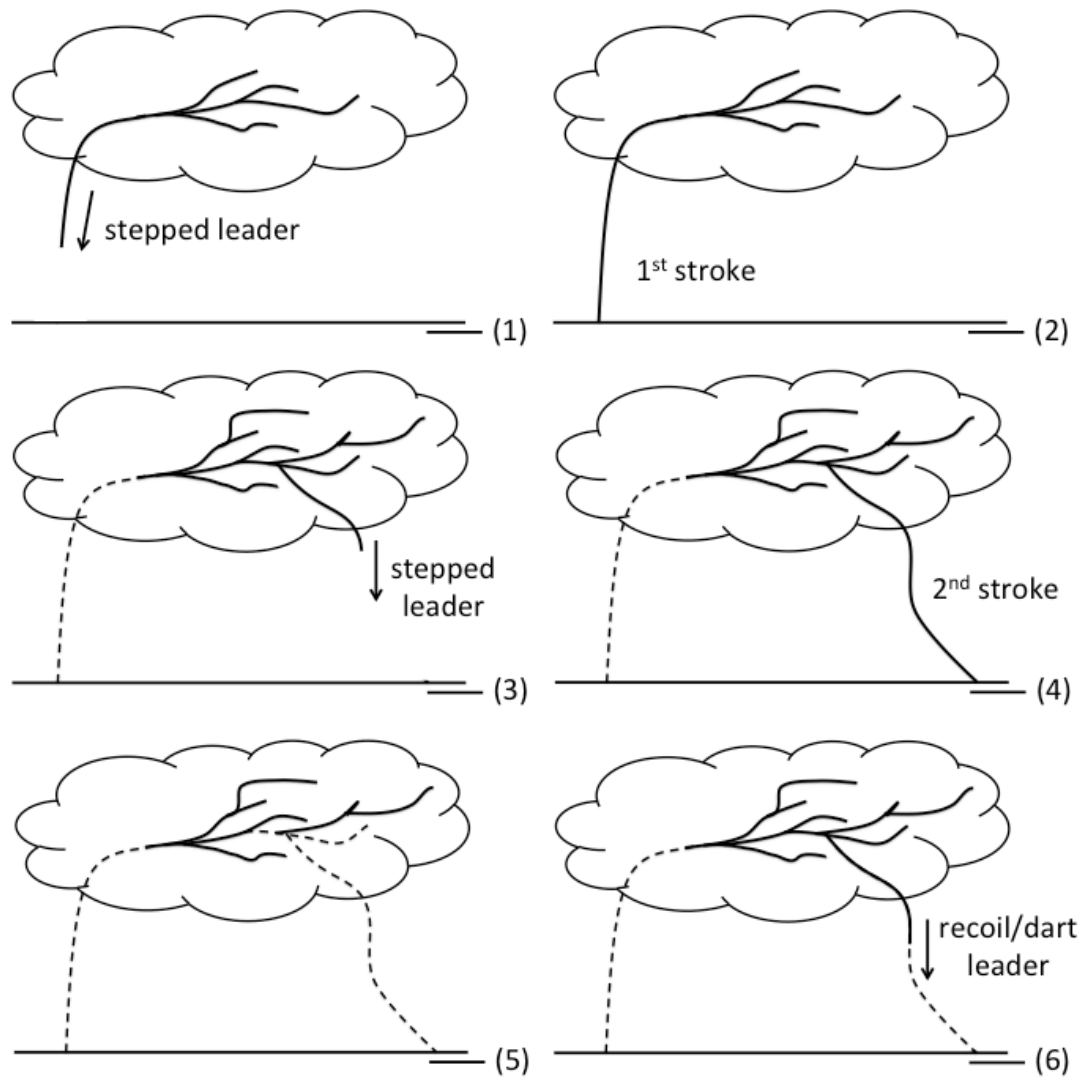
See description of Figure 6.1.

Source: produced by the author.

6.2.2.3. Type II conceptual scenario and mechanism

The interpretation of the LMA observation of all twelve cases of Type II NGC initiation is illustrated in Figure 6.23. After (1) the initial downward stepped leader and (2) the first return stroke (and sometimes after more than one stroke, as illustrated by Case II.2), (3) current cutoff occurs in the current channel to ground as an in-cloud portion of negative leader continues to propagate horizontally, eventually developing towards ground. When that downward moving branch reaches ground, (4) an NGC stroke is produced. When (5) current cutoff occurs in that new channel, (6) new recoil/dart leader sequences may lead to additional subsequent PEC return strokes.

Figure 6.23 – Illustration of the mechanism of a Type II new ground contact creation.



Source: produced by the author.

Given the extensive horizontal development between the creations of different GCPs in Type II events, greater distances between strike points are possible to occur (particularly when compared to what was observed in our sample of Type I events). In the sample of the present work (twelve events), the separation distances ranged from 1.7 km to 7.5 km, with an average value of 3.9 km. Additionally, the two chosen case studies to be presented in this work illustrate two possible specific scenarios in which a Type II NGC creation may occur: in Case II.1, the NGC stroke started as recoil activity in a “defunct” branch that was created after the first return stroke by the in-cloud leaders; while in

Case II.2 the horizontal branch that lead to the NGC stroke remained active during the entire interstroke interval, continuously developing.

Finally, it is important to note that Type II events are in agreement with the mechanism hypothesized by Zoghzoghy et al. (2014) based on their analysis of a space and time distribution of subsequent strokes from NLDN data. As discussed in subsection 2.5.2, there was a vertical, tilted feature in that space-time distribution (Figure 2.9) that corresponded to a speed of 230 km s^{-1} , compatible with typical negative stepped leader estimates (e.g., CAMPOS et al., 2014a). Their interpretation of that statistical result (reproduced in Figure 2.10) is essentially the same as ours for all LMA observations of Type II events, with horizontal, in-cloud channels continuously developing and eventually deviating downwards and producing subsequent NGC return strokes.

6.2.3. Type III: New channel with common origin

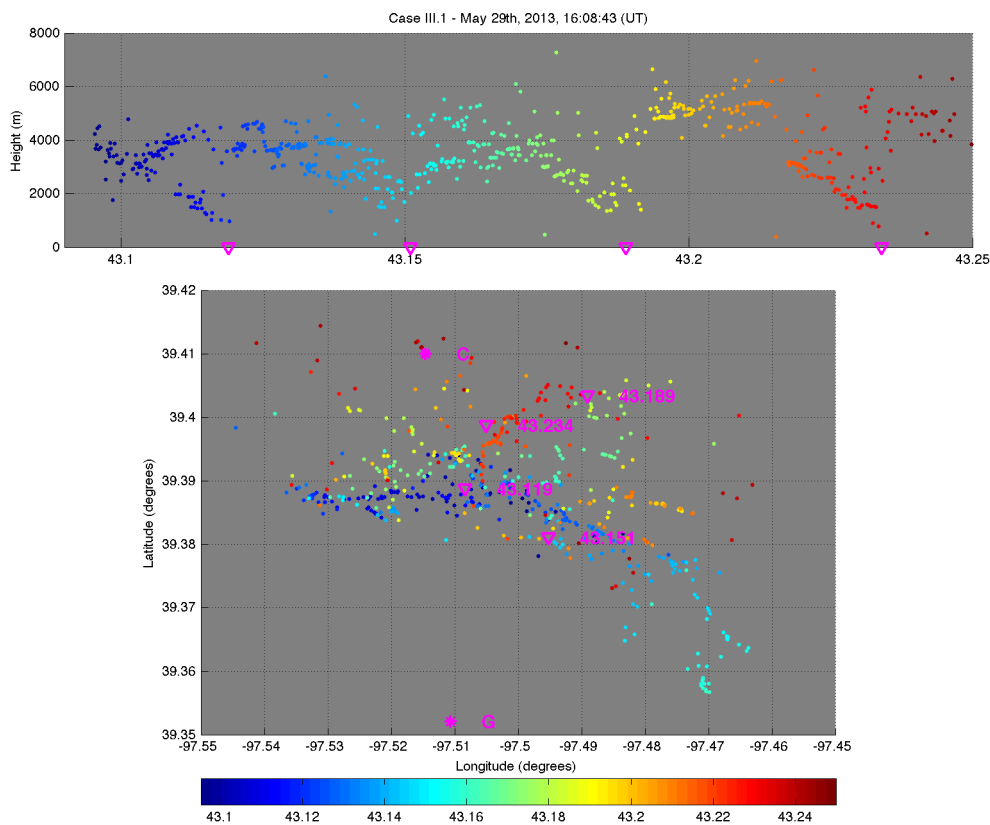
Type III, the third mode of NGC creation to be identified in this work, was observed in fifteen of the 33 cases that were analyzed. Events of this type are initiated by a stepped leader whose inception region is close to that of a preceding stroke but with no clear common channel branches. Initially (first phase, as described in section 6.1) it was identified in a very distant event (48 km away from the closest LMA sensor), so it was thought that the observed characteristics could be caused by the progressive reduction in the detection efficiency of VHF sources (even though according to Cummins et al., 2014, it should be close to 100% up to 150 km away from the network center, as discussed in subsection 3.2.1.1). Later, however, as events with no video records were analyzed, this type of NGC creation process was identified in many other –CG flashes. Two representative events were selected to be presented in detail and illustrate the main characteristics of this mechanism.

6.2.3.1. Case III.1: May 29th, 2013, 16:08:43 (UT)

The first example of Type III event occurred on May 29th, 2013, at 16:08:43 (UT). It produced four return strokes, each one of them with a different ground termination. Figure 6.24 shows a general plot of all VHF sources detected for this flash. In the top

panel it is possible to note that each stroke (whose instant of occurrence, as determined from NLDN data, is indicated by the down-pointing magenta triangles) seem to be preceded by its own VHF producing leader process. Also, in the bottom channel it is clear that their strike points (again indicated by magenta triangles) were well spatially separated.

Figure 6.24 – Full flash LMA plot of Case III.1.



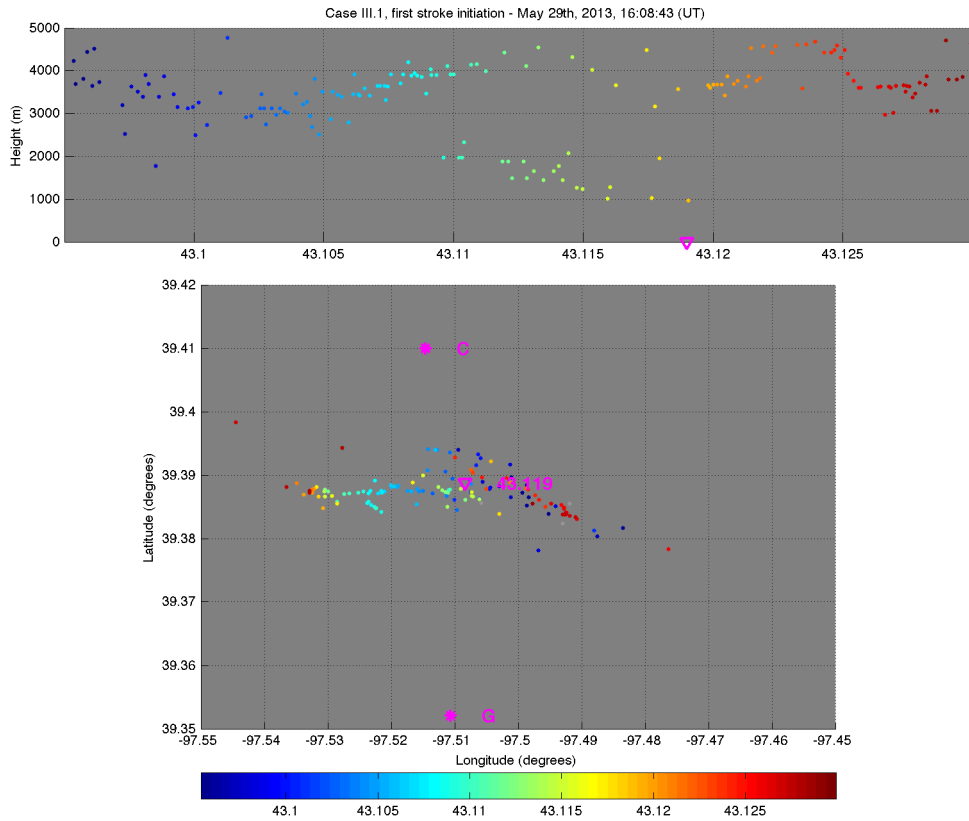
See description of Figure 6.1.

Source: produced by the author.

The first stroke of Case III.1 occurred at 16:08:43.119 (UT) with an estimated peak current of -15.8 kA. The VHF sources related to its initiation are mapped in Figure 6.25. It started as a horizontal leader moving towards west, until it branched towards ground around 43.11 s (light blue/green sources), reaching ground about 8 milliseconds later. The earliest (dark blue) VHF sources were mapped around latitude 39.39° ,

longitude -97.50° about 4 km above ground from which the westward leader was initiated.

Figure 6.25 – LMA plot of the initiation of the first stroke of Case III.1.

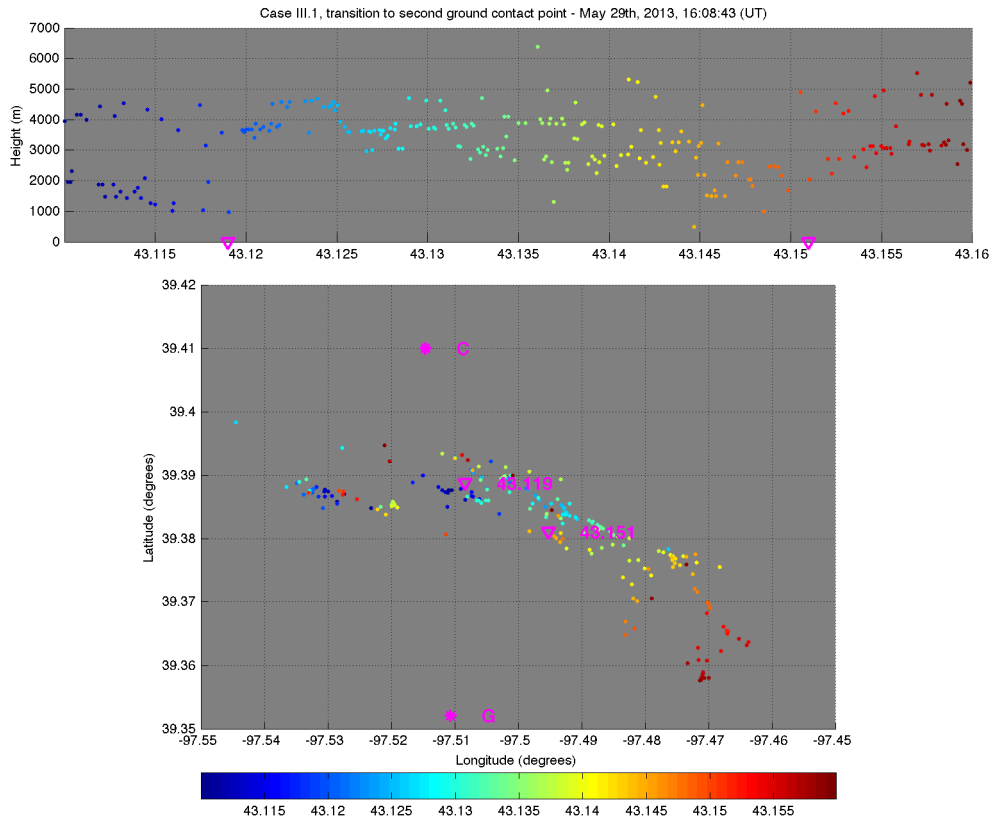


See description of Figure 6.1.

Source: produced by the author.

After the first stroke (starting at 43.125 s), new VHF sources were mapped around the inception point of its initial leader. This channel developed towards southeast, as shown in Figure 6.26, with some branches moving towards ground and eventually leading to the second stroke of the flash at 16:08:43.151 (UT). NLDN reported an estimated peak current of -12.6 kA and a GCP located 1.4 km away from that of the first stroke. Even though the inception point of the second stroke is very close to that of the first, LMA data does not indicate that they shared any common channel branches, developing as apparently independent breakdown, leader, return stroke sequences.

Figure 6.26 – LMA plot of the initiation of the second stroke (NGC) of Case III.1.

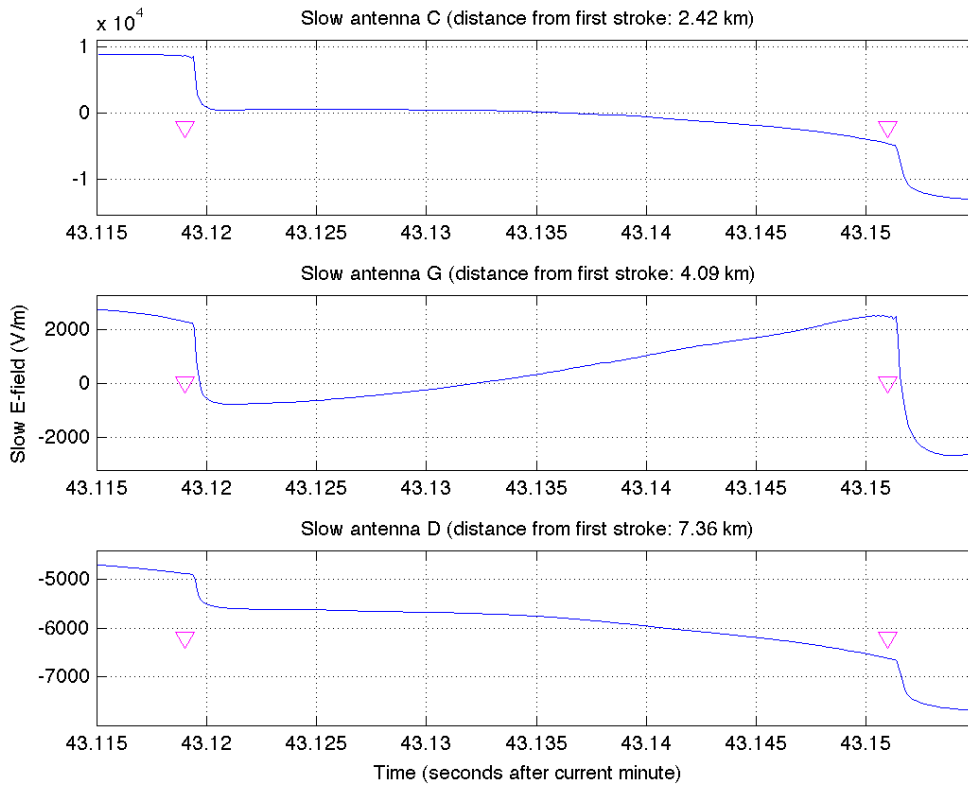


See description of Figure 6.1.

Source: produced by the author.

Electric field records of the transition from the first to the second stroke, shown in Figure 6.27, presented no short duration changes even in the closest stations (C and G, 2.4 km and 4.1 km away from the first stroke GCP). The slow downward and upward trends in the field prior to the second stroke reflect the net negative charge retreating from or approaching a given sensor, respectively.

Figure 6.27 – Waveforms of the closest three slow electric field antennas showing the interval between the first and second (NGC) return strokes of Case III.1.

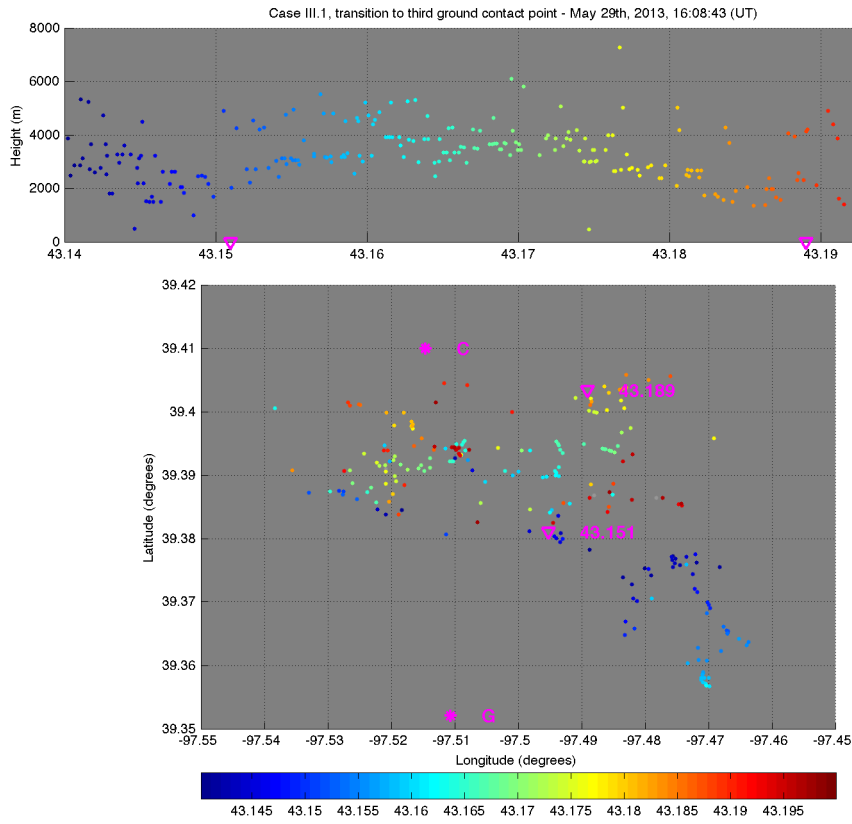


The down-pointing magenta triangles indicate the instant of occurrence of the first and second return strokes as reported by the NLDN.

Source: produced by the author.

After the second stroke, new channels start to develop from the first stroke inception point (latitude 39.39° , longitude -97.50° , about 4 km height) at 16:08:43.160 (UT), with one branch moving towards west and another towards northeast, as shown in the LMA plot of Figure 6.28. The latter started to develop towards ground (transition from light green to yellow and orange sources) over a period of about 20 milliseconds, leading to the third return stroke of this flash at 16:08:43.189 (UT), with an estimated peak current of -13.2 kA and a strike point 2.32 km away from the first stroke.

Figure 6.28 – LMA plot of the initiation of the third stroke (NGC) of Case III.1.

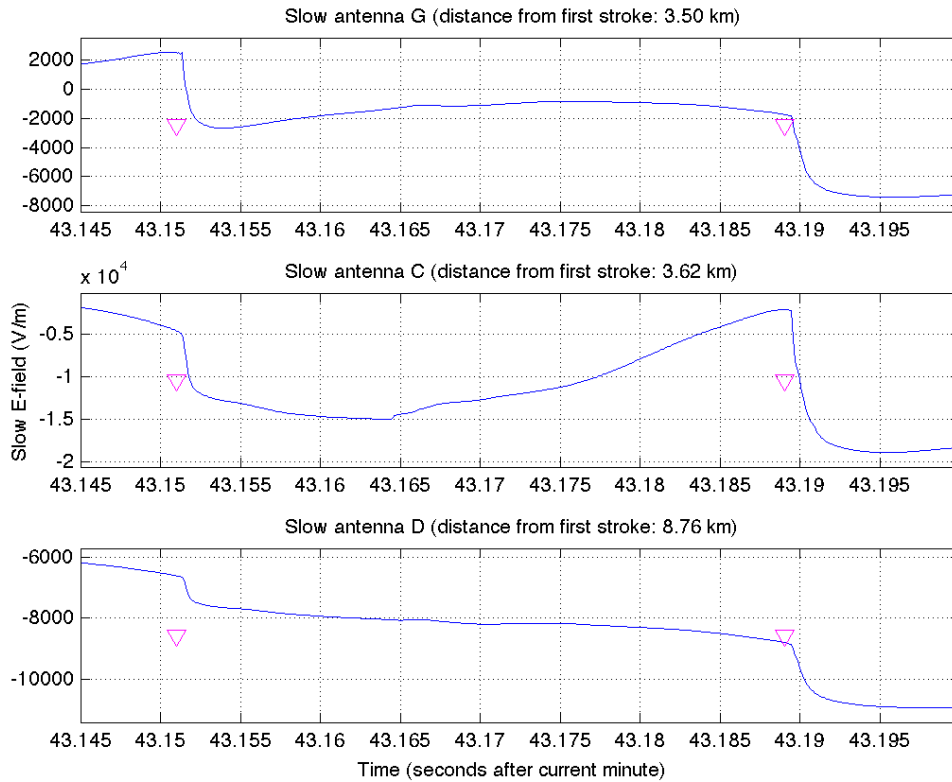


See description of Figure 6.1.

Source: produced by the author.

Figure 6.29 shows the electric field records corresponding to the transition from the second to the third stroke of Case III.1. Again, there is no characteristic waveform observed during that period.

Figure 6.29 – Waveforms of the closest three slow electric field antennas showing the interval between the second and third (NGC) return strokes of Case III.1.

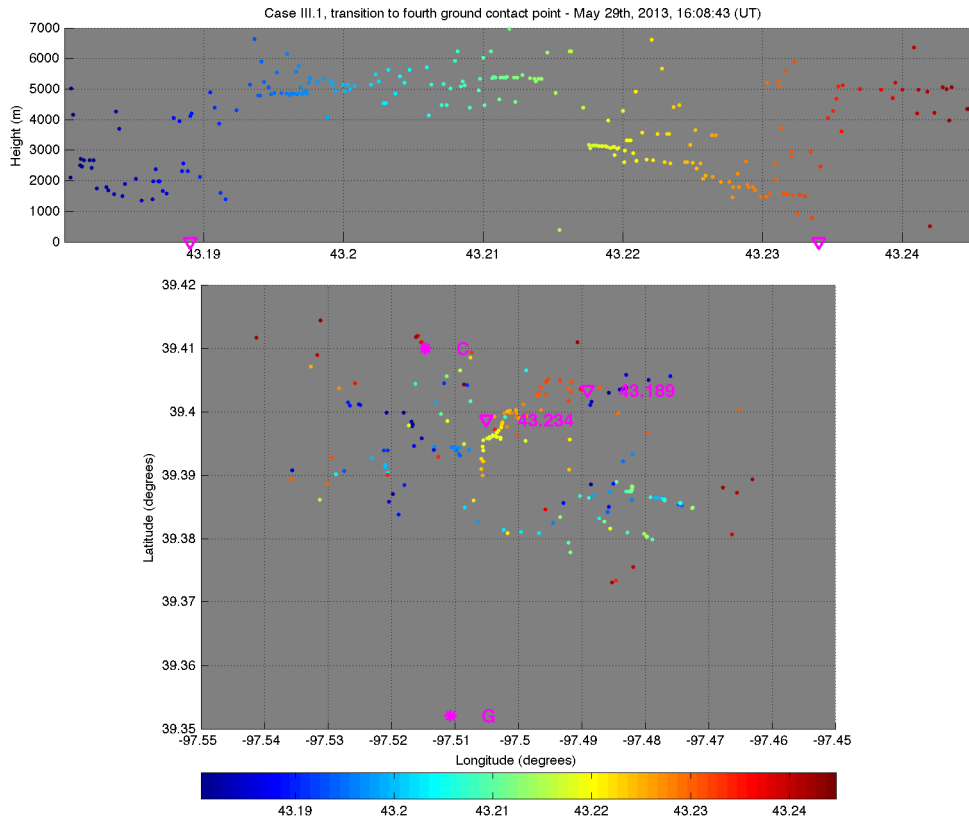


The down-pointing magenta triangles indicate the instant of occurrence of the second and third return strokes as reported by the NLDN. The distances are calculated based on the first stroke of this particular plot (i.e., the second one of the flash).

Source: produced by the author.

After the third stroke, new channel development started near the initial inception point of the flash, but this time slightly displaced to the west and at a lower height (latitude 39.39° , longitude -97.505° and 3 km above ground). This new downward leader is shown in Figure 6.30 by the yellow to orange sources that are first detected at 16:08:43.217 (UT). Its development lasts for about 17 milliseconds, leading to the fourth stroke of the flash at 16:08:43.234 (UT), with an estimated peak current of -18.6 kA and a GCP about 1.1 km away from the first stroke location.

Figure 6.30 – LMA plot of the initiation of the fourth stroke (NGC) of Case III.1.

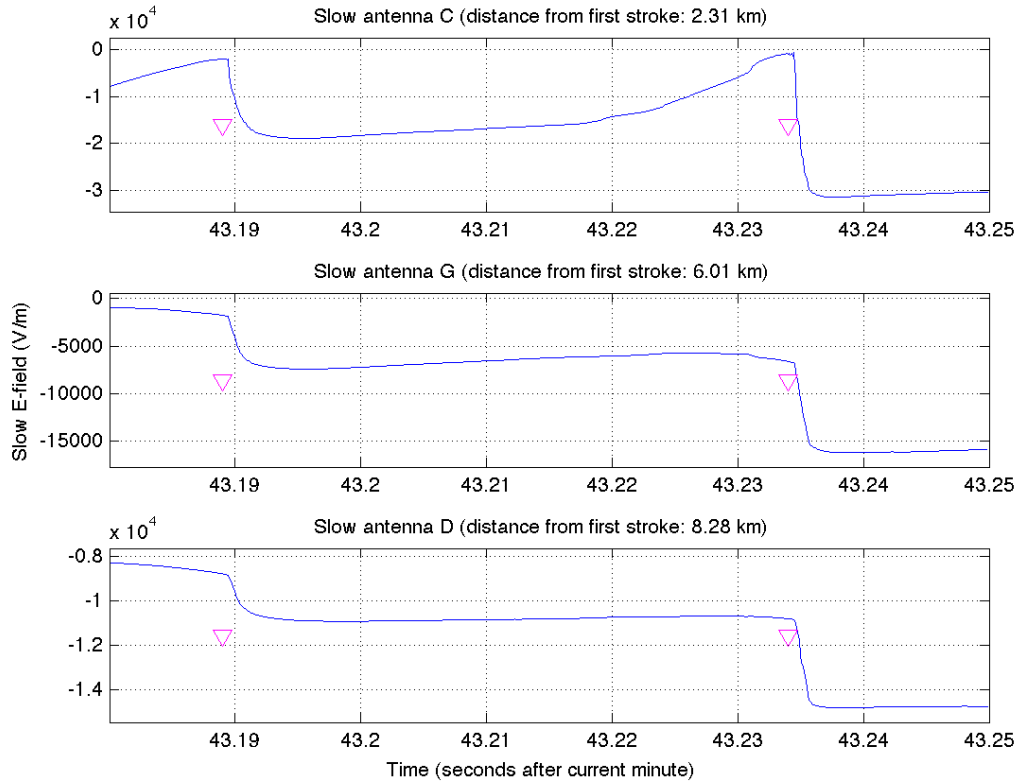


See description of Figure 6.1.

Source: produced by the author.

Finally, Figure 6.31 shows the electric field records of the interstroke interval between the third and fourth strokes of Case III.1. As in the previous interstroke intervals (Figures 6.27 and 6.29), no characteristic waveform was identified. This strongly suggests that no significant charge transfers were related to the transition to each new ground termination of this flash.

Figure 6.31 – Waveforms of the closest three slow electric field antennas showing the interval between the third and fourth (NGC) return strokes of Case III.1.



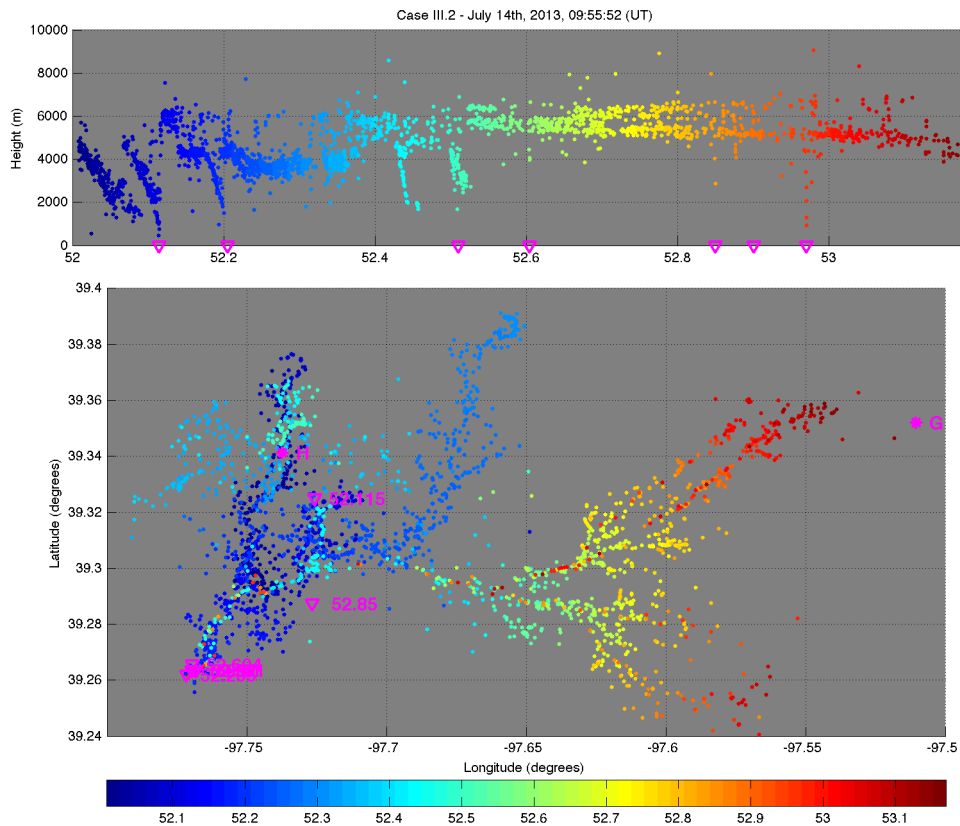
The down-pointing magenta triangles indicate the instant of occurrence of the third and fourth return strokes as reported by the NLDN. The distances are calculated based on the first stroke of this particular plot (i.e., the third one of the flash).

Source: produced by the author.

6.2.3.2. Case III.2: July 14th, 2013, 09:55:52 (UT)

The second example of Type III event occurred on July 14th, 2013, at 09:55:52 (UT) and produced seven return strokes with two ground terminations. Figure 6.32 shows a plot of all VHF sources detected by the LMA for this flash. Note that the fifth stroke (52.85 s) seems misplaced because its error ellipse had a very large SMA (8.4 km) and it was assigned by *groupGCP* to the second GCP of the flash, which was initiated by the second stroke.

Figure 6.32 – Full flash LMA plot of Case III.2.

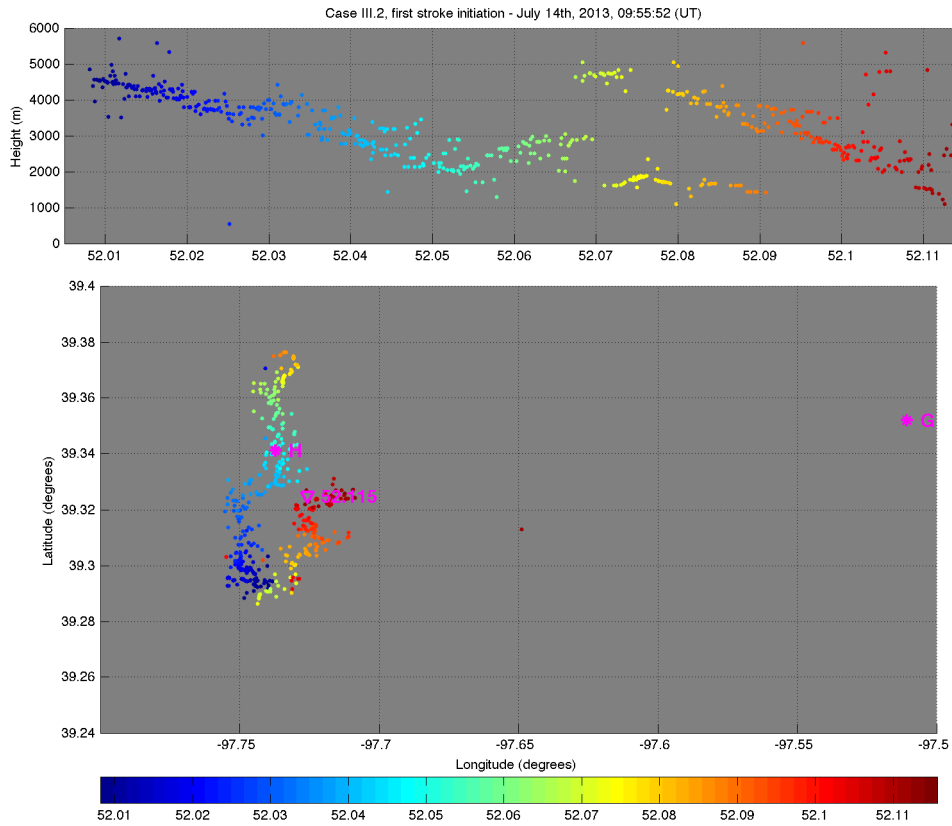


See description of Figure 6.1.

Source: produced by the author.

The first stroke initiation is shown in Figure 6.33. Early channel developments originate around latitude 39.29° and longitude -97.94° , moving towards north and with some downward development. It is then interrupted (without the occurrence of any return stroke that could be either reported by the NLDN or observed in the electric field records) and followed by a new leader initiation from the same location, propagating towards northeast of the inception point (yellow, orange and red sources). This second leader moves constantly towards ground, leading to the first stroke at 09:55:52.115 (UT), which had an estimated peak current of -13.6 kA.

Figure 6.33 – LMA plot of the initiation of the first stroke of Case III.2.

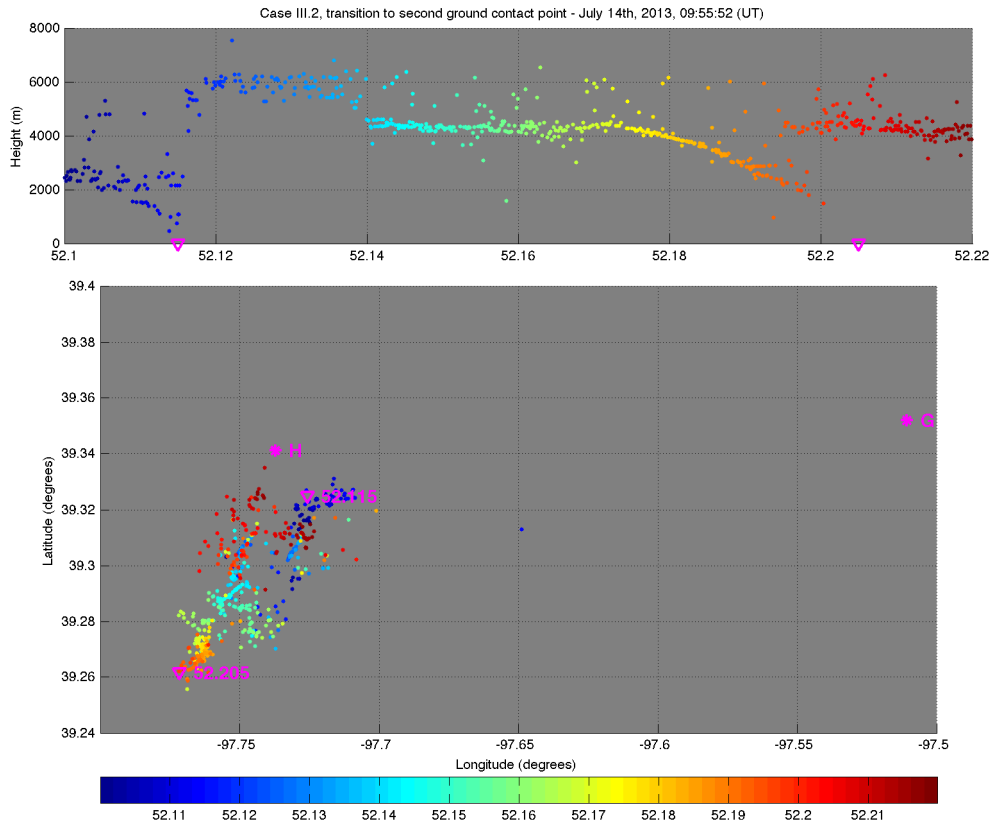


See description of Figure 6.1.

Source: produced by the author.

The initiation of the second stroke started at 09:55:52.140 (UT), as shown in the LMA plot of Figure 6.34. The light blue sources on both panels show that the horizontal and then downward development started near the inception region of the first stroke, similar to the initiation of all subsequent strokes of Case III.1. This new leader moves horizontally for more than 25 milliseconds (up to the transition from light green to yellow sources) before starting to move downwards until touching ground at 09:55:52.205 (UT), leading to the second stroke of the flash. Probably due to this long duration horizontal development in the early phase of its leader, the NGC was located 7.8 km away from the first stroke GCP, the largest horizontal separation that was observed in the entire sample of MGCFs analyzed in this study. The second stroke had an estimated peak current of -12.3 kA.

Figure 6.34 – LMA plot of the initiation of the second stroke (NGC) of Case III.2.

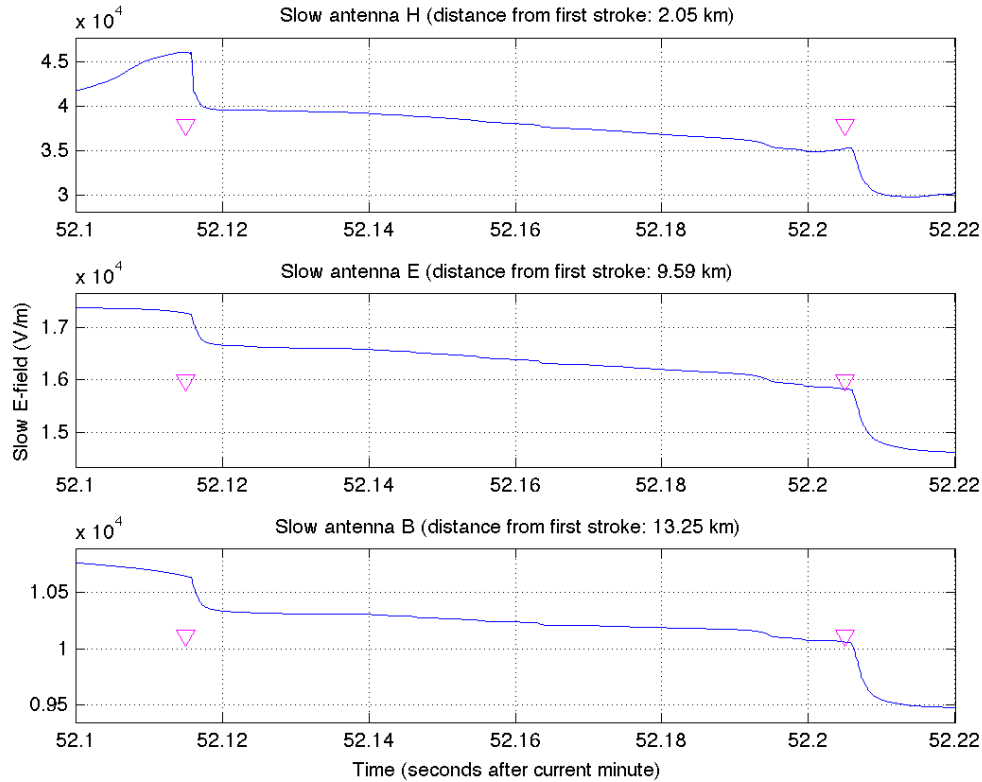


See description of Figure 6.1.

Source: produced by the author.

Electric field records of the transition between GCPs, shown in Figure 6.35, do not present any clear waveforms or signatures during that period. Five other strokes occur in the GCP initiated by the second stroke, with recoil/dart leader sequences initiating from different branches that are created by the extensive in-cloud development (shown in Figure 6.32). This is an interesting event due to its contrast when compared to Case III.1, in which each new leader-return stroke sequence leads to a completely new GCP.

Figure 6.35 – Waveforms of the closest three slow electric field antennas showing the interval between the first and second (NGC) return strokes of Case III.2.



The down-pointing magenta triangles indicate the instant of occurrence of the first and second strokes as reported by the NLDN.

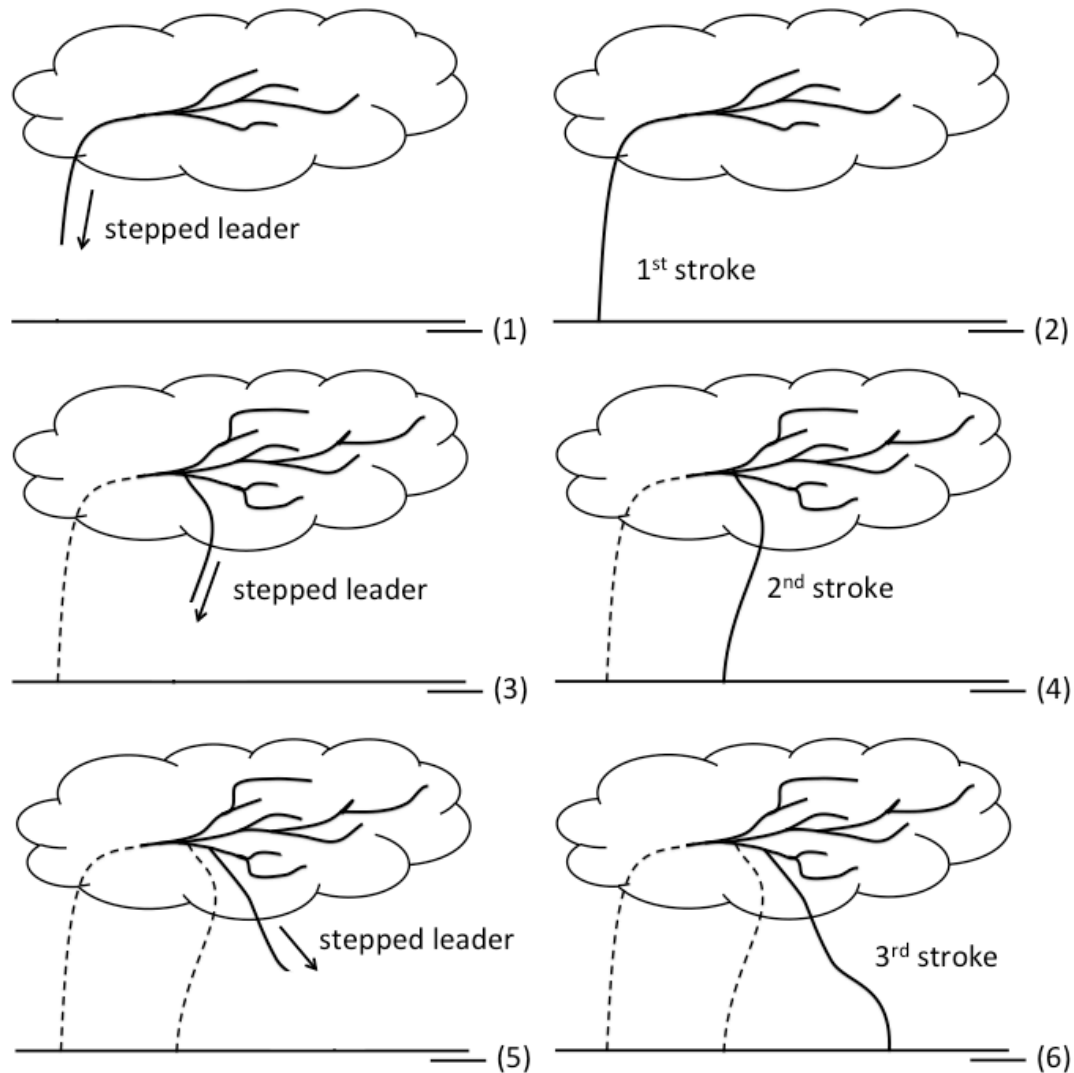
Source: produced by the author.

6.2.3.3. Type III conceptual scenario and mechanism

The common characteristics shared among the LMA observation of all fifteen cases of Type III NGC initiation are illustrated in Figure 6.36. After (1) the initial downward stepped leader and (2) the first return stroke, (3) new stepped leader processes may be initiated inside the cloud from the same inception region of the initial leader without necessarily sharing common channel branches, (4) leading to a NGC subsequent stroke. Additional (5) stepped leader processes may produce a (6) third return stroke (or even more, as in Case III.1). As the analysis of Case III.2 shows, however, the occurrence of one Type III NGC process in a flash does not dictate that other subsequent strokes will

be NGCs, with the possibility of PEC strokes occurring later on. The exact factors that lead to one way or another are not clear. It is clear, however, that there must be sufficient charge in a rather compact region in order to supply the current for multiple leader initiations and their related return strokes.

Figure 6.36 – Illustration of the mechanism of a Type III new ground contact creation.



Source: produced by the author.

Among the three modes of NGC creation observed in this study, Type III was the one with the widest range of possible separation distances, from 600 m to 7.8 km, with a mean of 2.5 km. This is highly dependent on the horizontal extension of the new leader

prior to its descent towards ground; when it is small, the resulting separation is comparable to a Type I event, but when it has long durations (as in Case III.2, in which it lasted about 25 milliseconds), the NGC can be several kilometers away from the first stroke.

Sun et al. (2016) briefly described the creation of a NGC subsequent stroke that is similar to Type III events (see Figure 2.11), with a leader inception point near the region where the preliminary breakdown of the flash was located. They argue that the new leader initially propagates in a previously developed channel segment, but our dataset does not provide any additional evidence that supports that result.

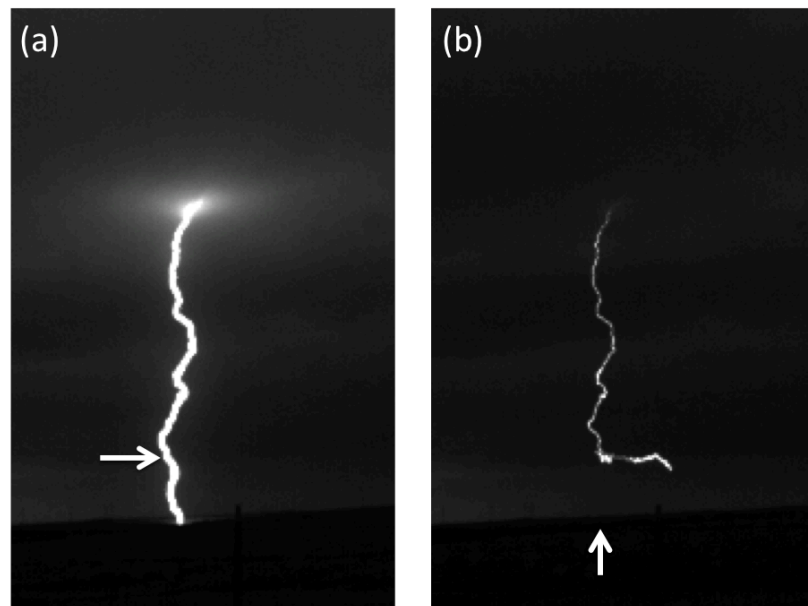
6.3. Unique events

Two interesting unique events are also briefly discussed, providing additional insights on the mechanisms through which a cloud-to-ground flash can create new ground terminations.

6.3.1. Attempted leader: May 28th, 2013, 00:59:01 (UT)

One unique event that was also analyzed is a case of attempted leader following a return stroke that deviated from the original channel at a relatively low height. Figure 6.37 shows sectioned frames of that event, with (a) the first stroke on the left and the (b) subsequent attempted leader on the right. The first stroke occurred at 00:59:01.604 (UT) with an estimated peak current of -10.7 kA, and was followed 117 milliseconds later by the attempted leader at 00:59:01.721 (UT).

Figure 6.37 – Selected high-speed video frames of the first stroke and subsequent attempted leader observed on May 28th, 2013, at 00:59:01 (UT).



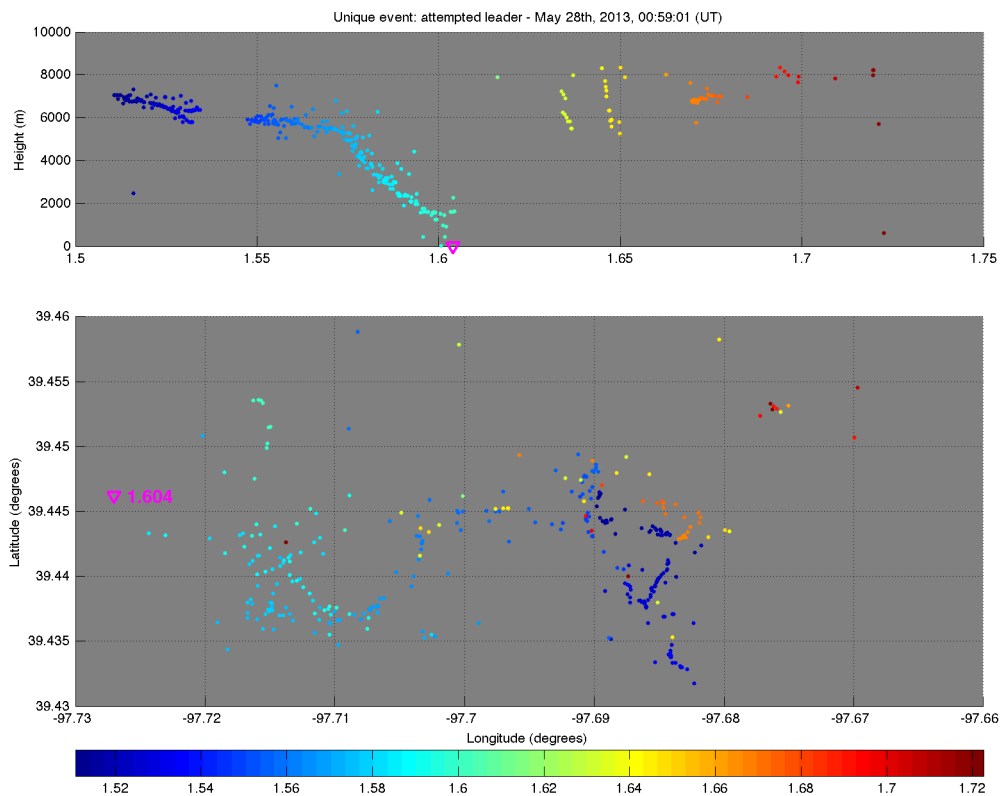
Selected frames, obtained at 1000 fps, of (a) the first stroke and (b) subsequent attempted leader. The horizontal white arrow in (a) shows where the attempted leader left the original channel and the vertical white arrow in (b) indicates the ground strike point of the first stroke.

Source: produced by the author.

LMA records for this event are shown in Figure 6.38. The initial horizontal development of the leader of the first stroke (dark blue sources) was interrupted for about 13 milliseconds before resuming and later turning towards ground. The red sources that precede the attempted leader are probably related to RLs retracing positive leader channels that were not directly mapped by the LMA. When the electric field records are compared with the LMA sources height *versus* time plot, as in Figure 6.39, it is possible to note that the electric field antennas detected the propagation of the attempted leader as an upward deflection (as in the initial leader that preceded the first stroke) but that was not followed by the short duration, intense change associated with a return stroke. Some LMA sources were also detected near the field change (indicated in dark red), including one that was mapped at 620 meters above ground. It is important to note that the electric field records shown were relatively close (3.9 km and 5.5 km) to the first stroke location and no characteristic waveform or signature was observed

during the interstroke interval preceding the attempted leader. However, it is worth noting that the electric field at the closest station (E) does not return to the low level that preceded the initial leader (around 1.57 s). This indicates that there may be stranded negative charges in the lower portion of the channel that were responsible for the deviation of the attempted leader. Additional observations of not only attempted leaders but also Type I NGC stroke processes in order to understand how these charges may be deposited in the channel, further evaluating the ideas discussed by Krehbiel (1981). Finally, some small, short duration changes were measured at both stations, and they seem to be coincident with RLs detected by the LMA (see the yellow, orange and light red sources).

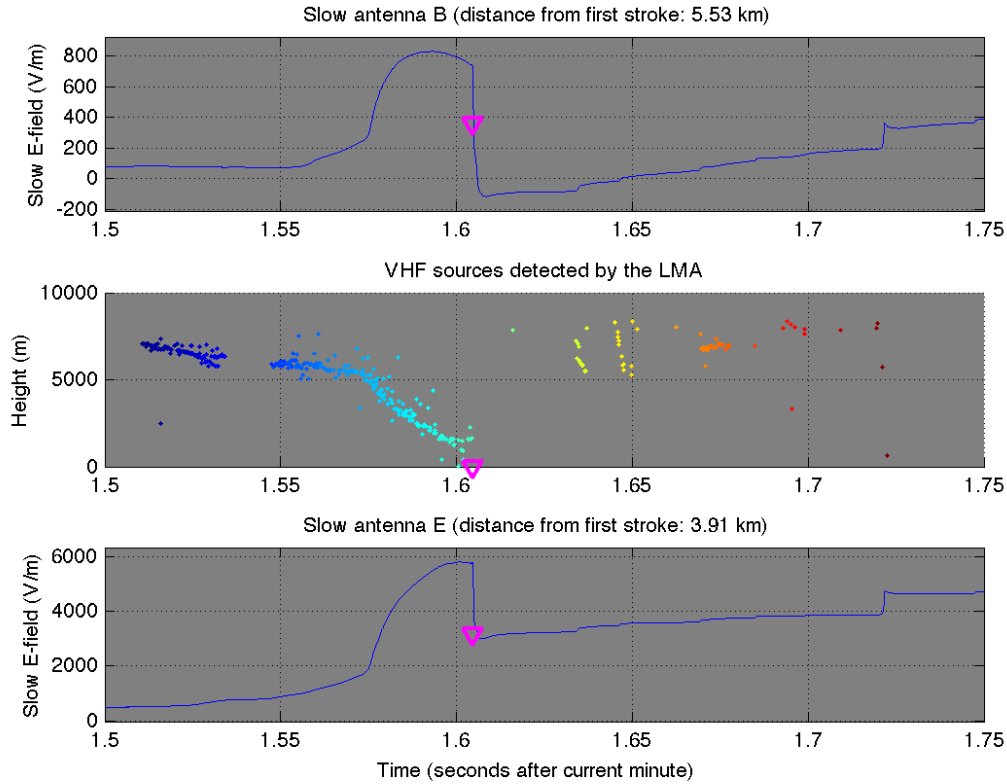
Figure 6.38 – LMA plot of the attempted leader.



See description of Figure 6.1.

Source: produced by the author.

Figure 6.39 – LMA sources height *versus* time plot compared with the electric field records of the attempted leader.



The down-pointing magenta triangles correspond to the return stroke time as estimated by the NLDN.

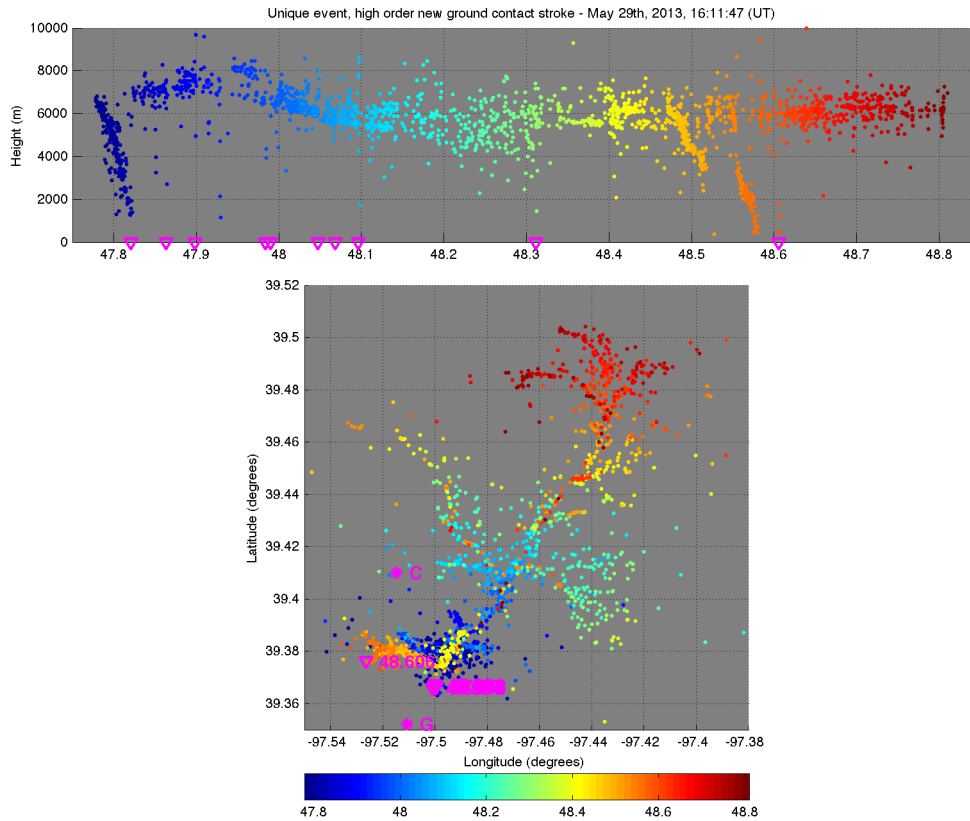
Source: produced by the author.

6.3.2. New ground contact of high stroke order: May 29th, 2013, 16:11:47 (UT)

The other unique event that was analyzed in this study is a NGC stroke of order ten that was preceded by nine strokes that shared a single ground termination. This event occurred on May 29th, 2013, at 16:11:47 (UT). The nine first strokes occurred between 16:11:47.821 (UT) and 16:11:48.312 (UT), with the tenth, NGC stroke occurring at 16:11:48.606 (UT), 294 milliseconds after the preceding PEC stroke at a GCP about 2.5 km away from all preceding strokes and with an estimated peak current of -16.4 kA. The full flash development of this case is shown in Figure 6.40. Different branches and regions of horizontal development were responsible for producing each subsequent

stroke as time advanced and the in-cloud leader propagated further northeast of its original inception region (and GCP of the first stroke).

Figure 6.40 – High order NGC stroke, full flash LMA plot.



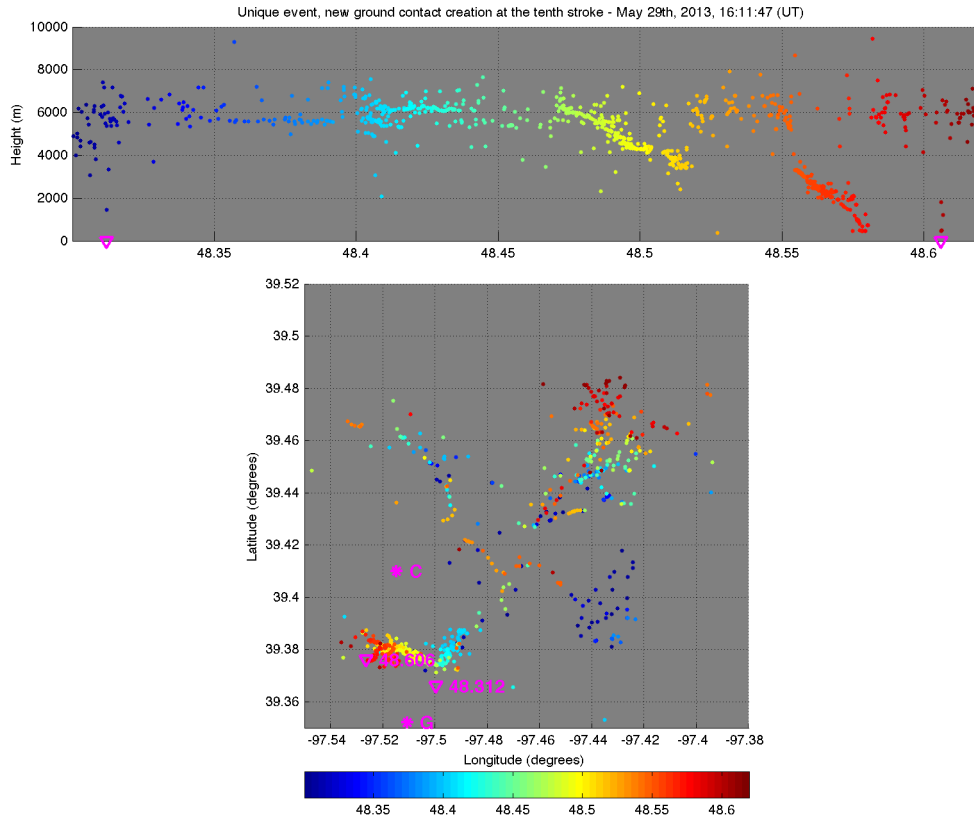
See description of Figure 6.1.

Source: produced by the author.

The initiation of the tenth (NGC) stroke can be better visualized if only its preceding interstroke interval is plotted, as in Figure 6.41. The northeastern branches seem to be the origin of three different attempted leader processes. The first one occurs around 16:11:48.400 (UT) about 6 km above ground, propagating mostly horizontally. Another one seems to occur about 70 milliseconds later (light green and yellow sources), reaching 4 km heights. Finally, a third attempted leader occurs after 16:11:48.550 (UT), developing from about 3.3 km above ground down to 470 m at 16:11:48.580 (UT). The tenth, NGC stroke finally occurs at 16:11:48.606 (UT), about 26 milliseconds after the

interruption of the third (and last) attempted stroke. The three sources detected right above the NGC (dark red on the top panel of Figure 6.41) indicate that the stroke was preceded by a dart leader that started to propagate in a stepped fashion in the final hundreds of meters before reaching ground.

Figure 6.41 – LMA plot of the initiation of the tenth (NGC) stroke.



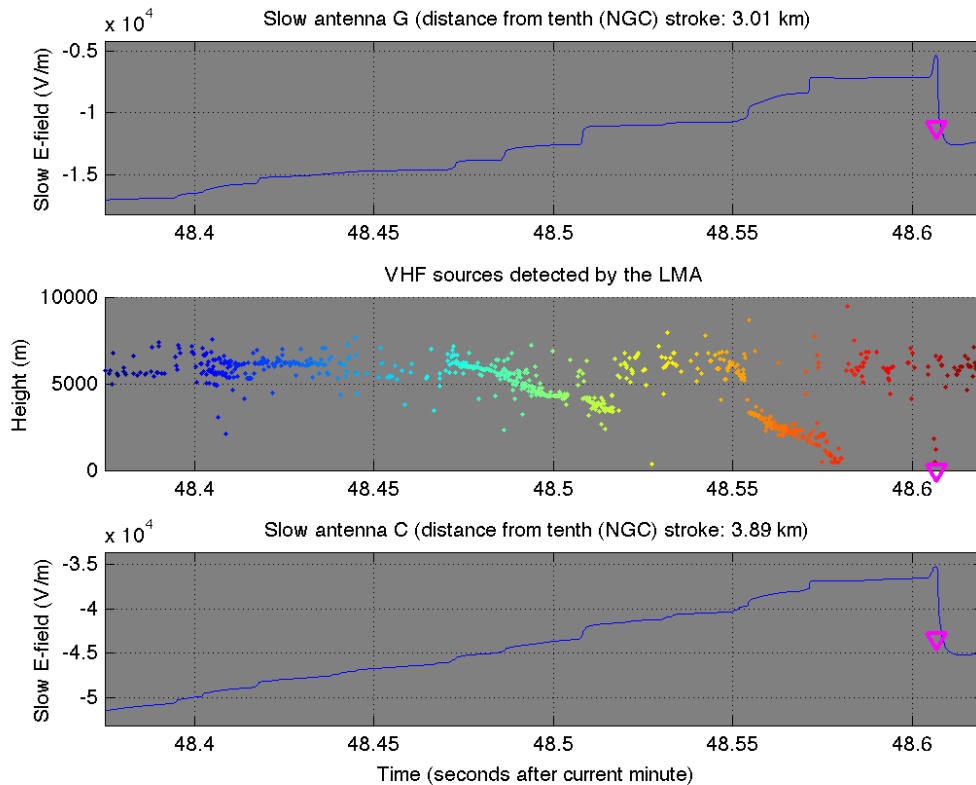
See description of Figure 6.1.

Source: produced by the author.

Figure 6.42 shows the measurements of the two electric field antennas closest to the GCP of the tenth stroke, along with the LMA source height *versus* time plot. Only the final 230 milliseconds leading to the NGC are shown in order to facilitate the visualization of the details of the waveforms. Even though the electric field is constantly increasing, the only signatures that can be found are short duration steps that are concentrated during the period of development of each downward attempted leader that

preceded the tenth stroke. This suggests that the changes are probably related to progressive charge deposition by each of the attempted leaders that further develop the channel that is later followed by the tenth and final stroke of the flash.

Figure 6.42 – LMA sources height *versus* time plot compared with the electric field records preceding the high order NGC stroke.



The down-pointing magenta triangles correspond to the time of the tenth return stroke as estimated by the NLDN.

Source: produced by the author.

The matter of how unlikely a NGC stroke is at higher orders have been previously discussed by a number of researchers, as summarized in subsection 2.5.5 of the literature review of this thesis. Apparently the NGC strokes of highest order in the existing literature were the two ninth strokes reported by Ferro et al. (2012, Section 3.2 and Figure 1), but no details are given concerning the number of strokes that occurred in the previous channel to ground. The preceding interstroke interval, 294 milliseconds

long, was probably responsible for the NGC creation. One possible cause might be the presence of intense horizontal winds dissipating the lower, vertical part of the preceding ionized channel to ground, without significantly affecting the upper, in-cloud horizontal segments (which was re-utilized by the tenth stroke). This is probably the highest order NGC stroke to be documented in detail.

6.4. Concluding remarks

This chapter presented an extensive analysis of the ways a –CG flash can produce multiple ground terminations, leading to the identification of three basic mechanisms/scenarios (illustrated in Figures 6.12, 6.23 and 6.36). Despite the small sample of each class of event, there seems to be a relationship between the process of NGC creation and the horizontal distance between the resulting GCP and the preceding return strokes.

No clear correlation between a characteristic electric field change signature and the creation of a NGC was found, as previously suggested by Krehbiel (1981). Although in two of the six Type I events step-like changes were identified (Cases I.1 and I.2, see Figures 6.4 and 6.10), that was not repeated consistently in the other four events of that class. Additionally, electric field records of one case of attempted leader that diverged from its preceding stroke channel (Figures 6.37 and 6.39) points toward the presence of low level stranded charges that possibly forced it to leave the original channel to ground even though no characteristic field signature was observed. Future analyses may provide a better idea not only of how frequent these field changes are but also if there are other mechanisms through which charges may be accumulated on a channel to ground and if they are one of the possible causes of NGC strokes in a subset of such events. The conclusion of this analysis, however, is that it is not a requirement for a subsequent stroke to create a new ground termination.

Although Types II and III were at least twice as common as Type I in the analyzed sample, the number of events is not sufficiently large to provide clear insight about their relative incidence.

7 REGIONAL DISTRIBUTION OF MULTIPLE GROUND CONTACT FLASHES AND THEIR CHARACTERISTICS

This chapter presents an analysis of the regional variations of the characteristics and parameters of multiple ground contact flashes and their possible relation with local terrain. Three very distinct domains of the United States were studied based on 11 years (2004-2014) of lightning information provided by the U.S. National Lightning Detection Network (NLDN) and topographical data obtained with the help of the Shuttle Radar Topography Mission (SRTM) that was conducted in February, 2000, onboard the space shuttle *Endeavour*. All lightning data was processed by the *groupGCP* algorithm (described in Chapter 4) in order to group individual return strokes into ground contact points. A discussion of the results and main conclusions is presented at the end of the chapter.

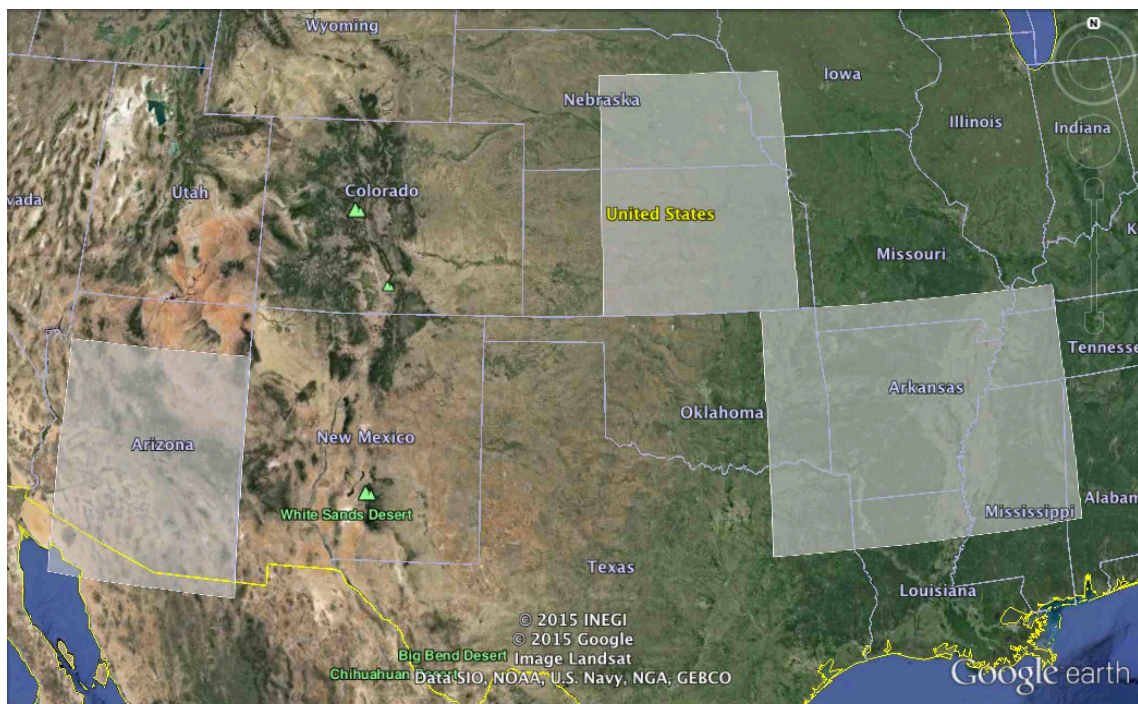
7.1. Domains, datasets and computational process

For this analysis, lightning data has been provided by the U.S. NLDN (described in subsection 3.2.1.2) for the full 11-year period from 2004 to 2014, after an important upgrade in 2003 (CUMMINS; MURPHY, 2009). Only negative cloud-to-ground (–CG) events were considered and an initial filter was applied in order to reduce the probability of false ground contact points (CGPs) due to poorly located return strokes. This filter removed all strokes whose NLDN solution was reported by less than five sensors, had a chi-squared value greater than 5.0 and a semi-major axis (SMA) greater than 0.8 km. Also, if the first stroke of a given flash did not fulfill these requirements, the entire flash was ignored. This reduced the dataset by about 27% to 55%, depending on the domain and year being processed.

Three different domains were considered in the analysis, as shown in the map of Figure 7.1. From west to east, the domains (and their respective total areas) enclose (i) Arizona and part of northern Mexico (5x5 degree); (ii) Kansas and Nebraska, with parts of Iowa (5x5 degree); and (iii) Arkansas and Mississippi, with parts of Tennessee, Missouri, Oklahoma and Louisiana (5x8 degree). From now on they will be referred to by name of state that corresponds to the majority of its territory, i.e., Arizona, Kansas and

Arkansas, respectively. They were chosen in order to represent three very distinct orographic scenarios, as their respective subsections describe in detail. The lightning data files obtained for each of the three domains were processed by the *groupGCP* algorithm with the following input parameters: *maxSMA_grouping* was set to 0.2 km and both *maxScaleFactor* and *pScale* to 2.0 (refer to Chapter 4 for a definition on each parameter).

Figure 7.1 – Relative positions of the three domains considered in this analysis.



Source: produced by the author based on the Google Earth software (GOOGLE, 2015).

Digital elevation data for the domains were obtained from the database of the Shuttle Radar Topography Mission (SRTM), described by Farr et al. (2007) and made available online by the United States Geological Survey (USGS, 2016).

There are many different steps in computing the data used in this analysis. All programs that were used for data processing and visualization were developed by the author using MATLAB. The sequence of the main steps can be outlined as follows:

1. lightning data were obtained from the U.S. NLDN as large (with sizes between 80 MB and 600 MB) text files, one for each year for each domain. They were processed by the *groupGCP* algorithm (Chapter 4), which is responsible for generating new text files with additional fields specific on the GCPs that were calculated;
2. SRTM terrain information were downloaded from the USGS (2016) data distribution website as GeoTIFF files with 3-arcsecond resolution. Those files were then loaded, smoothed and decimated by a factor of 10 (i.e., its resolution was reduced to 30-arcsecond, about 1 km horizontally) and used as reference for the creation of two-dimensional matrices that can map each lightning;
3. each –CG flash of the post-processed lightning data files (with GCP grouping information) was analyzed and mapped to the matrices created at step 2, with all its parameters of interest (number of GCPs, separation distance between them, performance-related LLS parameters, etc.) stored and indexed according to its location, then saved as *.mat* files (one for each year);
4. after multiple years have been analyzed (in the case of this study, 11 years), the *.mat* files were loaded by another program that aggregates them into multi-year mean value maps;
5. finally, the multi-year maps were converted into figures with overlaid constant altitude contour lines obtained from the terrain data in order to facilitate their comparison.

The comparison between lightning and terrain data included not only information on absolute altitudes but also spatial-frequency terrain variations. The latter were obtained computationally from the GeoTIFF altitude data files, as described in subsection 7.3.

7.2. Previous works and hypothesis outline

Bourscheidt et al. (2009) showed that, in the south of Brazil, terrain slope was more influential over the density of –CG flashes than the altitude. More recently, a discussion

was initiated by Cummins (2012) and further developed at later works (e.g., CUMMINS, 2014) concerning the possible influence of high spatial frequency terrain variations (and not absolute altitude) on the process related to lightning attachment to ground. Cummins (2012, 2014) found the occurrence of higher values of the mean number of channels per flash to be associated with high spatial frequency terrain variations in one domain, while in another it generally occurred in areas with higher terrain gradient. However, the methodology used by Cummins (2012, 2014) for the identification of NGC strokes depends explicitly on the rise-time of the return stroke, a parameter that seems to be impacted by the elevation in one of the domains he analyzed.

Cummins (2014) lists two main possible mechanisms through which complex terrain features and high spatial frequency terrain variations may affect the incidence and characteristics of MGCFs:

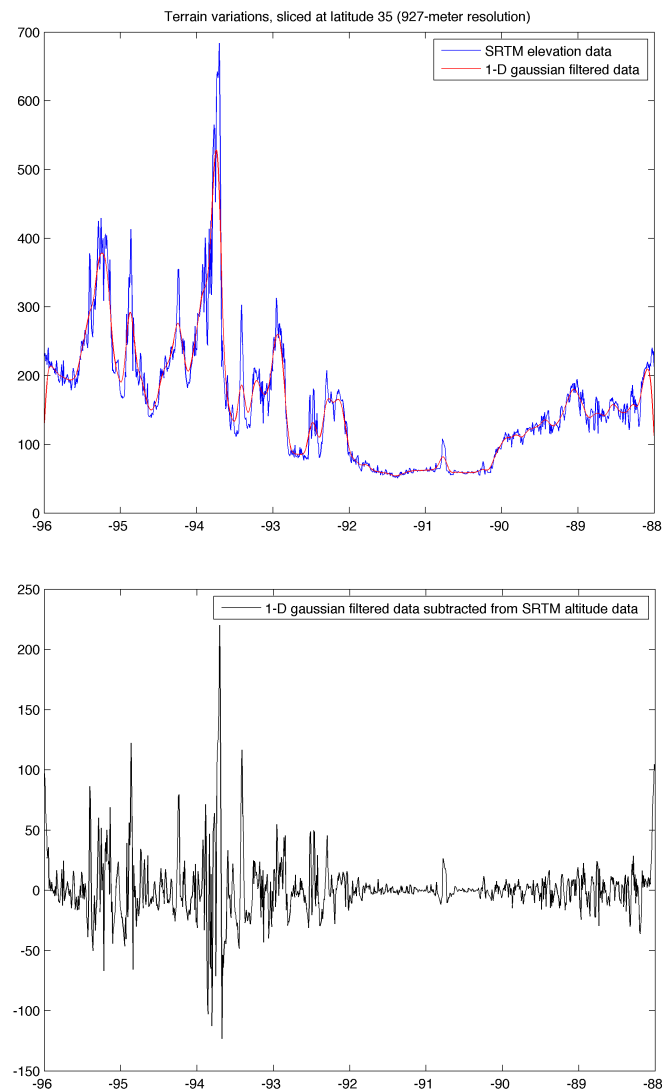
1. surface-driven turbulence caused by the orography, which may be responsible for causing inhomogeneities in the space charge distribution underneath an electrified thundercloud;
2. local enhancement of the electric field induced by the thunderstorm charge distribution, leading to well localized areas with higher near-surface electric fields. During the development and “final jump” attachment processes of a downward propagating leader, it is possible that these areas present themselves as equally likely, “concurrent” strike points, increasing the probability of a subsequent stroke to produce a new ground termination with specific separation distances.

If either (or both) mechanisms are influential over the creation and characteristics of NGC strokes, one might expect that the spatial distributions of accumulated multi-year lightning data can reveal patterns that are consistent among different domains. This hypothesis is evaluated through the analysis described in this chapter.

7.3. Obtaining spatial frequency terrain variations

Maps representing the spatial frequency variations of the terrain on each of the domains were obtained by a process that is illustrated in Figure 7.2 for one dimension. The blue line in the top plot corresponds to an altitude profile at latitude 35° of the Arkansas domain. A Gaussian filter is applied to that profile, resulting in the red line (shown in the same plot), in which most of the high spatial frequency variations were removed. By subtracting the filtered curve from the original one, only the peaks corresponding to the high frequency variations remain, as shown by the black line in the bottom plot of Figure 7.2.

Figure 7.2 – One-dimensional illustration of the process of obtaining terrain spatial frequency.



Source: produced by the author.

This basic process, extended to two dimensions, was applied to the SRTM terrain data for the three domains, and the resulting maps are shown in the next section, where the results of this analysis are presented.

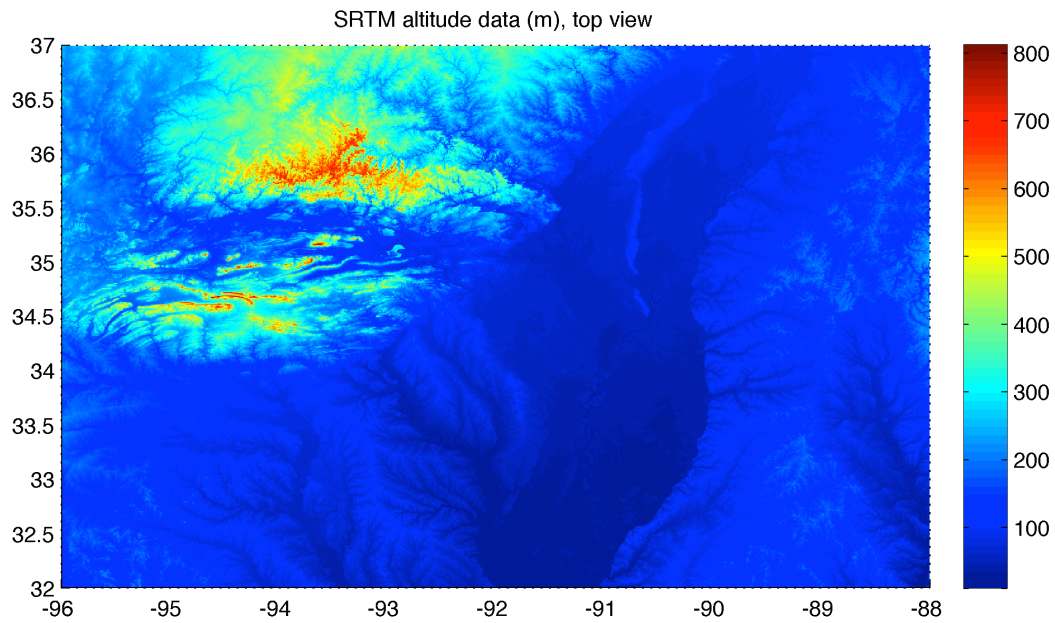
7.4. Results and discussions

Results for each of the three domains (Arkansas, Arizona and Kansas) are discussed in turn, stressing the particular characteristics of each one of them individually. The parameters that were considered are the return stroke density (considering only multi-stroke flashes), the mean number of channels per flash (CPF, considering both single- and multi-stroke flashes) and the mean separation distance between the first two ground contacts of each MGCF. The latter was considered so that each MGCF provided a single measurement for the statistical analysis. Also, the spatial resolution is the same for all plots of all domains, with approximately one kilometer between data points in both north-south and east-west directions. The only exceptions are the terrain variation maps, which were processed at a higher resolution (about 460 meters) in order to avoid missing small scale relevant information.

7.4.1. Arkansas

The altitude map of the Arkansas domain is shown in Figure 7.3, with the color bar values in meters. A smoothed version is presented in Figure 7.4, showing the constant altitude contour lines to be used as reference when comparing maps. This domain includes part of the Mississippi river to the east (the dark blue, low altitude region of the map) and the Ouachita and Ozark Mountains to the west (regions with altitudes above 300 meters). Spatial frequency terrain variations for this domain are shown in Figure 7.5. Note that the low altitude regions (to the east and south) present small, localized high frequency “filaments” surrounded by large extension low frequency regions. The mountainous regions, on the other hand, are characterized by high spatial frequencies over most of their extents. One may say that the Arkansas domain is characterized by the transition between a low altitude, low spatial frequency region and a large (about 4x3 degree) high altitude, high spatial frequency region. The differences in the MGCF parameters are discussed next.

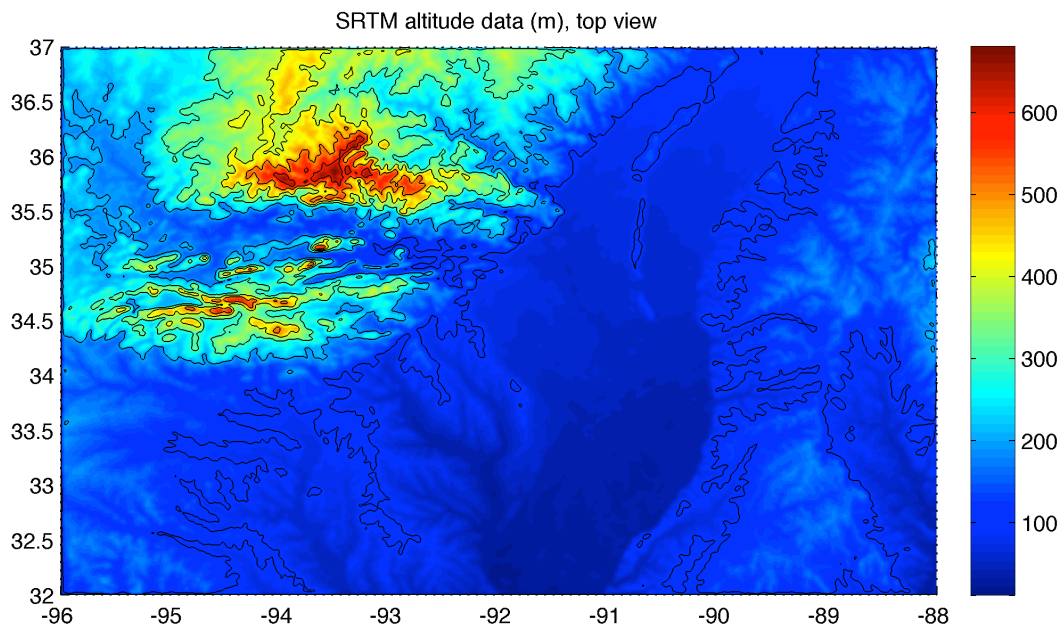
Figure 7.3 – Altitude map of the Arkansas domain.



The color bar to the right represents the altitude in meters.

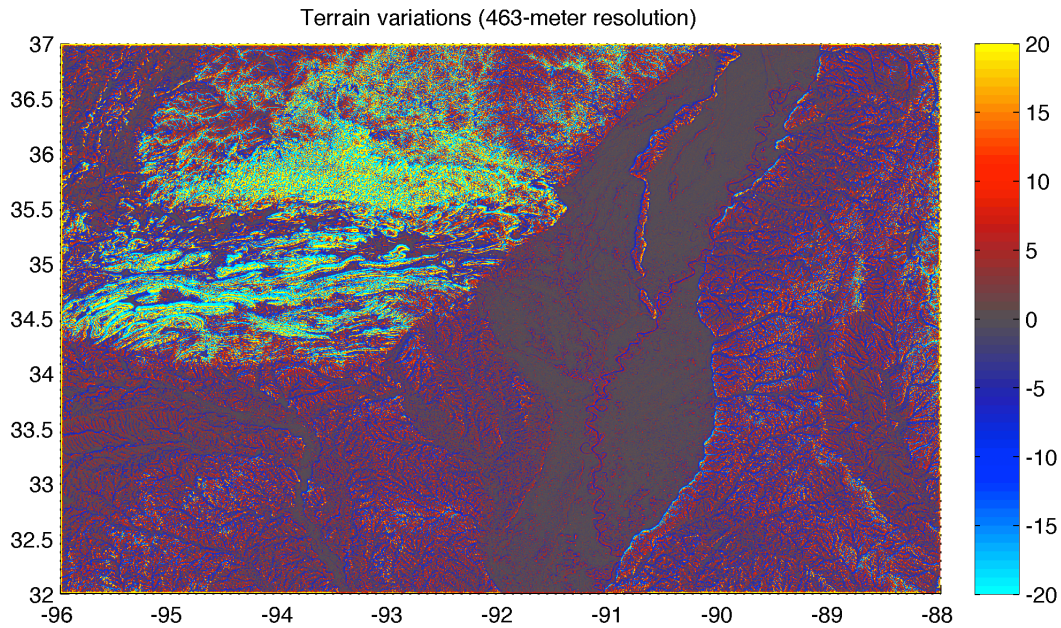
Source: produced by the author from data provided by the SRTM (USGS, 2016).

Figure 7.4 – Smoothed altitude map of the Arkansas domain with contour lines.



Source: produced by the author from data provided by the SRTM (USGS, 2016).

Figure 7.5 – Spatial frequency terrain variations of the Arkansas domain.

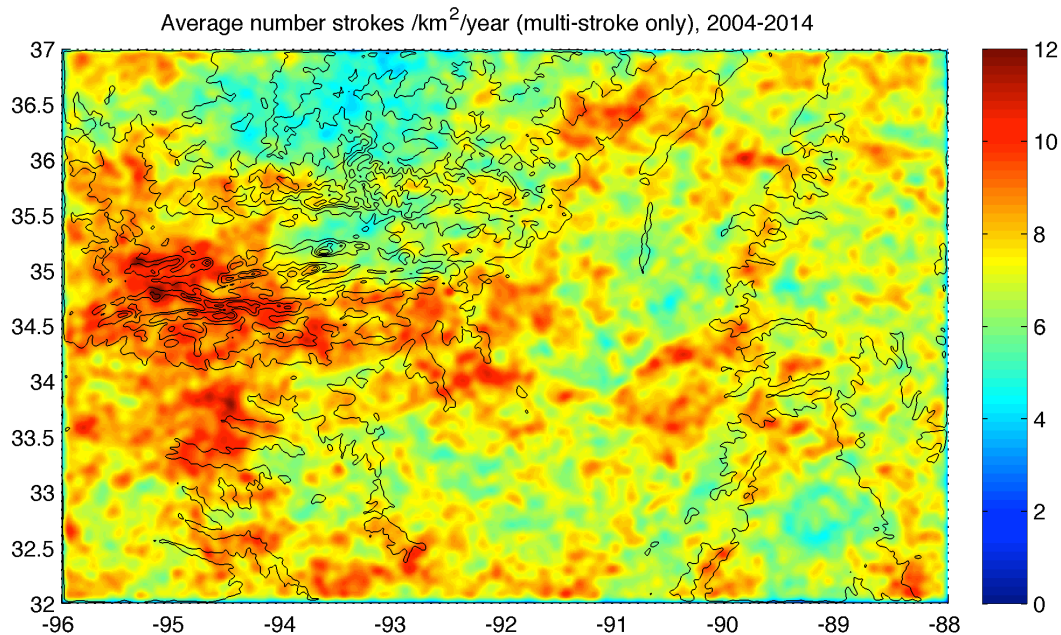


The color bar to the right attributes darker colors to low amplitude variations while lighter shades (towards both light blue and yellow) are associated with higher amplitudes.

Source: produced by the author.

The first parameter to be analyzed is the spatial distribution of the density of return strokes, defined in terms of number of strokes per square kilometer per year, shown in Figure 7.6. A significant part of the high-density regions (above 10 strokes/km²/year) are located at the transition from southern low altitude (and frequency) regions to the mountain ranges to the northwest of the domain. There is, however, a significant reduction at the northernmost mountains, with the density dropping to values closer to 6 strokes/km²/year. This is probably related to patterns of orographic thunderstorm development coming from the southern, low altitude regions, in addition to higher-elevation terrain blockage to the north of the domain. In the latter, on the other hand, there is no apparent correlation between either altitude or higher spatial frequency “filaments” and the density of return strokes, suggesting that a considerable horizontal extent is necessary for any effect to arise.

Figure 7.6 – Spatial distribution of the density of return strokes (from multi-stroke flashes only) of the Arkansas domain.

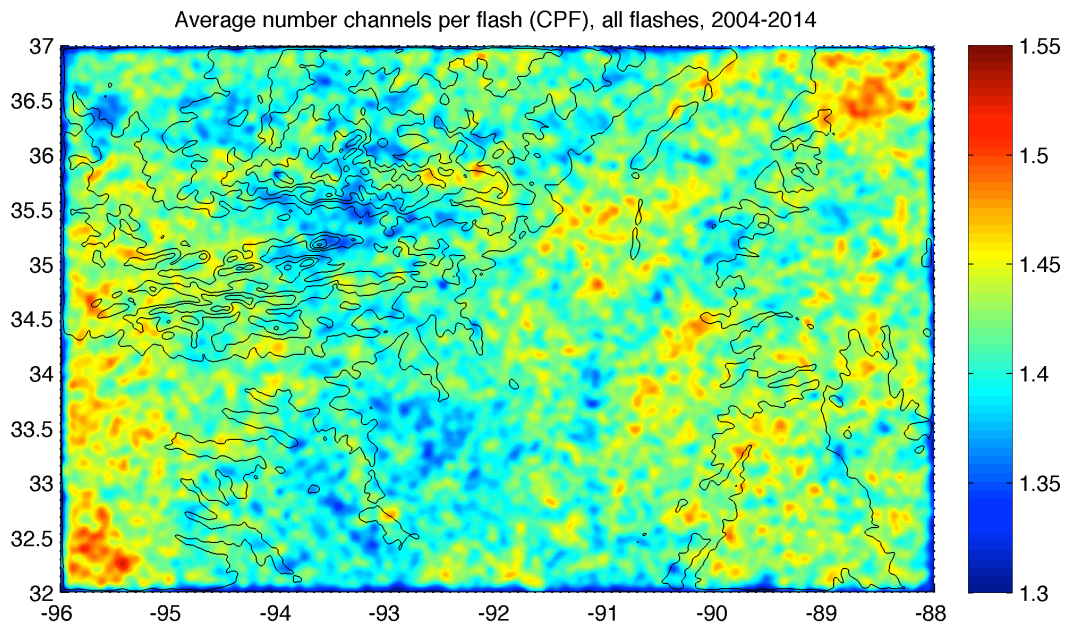


The color bar to the right is given in terms of number of return strokes per square kilometer per year.

Source: produced by the author.

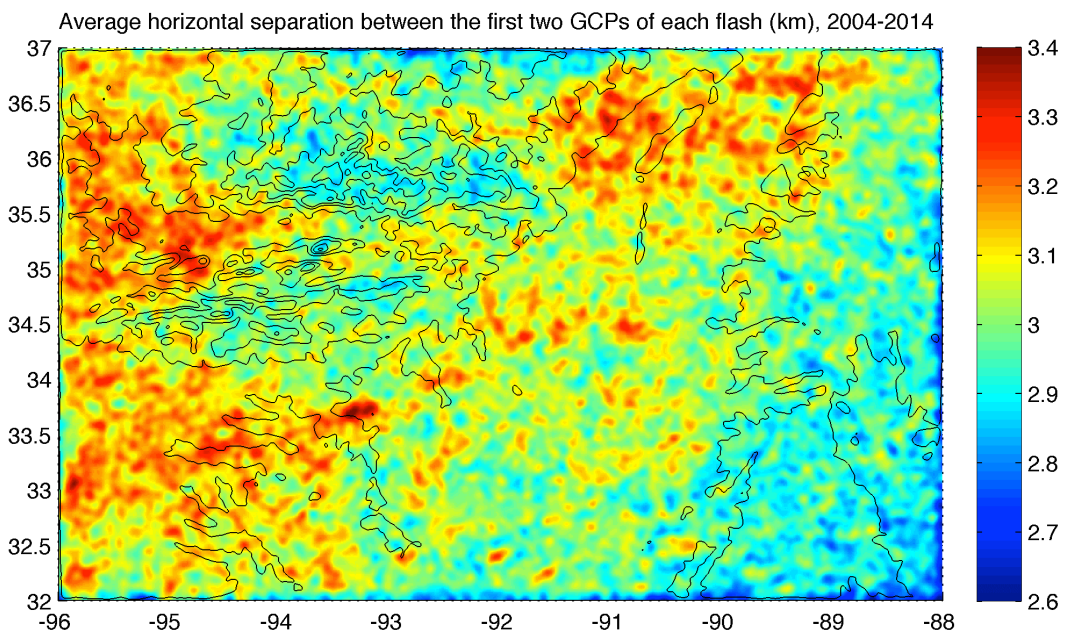
Figure 7.7 shows the spatial distribution of the mean number of channels per flash (CPF), including all flashes (single- and multi-stroke). For this parameter, in the Arkansas domain, no clear pattern could be found correlating it to either the altitude or spatial frequency variations. Low values of CPF (close to 1.3 channels per flash) were observed in both high and low frequency regions. On the other hand, the mean values of the horizontal separation distance between ground contacts (shown in Figure 7.8) seem to be affected by both high altitude and spatial frequency regions. In the region between the two mountain ranges at the northwest of the Arkansas domain it is possible to note that the mean separation distances drop to values below 3.1 km at altitudes greater than 350-400 meters. Figures 7.9 (smoothed terrain), 7.10 (spatial frequency) and 7.11 (mean separation distance) show the data on the mountainous regions in greater detail. Also, a similar correlation seems to be present at the eastern border of the domain as well, roughly coinciding with some of the high spatial frequency filaments (Figure 7.5).

Figure 7.7 – Spatial distribution of the mean number of channels per flash (CPF) of the Arkansas domain.



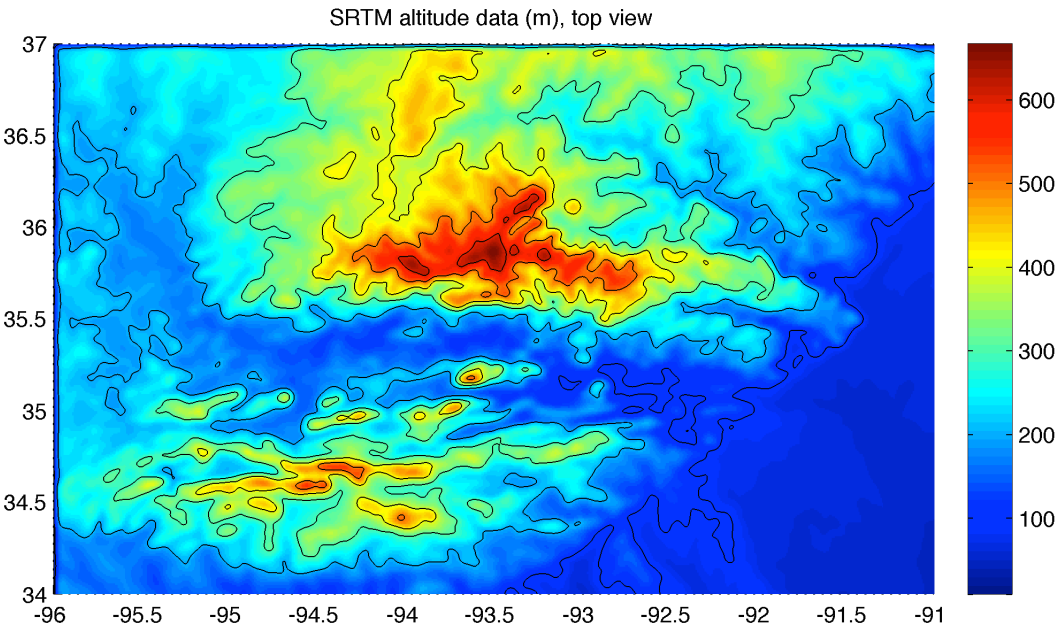
Source: produced by the author.

Figure 7.8 – Spatial distribution of the mean separation distance between the first two ground contact points of each MGCF of the Arkansas domain.



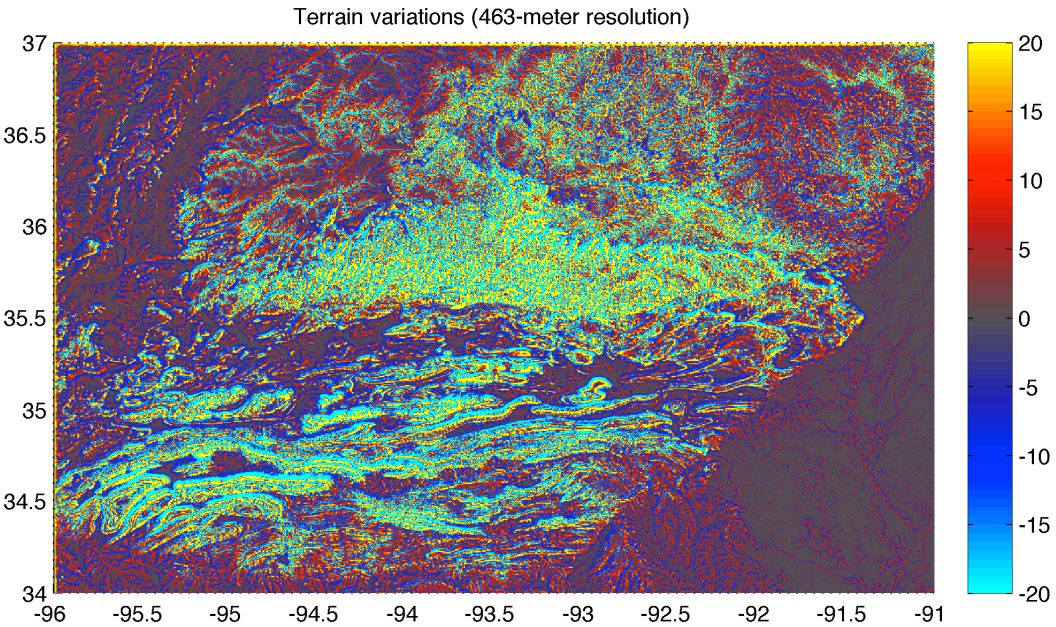
Source: produced by the author.

Figure 7.9 – Smoothed altitude map of the mountainous region of the Arkansas domain with contour lines.



Source: produced by the author from data provided by the SRTM (USGS, 2016).

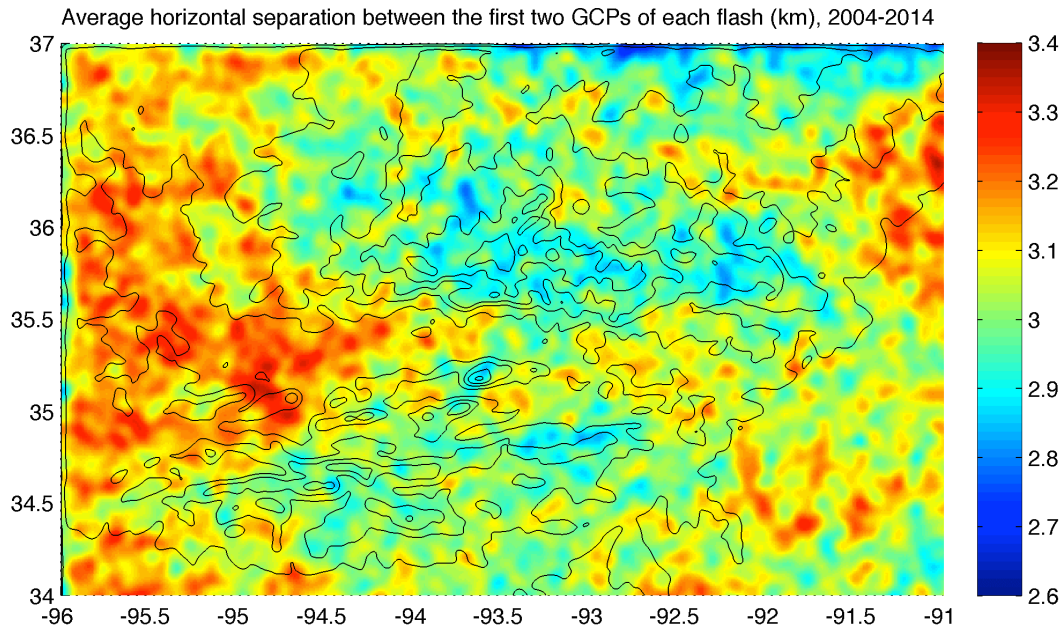
Figure 7.10 – Spatial frequency terrain variations of the mountainous region of the Arkansas domain.



See description of Figure 7.5.

Source: produced by the author.

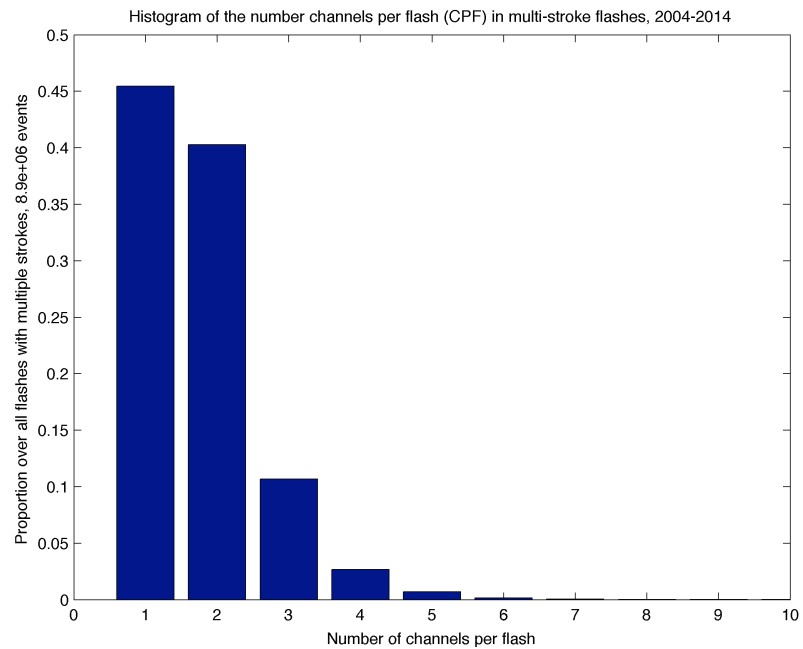
Figure 7.11 – Spatial distribution of the mean separation distance between the first two ground contact points of each MGCF of the mountainous region of the Arkansas domain.



Source: produced by the author.

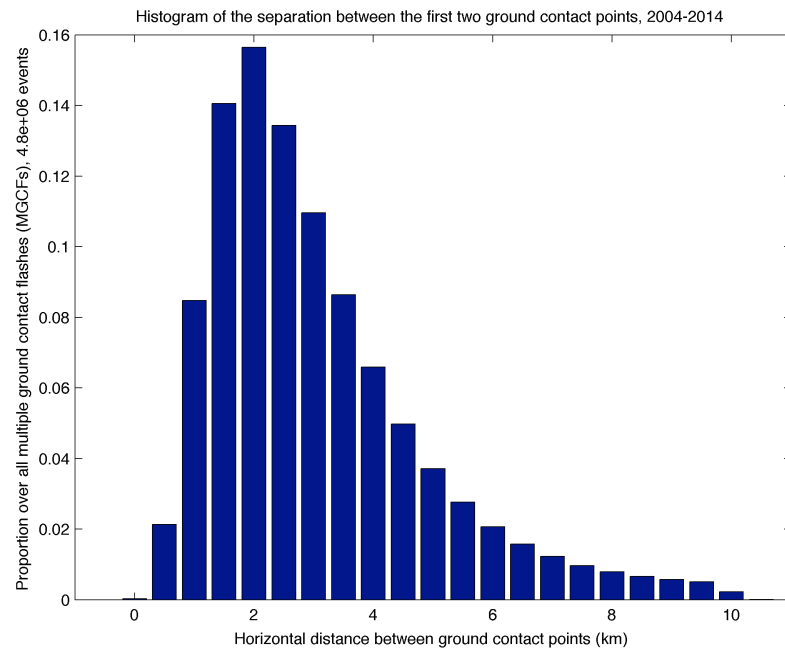
Histograms of the two parameters of MGCFs were obtained for the entire 11-year dataset, as shown in Figures 7.12 and 7.13. The histogram of CPF includes only multi-stroke flashes (with about 10^7 events), so that the one GCP bin includes only those that produced more than one return stroke. Single-channel flashes were the most common, although those with two ground terminations were almost as common. Also, note that the distribution rapidly decays above four channels per flash. Events with very high (above five) values of CPF were probably related to errors on either the *groupGCP* algorithm or in the NLDN dataset. Future versions of the algorithm, using additional LLS parameters, are expected to reduce the incidence of such misclassified events. The separation distance histogram has its bins centered at 0, 0.5 km, 1.0 km, etc., so the first bin corresponds to distances from 0 to 250 meters, the second from 250 m to 750 m, the third from 750 m to 1.25 km, etc. It has an approximately lognormal distribution, with its peak in the 1.75-2.25 km range. If one assumes that the ranges of distances observed in Chapter 6 for the three types of NGC stroke initiation are representative of their population, Type I possibly accounts for no more than 10% of all MGCFs.

Figure 7.12 – Histogram of number of channels per flash for multi-stroke flashes detected in the Arkansas domain.



Source: produced by the author.

Figure 7.13 – Histogram of the separation distance between the first two ground contact points of each MGCF of the Arkansas domain.



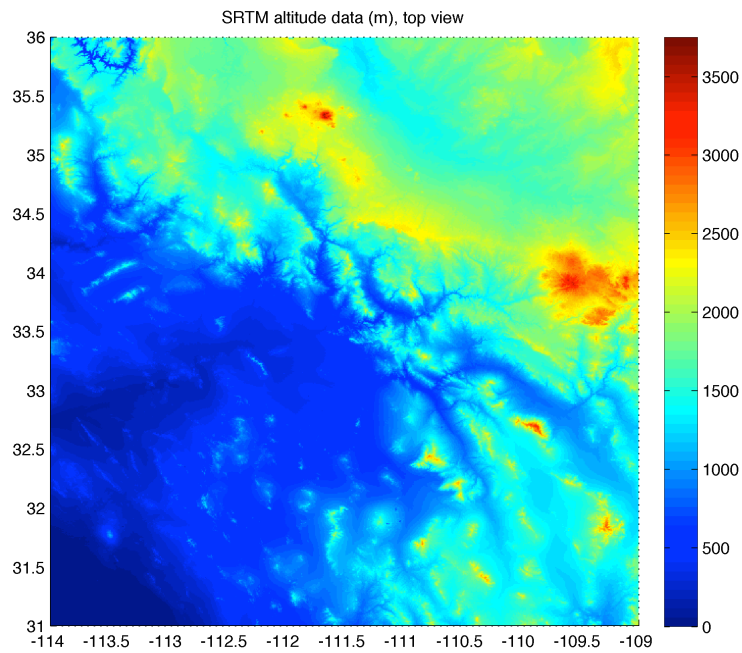
Source: produced by the author.

Spatial distributions of parameters related to LLS data quality are presented in Appendix B. Variations of the error ellipse semi-major axis (SMA), which may impact the performance efficiency (PE) of the *groupGCP* algorithm, were quite small over the entire Arkansas domain (Figure B.1). The mean chi-squared for stroke solutions was good (below 1.0 over most of the domain) and quite uniformly distributed, even in the higher altitude and spatial frequency regions (Figure B.2). The mean number of sensors reporting (NSR) did not drop significantly for return strokes detected at the northwestern mountainous regions (Figure B.3). Finally, the spatial distribution of the mean estimated negative return stroke peak currents seems to drop from 25-26 kA in the low altitude regions to 21-23 kA at higher altitudes (Figure B.4). However, even though this is an interesting result, the *groupGCP* algorithm does not depend explicitly on this parameter, so the observed spatial distribution should not affect its capacity to identify GCPs of flashes that occurred over the mountains.

7.4.2. Arizona

The altitude map of the Arizona domain and its smoothed version (with constant altitude contour lines) are shown in Figures 7.14 and 7.15, respectively. Its southwestern corner includes part of the northern edge of the Gulf of California, while the northwestern edge marginally includes part of the Grand Canyon. The main defining feature of this domain, however, is the sharp transition that cuts it roughly diagonally and includes the Mogollon Rim. From the center of the domain, going towards northeast, the altitudes change from a few hundred meters to 1500-2000 meters, with a few small features reaching over 3000-3500 meters. Other important orographic features become evident at the spatial frequency terrain variations shown in Figure 7.16. The small “islands” of elevated terrain at the southwestern quadrant of the domain (with altitudes close to 1500 meters and surrounded by regions at a few hundred meters) are well-localized regions of high spatial frequency, contrasting with the extensive elevated central feature. Finally, the northeastern corner of the domain remains at high altitudes (in comparison to the northwestern quadrant), although its regions of high spatial frequency are small, “filamentary” when compared to the central feature (where the great altitude transition is located).

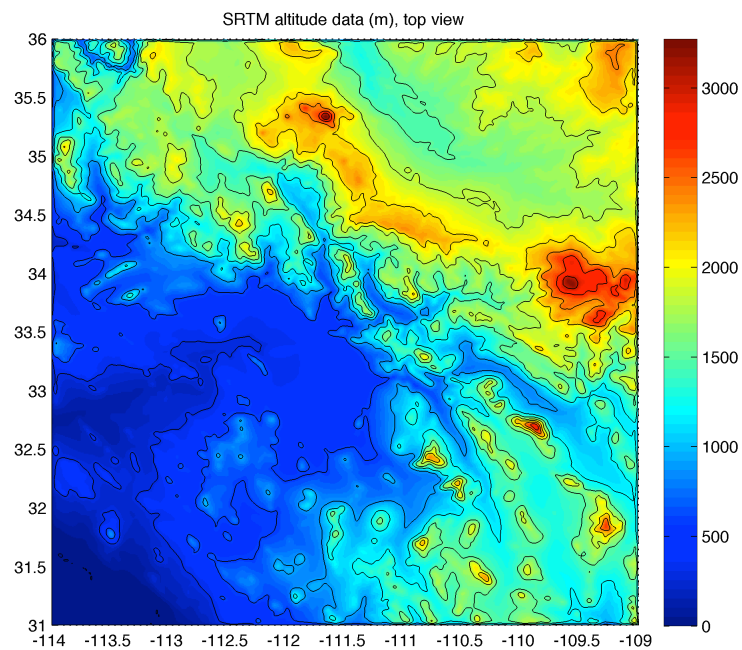
Figure 7.14 – Altitude map of the Arizona domain.



The color bar to the right represents the altitude in meters.

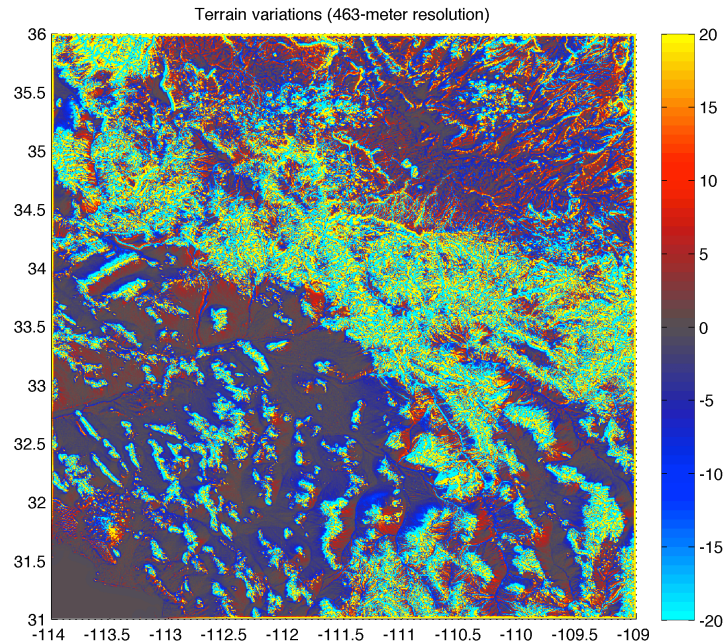
Source: produced by the author from data provided by the SRTM (USGS, 2016).

Figure 7.15 – Smoothed altitude map of the Arizona domain with contour lines.



Source: produced by the author from data provided by the SRTM (USGS, 2016).

Figure 7.16 – Spatial frequency terrain variations of the Arizona domain.



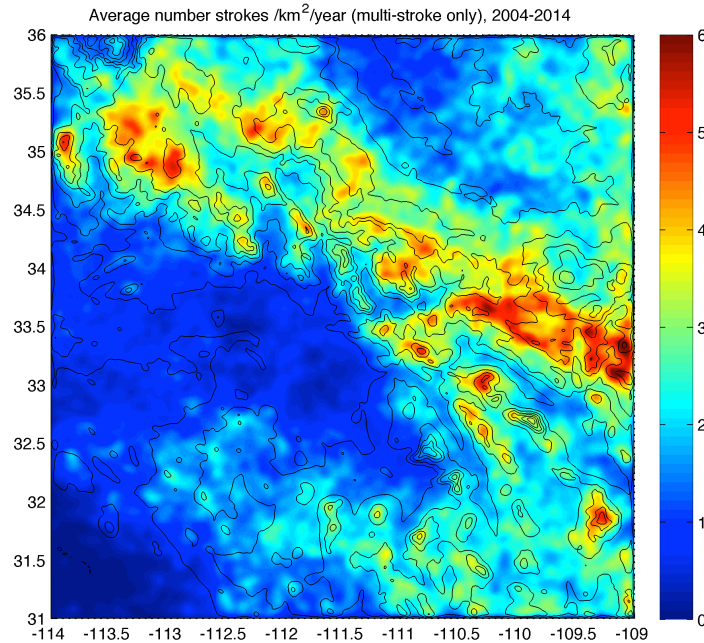
See description of Figure 7.5.

Source: produced by the author.

The density of return strokes per square kilometer per year, mapped in Figure 7.17, seems to correlate well with the spatial frequency map of Figure 7.16. Most of the regions with higher incidence (above 3 return strokes/km²/year) correspond to the higher spatial frequency feature that crosses the domain diagonally, although the higher density structures at the southeastern edge of the domain coincide with local peaks of absolute altitude. The northeastern corner also seems to be well correlated, as there is a significant drop in the return stroke density in the areas where the spatial frequency variations are also lower (darker features in Figure 7.17). One possible issue with this result, however, is the fact that the Arizona domain lies in the southern border of the U.S. NLDN, as evidenced by the maps of mean number of sensors reporting (NSR, Figure B.7) and mean estimated return stroke peak current (I_p , Figure B.8), shown in Appendix B. Strokes from a significant part of the low elevation (southern) area were reported by less than 10 NLDN sensors, favoring the detection of the most intense

return strokes (over 23 kA, compared to the mean values closer to 20 kA observed near the northern edge of the domain).

Figure 7.17 – Spatial distribution of the density of return strokes (from multi-stroke flashes only) of the Arizona domain.



The color bar to the right is given in terms of number of return strokes per square kilometer per year.

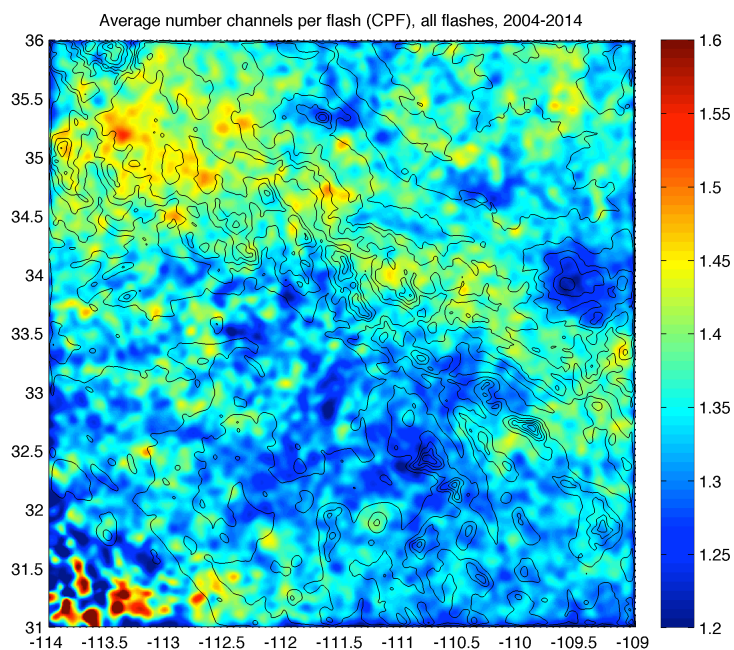
Source: produced by the author.

Spatial distributions of mean CPF and mean separation distance between contacts are given in Figure 7.18 and 7.19, respectively. One characteristic that is clearly visible is the significant reduction in both parameters over two of the most elevated points of the domain (above 3000 meters), where they drop to values close to the lower limit of the color bar of their maps (1.2 for CPF and 2.5 km for the separation distance). Other local altitude maxima (above 2500 m), further south, also were associated with low values of the separation distance (when compared with their vicinity), although that behavior was not repeated in the CPF spatial distribution. A similar effect was observed for Arkansas, as discussed in the previous subsection. The mean CPF also has a region of values above 1.4 coinciding with the diagonal region of high spatial frequency variations, but

its surroundings (both in the northeastern corner and the localized, high frequency spots to the southwest) does not seem to have a clear pattern when compared to both spatial frequency and altitude maps. On the other hand, the mean separation distance between contacts seems to be consistently impacted by the altitude not only in the local maxima previously mentioned but also over the entire region roughly located at the northeastern quadrant of the domain. In general, GCPs are more widely separated (over 3 km) at lower altitudes and closer together at higher locations. One data quality parameter that could impact the *groupGCP* algorithm performance and consequently this result, the spatial distribution of the mean SMA (shown in Figure B.5), is probably affecting only the southern edge of the domain, as mean values of 0.5 km and above were only measured to the south of latitude 32.5°.

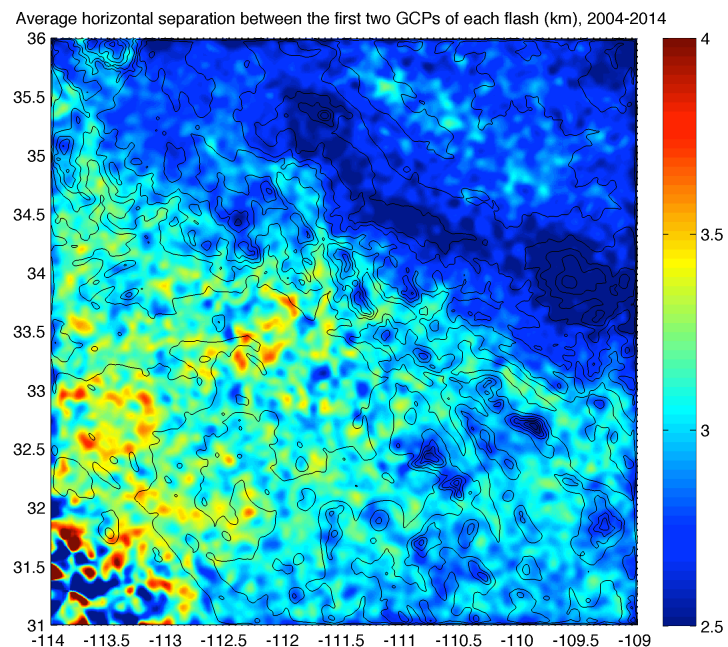
Histograms of CPF and GCP separation distance are presented in Figures 7.20 and 7.21. Also with large samples from the 11-year accumulated dataset (of the order of 10^6 events), both are very similar to their counterparts generated for the Arkansas domain (Figures 7.12 and 7.13). This suggests that, although specific characteristics of the spatial distributions of their mean values may change from domain to domain, their probability distribution are very similar when a sufficiently large region is considered.

Figure 7.18 – Spatial distribution of the mean number of channels per flash (CPF) of the Arizona domain.



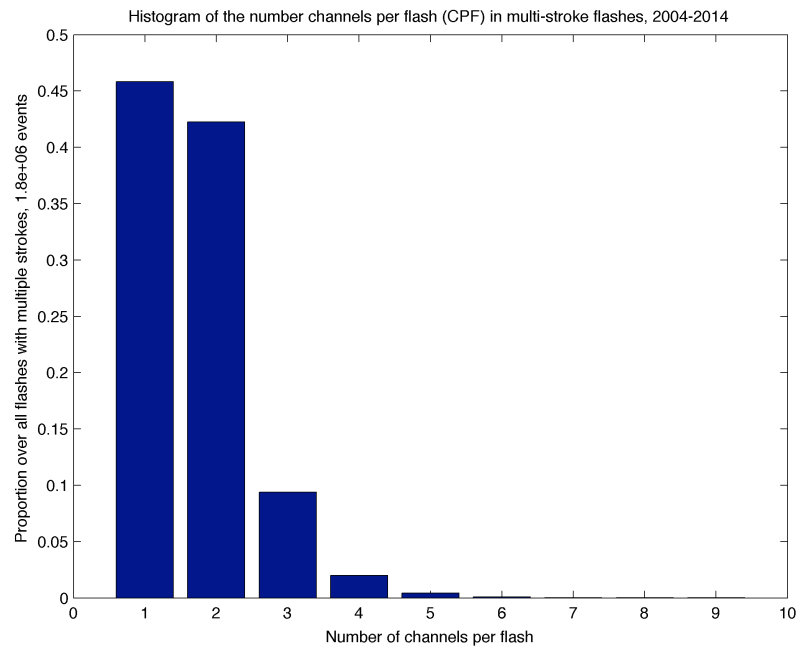
Source: produced by the author.

Figure 7.19 – Spatial distribution of the mean separation distance between the first two ground contact points of each MGCF of the Arizona domain.



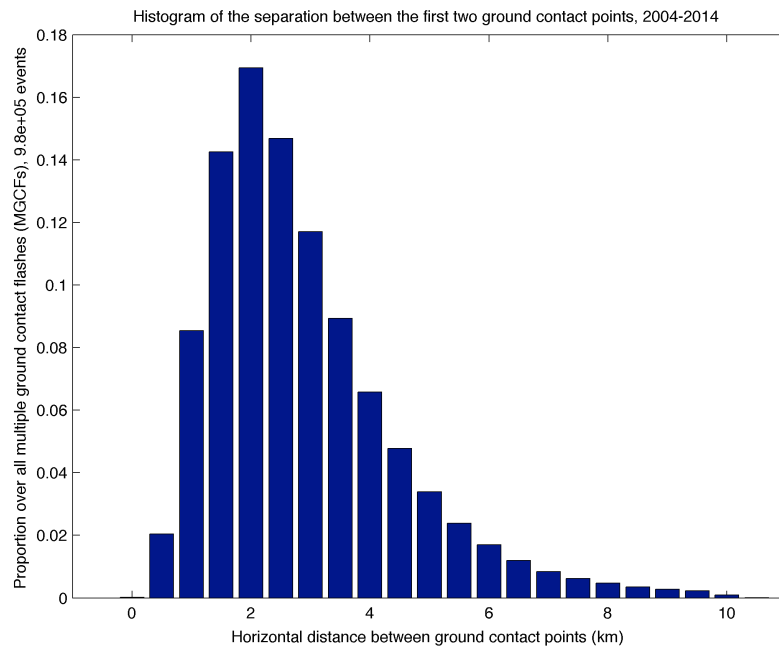
Source: produced by the author.

Figure 7.20 – Histogram of number of channels per flash for multi-stroke flashes detected in the Arizona domain.



Source: produced by the author.

Figure 7.21 – Histogram of the separation distance between the first two ground contact points of each MGCF of the Arizona domain.

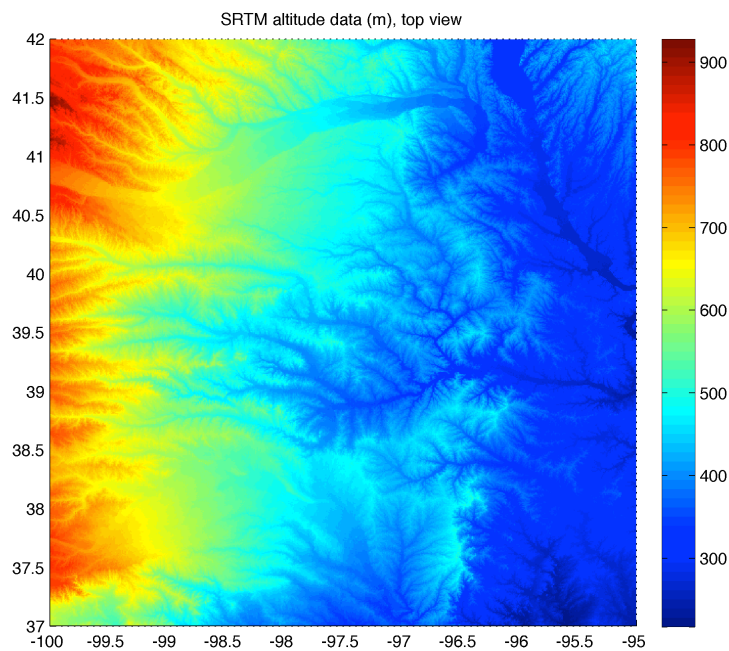


Source: produced by the author.

7.4.3. Kansas

The Kansas domain, whose altitude maps are shown in Figures 7.22 and 7.23, includes part of the eastern edge of the Great Plains, with a gradual increase in altitude from east to west. In contrast with the other two domains analyzed in the previous subsections, Figure 7.24 shows that the Kansas domain has no characteristic, extensive region of high spatial frequency variations, presenting only a few well-localized filamentary structures with higher frequencies. It is worth noting that the region where the observational studies conducted during the KSWFP is near the center of this domain. Also, as shown in Figure 7.01, the southeastern edge of the Kansas domain is connected to the northwestern edge of the Arkansas domain.

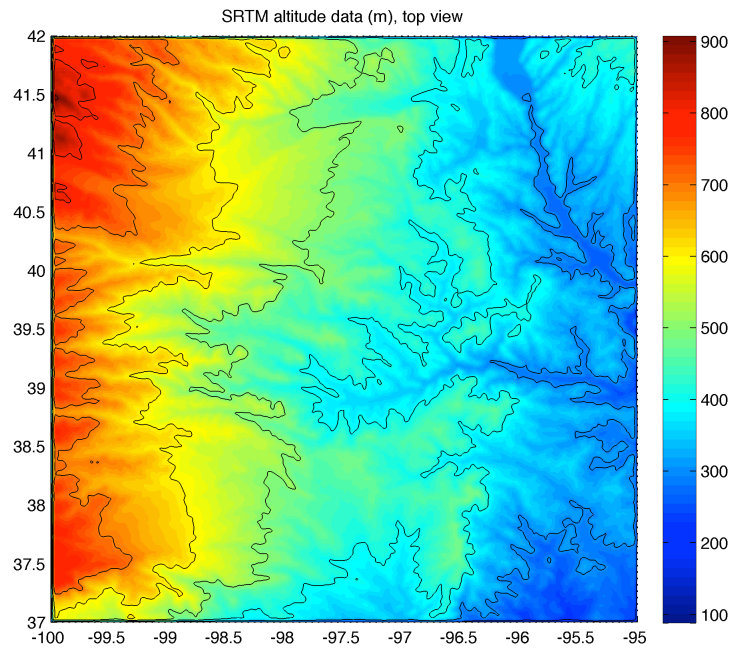
Figure 7.22 – Altitude map of the Kansas domain.



The color bar to the right represents the altitude in meters.

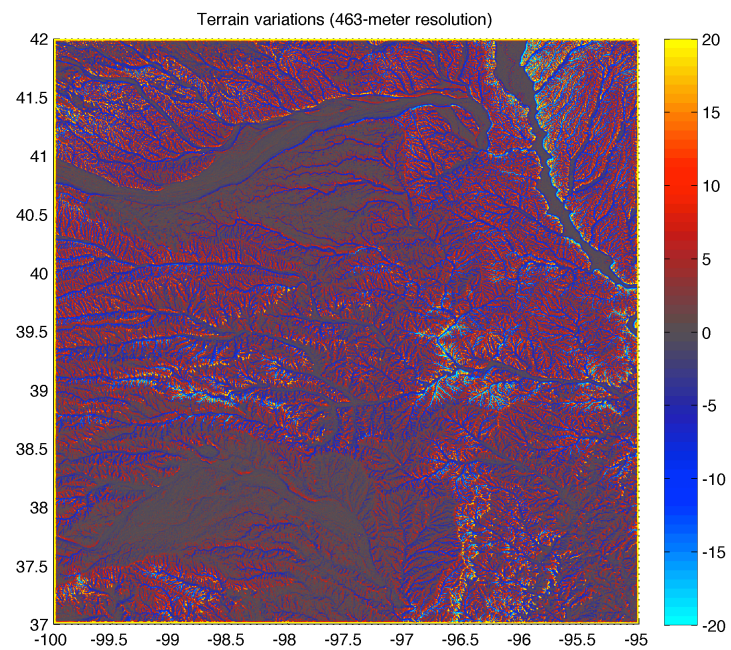
Source: produced by the author from data provided by the SRTM (USGS, 2016).

Figure 7.23 – Smoothed altitude map of the Kansas domain with contour lines.



Source: produced by the author from data provided by the SRTM (USGS, 2016).

Figure 7.24 – Spatial frequency terrain variations of the Kansas domain.

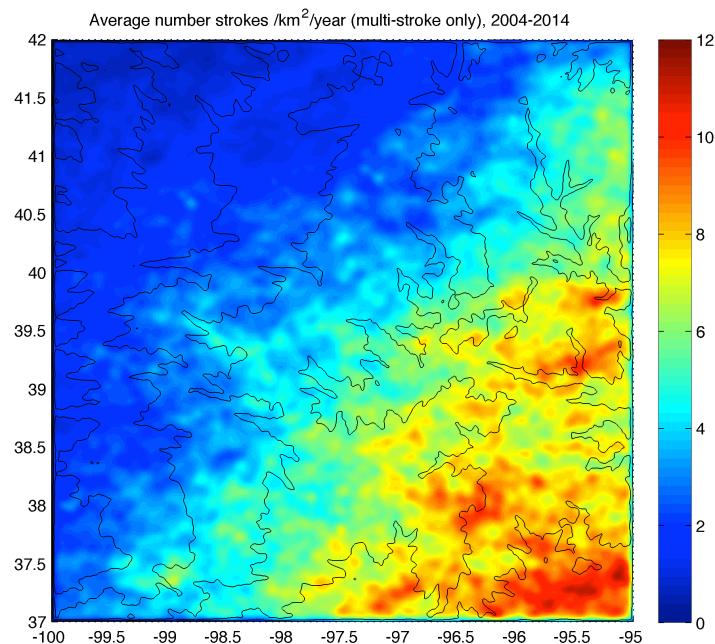


See description of Figure 7.5.

Source: produced by the author.

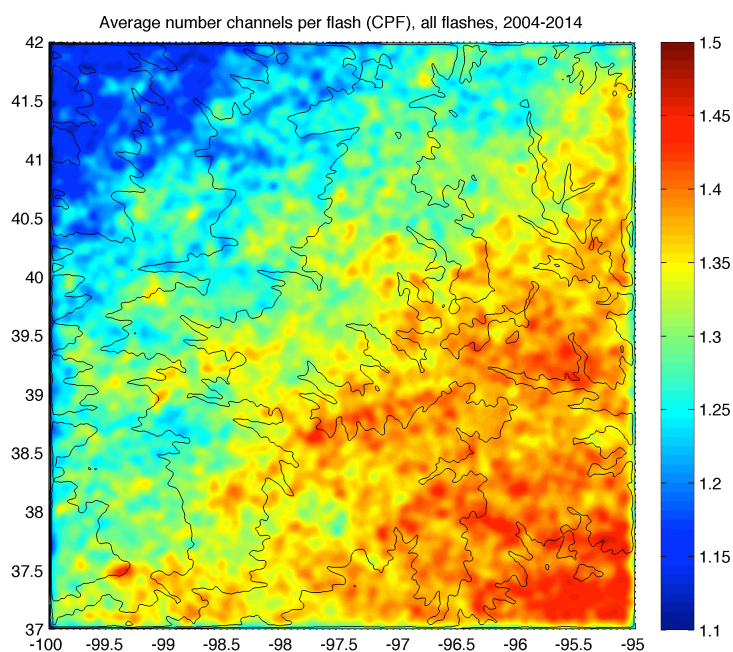
The spatial distribution of return strokes per square kilometer per year, shown in Figure 7.25, is characterized by a “hotspot” in the southeastern edge (with values greater than 12 return strokes/km²/year, in agreement with the neighboring values of the Arkansas domain, as seen in Figure 7.6) that is gradually “dissipated” if one moves towards the northwest. A very similar pattern is seen in the spatial distribution of mean CPF, shown in Figure 7.26, with a decrease in the number of ground contacts per flash when going from southeast towards northwest. The mean separation distance between contacts (shown in Figure 7.27), however, seems to be characterized by a mostly homogeneous distribution of regions with larger separations (above 3.6 km) surrounded by lower values (3.2-3.4 km). The absence of horizontally extensive orographic features in this domain apparently allows that other factors drive the density of strokes and the spatial distribution of mean CPF values, even though these two parameters seem to be correlated.

Figure 7.25 – Spatial distribution of the density of return strokes (from multi-stroke flashes only) of the Kansas domain.



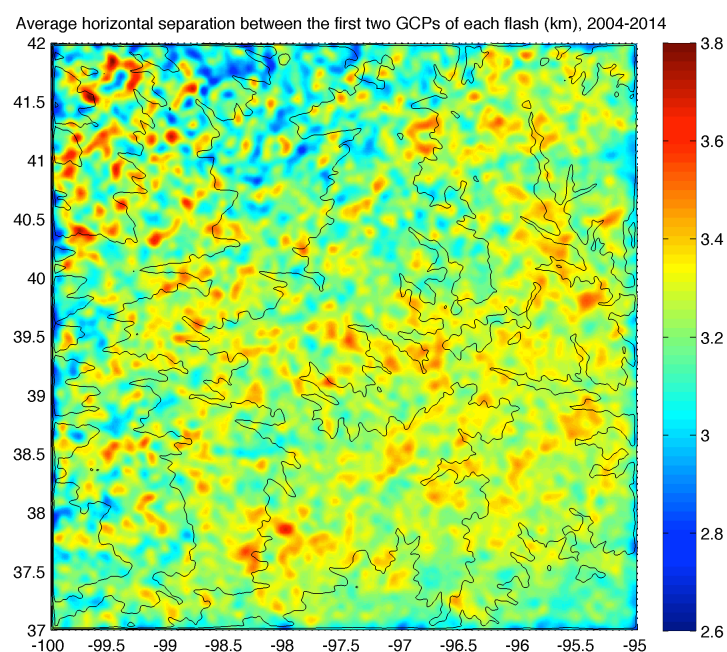
Source: produced by the author.

Figure 7.26 – Spatial distribution of the mean number of channels per flash (CPF) of the Kansas domain.



Source: produced by the author.

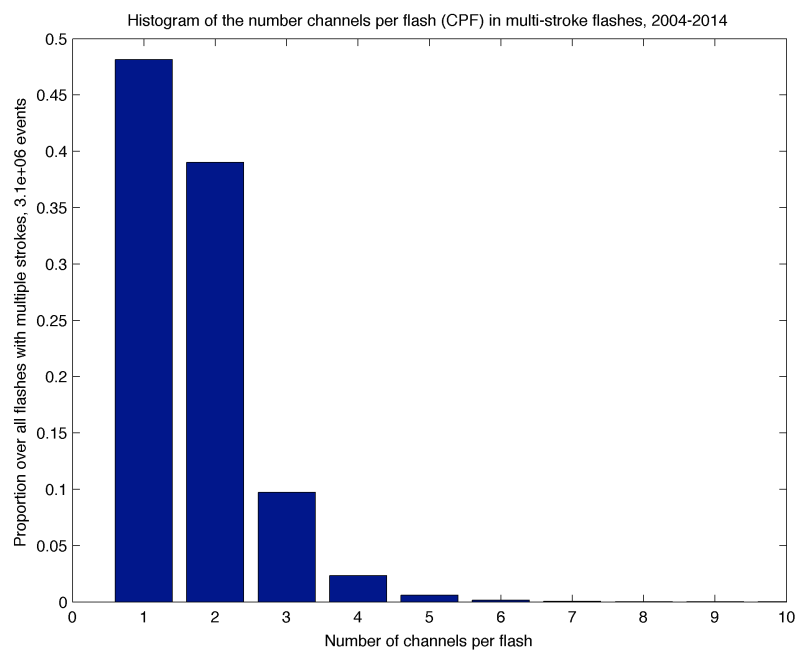
Figure 7.27 – Spatial distribution of the mean separation distance between the first two ground contact points of each MGCF of the Kansas domain.



Source: produced by the author.

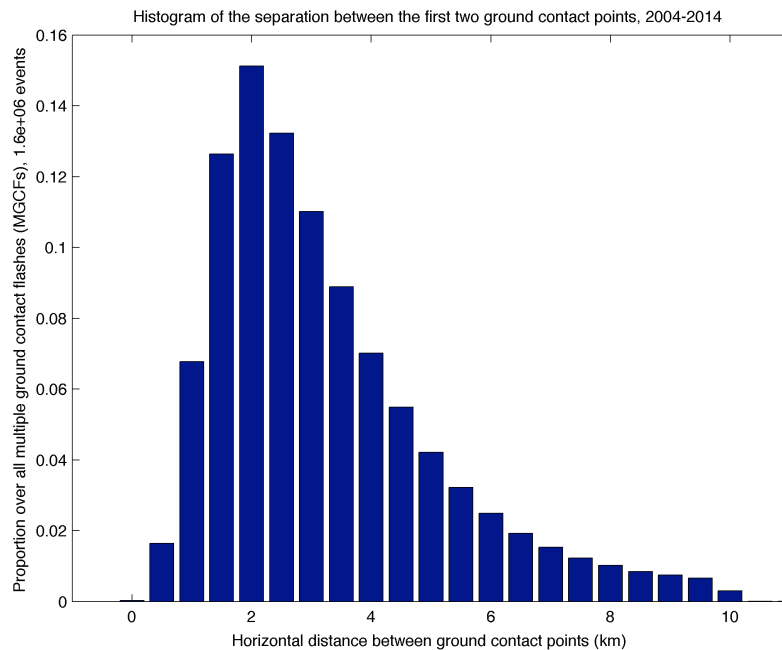
Again, the histograms of CPF and separation distance between ground contacts (Figures 7.28 and 7.29, respectively) obtained for Kansas are very similar to those that resulted from the Arkansas (Figures 7.12 and 7.13) and Arizona (Figures 7.20 and 7.21) domains. The only remarkable difference is the slightly higher incidence of single grounded flashes (among all those with multiple strokes) in Kansas. Finally, the spatial distributions of data quality parameters presented in Appendix B (Figures B.9 to B.12) show that the whole domain is practically uniformly covered by the NLDN. The mean SMA distribution (Figure B.9), of particular relevance to the performance of the *groupGCP* algorithm, is mostly uniform, so one may expect that the results presented in this subsection are not affected by the sensor topography.

Figure 7.28 – Histogram of number of channels per flash for multi-stroke flashes detected in the Kansas domain.



Source: produced by the author.

Figure 7.29 – Histogram of the mean separation distance between the first two ground contact points of each MGCF of the Kansas domain.



Source: produced by the author.

7.5. Concluding remarks

The analysis of spatial distributions of the parameters of multi-grounded flashes presented in this chapter showed that the dynamics are more complex than anticipated, suggesting that accumulated lightning data and terrain parameterizations may not be enough information to identify, understand and quantify the processes and modulating factors. There was no uniform tendency or pattern that was observed in all three domains for the distribution of mean number of channels per flash. While no clear pattern was found either on Arkansas (Figure 7.7) or Kansas (Figure 7.26), in Arizona (Figure 7.18) an accumulation of higher CPF values was observed over one of the regions with high spatial frequency variations. The mean separation distances between ground contacts was reduced in multi-grounded flashes that occurred on or near altitude local maxima in both Arkansas (Figure 7.8) and Arizona (Figure 7.19) domains, even though this parameter seemed almost homogeneous in Kansas (Figure 7.27). This lack of pattern observed in Kansas, in contrast with the other two domains, strongly suggests that larger areas of terrain variations impact the mean separation distance. In any case, a

different domain with a terrain profile similar to that of Arizona should be analyzed in a future work, as the proximity to the U.S. NLDN southern edge may have induced an inhomogeneous performance of the *groupGCP* algorithm. Additionally, more domains such as Kansas, with its small, filamentary regions with high spatial frequency, must be analyzed in order to confirm whether or not a given terrain feature must be horizontally extensive to affect the spatial distribution of the analyzed parameters.

As the main computational tools necessary for processing and visualization of lightning data have already been developed for this thesis work, additional instruments and datasets must be used for future studies, particularly wind profiles, meteorological radar and, if possible, a large extension network of electric field mills. This may allow the identification of thunderstorm dynamics so that the results provided by the *groupGCP* algorithm have additional context when being interpreted.

8 DIURNAL CLIMATOLOGY OF MULTIPLE GROUND CONTACT FLASHES

The lack of clear patterns in the analysis of spatial distributions of multi-grounded flashes and their relationship with terrain variations, presented in the previous chapter, inspired the hypothesis regarding whether a diurnal climatology may play a role in modulating their characteristics. A number of studies and researchers have showed the link between diurnal variations of lightning activity and characteristics and local solar time, mainly due to the typical “afternoon thunderstorms” in some locations, and mesoscale convective systems in others (two very recent studies on this subject were published by Blakeslee et al., 2014, and Chronis et al., 2015).

These ideas are aligned with the case studies presented in Chapter 6, which suggested that the formation of a new ground contact stroke may be more influenced by processes that occur inside the thundercloud than by interactions involving the ground (with Type I events being the possible exception, as it still remains unclear which processes lead to the deviation from the original channel observed in the subsequent leaders). For this reason, diurnal hourly plots of the two main parameters related to multiple ground contact flashes (MGCF), the number of channels per flash (CPF) and the horizontal separation distance between ground contacts, were produced.

8.1. Computational method

The computational procedure to obtain the climatology is based on the methodology adopted by Chronis et al. (2015), who analyzed the diurnal variations of –CG lightning peak currents over the continental United States based on data from the NLDN. The exact same output files provided by the *groupGCP* algorithm for the spatial distribution analysis of Chapter 7 (i.e., processed with *maxSMA_grouping* set to 0.2 km and both *maxScaleFactor* and *pScale* to 2.0) were used for the diurnal climatology, and each of the three domains were analyzed separately. The main steps are outlined as follows:

1. create masks to “filter” the lightning data according to the hours they occurred, saving them as *.mat* files to be reused later. This way, all return strokes that were

detected, for instance, between 01:00:00.000 (UT) and 01:59:59.999 (UT), can be listed and analyzed separately through a simple matrix operation. That strategy is important since the process of obtaining the hourly masks is computationally demanding (taking a few hours to be completed in a laptop computer);

2. a separate program loads each file (corresponding to each year worth of lightning data) and its respective hourly masks and pre-allocates matrices that can store the parameters that will be analyzed (at this point, separately for each year);
3. data from each individual stroke and flash (stored in the matrices of step 2) are then compiled into a single multi-year matrix, sorted by each one-hour interval;
4. hourly values of the arithmetic means (AM), geometric means (GM), standard deviations (SD) are then calculated for each parameter, and from the total count of flashes and strokes and the SD of each parameters, the hourly standard errors (SE) are also obtained;
5. finally, the data are shifted according to the local solar time (LST) of the center of each of the three domains and then plotted.

After the first exploratory analysis of the resulting plots, it was noted that the diurnal variations of mean CPF were strongly correlated with the hourly mean error ellipse semi-major axis (SMA). As this parameter is highly influential on the capacity of the *groupGCP* algorithm to identify and group ground contact points, it was concluded that the climatology was actually being caused by variations in the quality of the data. Two additional steps were then added before step 1 of the procedure that was previously outlined: (i) only the 2011-2014 period was considered (when the minimum SMA reported by the U.S. NLDN was reduced from 0.4 km to 0.2 km); and (ii) another mask was applied to the datasets, removing all flashes in which at least one of the reported return stroke solutions had an SMA value greater than 0.2 km. This way it was ensured that all flashes considered in the analysis were optimally located by the LLS even

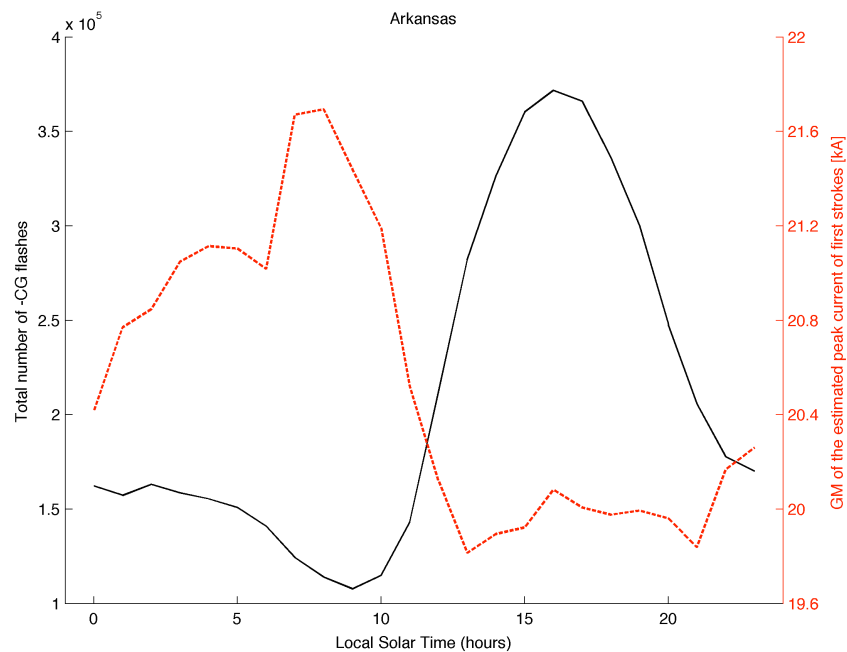
before they were filtered according to the time they were detected (considering the current state of the NLDN at the time this study was conducted).

8.2. Results

In order to evaluate whether the computational process was correct or not, results were compared to those reported by Chronis et al. (2015); the hourly accumulated number of negative CG flashes and the GM of the peak currents of first strokes were plotted, as shown in Figures 8.1 (Arkansas), 8.2 (Arizona) and 8.3 (Kansas). The domains considered in this study do not perfectly match the 5x5 degree regions into which Chronis et al. (2015, Figure 1) have divided the continental USA, however, in order to allow the reader to compare the resulting curves, the Arkansas domain correspond approximately to regions 52 and 62; the Arizona domain to most of region 22, with small parts of regions 11, 12 and 21; and the Kansas domain to parts of regions 43 and 53, with its southern edge including a small portion of regions 42 and 52.

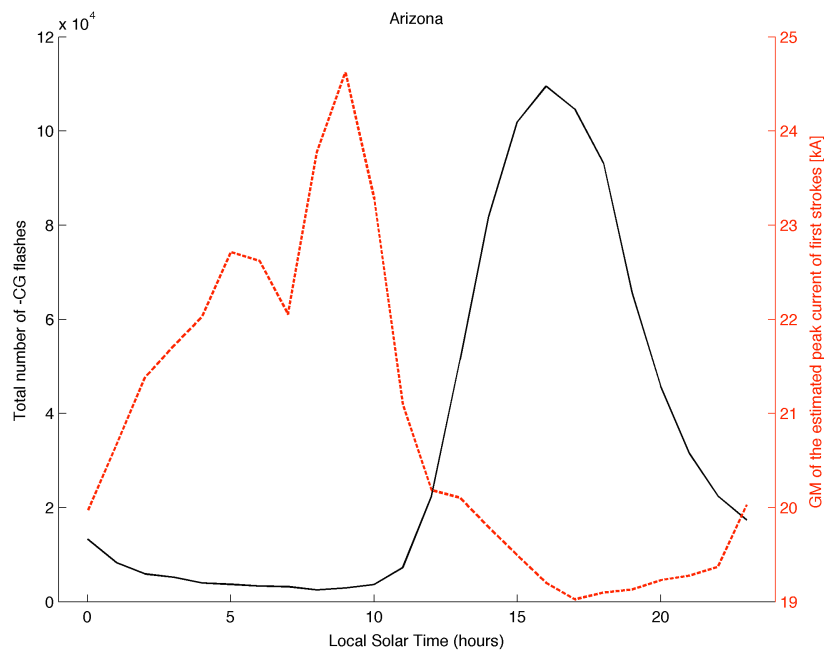
The lightning activity of the Arizona domain (solid black lines Figure 8.2) is characterized by a low and almost constant incidence of discharges during late night to late morning (roughly 00:00-10:00 LST) followed by a rapid increase with maximum activity in the afternoon (14:00-16:00 LST). The Kansas domain (Figure 8.3), on the other hand, is characterized by peak activity at later times (19:00-21:00 LST), with most lightning occurring between late night and early morning and a minimum at 10:00-11:00 LST. This is consistent with a region where the occurrence of Mesoscale Convective Systems (MCS) is common (see, for instance, Rudledge and MacGorman, 1988, and MacGorman and Morgenstern, 1998). Finally, the Arkansas domain (Figure 8.1) is a midterm between the other two, with a relatively slow reduction in lightning activity during the late night and early morning. This is consistent with the fact that it is very close to the Kansas domain, suggesting the presence of some MCSs in that region as well. The diurnal variation of the GM of the estimated peak currents of first strokes is shown by the dashed red lines of Figures 8.1, 8.2 and 8.2. In all three domains the maximum GM of the peak currents occur at the minimum of lightning activity, and vice-versa, as was reported by Chronis et al. (2015).

Figure 8.1 – Hourly plots of the total negative CG lightning incidence and the GM of the estimated peak current of first return strokes in the Arkansas domain.



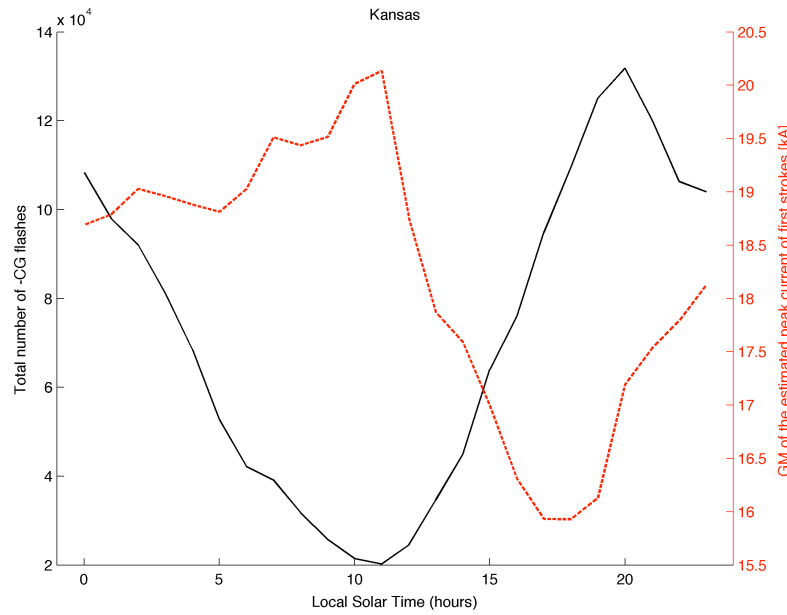
Source: produced by the author.

Figure 8.2 – Hourly plots of the total negative CG lightning incidence and the GM of the estimated peak current of first return strokes in the Arizona domain.



Source: produced by the author.

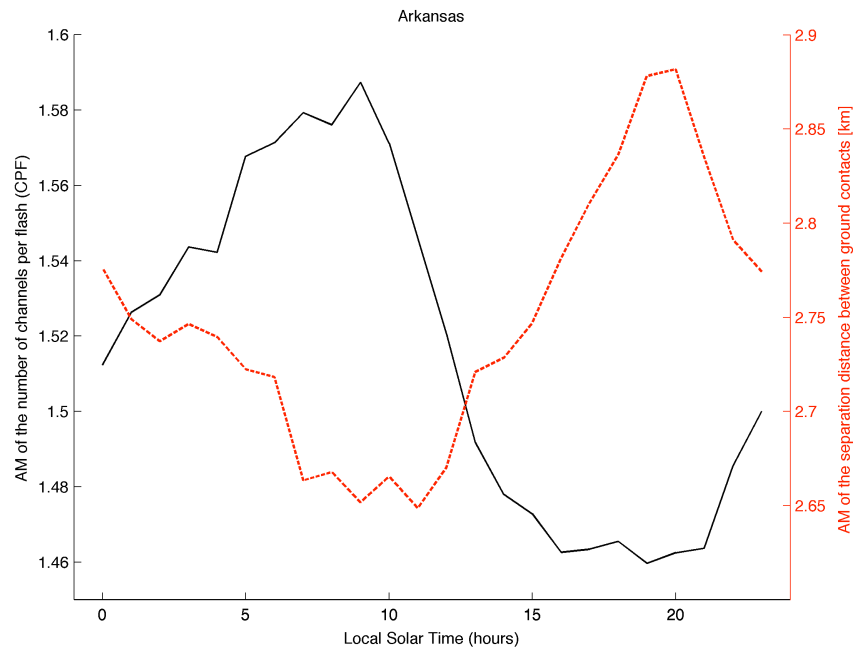
Figure 8.3 – Hourly plots of the total negative CG lightning incidence and the GM of the estimated peak current of first return strokes in the Kansas domain.



Source: produced by the author.

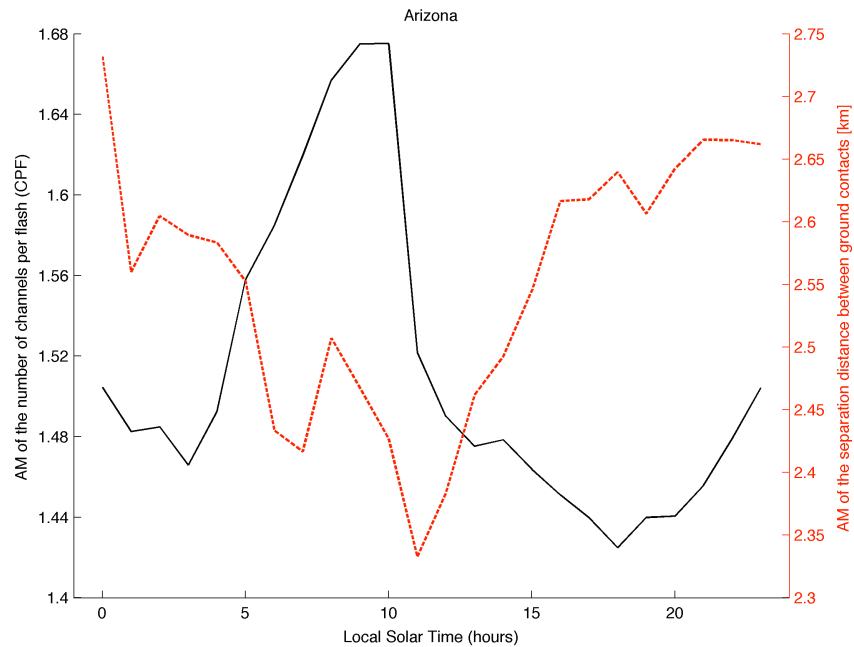
Figures 8.4 through 8.6 show similar hourly diurnal plots of the AM of the number of channels per flash (CPF) and the horizontal separation distance between the first two ground contacts of each MGCF. In all three domains the mean CPF (black solid line) has its maximum value either at or close to 10:00 (LST) and its minimum at either around 19:00 (LST). Differently from the lightning activity/estimated peak current plots, even though the separation distance has the overall opposite behavior, its minimum/maximum values do not perfectly coincide with the maximum/minimum values of the mean CPF. The factors that favor the higher incidence of MGCFs (reflected on larger values of the mean CPF) seem to be responsible for causing their GCPs to be spatially closer (as indicated by the smaller horizontal separation values). It is important to note that the SE of both parameters are not shown in Figures 8.4 to 8.6 because they are very small compared to the observed variations. This is due to the fact that the SE of the mean is calculated as the SD of the sample divided by the square root of the sample size and the sample of each calculated hourly mean is of the order of 10^4 to 10^6 (as shown by the lightning incidence plots of Figures 8.1 to 8.3).

Figure 8.4 – Hourly plots of the AM of the number of channels per flash (CPF) and the separation distance between ground contacts in the Arkansas domain.



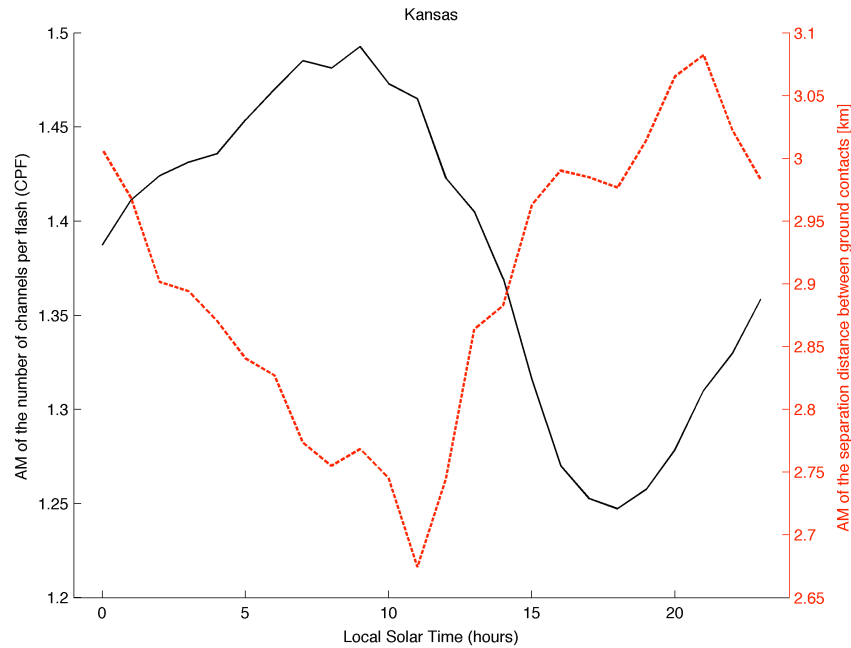
Source: produced by the author.

Figure 8.5 – Hourly plots of the AM of the number of channels per flash (CPF) and the separation distance between ground contacts in the Arizona domain.



Source: produced by the author.

Figure 8.6 – Hourly plots of the AM of the number of channels per flash (CPF) and the separation distance between ground contacts in the Kansas domain.



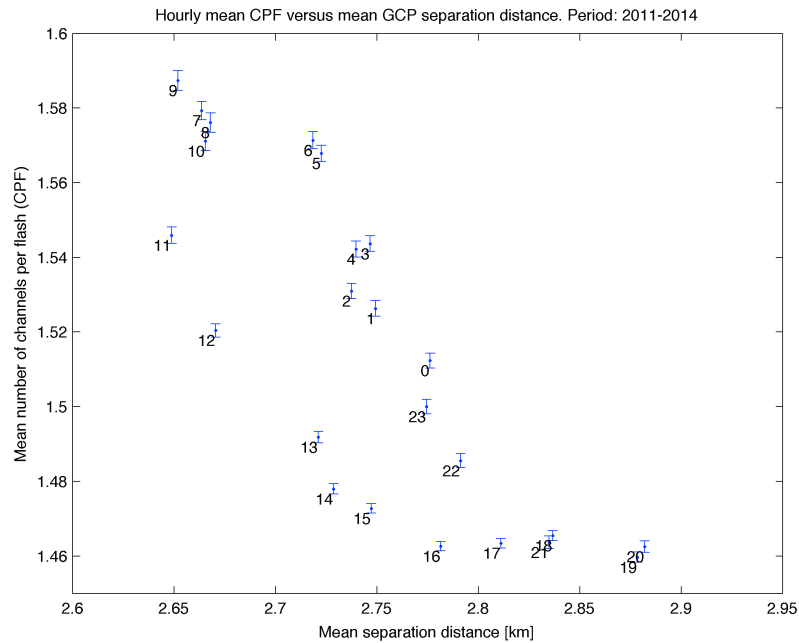
Source: produced by the author.

One possible explanation for the diurnal climatology that was observed in the parameters of MGCFs is the presence of other sources of GCP misclassification in the *groupGCP* algorithm that also have a diurnal variation (other than fluctuations in the error ellipse SMA, which was removed from this analysis). Statistically, these unknown factors could at some times cause an increase in the number of close strokes that are grouped into a single GCP, reducing the mean CPF while increasing the mean separation distance between contacts (i.e., only more distant strokes would be considered to produce NGCs). At other times, close strokes would be grouped together less frequently (increasing the mean CPF), decreasing the mean separation distance (as closer strokes would produce new ground terminations). With the removal of the SMA to decrease the chances of having such a classification problem, other parameters that may be evaluated are the mean number of sensors reporting (NSR) for all detected strokes and the mean chi-squared values for their solutions (which gives a sense of “agreement” between different sensors regarding the optimal solution location of a given stroke). Their diurnal cycles are shown in Appendix C, Figures C.1 (Arkansas),

C.2 (Arizona) and C.3 (Kansas), and none of them coincided with the diurnal variation of CPF or mean GCP separation distances. In the case of chi-squared, it remained below 1.0 for Arkansas and Kansas, and below 1.3 for Arizona. According to Cummins (2014, p.11), “for properly calibrated LLSs, the mean value [of chi-squared] should be close to 1; values below 3 are good, and values below ~10 are considered acceptable”, so all three domains are expected to have provided reliable stroke solutions for this analysis. The mean NSR ranged from 12 to 16 for Arkansas and Kansas, and from 9.5 to 12.5 for Arizona, well above the minimum of 5 used in the data quality control applied in the NLDN data before it was processed by *groupGCP* (see section 7.1). Appendix C also shows a comparison between the mean NSR and the GM of the estimated peak current, both for all strokes (including both first and subsequent), in Figures C.4 to C.6. The diurnal cycle of NSR may be influenced by atmospheric heating (as it reaches a minimum between 20:00 and 21:00 LST before starting to steeply rise again in the hours preceding sunrise) with its maximum either coinciding with or very close to the maximum of the peak current values (i.e., more intense strokes tend to be reported by a larger number of sensors).

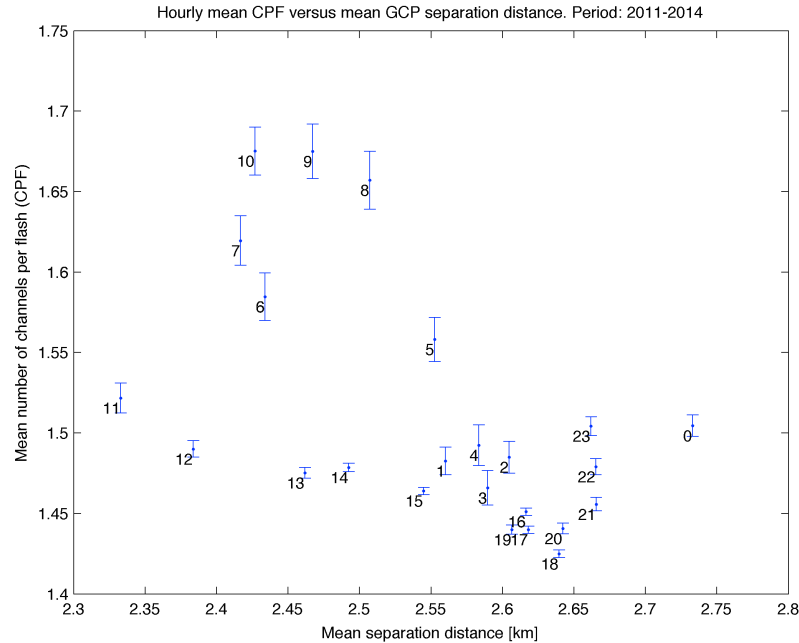
Hourly scatterplots of the mean CPF *versus* the mean GCP horizontal separation distance are shown in Figures 8.7 to 8.9 for each of the three domains, with each point labeled according to its respective local time. There is a considerable dispersion in the plots, reducing the probability that their diurnal cycles are caused by systematic grouping errors. For instance, in the Arkansas domain it is possible to note that after the minimum value of CPF (approximately 1.46) is reached at 16:00 (LST), it remains mostly unchanged for about five hours (until 21:00 LST) while the mean GCP separation distance oscillates over a range of approximately 100 meters (almost half of the total amplitude of the observed diurnal oscillation).

Figure 8.7 – Hourly scatterplot of the mean number of channels per flash *versus* the mean separation distance between ground contacts in the Arkansas domain.



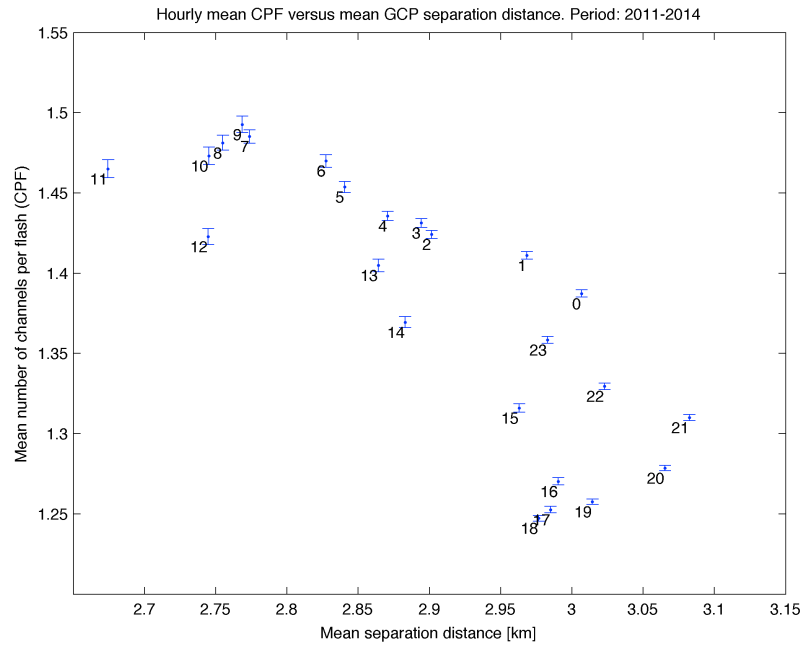
Source: produced by the author.

Figure 8.8 – Hourly scatterplot of the mean number of channels per flash *versus* the mean separation distance between ground contacts in the Arizona domain.



Source: produced by the author.

Figure 8.9 – Hourly scatterplot of the mean number of channels per flash *versus* the mean separation distance between ground contacts in the Kansas domain.



Source: produced by the author.

8.3. Concluding remarks

A diurnal climatology of the characteristics of MGCFs was obtained from NLDN data processed by the *groupGCP* algorithm. Results suggest that the mechanisms that lead to larger number of channels per flash are also responsible for reducing the mean distance between them. In all three domains it was found that the mean CPF reach a maximum around 10:00 (LST) and a minimum around 18:00 (LST). The minimum mean separation distances generally coincided with the maximum mean CPF, although its maximum value occurred at different times for each of the domains. Additionally, if the mean distance is reduced by a large population of small-distance cases, then this may reflect a relative increase in the in Type I flashes. At the moment there is no hypothesis to explain the diurnal climatology of these parameters.

Even though it is possible that the observed cycle may be caused by incorrect classification by the algorithm, the main possible source of errors (variations in the mean SMA) has been removed with the help of a filter. Also, none of the other data

quality parameters (namely, NSR and chi-squared), shown in Appendix C, presented a diurnal cycle that coincides with those observed for the MGCF characteristics.

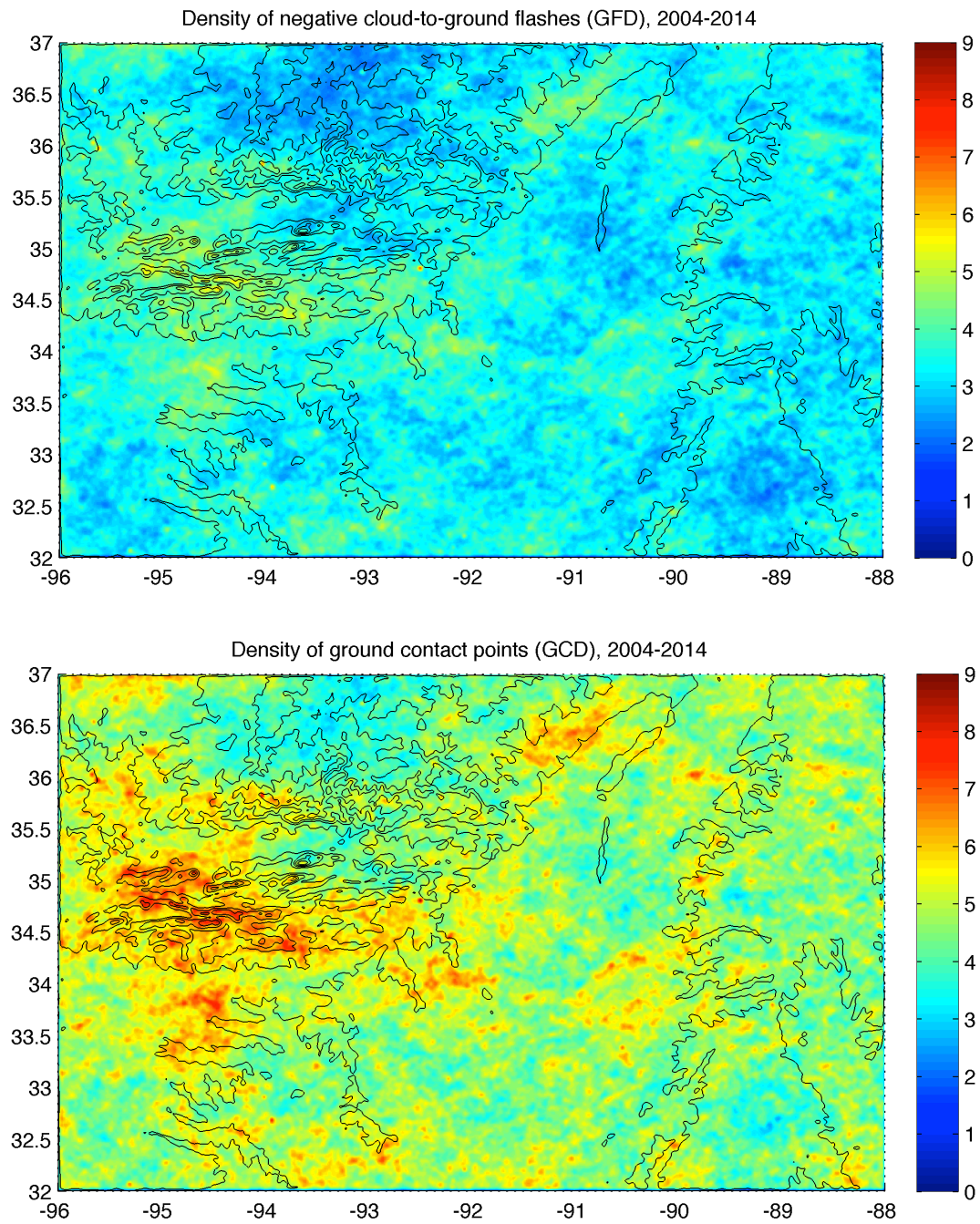
9 TECHNOLOGICAL AND ENGINEERING APPLICATIONS OF THE GROUND CONTACT POINT IDENTIFICATION ALGORITHM

Data provided by Lightning Location Systems have a wide range of practical applications for lightning risk assessment, protection and damage mitigation. In this context, the additional information on ground contact points that can be provided by the *groupGCP* algorithm may have some positive impact on those applications. Two possible uses are briefly outlined in this chapter.

9.1. Evaluating the lightning strike point density (N_{sg})

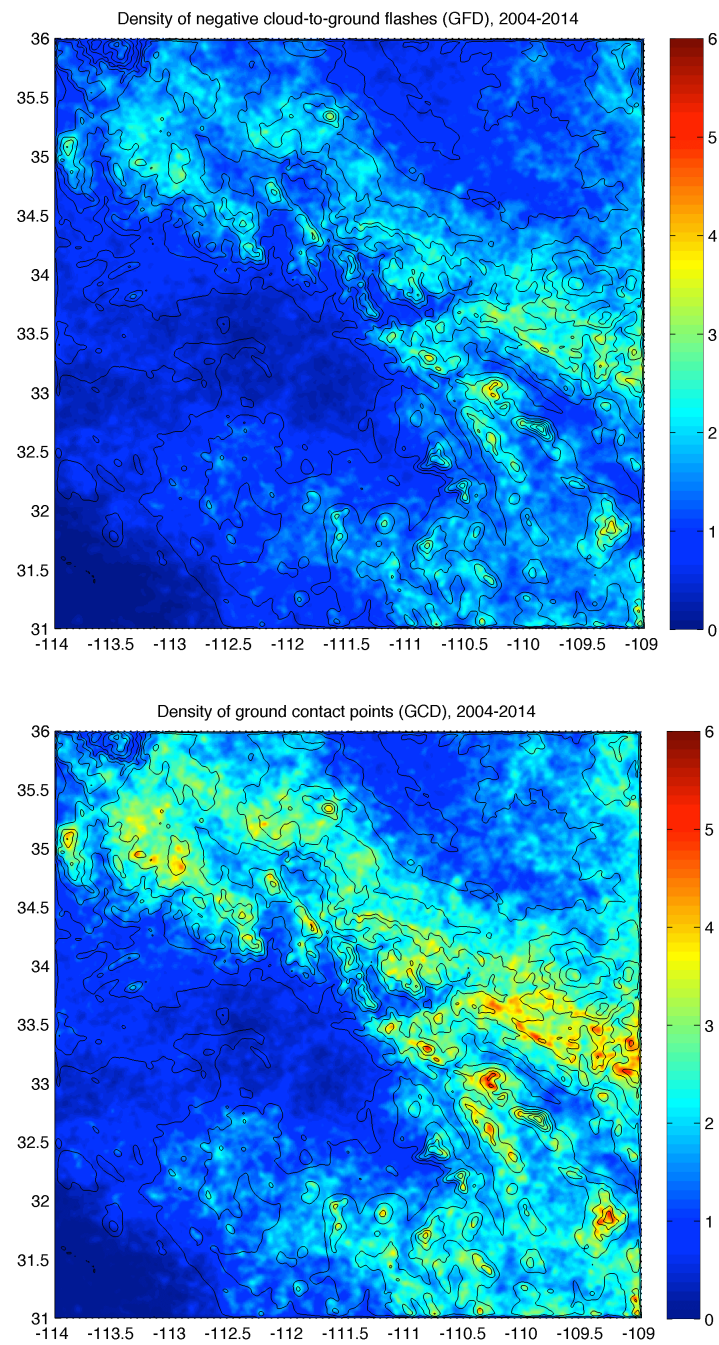
Lightning risk assessment calculations for buildings and structures, as determined by current protection standards (IEC, 2010), are based mainly on the lightning flash density (N_g), which is defined as the number of lightning flashes per square kilometer per year. However, researchers such as Bouquegneau (2014) and Visacro (2015) have been advocating towards the use of the lightning strike point density (N_{sg}) instead, as it would better reflect the expected number of damages and faults on exposed structures, power lines, etc. The *groupGCP* algorithm, combined with minor adaptations to the computational tools developed for the spatial distribution analysis (Chapter 7), can be used to produce maps of the lightning strike point density. As a demonstration of this potential use, N_g maps were produced for the three domains analyzed in Chapters 7 and 8 (Arkansas, Arizona and Kansas) and, using the same mapping procedure, N_{sg} maps were also generated based on the output data of the *groupGCP* algorithm. The color scale of the resulting maps was forced to be the same on both in order to facilitate the comparison between the parameters. They are shown in Figure 9.1 (Arkansas), 9.2 (Arizona) and 9.3 (Kansas). All three domains exhibit much greater spatial variability for N_{sg} when compared to N_g . The differences are not simply defined by a scaling of N_g by an overall average number of ground contacts per flash.

Figure 9.1 – Maps of lightning flash density (N_g) and lightning strike point density (N_{sg}) for the Arkansas domain.



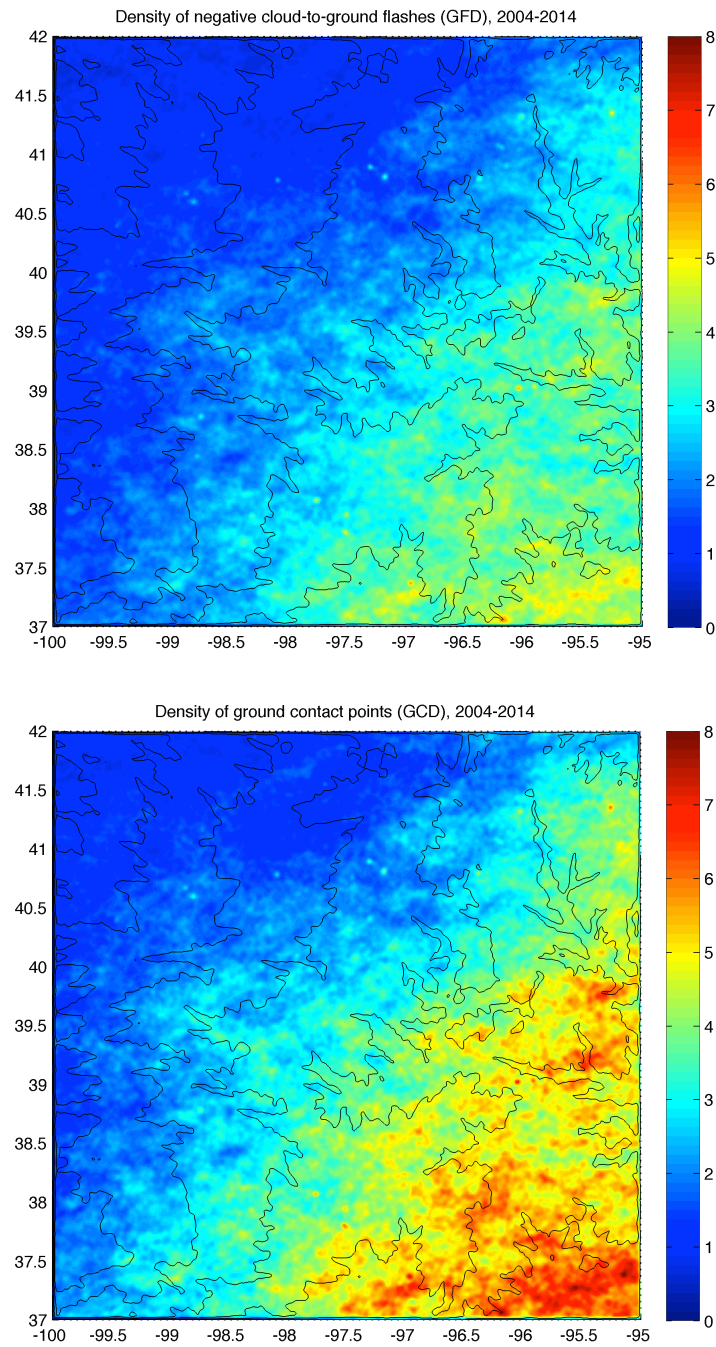
Source: produced by the author.

Figure 9.2 – Maps of lightning flash density (N_g) and lightning strike point density (N_{sg}) for the Arizona domain.



Source: produced by the author.

Figure 9.3 – Maps of lightning flash density (N_g) and lightning strike point density (N_{sg}) for the Kansas domain.



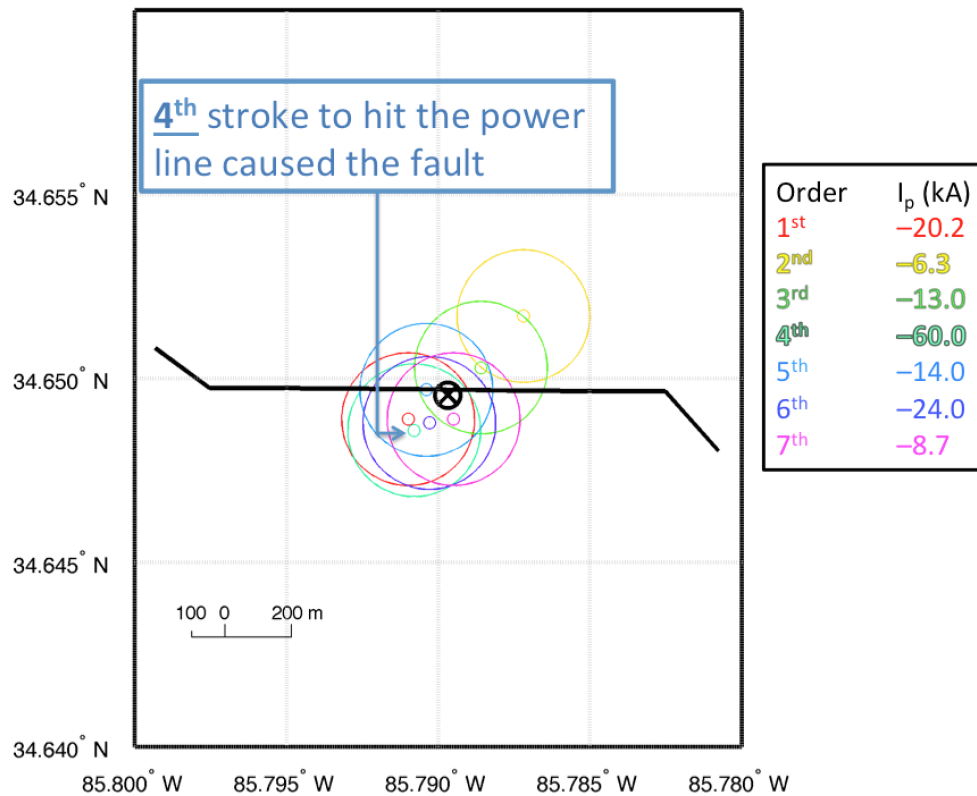
Source: produced by the author.

9.2. Analysis of lightning-caused power line faults

The process of monitoring and repairing power lines that are damaged by direct lightning strikes is a common application of LLS data. Through the use of a Digital Fault Recorder (DFR) it is possible to determine the instant the fault occurred with millisecond precision, allowing the identification of which return stroke of a given flash caused it. However, the location provided in the LLS solution of a single return stroke may not be accurate enough to allow the efficient identification of where the line must be repaired. When multiple return strokes share the same ground contact point (GCP) and it is successfully identified by the *groupGCP* algorithm, however, the resulting optimal location of the GCP is a more precise estimate. This idea was used in the analysis of two cases of lightning-induced faults recorded by a DFR on a line operated by the Tennessee Valley Authority (TVA).

The first case occurred on October 8th, 2014, at 11:00:51 (UT) and was associated with a seven-stroke flash. DFR data, however, indicated that the fault occurred when the fourth stroke of the flash was reported by the NLDN. About 105 milliseconds before that, however, a small bipolar transient was detected in the DFR, coinciding with the time the first stroke of the flash was detected. The *groupGCP* algorithm was then applied to all seven strokes of this flash, and it has grouped all of them into a single GCP based on the relative positions and sizes of the error ellipses. A plot of this event is shown in Figure 9.4. It is worth noting that the optimal GCP location (black circle) is closer to the power line actual location than most of the individual strokes of this flash. Also, the fault was caused by the most intense return stroke of this flash, with estimated peak current of -60 kA, about three times more intense than the first stroke.

Figure 9.4 – First example of lightning-caused power line fault.



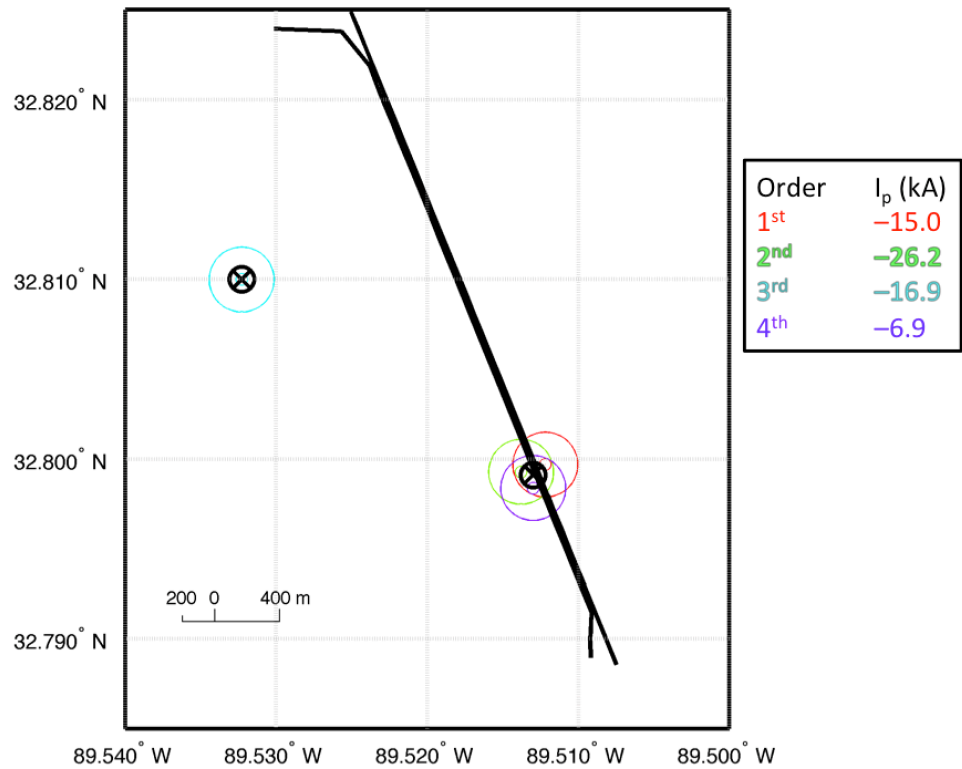
The solid black line indicates the power line. Each return stroke is colored according to its stroke order, as indicated by the small table to the right. The optimal location of this flash ground contact point is indicated by the black circle.

Source: produced by the author.

Another example of a similar lightning-caused fault is shown in Figure 9.5. In this case it was the second stroke that struck the line and was responsible for the fault and, again, it had the largest peak current of the flash (-26.2 kA). The third stroke produced a new ground termination but the fourth returned to the original channel, striking the line again. The error ellipses corresponding to the three strokes that struck the power line (first, second and fourth) are shown in greater detail in Figure 9.6. As in the previous example, the optimal GCP location provides a more precise estimate of where the fault occurred, potentially helping in the line repair process.

In addition to the possibility of improving the information on the fault location of individual events, the documentation of faults occurring after more than one return stroke hitting the line may help with planning for lightning protection repairs and improvements, providing some refinement on the peak current threshold at which a fault may occur.

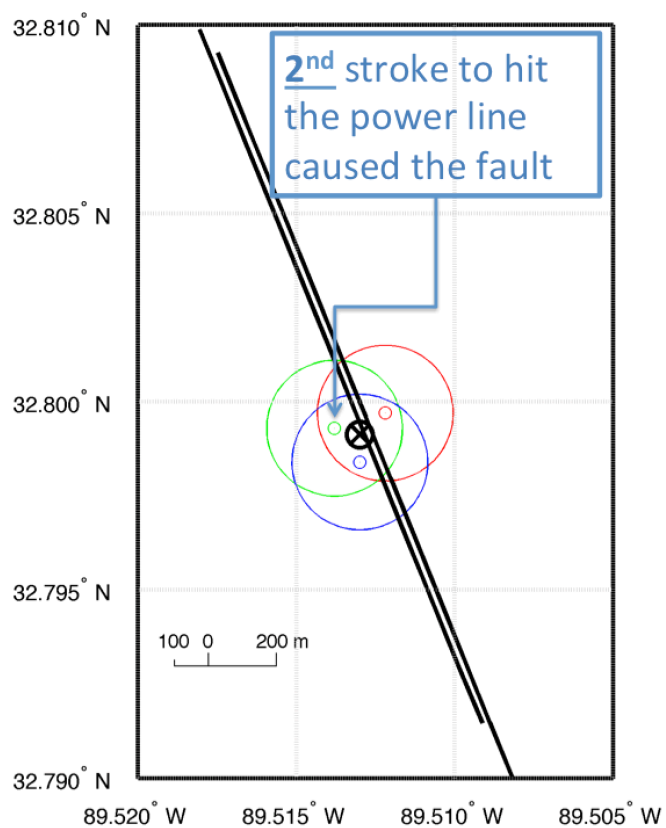
Figure 9.5 – Second example of lightning-caused power line fault.



The solid black lines indicate the parallel power lines. Each return stroke is colored according to its stroke order, as indicated by the small table to the right. The optimal locations for the ground contact points of this flash are indicated by the two black circles (one struck by the first, second and fourth strokes, another struck by the third).

Source: produced by the author.

Figure 9.6 – Second example of lightning-caused power line fault, zoomed into the three strokes that hit the power line (first, second and fourth strokes).



See description of Figure 9.5.

Source: produced by the author.

10 CONCLUSIONS

This thesis work presented a number of analyses focused on the mechanisms through which a negative cloud-to-ground lightning flash may produce multiple ground terminations and the statistical behavior of these flashes. It can be divided into three main contributions: (i) development of a new tool that allows the automatic and optimized identification of ground contact points from data provided by VLF/LF Lightning Location Systems; (ii) phenomenological analyses and case studies of the processes through which multiple ground terminations can be produced; and (iii) two statistical analyses of the possible factors that may lead to or modulate the production and characteristics of the lightning flashes with multiple ground terminations.

The first contribution, addressed in Chapter 4, consisted of the development and validation of a novel algorithm that is capable of deriving ground contact point (GCP) information from individual return stroke solutions that were reported by VLF/LF Lightning Location Systems (LLS). Named *groupGCP*, this algorithm makes full use of the statistical information embedded in the error ellipse provided by many modern day LLS, making it particularly useful when processing flashes with one or more poorly located strokes (i.e., with large error ellipses). This unique approach provides a rigorous framework for objectively handling location errors.

Optimal input parameters were obtained by validating the algorithm for a dataset of 25 negative flashes (with 114 return strokes) recorded by standard and high-speed video cameras. More than one combination of parameters performed equally well (with a performance efficiency that ranged from 96.5% to 98.2% for individual strokes and from 88% to 92% for full flashes), and in the future it will be necessary to perform further validation (and fine tuning) from larger datasets. Also, in its current implementation, the *groupGCP* algorithm is only adapted for networks based on the IMPACT technology, making full use of the error information it provides. It needs to be adapted accordingly so that it is able to derive ground contact point information from data provided by ENTLS networks, such as BrasilDAT. As this technology does not currently provide error ellipse information, it is necessary to analyze a significantly

large dataset of video observations along with detection data in order to define the optimal criteria to be used when grouping strokes into contact points. A brief addendum to this section was provided at the end of the thesis, presenting two possible technological uses for the algorithm in lightning risk assessment, protection and damage mitigation. One application consisted of obtaining estimates of the density of ground contact points, a parameter that may improve the standards, design and reliability of lightning protection systems, as proposed by other researchers. Another application consisted of the evaluation, documentation and analysis of lightning-caused power line faults. Having strike point information will allow not only a more precise determination of where the fault occurred but also may be used in refining the current threshold at which a return stroke may induce the fault. This is particularly interesting when the fault was not caused by the first stroke of the flash that struck the line, as shown in the two examples that were analyzed. As far as the author knows, this is the first work of this nature.

The second contribution had two main parts. In the first one a detailed analysis of multiple ground contact strokes (MGCS) was conducted, aiming at better characterizing forked and upward-illumination (UI) strokes. The temporal separation between the creations of their ground contact points is very short (ranging from a few microseconds up to about three milliseconds) leading to current LLS to locate only the first one. It was found that MGCSs of both categories (forked and UI) might occur in up to 15% of the flashes, with the exact proportion varying from thunderstorm to thunderstorm. Also, the analysis showed that the non-uniform luminosity observed in the channel of UI strokes may be related to a difference on channel conductivity régimes that is reflected in slower downward leader speeds (before ground contact is made) and in relatively lower peak currents (when compared to forked strokes).

In the other part of the second contribution the most common type of process that leads to multiple ground terminations was analyzed, which is the new ground contact (NGC) subsequent strokes. With the help of detailed case studies of 23 multiple ground contact flashes (MGCFs) which presented 33 processes of creation of NGC strokes it was possible to identify three different scenarios through which a subsequent stroke may

follow a new path to ground. The case studies were mainly based on data provided by an LMA (Lightning Mapping Array), which is capable of locating VHF sources in time and three spatial dimensions, in addition to video (either standard or high-speed) for part of the events and LLS data (from which strike point information was derived with the help of the *groupGCP* algorithm) for all of them.

All case studies could be grouped into one of three categories of NGC creation processes. In events of Type I, the dart leader that initiates the subsequent stroke starts in the original channel and then diverges from the original path of the first stroke, ionizing a new path and reaching ground at a different location. In high-speed video records, these events eventually have their “diverging” point visible below cloud base and their strike locations are separated by a few hundreds of meters. Type II, on the other hand, comprises processes in which the subsequent stroke is initiated in an in-cloud branch that is away from the inception region of the first return stroke, moving in another direction and touching ground at farther distances (up to more than 7 km away from the initial strike location). Finally, Type III processes are characterized by stepped leader processes that are initiated from the same region in the cloud without sharing common channel branches, frequently (although not always) giving rise to several different ground strike points. Processes of this last type may lead to a wide range of separation distances between ground terminations, ranging from a few hundreds of meters to several kilometers. This is the first work to systematically identify, describe and characterize NGC creation processes.

Once the mechanisms through which a negative lightning flash can create multiple ground termination were identified, the third contribution of the thesis was focused on trying to identify the factors that may modulate their occurrence and characteristics. Two analyses based on LLS data processed by the *groupGCP* algorithm were conducted, one to evaluate the influence of complex terrain features over the spatial distributions of MGCFs and their characteristics and another focused on obtaining a diurnal climatology of those characteristics.

Three very distinct domains were considered in the spatial distribution analysis. In only one of them (Arizona) the mean number of channel per flashes (CPF) seemed to be impacted by spatial frequency terrain variations, presenting higher values over an extensive region that crossed the domain diagonally (where spatial frequency variations were particularly high). In the other two domains (Arkansas and Kansas), on the other hand, the mean CPF did not seem to be influenced by either absolute elevation or spatial frequency variations. One tendency that was consistent in two domains (Arkansas and Arizona) was the localized reduction of the mean separation distance between ground contacts over local altitude maxima (above 3 km in Arizona and above 400 meters in Arkansas). It is important to note that the domain with minimal (i.e., small horizontal extension) terrain variations (Kansas) presented very little variations in separation distance, resulting in a mostly homogeneous spatial distribution. This suggests that there may be a minimum extension for region with high frequency terrain variations for it to affect this parameter.

The second analysis of the third section of the thesis was mainly motivated by the fact that, with the possible exception of Type I, the mechanisms of NGC creation that were identified through the case studies seemed to be more influenced by the thundercloud structure than by flash-scale interaction between downward propagating leaders and ground. An hourly diurnal climatology was then generated for the mean CPF and separation distance between ground terminations. It was found in all three domains that the mean CPF reaches a maximum value at late morning (around 10:00 LST) and a minimum around late afternoon or early evening (between 16:00 and 20:00 LST). The mean GCP separation distances, on the other hand, had an opposite behavior, reaching its maximum value around late evening and then a minimum around late morning. At the moment there is no clear hypothesis to explain this result, and a discussion on the possibility that this effect may be caused by GCP misclassification is presented at Chapter 8.

Finally, future works may address some questions that remained unanswered and refine some of the results presented here, such as:

1. adapt the *groupGCP* algorithm for other types of networks and technologies,, validating its performance with video observations (with particular interest on ENTLS sensors and BrasilDAT);
2. further validate the *groupGCP* algorithm with additional video records obtained in both the U.S. NLDN and EUCLID, allowing the fine tuning of each input parameter so that the performance efficiency may be optimized;
3. analyze a larger sample of events of Type I NGC creation mechanism with multiple-station electric field records. With such dataset it would be possible to evaluate the charge deposition mechanism proposed by Krehbiel (1981) and whose characterizing field change signature was not consistently observed in all events of the sample of this thesis;
4. obtain and analyze additional instruments and datasets for the evaluation of the spatial distribution of multi-grounded flashes and their parameters. Wind, radar and electric field mill data would bring insights into the thunderstorm dynamics of a given domain, allowing a systematic process of “separation of variables”. Once the main mechanisms are identified, the influence of orography can then be better evaluated.

REFERENCES

- ANDERSON, R. B.; ERIKSSON, A. J. Lightning parameters for engineering applications. **Electra**, v.69, p.65-102, March 1980.
- ANTUNES, L. S.; SARAIVA, A. C. V.; PINTO Jr., O.; ALVES, J.; CAMPOS, L. Z. S.; LUZ, E. S. A. M.; MEDEIROS, C.; BUZATO, T. S. Day-to-day differences in the characterization of lightning observed by multiple high-speed cameras. **Electric Power Systems Research**, v.118, p.93-100, January 2015.
- BALLAROTTI, M. G.; SABA, M. M. F.; PINTO Jr., O. High-speed camera observations of negative ground flashes on a millisecond-scale. **Geophysical Research Letters**, v.32, n.23, p.L23802, December 2005.
- BALLAROTTI, M. G.; MEDEIROS, C.; SABA, M. M. F.; SCHULZ, W.; PINTO Jr., O. Frequency distributions of some parameters of negative downward lightning flashes based on accurate-stroke-count studies. **Journal of Geophysical Research**, v.117, n.D6, p.D06112, March 2012.
- BARASCH, G. E. Spectral intensities emitted by lightning discharges. **Journal of Geophysical Research**, v.75, n.6, p.1049-1057, February 1970.
- BEASLEY, W.; UMAN, M. A.; RUSTAN Jr., P. L. Electric fields preceding cloud-to-ground lightning flashes. **Journal of Geophysical Research**, v.87, n.C7, p.4883-4902, June 1982.
- BEASLEY, W. H.; UMAN, M. A.; JORDAN, D. M.; GANESH, C. Simultaneous pulses in light and electric field from stepped leaders near ground level. **Journal of Geophysical Research**, v.88, n.C13, p.8617-8619, October 1983.
- BERGER, G.; HERMANT, A.; LABBE, A.-S. Observations of natural lightning in France. In: INTERNATIONAL CONFERENCE ON LIGHTNING PROTECTION, 23., 1996, Florence. **Proceedings...** Florence: Associazione Elettrotecnica ed Elettronica Italiana, 1996. p.67-72.

BIAGI, C. J.; CUMMINS, K. L.; KEHOE, K. E.; KRIDER, E. P. National Lightning Detection Network (NLDN) performance in southern Arizona, Texas and Oklahoma in 2003-2004. **Journal of Geophysical Research**, v.112, n.D5, p.D05208, March 2007.

BLAKESLEE, R. J.; MACH, D. M.; BATEMAN, M. G.; BAILEY, J. C. Seasonal variations in the lightning diurnal cycle and implications for the global electric circuit. **Atmospheric Research**, v.135-136, p.228-243, January 2014.

BOCCIPPIO, D. J.; CUMMINS, K. L.; CHRISTIAN, H. J.; GOODMAN, S. J. Combined satellite- and surface-based estimation of the intracloud-cloud-to-ground lightning ratio over the continental United States. **Monthly Weather Review**, v.129, n.1, p.108-122, January 2001.

BOUQUEGNEAU, C. The need for an international standard on Lightning Location Systems. In: INTERNATIONAL LIGHTNING DETECTION CONFERENCE, 23., 2014, Tucson. **Proceedings...** Tucson: Vaisala, 2014. Available at: <http://www.vaisala.com/Vaisala%20Documents/Scientific%20papers/2014%20ILDC%20ILMC/ILDC-Tuesday/Bouquegneau-The%20Need%20for%20an%20International%20Standard%20on%20Lightning%20Location%20Systems-2014-ILDC-ILMC.pdf>. Accessed on: Jan. 12 2016.

BOURSCHEIDT, V.; PINTO Jr., O.; NACCARATO, K. P.; PINTO, I. R. C. A. The influence of topography on the cloud-to-ground lightning density in South Brazil. **Atmospheric Research**, v.91, n.2-4, p.508-513, February 2009.

BRANTLEY, R. D.; TILLER, J. A.; UMAN, M. A. Lightning properties in Florida thunderstorms from video tape records. **Journal of Geophysical Research**, v.80, n.24, p.3402-3406, August 1975.

CAMPOS, L. Z. S.; SABA, M. M. F. Visible channel development during the initial breakdown of a natural negative cloud-to-ground flash. **Geophysical Research Letters**, v.40, n.17, p.4756-4761, September 2013.

CAMPOS, L. Z. S.; ALVES, J.; SARAIVA, A. C. V.; WILLIAMS, E. R.; PINTO Jr. O. On the relation between return stroke peak currents provided by Lightning Location Systems and its peak luminosity obtained from high-speed video cameras: Preliminary results. In: CHUVA INTERNATIONAL WORKSHOP, 1., 2013, São Paulo.

Proceedings... São Paulo: INPE, 2013. Available at:

<http://chuvaproject.cptec.inpe.br/portal/workshop/abstracts/abstract-Leandro_Campos.pdf>. Accessed on: Feb. 12 2016.

CAMPOS, L. Z. S.; SABA, M. M. F.; WARNER, T. A.; PINTO Jr., O.; KRIDER, E. P.; ORVILLE, R. E. High-speed video observations of natural clout-to-ground lightning leaders – A statistical analysis. **Atmospheric Research**, v.135-136, p.285-305, January 2014a.

CAMPOS, L. Z. S.; SABA, M. M. F.; KRIDER, E. P. On β_2 stepped leaders in negative cloud-to-ground lightning. **Journal of Geophysical Research: Atmospheres**, v.119, n.11, p.6749-6767, June 2014b.

CAMPOS, L. Z. S.; SARAIVA, A. C. V.; CUMMINS, K. L.; ANTUNES, L.; PINTO Jr. O.; GUEDES, D. G. Phenomenology and characterization of multiple ground contact strokes in natural lightning. In: INTERNATIONAL CONFERENCE ON ATMOSPHERIC ELECTRICITY, 15., 2014, Norman. **Proceedings...** Norman: NOAA/NSSL, 2014c. Available at: <http://www.nssl.noaa.gov/users/mansell/icae2014/preprints/Campos_57.pdf>. Accessed on: Jan. 12 2016.

CAMPOS, L. Z. S.; CUMMINS, K. L.; PINTO Jr., O. An algorithm for identifying ground strike points from return stroke data provided by Lightning Location Systems. In: ASIA-PACIFIC INTERNATIONAL CONFERENCE ON LIGHTNING, 9., 2015, Nagoya. **Proceedings...** Nagoya: IEIE of Japan, 2015. p.475-478. Pen drive.

CAREY, L. D.; BUFFALO, K. M. Environmental control of cloud-to-ground lightning polarity in severe storms. **Monthly Weather Review**, v.135, n.4, p.1327-1353, April 2007.

CHRONIS, T.; CUMMINS, K.; SAID, R.; KOSHAK, W.; MCCAUL, E.; WILLIAMS, E. R.; STANO, G. T.; GRANT, M. Climatological diurnal variation of negative CG lightning peak current over the continental United States. **Journal of Geophysical Research: Atmospheres**, v.120, n.2, p.582-589, January 2015.

CRAMER, J. A.; CUMMINS, K. L. Evaluating location accuracy of lightning location networks using tall towers. In: INTERNATIONAL LIGHTNING DETECTION CONFERENCE, 23., 2014, Tucson. **Proceedings...** Tucson: Vaisala, 2014. Available at:

<<http://www.vaisala.com/Vaisala%20Documents/Scientific%20papers/2014%20ILDC%20ILMC/ILDC-Wednesday/Cramer%20et%20al-Evaluating%20LA%20of%20LLN%20using%20tall%20towers-2014-ILDC-ILMC.pdf>>. Accessed on: Jan. 12 2016.

CUMMINS, K. L. Analysis of multiple ground contacts in cloud-to-ground flashes using LLS data: The impact of complex terrain. In: INTERNATIONAL LIGHTNING DETECTION CONFERENCE, 22., 2012, Broomfield. **Proceedings...** Broomfield: Vaisala, 2012. Available at:

<<http://www.vaisala.com/en/events/ildcilmc/Documents/Detection%20Technology/Analysis%20of%20Multiple%20Ground%20Contacts%20in%20Cloud-to-Ground%20Flashes%20Using%20LLS%20Data.pdf>>. Accessed on: Jan. 12 2016.

CUMMINS, K. L. Mapping the impact of terrain on lightning incidence and multiple ground contacts in cloud-to-ground flashes. In: INTERNATIONAL CONFERENCE ON ATMOSPHERIC ELECTRICITY, 15., 2014, Norman. **Proceedings...** Norman: NOAA/NSSL, 2014. Available at:

<http://www.nssl.noaa.gov/users/mansell/icae2014/preprints/Cummins_68.pdf>. Accessed on: Jan. 12 2016.

CUMMINS, K. L.; MURPHY, M. J. An overview of Lightning Locating Systems: History, techniques, and data uses, with an in-depth look at the U.S. NLDN. **IEEE Transactions on Electromagnetic Compatibility**, v.51, n.3, p.499-518, August 2009.

CUMMINS, K. L.; MURPHY, M. J.; BARDO, E. A.; HISCOX, W. L.; PYLE, R. B.; PIFER, A. E. A combined TOA/MDF technology upgrade of the U.S. National Lightning Detection Network. **Journal of Geophysical Research**, v.103, n.D8, p.9035-9044, April 1998.

CUMMINS, K. L.; QUICK, M. G.; RISON, W.; KREHBIEL, P.; THOMAS, R.; RODEHEFFER, D.; MCHARG, G.; ENGLE, J.; MYERS, J.; NAG, A.; CRAMER, J.; TURNER, T.; WARNER, T. A.; SABA, M. M. F.; SCHUMANN, C.; LYONS, W.; SAMARAS, T.; SAMARAS, P.; YOUNG, C.; CUMMER, S. A.; LU, G. Overview of the Kansas Windfarm2013 Field Program. In: INTERNATIONAL LIGHTNING DETECTION CONFERENCE, 23., 2014, Tucson. **Proceedings...** Tucson: Vaisala, 2014. Available at:

<<http://www.vaisala.com/Vaisala%20Documents/Scientific%20papers/2014%20ILDC%20ILMC/ILDC-Wednesday/Cummins%20et%20al-Overview%20of%20the%20Kansas%20Windfarm2012-2013-ILDC-ILMC.pdf>>.

Accessed on: Jan. 12 2016.

FARR, T. G.; ROSEN, P. A.; CARO, E.; CRIPPEN, R.; DUREN, R.; HENSLEY, S.; KOBRICK, M.; PALLER, M.; RODRIGUEZ, E.; ROTH, L.; SEAL, D.; SHAFFER, S.; SHIMADA, J.; UMLAND, J.; WERNER, M.; OSKIN, M.; BURBANK, D.; ALSDORF, D. The Shuttle Radar Topography Mission. **Reviews of Geophysics**, v.45, n.2, p.RG2004, May 2007.

FERRO, M. A. S. Características dos relâmpagos nuvem-solo negativos que apresentam múltiplos canais. 2008. 242 p. (INPE-15400-TDI/1414). Tese (Doutorado em Geofísica Espacial) - Instituto Nacional de Pesquisas Espaciais, São José dos Campos, 2008. Disponível em: <<http://urlib.net/8JMKD3MGP8W/347HTRP>>. Acesso em: 12 jan. 2016.

FERRO, M. A. S.; SABA, M. M. F.; PINTO Jr., O. Continuing current in multiple channel cloud-to-ground lightning. **Atmospheric Research**, v.91, n.2-4, p.399-403, February 2009.

FERRO, M. A. S.; SABA, M. M. F.; PINTO Jr., O. Time-intervals between negative lightning strokes and the creation of new ground terminations. **Atmospheric Research**, v.116, p.130-133, October 2012.

FLEENOR, S. A.; BIAGI, C. J.; CUMMINS, K. L.; KRIDER, E. P.; SHAO, X.-M. Characteristics of cloud-to-ground lightning in warm-season thunderstorms in the Central Great Plains. **Atmospheric Research**, v.91, n.2-4, p.333-352, February 2009.

FUQUAY, D. M. Positive cloud-to-ground lightning in summer thunderstorms. **Journal of Geophysical Research**, v.87, n.C9, p.7131-7140, August 1982.

GOMES, C.; COORAY, V. Radiation field pulses associated with the initiation of positive cloud to ground lightning flashes. **Journal of Atmospheric and Solar-Terrestrial Physics**, v.66, n.12, p.1047-1055, August 2004.

GOOGLE. **Google Earth**. 7.1.5 (build date: May 20th, 2015). Mountain View, CA: Google Inc., 2015. Available at: <<https://www.google.com/earth/>>. Accessed on: Feb. 10 2016.

GUO, C.; KRIDER, E. P. The optical and radiation field signatures produced by lightning return strokes. **Journal of Geophysical Research**, v.87, n.C11, p.8913-8922, October 1982.

GUREVICH, A. V.; KARASHTIN, A. N. Runaway breakdown and hydrometeors in lightning initiation. **Physical Review Letters**, v.110, n.18, p.185005, May 2013.

HOLLE, R. L.; LOPEZ, R. E. **Overview of real-time lightning detection systems and their meteorological uses**. Norman: NSSL/NOAA, 1993. 68p. (NOAA Technical Memorandum, reference ERL NSSL-102).

INTERNATIONAL ELECTROTECHNICAL COMMISSION (IEC). **IEC-62305-2:2010**: Protection against lightning – Part 2: Risk management. Geneva, Dec. 2010. 171p.

ISHII, M.; SHIMIZU, K.; HOJO, J.; SHINJO, K. Termination of multiple-stroke flashes observed by electromagnetic field. In: INTERNATIONAL CONFERENCE ON LIGHTNING PROTECTION, 24., 1998, Birmingham. **Proceedings...** Birmingham: [s.n.], 1996. p.11-16.

JERAULD, J.; RAKOV, V. A.; UMAN, M. A.; RAMBO, K. J.; JORDAN, D. M.; CUMMINS, K. L.; CRAMER, J. A. An evaluation of the performance characteristics of the U.S. National Lightning Detection Network in Florida using rocket-triggered lightning. **Journal of Geophysical Research**, v.110, n.D9, p.19106, October 2005.

JORDAN, D. J.; RAKOV, V. A.; BEASLEY, W. H.; UMAN, M. A. Luminosity characteristics of dart leaders and return strokes in natural lightning. **Journal of Geophysical Research**, v.102, n.D18, p.22025-22032, September 1997.

KASEMIR, H.-W. Qualitative overview of potential, field and charge conditions in the case of a lightning discharge in the storm cloud. In: MAZUR, V.; RUHNKE, L. H. (Ed.). **Heinz-Wolfram Kasemir: His collected works**. 1. ed. Washington, DC: American Geophysical Union, 2012a. chap. 4.1, p.398-411. ISBN 978-0-87590-737-6.

KASEMIR, H.-W. A contribution to the electrostatic theory of a lightning discharge. In: MAZUR, V.; RUHNKE, L. H. (Ed.). **Heinz-Wolfram Kasemir: His collected works**. 1. ed. Washington, DC: American Geophysical Union, 2012b. chap. 4.2, p.412-417. ISBN 978-0-87590-737-6.

KASEMIR, H.-W. Static discharge and triggered lightning. In: MAZUR, V.; RUHNKE, L. H. (Ed.). **Heinz-Wolfram Kasemir: His collected works**. 1. ed. Washington, DC: American Geophysical Union, 2012c. chap. 4.3, p.418-428. ISBN 978-0-87590-737-6.

KITAGAWA, N.; KOBAYASHI, M. Field changes and variations of luminosity due to lightning flashes. In: SMITH, L. G. (Ed.). **Recent advances in atmospheric electricity**. 1. ed. Oxford: Pergamon, 1959. p.485-501, ISBN 978-0-080-09193-8.

KITAGAWA, N.; BROOK, M.; WORKMAN, E. J. Continuing current in cloud-to-ground lightning discharges. **Journal of Geophysical Research**, v.67, n.2, p.637-647, February 1962.

KONG, X. Z.; QIE, X. S.; ZHAO, Y.; ZHANG, T. Characteristics of negative lightning flashes presenting multiple-ground terminations on a millisecond-scale. **Atmospheric Research**, v.91, n.2-4, p.381-386, February 2009.

KREHBIEL, P. R. **An analysis of the electric field change produced by lightning**. 1981. 245 p. Thesis (Doctorate in Physics) – University of Manchester, Manchester, UK, 1981.

KREHBIEL, P. R. The electrical structure of thunderstorms. In: KRIDER, E. P.; ROBLE, R.G. (Ed.). **The Earth's electrical environment**. 1. ed. Washington, DC: National Academy Press, 1986. chap.8, p.90-113. ISBN 978-0-309-03680-1.

KREHBIEL, P. R.; BROOK, M.; MCCRORY, R. A. An analysis of the charge structure of lightning discharges to ground. **Journal of Geophysical Research**, v.84, n.C5, p.2432-2456, May 1979.

KRIDER, E. P. Some photoelectric observations of lightning. **Journal of Geophysical Research**, v.71, n.12, p.3095-3098, June 1966.

KRIDER, E. P.; NOGGLE, R. C.; UMAN, M. A. A gated wideband magnetic direction-finder for lightning return strokes. **Journal of Applied Meteorology**, v.15, p.301-306, March 1976.

LIVINGSTON, J. M.; KRIDER, E. P. Electric fields produced by Florida thunderstorms. **Journal of Geophysical Research**, v.83, n.C1, p.385-401, January 1978.

LLOYD, S. P. Least squares quantization in PCM. **IEEE Transactions on Information Theory**, v.IT-28, n.2, p.129-137, March 1982.

MACGORMAN, D. R.; MORGENSTERN, C. D. Some characteristics of cloud-to-ground lightning in mesoscale convective systems. **Journal of Geophysical Research**, v.103, n.D12, p.14011-14023, June 1998.

MAIER, L.; LENNON, C.; BRITT, T.; SCHAEFER, S. Lightning detection and ranging (LDAR) system performance analysis. In: CONFERENCE ON AVIATION WEATHER SYSTEMS, 6., 1995, Dallas. **Proceedings...** Dallas: AMS, 1995, p.8.9.

MALLICK, S.; RAKOV, V. A.; NGIN, T.; GAMEROTA, W. R.; PILKEY, J. T.; HILL, J. D.; UMAN, M. A.; JORDAN, D. M.; CRAMER, J. A.; NAG, A. An update on the performance characteristics of the NLDN. In: INTERNATIONAL LIGHTNING DETECTION CONFERENCE, 23., 2014, Tucson. **Proceedings...** Tucson: Vaisala, 2014. Available at:

<<http://www.vaisala.com/en/events/ildcilmc/Documents/An%20Update%20on%20the%20Performance%20Characteristics%20of%20the%20NLDN.pdf>>. Accessed on: Jan. 20 2016.

MAZUR, V. Triggered lightning strikes to aircraft and natural intracloud discharges. **Journal of Geophysical Research**, v.94, n.D3, p.3311-3325, March 1989.

MAZUR, V. Physical processes during development of lightning flashes. **Comptes Rendus Physique**, v.3, n.10, p.1393-1409, December 2002.

MAZUR, V.; RUHNKE, L. H. Common physical processes in natural and artificially triggered lightning. **Journal of Geophysical Research**, v.98, n.D7, p.12913-12930, July 1993.

MAZUR, V.; RUHNKE, L. H. Physical processes during development of upward leaders from tall structures. **Journal of Electrostatics**, v.69, n.2, p.97-110, April 2011.

MAZUR, V.; KREHBIEL, P. R.; SHAO, X.-M. Correlated high-speed video and radio interferometric observations of a cloud-to-ground lightning flash. **Journal of Geophysical Research**, v.100, n.D12, p.25731-25753, December 1995.

MEDEIROS, C. **Estudo da ocorrência de corrente contínua em relâmpagos nuvem-solo negativos**. 2011. 108 p. (sid.inpe.br/mtc-m19/2011/08.02.04.04-TDI). Dissertação (Mestrado em Geofísica Espacial/Ciências Atmosféricas) - Instituto Nacional de Pesquisas Espaciais, São José dos Campos, 2011. Disponível em: <<http://urlib.net/8JMKD3MGP7W/3A79PQ8>>. Acesso em: 12 jan. 2016.

NACCARATO, K. P.; SARAIVA, A. C. V.; SABA, M. M. F.; SCHUMANN, C. First performance analysis of BrasilDAT total lightning network in southeastern Brazil. In: INTERNATIONAL CONFERENCE ON LIGHTNING ON GROUNDING AND EARTHING, 8., 2012, Bonito. **Proceedings...** Bonito: SBRAI, 2012. Pen drive.

NAGAI, Y.; EDANO, Y.; KAWAMATA, S. Characteristics of multi-stroke flash in summer. In: INTERNATIONAL AEROSPACE AND GROUND CONFERENCE ON LIGHTNING AND STATIC ELECTRICITY, 16., 1994, Mannheim. **Proceedings...** Mannheim: [s.n.], 1994. p.97-104.

OETZEL, G. N.; PIERCE, E. T. VHF techniques for locating lightning. **Radio Science**, v.4, n.3, p.199-202, March 1969.

ORVILLE, R. E.; IDONE, V. P. Lightning leader characteristics in the Thunderstorm Research International Program (TRIP). **Journal of Geophysical Research**, v.87, n.C13, p.11177-11192, December 1982.

PARKER, N. G.; KRIDER, E. P. A portable, PC-based system for making optical and electromagnetic measurements of lightning. **Journal of Applied Meteorology**, v.42, n.2, p.739-751, June 2003.

PÉDEBOY, S. Identification of the multiple ground contacts flashes with Lightning Location Systems. In: INTERNATIONAL LIGHTNING DETECTION CONFERENCE, 22., 2012, Broomfield. **Proceedings...** Broomfield: Vaisala, 2012. Available at:
<<http://www.vaisala.com/en/events/ildcilmc/Documents/Protection%20and%20Risk/Identification%20of%20the%20Multiple%20Ground%20Contacts%20Flashes%20with%20Lightning%20Location.pdf>>. Accessed on: Jan. 12 2016.

PÉDEBOY, S.; SCHULZ, W. Validation of a ground strike point identification algorithm based on ground truth data. In: INTERNATIONAL LIGHTNING DETECTION CONFERENCE, 23., 2014, Tucson. **Proceedings...** Tucson: Vaisala, 2014. Available at:
<<http://www.vaisala.com/Vaisala%20Documents/Scientific%20papers/2014%20ILDC%20ILMC/ILDC-Tuesday/Pedeboy%20and%20Schulz-Validation%20of%20the%20ground%20strike%20point%20algorithm-2014-ILDC-ILMC.pdf>>. Accessed on: Jan. 12 2016.

PRENTICE, S. A.; MACKERRAS, D. The ratio of cloud to cloud-to-ground lightning flashes in thunderstorms. **Journal of Applied Meteorology**, v.16, n.5, p.545-550, May 1977.

PROCTOR, D. E. A hyperbolic system for obtaining VHF radio pictures of lightning. **Journal of Geophysical Research**, v.76, n.6, p.1478-1489, February 1971.

QIE, X.; KONG, X. Progression features of a stepped leader process with four grounded leader branches. **Geophysical Research Letters**, v.34, n.6, p.L06809, March 2007.

QIE, X.; KONG, X.; ZHANG, G.; ZHANG, T.; YUAN, T.; ZHOU, Y.; ZHANG, Y.; WANG, H.; SUN, A. The possible charge structure of thunderstorm and lightning discharges in northeastern verge of Qinghai-Tibetan Plateau. **Atmospheric Research**, v.76, n.1-4, p.231-246, July-August 2005.

RAKOV, V. A.; UMAN, M. A. Some properties of negative cloud-to-ground lightning flashes versus stroke order. **Journal of Geophysical Research**, v.95, n.D5, p.5447-5453, April 1990a.

RAKOV, V. A.; UMAN, M. A. Long continuing current in negative lightning ground flashes. **Journal of Geophysical Research**, v.95, n.D5, p.5455-5470, April 1990b.

RAKOV, V. A.; UMAN, M. A. Origin of lightning electric field signatures showing two return-stroke waveforms separated in time by a millisecond or less. **Journal of Geophysical Research**, v.99, n.D4, p.8157-8165, April 1994.

RAKOV, V. A.; UMAN, M. A. **Lightning: physics and effects**. 1. ed. New York: Cambridge University Press, 2003. 687p. ISBN 978-0-521-58327-5.

RAKOV, V. A.; THOTTAPPILLIL, R.; UMAN, M. A. Electric field pulses in K and M changes of lightning ground flashes. **Journal of Geophysical Research**, v.97, n.D9, p.9935-9950, June 1992.

RAKOV, V. A.; UMAN, M. A.; THOTTAPPILLIL, R. Review of lightning properties from electric field and TV observations. **Journal of Geophysical Research**, v.99, n.D5, p.10745-10750, May 1994.

RHODES, C. T.; SHAO, X.-M.; KREHBIEL, P. R.; THOMAS, R. J.; HAYENGA, C. O. Observations of lightning phenomena using radio interferometry. **Journal of Geophysical Research**, v.99, n.D6, p.13059-13082, June 1994.

RISON, W.; THOMAS, R. J.; KREHBIEL, P. R.; HAMLIN, T.; HARLIN, J. A GPS-based three-dimensional lightning mapping system: Initial observations in Central New Mexico. **Geophysical Research Letters**, v.26, n.23, p.3573-3576, December 1999.

RISON, W.; THOMAS, R.; KREHBIEL, P.; RODEHEFFER, D.; CUMMINS, K.; QUICK, M.; MYERS, J.; WARNER, T.; SABA, M.; SCHUMANN, C.; LYONS, W.; SAMARAS, T.; SAMARAS, P.; YOUNG, C.; CUMMER, S. A.; LU, G. Lightning mapping and electric field observations of naturally induced upward positive leaders from wind turbines. In: INTERNATIONAL CONFERENCE ON ATMOSPHERIC ELECTRICITY, 15., 2014, Norman. **Proceedings...** Norman: NOAA/NSSL, 2014.

Available at:

<http://www.nssl.noaa.gov/users/mansell/icae2014/preprints/abstract_short/Rison_235.pdf>. Accessed on: Jan. 12 2016.

RUST, W. D.; MACGORMAN, D. R. Possibly inverted-polarity electrical structures in thunderstorms during STEPS. **Geophysical Research Letters**, v.29, n.12, p.GL014303, June 2002.

RUST, W. D.; MACGORMAN, D. R.; ARNOLD, R. T. Positive cloud-to-ground lightning flashes in severe storms. **Geophysical Research Letters**, v.8, n.7, p.791-794, July 1981.

RUST, W. D.; MACGORMAN, D. R.; ARNOLD, R. T. Inverted-polarity electrical structures in thunderstorms in the Severe Thunderstorm Electrification and Precipitation Study (STEPS). **Atmospheric Research**, v.76, n.1-4, p.247-271, July-August 2005.

RUTLEDGE, S. A.; MACGORMAN, D. R. Cloud-to-ground lightning activity in the 10-11 June 1985 Mesoscale Convective System observed during the Oklahoma-Kansas PRE-STORM project. **Monthly Weather Review**, v.116, n.7, p.1393-1408, July 1988.

SABA, M. M. F.; BALLAROTTI, M. G.; PINTO Jr., O. Negative cloud-to-ground lightning properties from high-speed video observations. **Journal of Geophysical Research**, v.111, n.D13, p.D03101, February 2006a.

SABA, M. M. F.; PINTO Jr., O.; BALLAROTTI, M. G. Relation between lightning return stroke peak current and following continuing current. **Geophysical Research Letters**, v.33, n.23, p.L23807, December 2006b.

SABA, M. M. F.; CUMMINS, K. L.; WARNER, T. A.; KRIDER, E. P.; CAMPOS, L. Z. S.; BALLAROTTI, M. G.; PINTO Jr., O.; FLEENOR, S. A. Positive leader characteristics from high-speed video observations. **Geophysical Research Letters**, v.35, n.7, p.L07802, April 2008.

SABA, M. M. F.; CAMPOS, L. Z. S.; KRIDER, E. P.; PINTO Jr., O. High-speed video observations of positive ground flashes produced by intracloud lightning. **Geophysical Research Letters**, v.36, n.12, p.L12811, June 2009.

SARAIVA, A. C. V.; SABA, M. M. F.; PINTO Jr., O.; CUMMINS, K. L.; KRIDER, E. P.; CAMPOS, L. Z. S. A comparative study of negative cloud-to-ground lightning characteristics in São Paulo (Brazil) and Arizona (United States) based on high-speed video observations. **Journal of Geophysical Research**, v.115, n.D11, p.D11102, June 2010.

SARAIVA, A. C. V.; PINTO Jr., O.; ZEPKA, G. S. RAMMER network observations during summer 2011/2012. In: INTERNATIONAL LIGHTNING DETECTION CONFERENCE, 22., 2012, Broomfield. **Proceedings...** Broomfield: Vaisala, 2012. Available at:

<http://www.vaisala.com/en/events/ildcilmc/Documents/Detection%20Technology/RAMMER%20Network%20Observations%20During%20Summer%202011-2012.pdf>.

Accessed on: Jan. 12 2016.

SARAIVA, A. C. V.; CAMPOS, L. Z. S.; WILLIAMS, E. R.; ZEPKA, G. S.; ALVES, J.; PINTO Jr., O.; HECKMAN, S.; BUZATO, T. S.; BAILEY, J. C.; MORALES, C. A.; BLAKESLEE, R. J. High-speed video and electromagnetic analysis of two natural bipolar cloud-to-ground lightning flashes. **Journal of Geophysical Research Atmospheres**, v.119, n.10, p.6105-6127, May 2014a.

SARAIVA, A. C. V.; CAMPOS, L. Z. S.; ANTUNES, L. S.; PINTO Jr., O.; CUMMINS, K. L. Analysis of forked strokes characteristics over southeastern Brazil during the summer season of 2013. In: INTERNATIONAL LIGHTNING DETECTION CONFERENCE, 23., 2014b, Tucson. **Proceedings...** Tucson: Vaisala, 2014. Available at:

<<http://www.vaisala.com/Vaisala%20Documents/Scientific%20papers/2014%20ILDC%20ILMC/ILDC-Tuesday/Saraiva-Analysis%20of%20Forked%20Strokes%20Characteristics%20over%20Southeastern%20Brasil-2014-ILDC-ILMC.pdf>>. Accessed on: Jan. 12 2016.

SCHONLAND, B. F. J. Progressive lightning IV – The discharge mechanism. **Proceedings of the Royal Society of London. Series A, Mathematical and Physical Sciences**, v.164, n.916, p.132-150, January 1938.

SCHONLAND, B. F. J.; MALAN, D. J.; COLLENS, H. Progressive lightning–II. **Proceedings of the Royal Society of London. Series A, Mathematical and Physical Sciences**, v.152, n.877, p.595-625, November 1935.

SCHUMANN, C.; SABA, M. M. F.; DA SILVA, R. B. G.; SCHULZ, W. Electric fields changes produced by positives cloud-to-ground lightning flashes. **Journal of Atmospheric and Solar-Terrestrial Physics**, v.92, p.37-42, January 2013.

SHAO, X.-M.; KREHBIEL, P. R.; THOMAS, R. J.; RISON, W. Radio interferometric observations of cloud-to-ground lightning phenomena in Florida. **Journal of Geophysical Research**, v.100, n.D2, p.2749-2783, February 1995.

STALL, C. A.; CUMMINS, K. L.; KRIDER, E. P.; CRAMER, J. A. Detecting multiple ground contacts in cloud-to-ground lightning flashes. **Journal of Atmospheric and Oceanic Technology**, v.26, n.11, p.2392-2402, November 2009.

STOLZENBURG, M.; RUST, W. C.; MARSHALL, T. C. Electrical structure in thunderstorm convective regions: 3. Synthesis. **Journal of Geophysical Research**, v.103, n.D12, p.14097-14108, June 1998.

- STOLZENBURG, M.; MARSHALL, T. C.; KARUNARATHNE, S.;
KARUNARATHNA, N.; WARNER, T. A.; ORVILLE, R. E.; BETZ, H.-D. Strokes of upward illumination occurring within a few milliseconds after typical lightning return strokes. **Journal of Geophysical Research**, v.117, n.D15, p.D15203, August 2012.
- STOLZENBURG, M.; MARSHALL, T. C.; KARUNARATHNE, S.;
KARUNARATHNA, N.; VICKERS, L. E.; WARNER, T. A.; ORVILLE, R. E.; BETZ, H.-D. Luminosity of initial breakdown in lightning. **Journal of Geophysical Research: Atmospheres**, v.118, n.7, p.2918-2937, April 2013a.
- STOLZENBURG, M.; MARSHALL, T. C.; KARUNARATHNE, S.;
KARUNARATHNA, N.; WARNER, T. A.; ORVILLE, R. E. Competing and cutoff leaders before “upward illumination”-type lightning ground strokes. **Journal of Geophysical Research: Atmospheres**, v.118, n.13, p.7182-7198, July 2013b.
- SUN, Z.; QIE, X.; LIU, M.; JIANG, R.; WANG, Z.; ZHANG, H. Characteristics of a negative lightning with multiple-ground terminations observed by a VHF lightning location system. **Journal of Geophysical Research: Atmospheres**, v.121, n.1, p.413-426, January 2016.
- THOMAS, R. J.; KREHBIEL, P. R.; RISON, W.; HUNYADY, S. J.; WINN, W. P.;
HAMLIN, T.; HARLIN, J. Accuracy of the Lightning Mapping Array. **Journal of Geophysical Research**, v.109, n.D14, p.D14207, July 2004.
- THOMSON, E. M.; GALIB, M. A.; UMAN, M. A.; BEASLEY, W. H.; MASTER, M. J. Some features of stroke occurrence in Florida lightning flashes. **Journal of Geophysical Research**, v.89, n.D3, p.4910-4916, June 1984.
- THOTTAPPILLIL, R.; RAKOV, V. A.; UMAN, M. A. K and M changes in close lightning ground flashes in Florida. **Journal of Geophysical Research**, v.95, n.D11, p.18631-18640, October 1990.

THOTTAPPILLIL, R.; RAKOV, V. A.; UMAN, M. A.; BEASLEY, W. H.; MASTER, M. J.; SHELUKHIN, D. V. Lightning subsequent-stroke electric field peak greater than the first stroke peak and multiple ground terminations. **Journal of Geophysical Research**, v.97, n.D7, p.7503-7509, May 1992.

UMAN, M. A. **The lightning discharge**. 1. ed. Orlando: Academic Press, 1987. 377p. ISBN 0-12-708350-2.

UMAN, M. A.; VOSHALL, R. E. Time interval between lightning strokes and the initiation of dart leaders. **Journal of Geophysical Research**, v.73, n.2, p.497-506, January 1968.

UNITED STATES GEOLOGICAL SURVEY (USGS). **Shuttle Radar Topography Mission (SRTM)**. 2016. Available at: <<https://lta.cr.usgs.gov/SRTM>>. Accessed on: Feb. 10 2016.

VALINE, W. C.; KRIDER, E. P. Statistics and characteristics of cloud-to-ground lightning with multiple ground contacts. **Journal of Geophysical Research**, v.107, n.D20, p.AAC 8-1-AAC 8-11, October 2002.

VISACRO, S. Lightning, grounding and transmission lines. In: ASIA-PACIFIC INTERNATIONAL CONFERENCE ON LIGHTNING, 9., 2015, Nagoya. **Proceedings...** Nagoya: IEIE of Japan, 2015. p.1037-1043. Pen drive.

WANG, D.; RAKOV, V. A.; UMAN, M. A.; TAKAGI, N.; WATANABE, T.; CRAWFORD, D. E.; RAMBO, K. J.; SCHNETZER, G. H.; FISHER, R. J.; KAWASAKI, Z.-I. Attachment process in rocket-triggered lightning strokes. **Journal of Geophysical Research**, v.104, n.D2, p.2143-2150, January 1999.

WANG, D.; TAKAGI, N.; WATANABE, T.; RAKOV, V. A.; UMAN, M. A. Luminosity waves in branched channels of two negative lightning flashes. **Journal of Atmospheric Electricity**, v.20, n.2, p.91-97, 2000.

WILLETT, J. C.; LE VINE, D. M.; IDONE, V. P. Lightning-channel morphology revealed by return-stroke radiation field waveforms. **Journal of Geophysical Research**, v.100, n.D2, p.2727-2738, February 1995.

WILLIAMS, E. R. The tripole structure of thunderstorms. **Journal of Geophysical Research**, v.95, n.D11, p.13151-13167, September 1989.

WILLIAMS, E. R. Problems in lightning physics – the role of polarity asymmetry. **Plasma Sources Science and Technology**, v.15, n.2, p.S91-S108, April 2006.

WINN, W. P.; ALDRIDGE, T. V.; MOORE, C. B. Video tape recordings of lightning flashes. **Journal of Geophysical Research**, v.78, n.21, p.4515-4519, July 1973.

ZOGHZOGHY, F. G.; COHEN, M. B.; SAID, R. K.; BASILICO, S. S.; BLAKESLEE, R. J.; INAN, U. S. Lightning activity following the return stroke. **Journal of Geophysical Research: Atmospheres**, v.119, n.13, p.8329-8339, July 2014.

APPENDIX A – SUMMARY OF THE PERFORMANCE EVALUATION OF THE CONTACT POINT IDENTIFICATION ALGORITHM

Table A.1 summarizes the performance efficiency of the *groupGCP* algorithm for a dataset of 25 flashes (with 114 individual return strokes) using 36 different combinations of input parameters. The shaded rows indicate the combination of parameters that resulted in the optimal performance. See Chapter 4 (and particularly section 4.2) for details.

Table A.1 – Performance efficiency for different combinations of input parameters of the *groupGCP* algorithm.

Input parameters			Individual strokes			Full flashes (all strokes, all GCPs)		
<i>maxSMA_grouping</i>	<i>maxScaleFactor</i>	<i>pScale</i>	Correctly classified	Total	Percentage	Correctly classified	Total	Percentage
0.1	1.5	1.0	112	114	98.2%	23	25	92.0%
0.1	1.5	1.5	112	114	98.2%	23	25	92.0%
0.1	1.5	2.0	112	114	98.2%	23	25	92.0%
0.1	1.8	1.0	112	114	98.2%	23	25	92.0%
0.1	1.8	1.5	112	114	98.2%	23	25	92.0%
0.1	1.8	2.0	112	114	98.2%	23	25	92.0%
0.1	2.0	1.0	112	114	98.2%	23	25	92.0%
0.1	2.0	1.5	112	114	98.2%	23	25	92.0%
0.1	2.0	2.0	112	114	98.2%	23	25	92.0%

(Continues)

Table A.1 – Continued.

Input parameters			Individual strokes			Full flashes (all strokes, all GCPs)		
<i>maxSMA_grouping</i>	<i>maxScaleFactor</i>	<i>pScale</i>	Correctly classified	Total	Percentage	Correctly classified	Total	Percentage
0.2	1.5	1.0	110	114	96.5%	22	25	88.0%
0.2	1.5	1.5	112	114	98.2%	23	25	92.0%
0.2	1.5	2.0	112	114	98.2%	23	25	92.0%
0.2	1.8	1.0	110	114	96.5%	22	25	88.0%
0.2	1.8	1.5	112	114	98.2%	23	25	92.0%
0.2	1.8	2.0	112	114	98.2%	23	25	92.0%
0.2	2.0	1.0	110	114	96.5%	22	25	88.0%
0.2	2.0	1.5	112	114	98.2%	23	25	92.0%
0.2	2.0	2.0	112	114	98.2%	23	25	92.0%
0.3	1.5	1.0	110	114	96.5%	22	25	88.0%
0.3	1.5	1.5	112	114	98.2%	23	25	92.0%
0.3	1.5	2.0	110	114	96.5%	22	25	88.0%
0.3	1.8	1.0	110	114	96.5%	22	25	88.0%
0.3	1.8	1.5	112	114	98.2%	23	25	92.0%
0.3	1.8	2.0	110	114	96.5%	22	25	88.0%
0.3	2.0	1.0	110	114	96.5%	22	25	88.0%
0.3	2.0	1.5	112	114	98.2%	23	25	92.0%
0.3	2.0	2.0	110	114	96.5%	22	25	88.0%

(Continues)

Table A.1 – Conclusion.

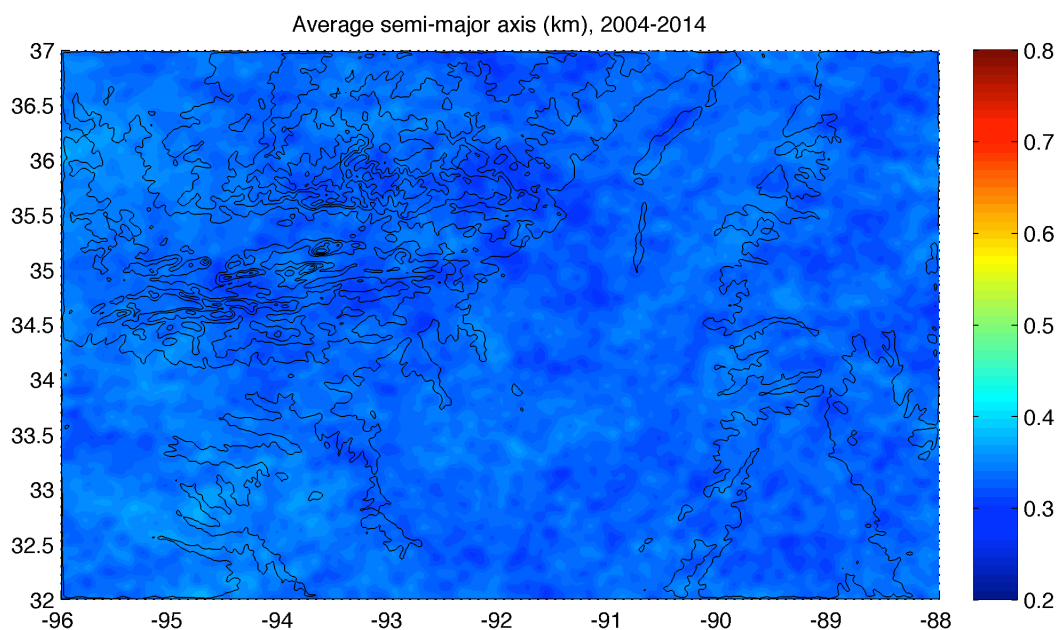
Input parameters			Individual strokes			Full flashes (all strokes, all GCPs)		
<i>maxSMA_grouping</i>	<i>maxScaleFactor</i>	<i>pScale</i>	Correctly classified	Total	Percentage	Correctly classified	Total	Percentage
0.5	1.5	1.0	112	114	98.2%	23	25	92.0%
0.5	1.5	1.5	112	114	98.2%	23	25	92.0%
0.5	1.5	2.0	111	114	97.4%	23	25	92.0%
0.5	1.8	1.0	112	114	98.2%	23	25	92.0%
0.5	1.8	1.5	112	114	98.2%	23	25	92.0%
0.5	1.8	2.0	111	114	97.4%	23	25	92.0%
0.5	2.0	1.0	112	114	98.2%	23	25	92.0%
0.5	2.0	1.5	112	114	98.2%	23	25	92.0%
0.5	2.0	2.0	111	114	97.4%	23	25	92.0%

Source: produced by the author.

APPENDIX B – MAPS OF LIGHTNING LOCATION SYSTEM DATA QUALITY PARAMETERS OF THE THREE ANALYZED DOMAINS

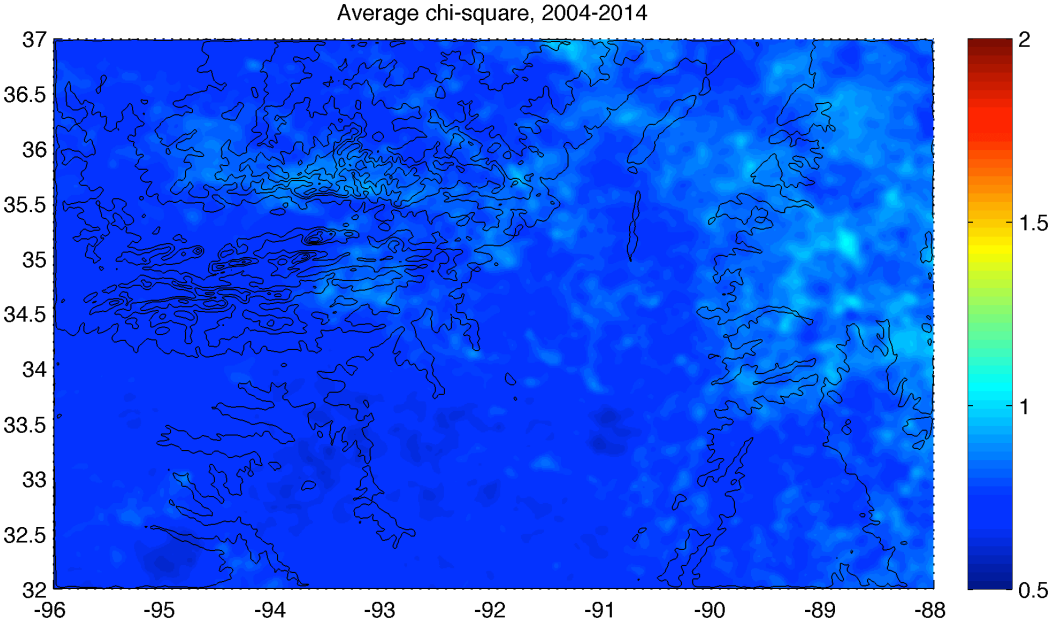
This Appendix presents the spatial distribution of parameters provided by a Lightning Location Systems that are related to its data quality. Maps for each one of the three analyzed domains (Arkansas, Arizona and Kansas) are presented. See section 7.4 (and its respective subsections) for a discussion on these results.

Figure B.1 – Spatial distribution of the mean error ellipse semi-major axis (SMA) in kilometers of the Arkansas domain.



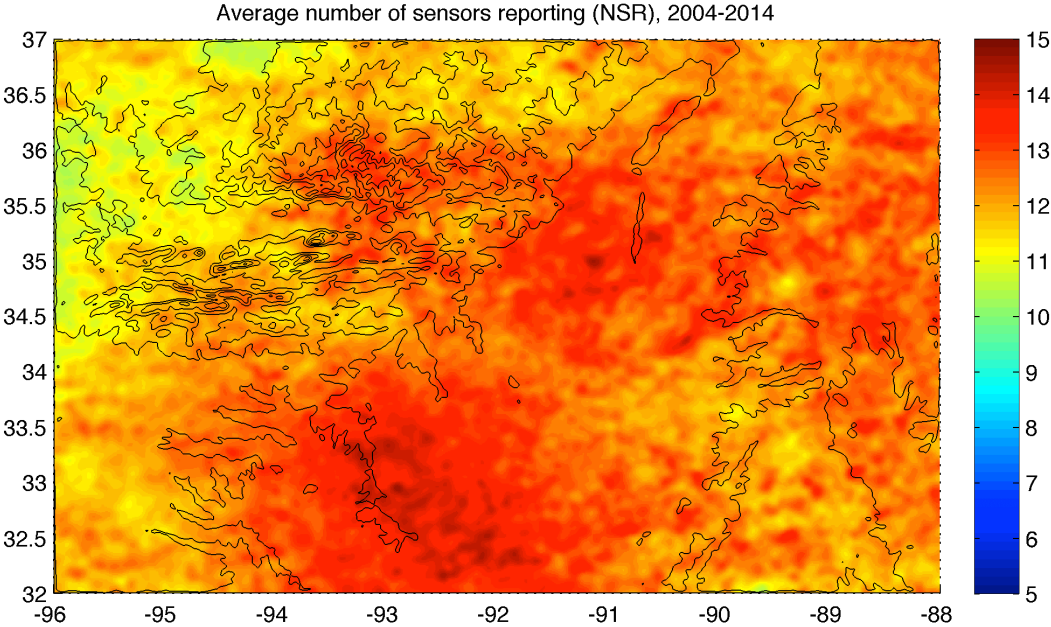
Source: produced by the author.

Figure B.2 – Spatial distribution of the mean chi-squared value of the Arkansas domain.



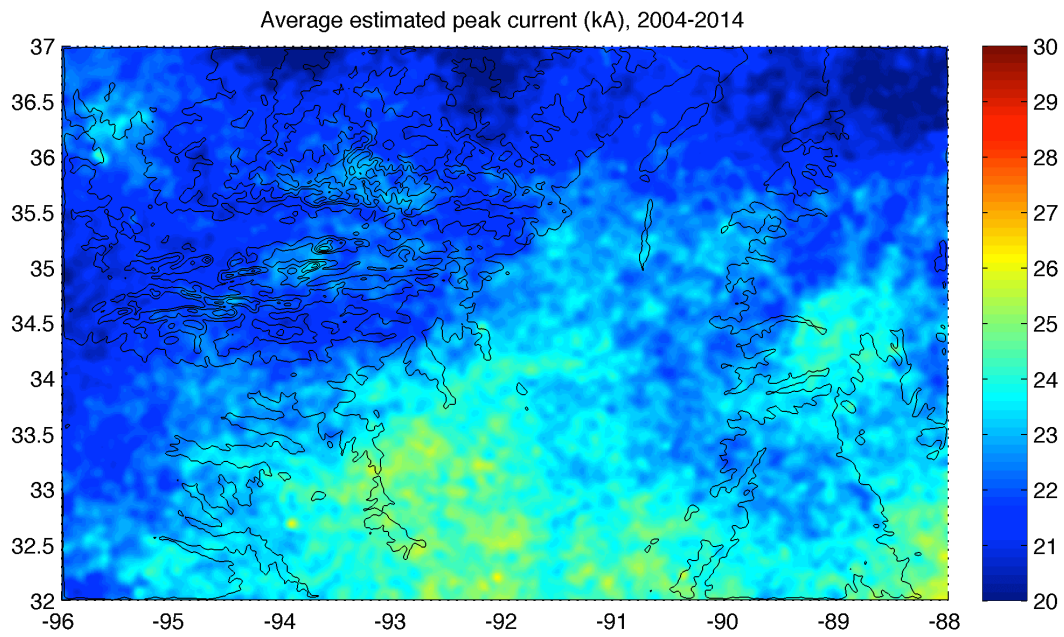
Source: produced by the author.

Figure B.3 – Spatial distribution of the mean number of sensors reporting (NSR) of the Arkansas domain.



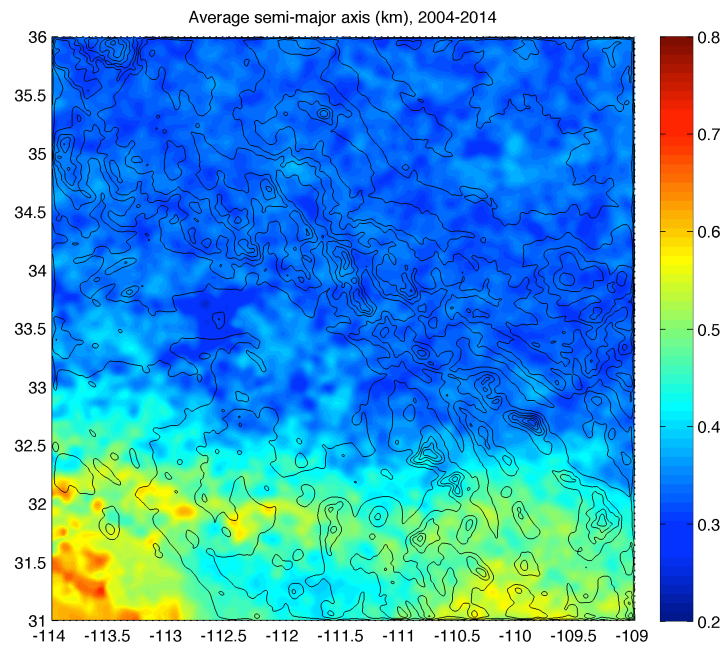
Source: produced by the author.

Figure B.4 – Spatial distribution of the mean estimated peak current (I_p) in kiloamperes of the Arkansas domain (negative return strokes only).



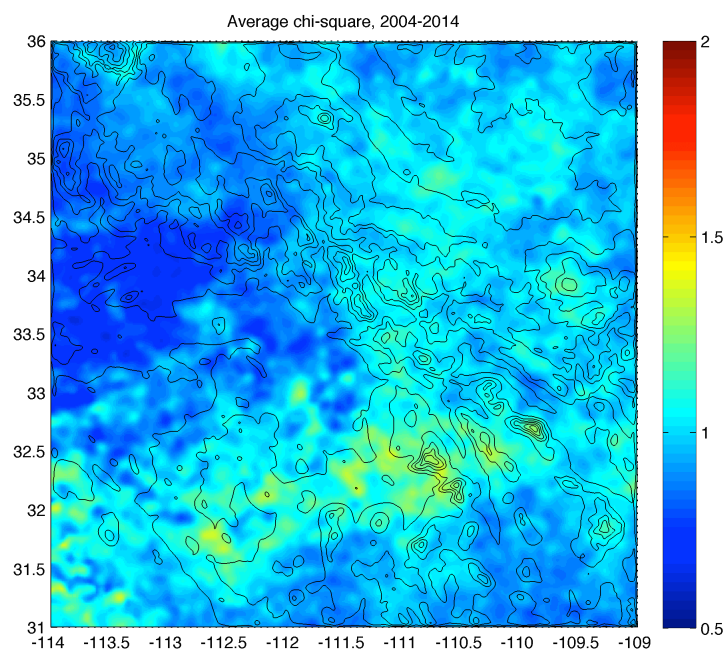
Source: produced by the author.

Figure B.5 – Spatial distribution of the mean error ellipse semi-major axis (SMA) in kilometers of the Arizona domain.



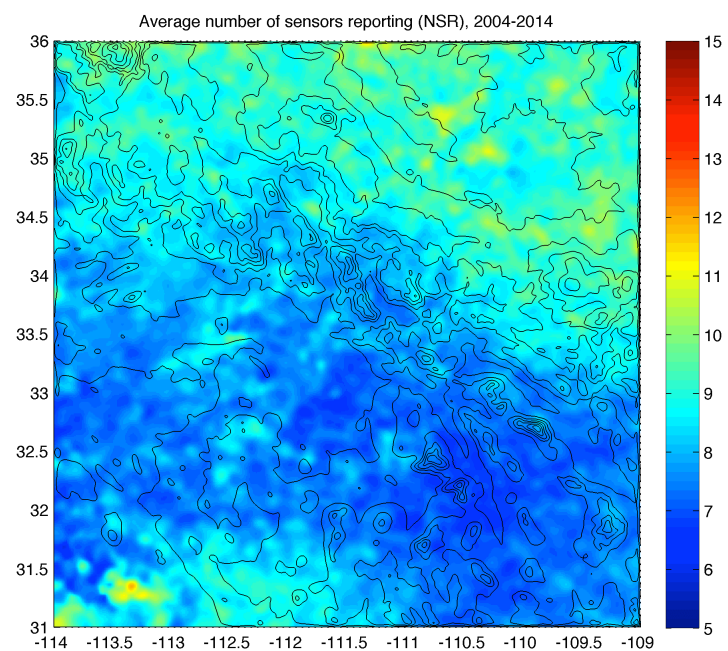
Source: produced by the author.

Figure B.6 – Spatial distribution of the mean chi-squared value of the Arizona domain.



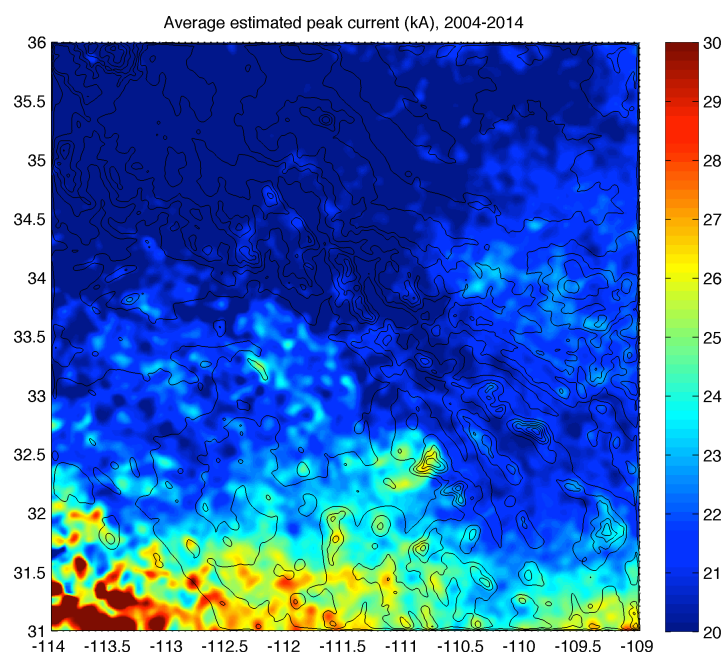
Source: produced by the author.

Figure B.7 – Spatial distribution of the mean number of sensors reporting (NSR) of the Arizona domain.



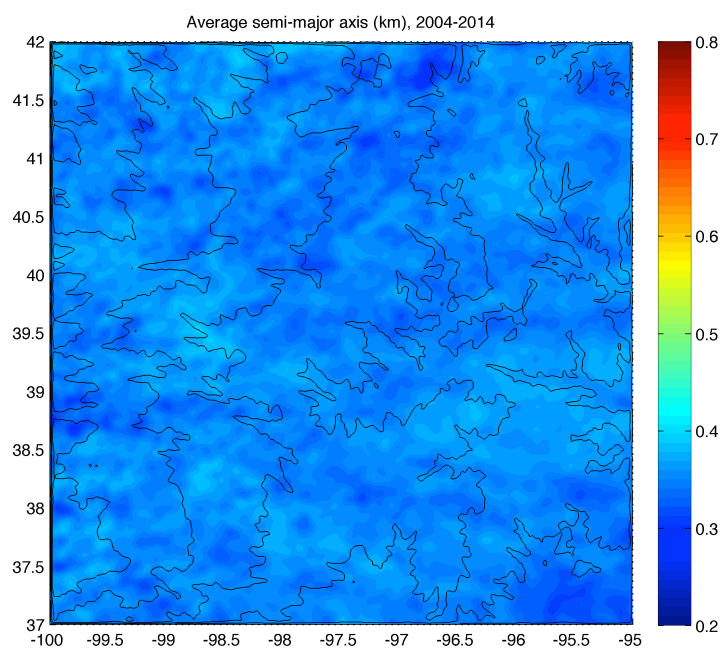
Source: produced by the author.

Figure B.8 – Spatial distribution of the mean estimated peak current (I_p) in kiloamperes of the Arizona domain (negative return strokes only).



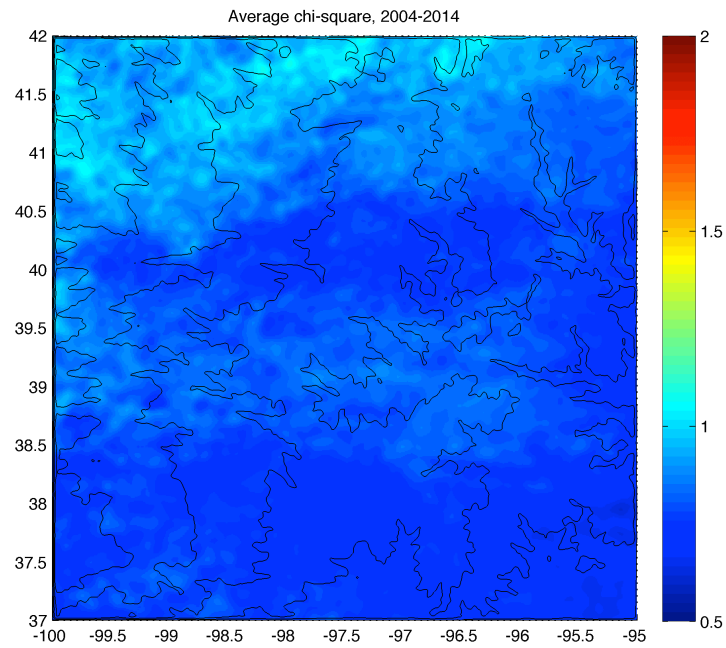
Source: produced by the author.

Figure B.9 – Spatial distribution of the mean error ellipse semi-major axis (SMA) in kilometers of the Kansas domain.



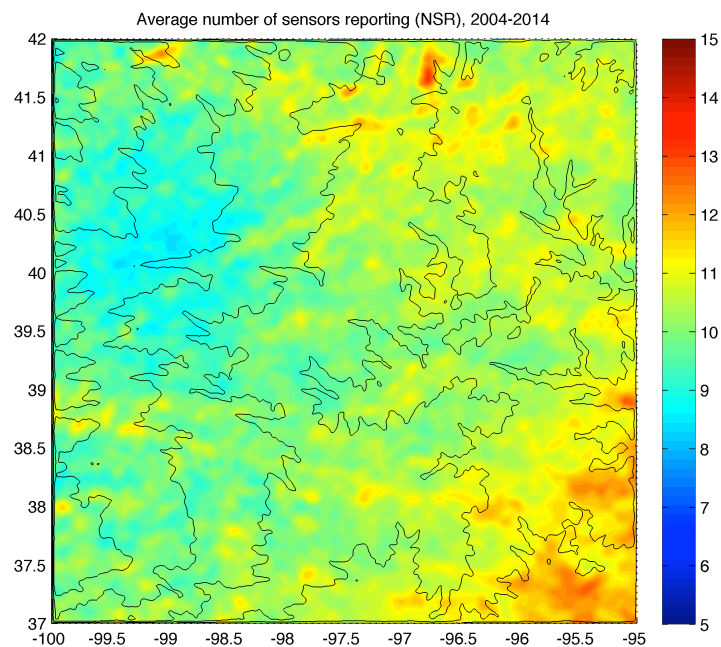
Source: produced by the author.

Figure B.10 – Spatial distribution of the mean chi-squared value of the Kansas domain.



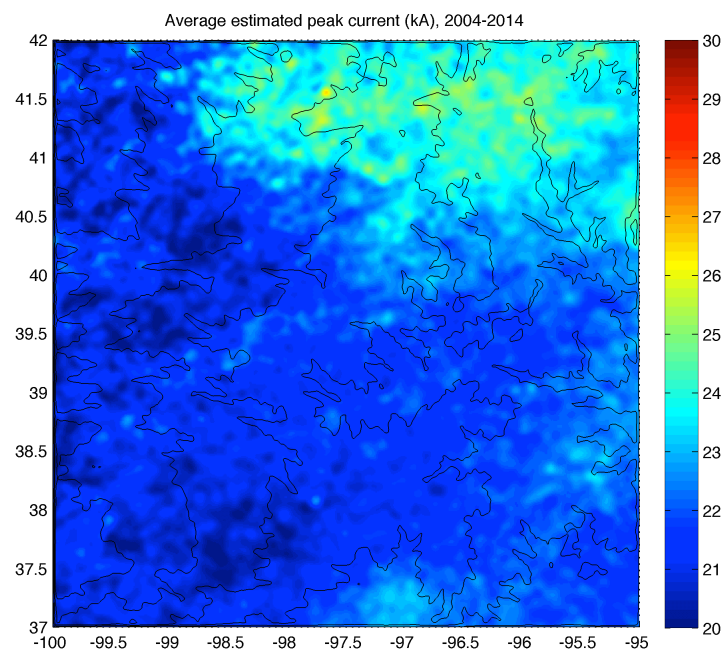
Source: produced by the author.

Figure B.11 – Spatial distribution of the mean number of sensors reporting (NSR) of the Kansas domain.



Source: produced by the author.

Figure B.12 – Spatial distribution of the mean estimated peak current (I_p) in kiloamperes of the Kansas domain (negative return strokes only).

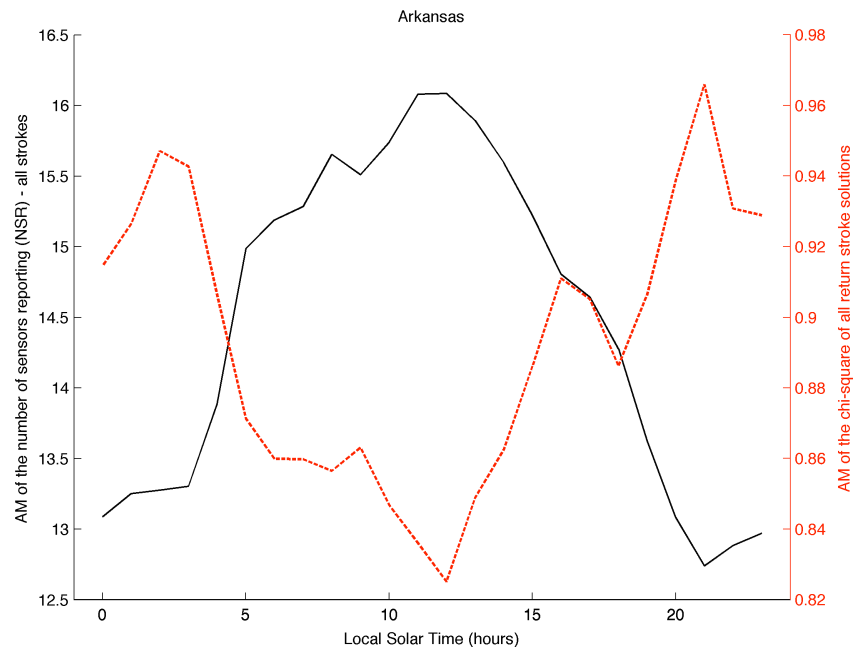


Source: produced by the author.

APPENDIX C – DIURNAL VARIATIONS OF LIGHTNING LOCATION SYSTEM DATA QUALITY PARAMETERS OF THE THREE ANALYZED DOMAINS

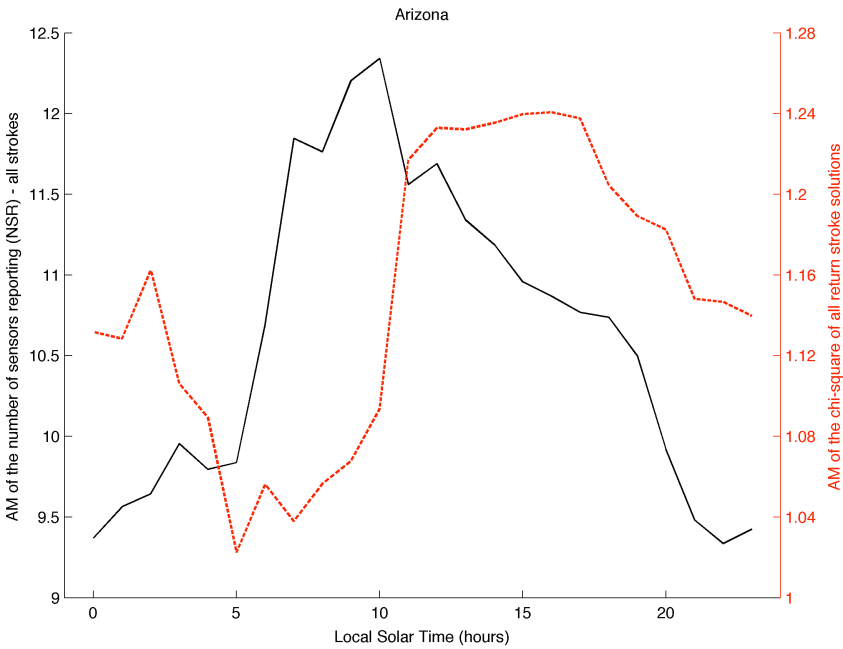
This Appendix presents the diurnal variation of parameters provided by a Lightning Location Systems that are related to its data quality. The cycles correspond to each one of the three analyzed domains (Arkansas, Arizona and Kansas) including only flashes in which no return stroke presented a value of error ellipse semi-major axis (SMA) greater than 0.2 km. See section 8.2 for a discussion on these results.

Figure C.1 – Hourly plots of the AM of the number of sensors reporting (NSR) and the chi-squared value of all return stroke solutions in the Arkansas domain.



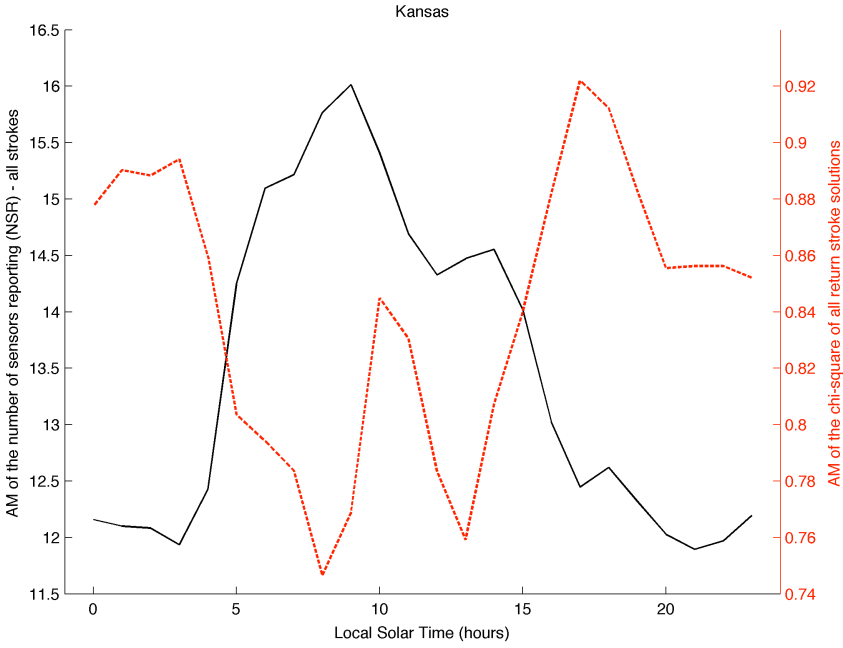
Source: produced by the author.

Figure C.2 – Hourly plots of the AM of the number of sensors reporting (NSR) and the chi-squared value of all return stroke solutions in the Arizona domain.



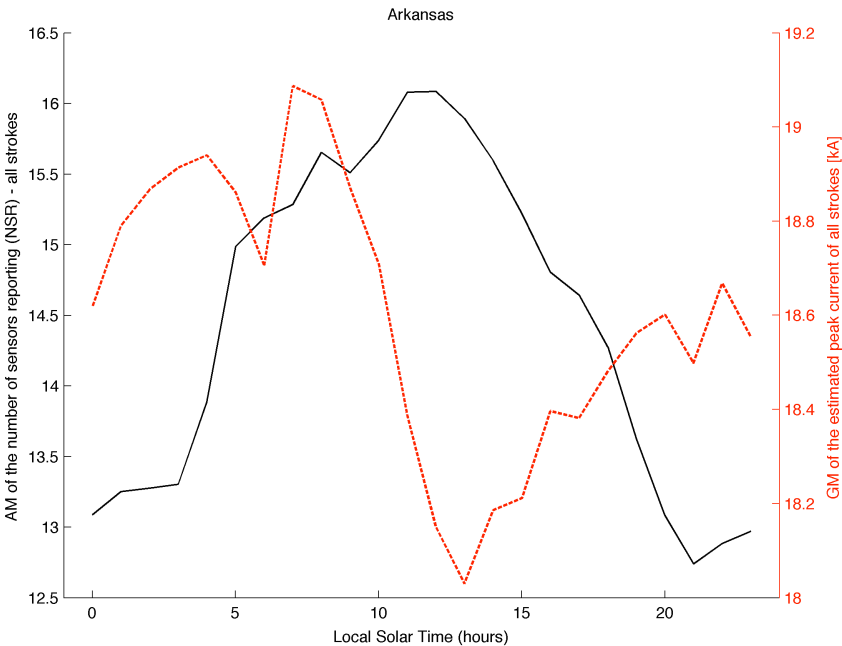
Source: produced by the author.

Figure C.3 – Hourly plots of the AM of the number of sensors reporting (NSR) and the chi-squared value of all return stroke solutions in the Kansas domain.



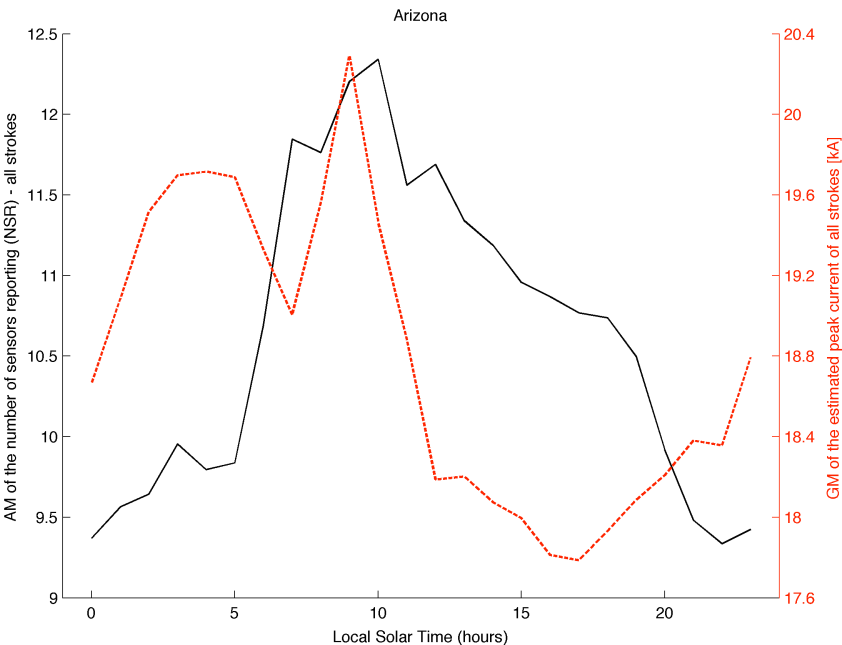
Source: produced by the author.

Figure C.4 – Hourly plots of the AM of the number of sensors reporting (NSR) and the GM of the estimated peak current of all return stroke solutions in the Arkansas domain.



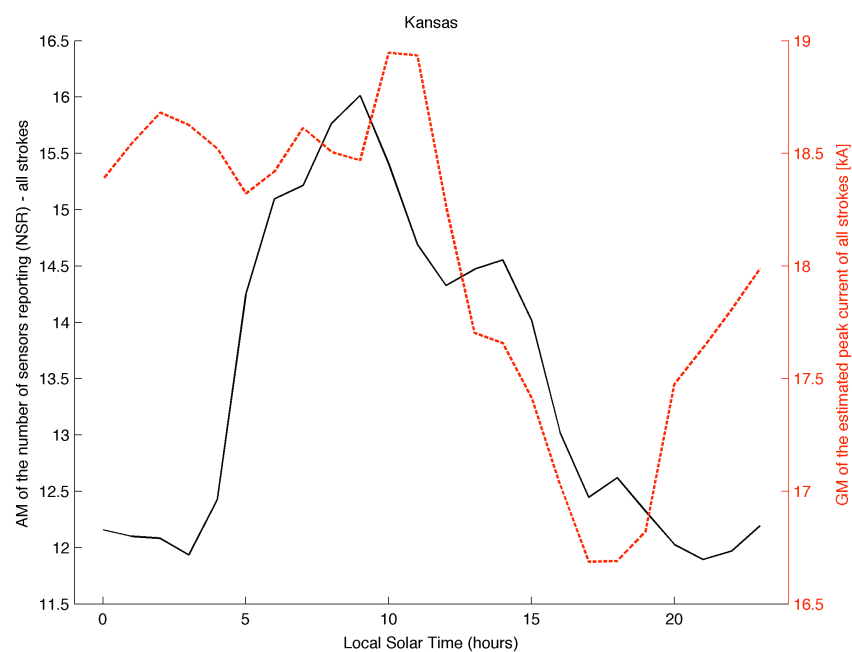
Source: produced by the author.

Figure C.5 – Hourly plots of the AM of the number of sensors reporting (NSR) and the GM of the estimated peak current of all return stroke solutions in the Arizona domain.



Source: produced by the author.

Figure C.6 – Hourly plots of the AM of the number of sensors reporting (NSR) and the GM of the estimated peak current of all return stroke solutions in the Kansas domain.



Source: produced by the author.

PUBLICAÇÕES TÉCNICO-CIENTÍFICAS EDITADAS PELO INPE

Teses e Dissertações (TDI)

Teses e Dissertações apresentadas nos Cursos de Pós-Graduação do INPE.

Manuais Técnicos (MAN)

São publicações de caráter técnico que incluem normas, procedimentos, instruções e orientações.

Notas Técnico-Científicas (NTC)

Incluem resultados preliminares de pesquisa, descrição de equipamentos, descrição e ou documentação de programa de computador, descrição de sistemas e experimentos, apresentação de testes, dados, atlas, e documentação de projetos de engenharia.

Relatórios de Pesquisa (RPQ)

Reportam resultados ou progressos de pesquisas tanto de natureza técnica quanto científica, cujo nível seja compatível com o de uma publicação em periódico nacional ou internacional.

Propostas e Relatórios de Projetos (PRP)

São propostas de projetos técnico-científicos e relatórios de acompanhamento de projetos, atividades e convênios.

Publicações Didáticas (PUD)

Incluem apostilas, notas de aula e manuais didáticos.

Publicações Seriadas

São os seriados técnico-científicos: boletins, periódicos, anuários e anais de eventos (simpósios e congressos). Consta destas publicações o Internacional Standard Serial Number (ISSN), que é um código único e definitivo para identificação de títulos de seriados.

Programas de Computador (PDC)

São as sequências de instruções ou códigos, expressos em uma linguagem de programação compilada ou interpretada, a ser executada por um computador para alcançar um determinado objetivo. São aceitos tanto programas fonte quanto executáveis.

Pré-publicações (PRE)

Todos os artigos publicados em periódicos, anais e como capítulos de livros.